UNIVERSITY OF CALIFORNIA SAN DIEGO

Seismic Response Verification of Reinforced Concrete Structural Wall Systems

A dissertation submitted in partial satisfaction of the

requirements for the degree Doctor of Philosophy

in

Structural Engineering

by

Rodolfo Alvarez Sanchez

Committee in charge:

Professor José I. Restrepo, Chair
Professor Joel P. Conte
Professor Veronica Eliasson
Professor Yuri Fialko
Professor Sashi Kunnath

2020

The dissertation of Rodolfo Alvarez Sanchez is approved, and it is acceptable in quality and form for publication on microfilm and electronically:

_____

_____

_____

_____

_____
Chair

University of California San Diego

2020

DEDICATION

To my wife, Thelma, and my children, Santiago and Rodolfo.

To my parents, Rodolfo and Maria Elena, and my sisters, Alma and Isela

TABLE OF CONTENTS

SIGNATURE PAGE ……iii

DEDICATION …….....iv

TABLE OF CONTENTS..... v

LIST OF SYMBOLS viii

LIST OF FIGURES xvi

LIST OF TABLES..... xxii

ACKNOWLEDGMENTS xxiii

VITA..... xxv

ABSTRACT OF THE DISSERTATION xxvii

Chapter 1. Introduction..... 1

1.1 Motivation..... 1

1.2 Objectives and scope..... 3

1.3 Outline..... 5

Chapter 2. Nonlinear Cyclic Truss Model for Analysis of Reinforced Concrete Coupled Structural Walls..... 8

2.1 Abstract..... 8

2.2 Introduction..... 9

2.3 Description of the Truss Model 11

2.4 Case studies..... 16

2.5 Comparison of responses 24

2.6 Evaluation of computed responses not measured in the tests 31

2.7 Conclusions 35

2.8 Acknowledgements 37

Chapter 3. Analysis of Reinforced Concrete Coupled Structural Walls Via the Beam-Truss Model 38

3.1 Abstract 38

3.2 Introduction 39

3.3 Description of specimens 43

3.4 Description of the modified Beam-Truss Model 46

3.5 Description of the Enhanced Beam-Truss Model 53

3.6 Model validation 56

3.7 Impact of findings on current practice. 78

3.8 Conclusions 80

3.9 Acknowledgements 82

Chapter 4. RC Wall Plastic Hinge Out-of-Plane Buckling – Analysis Using the Nonlinear Beam-Truss Model 84

4.1 Abstract 84

4.2 Introduction 84

4.3 Literature review 87

4.4 Description of the analysis methodology 90

4.5 Parametric studies 99

4.6 Model validation 107

4.7 Conclusions 125

4.8 Acknowledgments 127

Chapter 5. Enhanced Beam-Truss Model for Nonlinear Analysis of RC Core Walls 129

5.1 Abstract 129

5.2 Introduction 130

5.3 Literature review 134

5.4 Core wall case study building 138

5.5 Hybrid Fiber-Section – Enhanced Beam-Truss Model 145

5.6 Hybrid Fiber-Section – Enhanced Beam-Truss Model for case study . 154

5.7 Nonlinear static analysis 158

5.8 Conclusions 185

5.9 Acknowledgments 188

REFERENCES 190

LIST OF SYMBOLS

a	Horizontal dimension of a quadrilateral in the grid
A_{cc}	Confined area
A_{cv}	Area considered for shear
A_{cw}	Area of concrete cross-section
A_g	Gross area
A_s	Area of reinforcement
A_v	Area of transverse reinforcement
$A_{v,min}$	Minimum area of transverse reinforcement
b_{eff}	Effective width of diagonals
b_w	Width of the cross-section
BTM	Beam-Truss Model
c	Length of the compression zone
C_d	Deflection amplification factor
CEC	Coupling efficiency coefficient
CEC_{EBTM}	Coupling efficiency coefficient for EBTM
CEC_{TM}	Coupling efficiency coefficient for TM
CQC	Complete quadratic combination
d	Effective depth
d_b	Bar diameter
d_{vl}	Distance between the vertical outer lines of the grid
DBE	Displacement-based element
DOF	Degree of freedom

DSFM	Disturbed-Stress-Field-Model
e_1, e_2, e_3	Characteristic displacements of slip element
E_c	Modulus of elasticity of concrete
EBTM	Enhanced Beam-Truss Model
ELF	Equivalent lateral force
f'_c	Compressive strength of concrete
f_{cc}	Compressive strength of confined concrete
f_{cu}	Residual compressive strength
f_l	Confining stress
f_r	Modulus of rupture of concrete
f_{sh}	Strength at the onset of hardening
$f_{sh,1}$	Strength in hardening branch
f_t	Tensile strength of concrete
f_{td}	Tensile strength in diagonals
f_u	Stress at ultimate strength
f_{Vc}	Factor to consider the interaction of shear forces
f_{Vo}	Factor to adjust nominal to ultimate shear capacity
f_{Vs}	Factor to consider the efficiency of shear reinforcement
f_y	Yield stress
$f_{y,t}$	Yield stress of the transversal reinforcement
f_1	Maximum vertical stress
FBE	Force-based element
FEM	Finite element method

G	Shear modulus
G_{fc}	Fracture energy in compression
G_{fcc}	Fracture energy in compression of confined concrete
GUI	Graphic user interface
h	Coupling beam depth
h_c	Height of the control point
h_{EBTM}	Height of the EBTM portion
h_u	Laterally unsupported height
h_v	Shear span
h_w	Height of the wall
HyEBTM	Hybrid Fiber-Section – Enhanced Beam-Truss Model
I_g	Inertia of the gross section
I_y	Out-of-plane inertia
I_z	In-plane inertia
J	Torsional constant of the gross section
k_e	Confinement efficiency coefficient
K_o	Stiffness of the elastic branch
l_c	Coupling beam length
l_d	Development length of reinforcement
l_{flange}	Length of the flange
l_n	Length of the clear span measured face-to-face of supports
l_{SR}	Slenderness ratio of bar
l_v	Vertical element length

l_w	Length of the wall
l_{web}	Length of web
L	Wall pier span
L_b	Length of slip-element
L_c	Tributary length
L_e	Length of the element
L_g	Length of the gauge-element
L_r	Reference length
L_u	Unsupported length of the bar
M	Base bending moment
M_a, M_b	Base moments of the wall piers
M_{OT}	Overturning moment
M_w	Moment magnitude
MBTM	Modified Beam-Truss Model
MCFT	Modified-Compression-Field-Theory
MRSA	Modal Response Spectrum Analysis
MVLEM	Multiple-Vertical-Line-Element-Model
N	Total vertical load including self-weight
N_u	Axial load
NLRHA	Nonlinear response history analysis
NTM	Nonlinear Truss Model
OS	OpenSees
P	Vertical force

P_{sh}	Exponent of power function in *SteelDRC*
PBD	Performance-based design
PGA	Peak ground acceleration
R	Response modification coefficient
R_x, R_y, R_z	Rotational degree of freedom
RC	Reinforced concrete
s	Spacing of transverse reinforcement
sK_o	Slope of softening branch
s_y	Elongation at the yield
s_1, s_2, s_3	Characteristic forces of slip-element
SP	Strain penetration
SRC	Steel reinforced concrete
STRC	Steel truss reinforced concrete
t_w	Wall thickness
T_{1X}, T_{1Y}	Period of the first mode in X and Y directions, respectively
T_{2X}, T_{2Y}	Period of the second mode in X and Y directions, respectively
U_x, U_y, U_z	Translational degrees of freedom
V	Base shear
$V_{ave\text{-}ACI\text{-}limit}$	$\phi \cdot 0.66A_{cv}\sqrt{f'_c}$ (MPa), $\phi = 0.75$
$V_{ACI\ limit}$	$0.83A_{cv}\sqrt{f'_c}$ (MPa) [$10A_{cv}\sqrt{f'_c}$ (psi)]
V_{max}	Computed peak base shear
$\hat{V}_{max}$	Measured peak base shear
V_n	Nominal shear strength

$V_{n\ min}$	Minimum shear strength
V_o	Ultimate shear strength
$V_{pier\text{-}ACI\text{-}limit}$	$\phi \cdot 0.83 A_{cv} \sqrt{f'_c}$ (MPa), $\phi = 0.75$
V_{res}	Residual strength
V_s	Shear reinforcement strength
V_u	Factored shear force
V^*	Theoretical ultimate base shear
W	Simulated gravitational force
W_t	Seismic weight
2D	Two dimensional
3D	Three dimensional
β	Compressive strength reduction factor
β_{int}, β_{res}	Characteristic strength reduction factors
γ	Shear strain of the coupling beam
γ_{max}	Maximum shear strain
γ_{xy}	Shear strain
γ_1, γ_2,	Inclination of vertical and horizontal sections, respectively
Δ_p	Peak in-plane lateral displacement
Δ_r	Residual deformation
Δ_Y	Out-of-plane displacements
Δ'_{Yp}	Peak measured out-of-plane displacements
ε_{bint}, ε_{bres}	Characteristic stains for the strength reduction factor
ε_{co}	Strain at compressive strength of confined concrete

ε_{cs}	Strain at the onset of softening
ε_{cu}	Strain at crushing
ε_{ccu}	Strain at the crushing of confined concrete
ε_{jm}, ε_{il}	Strains of the diagonals
ε_o	Strain at the compressive strength
ε_{sh}	Strain at the onset of hardening
$\varepsilon_{sh,1}$	Strain in hardening branch
ε_{tb}	Maximum computed steel strain prior to peak out-of-plane displacement
ε_u	Strain at ultimate strength
ε_x, ε_{x1}, ε_y	Strains of horizontal, diagonal, and vertical elements, respectively
ε_y	Yield strain
ε_z	Vertical strain
ε_1, ε_2	Maximum and minimum principal strains, respectively
ξ	Damping ratio
θ_d	Inclination of diagonals
Θ	In-plane lateral drift, or top drift ratio
Θ_{pk}	Peak in-plane lateral drift
Θ_{pp}	Peak drift ratio prior to computed Δ_Y
Θ_s	Inter-story drift ratio
λ_s	Size effect modification factor
ρ	Amplification redundancy factor
ρ_h	Horizontal steel ratio

ρ_l	Average vertical steel ratio
ρ_s	Steel ratio
ρ_t	Steel ratio of transversal reinforcement
ρ_w	Longitudinal steel ratio
ϕ	Strength reduction factor
Ω_{fac}	Factor to control Bauschinger effect in *SteelDRC*

LIST OF FIGURES

Figure 2.1. Determination of components geometry for the 2D version of the Truss Model methodology. 14

Figure 2.2. Uniaxial materials used in the Truss Model. **(a)** Strain-stress relationship for *ConcretewBeta* (Lu and Panagiotou 2013). **(b)** Model parameters for material *SteelDRC* (Carreño 2018). 15

Figure 2.3. Dimensions and reinforcement details for wall piers and coupling beams of Wall A and Wall B. 17

Figure 2.4. Description of the Truss Models of Walls A and B. 21

Figure 2.5. Comparison of Truss Models and test results: base shear – roof displacement. **(a)** Wall A. **(b)** Wall B (theoretical ultimate base shear in Wall A V^* = 230 kN and Wall B V^* = 252 kN).. 26

Figure 2.6. (a) Deformed shape of model Wall A at maximum displacement (2x). **(b)** Wall A after the test. **(c)** Deformed shape of model Wall B at maximum displacement (2x). **(d)** Wall B after the test.. 27

Figure 2.7. (a) Minimum principal strains ε_2 at maximum drift in Wall A (strains calculated according to Zhang et al. 2017). **(b)** Cracks formed in the Wall A at the base in the semi-cycle 12 (pictures from Santhakumar 1974). 27

Figure 2.8. (a) Average strains in flexural reinforcement of tension corners in coupling beams of Wall A. **(b)** Average strains of diagonal reinforcement in tension for coupling beams of Wall B. 29

Figure 2.9. Dilatation of coupled walls last cycles. **(a)** Wall A. **(b)** Wall B..... 30

Figure 2.10. (a) History of axial force distribution in Wall A. **(b)** History of axial force distribution in Wall B (simulated gravitational force W = -222 kN). 33

Figure 2.11. Normalized shear force - shear strain relationships computed for the first-level coupling beam and for the roof coupling beam. **(a)** Wall A. **(b)** Wall B.. 34

Figure 2.12. Distribution of base shear in the left wall and right wall for peaks of semi-cycles (blue color indicates the wall is in compression while green corresponds to the wall in tension). **(a)** Wall A. **(b)** Wall B..... 35

Figure 3.1. Geometry and reinforcement details of specimens Wall A and B. ... 44

Figure 3.2. Description of the geometry and the type of elements used in the MBTM. 48

Figure 3.3. Uniaxial constitutive material stress-strain relationships. **(a)** Stress-strain relationship for *SteelDRC*. **(b)** Stress-strain relationship for *ConcretewBeta*. 49

Figure 3.4. Specific details of the MBTM of the specimens Wall A and Wall B. 52

Figure 3.5. Coupling beam modeling details used in the EBTM. **(a)** Specimen Wall A. **(b)** Specimen Wall B. 54

Figure 3.6. Calibration of the Hysteretic Material for bond-slip of the reinforcement of the coupling beams. 56

Figure 3.7. MBTM computed and measured the base shear - drift ratio. **(a)** Specimen Wall A. **(b)** Specimen Wall B. Where the code-calculated ultimate base shear, V^*, is 230 kN for specimen Wall A and 252 kN for specimen Wall B. 57

Figure 3.8. EBTM computed and measured the base shear - drift ratio. **(a)** Specimen Wall A. **(b)** Specimen Wall B. Where the code-calculated ultimate base shear, V^*, is 230 kN for specimen Wall A and 252 kN for specimen Wall B. 60

Figure 3.9. (a) EBTM deformed the shape of specimen Wall A at maximum drift ratio (2x). **(b)** Specimen Wall A at the end of the test. **(c)** EBTM deformed the shape of specimen Wall B at maximum drift ratio (2x). **(d)** Specimen Wall B at the end of the test. 61

Figure 3.10. EBTM computed and measured strains of the reinforcement at the tension corners of the coupling beams. **(a)** Specimen Wall A. **(b)** Specimen Wall B. Where x / x.xx = Semi-cycle / Ratio V/V^*. 62

Figure 3.11. EBTM computed and measured specimen dilatations. **(a)** Specimen Wall A. **(b)** Specimen Wall B. Where x / x.xx = Semi-cycle / Ratio V/V^* 64

Figure 3.12. EBTM computed and measured strains at the outermost longitudinal reinforcement of the left wall pier (Bars F). **(a)** Specimen Wall A. **(b)** Specimen Wall B. Where x / x.xx = Semi-cycle / Ratio V/V^*. 64

Figure 3.13. EBTM computed and measured strains at the innermost longitudinal reinforcement of the left wall pier (Bars D). **(a)** Specimen Wall A. **(b)** Specimen Wall B. Where x / x.xx = Semi-cycle / Ratio V/V^*. 65

Figure 3.14. Strain color plots calculated using the EBTM of specimen Wall B at the peak of the semi-cycle 15 (drift ratio 2.5%). **(a)** Vertical strains ε_y. **(b)** Minimum principal strains ε_2. 67

Figure 3.15. Strain color plots calculated using the EBTM at the base of specimen Wall B at the peak of the semi-cycle 15 (drift ratio 2.5%). **(a)** Horizontal strains ε_x. **(b)** Vertical strains ε_y. **(c)** Shear strains γ_{xy}. **(d)** Maximum principal strains ε_1. **(e)** Minimum principal strains ε_2. **(f)** Maximum shear strains γ_{max}. 68

Figure 3.16. EBTM and NTM computed base shear - drift ratio. **(a)** Specimen Wall A. **(b)** Specimen Wall B. Where the code-calculated ultimate base shear, V^*, is 230 kN for specimen Wall A and 252 kN for specimen Wall B. 70

Figure 3.17. EBTM and NTM computed reinforcement tensile strains at the coupling beam corners. **(a)** Specimen Wall A. **(b)** Specimen Wall B. Where x / x.xx = Semi-cycle / Ratio V/V^*. 72

Figure 3.18. Base shear distribution in the wall piers for semi-cycles peaks computed using EBTM and NTM. **(a)** Specimen Wall A. **(b)** Specimen Wall B. 74

Figure 3.19. EBTM and NTM computed shear force - shear strain in coupling beams of Wall A. **(a)** Level 7. **(b)** Level 1. The code-calculated capacity was computed using measured material properties. 76

Figure 3.20. EBTM and NTM computed shear force - shear strain in coupling beams of Wall B. **(a)** Level 7. **(b)** Level 1. The code-calculated capacity was computed using measured material properties. 77

Figure 3.21. Computation of shear strain (γ) in a coupling beam. 78

Figure 4.1. Description of the Beam-Truss Model – Structural component..... 92

Figure 4.2. Description of the Beam-Truss Model. **(a)** Definition of the geometry and type of elements used. **(b)** Approach for modeling strain penetration. 93

Figure 4.3. Materials used in the Beam-Truss Model. **(a)** Stress-strain relationship for ConcretewBeta (reprinted from Lu and Panagiotou 2013,©ASCE). **(b)** Compressive strength reduction factor β (Lu et al. 2014). **(c)** Stress-strain relationship for SteelDRC (adapted from Carreño 2018). 96

Figure 4.4. Implementation of the Beam-Truss Model in OpenSees using displacement-based elements and fiber-section with layers. 98

Figure 4.5. (a) Case Study 1 – TW1, south end at the end of the test after failure (Almeida et al. 2017). **(b)** Case Study 2 – RWL, west end out-of-plane instability

(Dashti 2017). **(c)** Case Study 3 – Wall2, east end showing buckling to the south (Goodsir 1985). 100

Figure 4.6. Comparison of base shear force − top displacement computed using torsional rigidity equal to 0.02GJ (BTM) and 0.1GJ. **(a)** Case Study 1 − TW1. **(b)** Case Study 2 – RWL. **(c)** Case Study 3 – Wall2. 104

Figure 4.7. Description of the Beam-Truss Model with Cages for Case Study 3 − Wall2. 105

Figure 4.8. BTM-Cages responses, Case Study 3 – Wall2. **(a)** Base moment − top displacement. **(b)** Out-of-plane displacement (Δ_Y) at height $0.53h_u$ (height of computed peak Δ_Y) at the east end. **(c)** Line color map at peak out-of-plane displacement (inches, 10x)..... 107

Figure 4.9. Case Study 1 − TW1. **(a)** Description of the test specimen. **(b)** Description of the Beam-Truss Model. **(c)** Material properties..... 109

Figure 4.10. Results of the BTM for Case Study 1 − TW1. **(a)** Base shear force − top displacement. **(b)** Out-of-plane displacement (Δ_Y) at height $0.4h_u$ (height of measured peak Δ_Y) at the south end. **(c)** South end vertical reinforcement strains for cycle 1 of large amplitude positive peak drift ratios (Θ_{pk}). 111

Figure 4.11. Contours of the BTM for Case of Study 1 − TW1. **(a)** Out-of-plane displacement ratio Δ_Y/t_w. **(b)** Minimum principal strains ε_2 in the compression face. **(c)** Vertical strains ε_z in the axis of the wall 113

Figure 4.12. Case Study 2 – RWL. **(a)** Description of the test specimen. **(b)** Description of the Beam-Truss Model. **(c)** Material properties..... 115

Figure 4.13. Results of the BTM for Case Study 2 – RWL. **(a)** Base shear force − top displacement. **(b)** Out-of-plane displacement (Δ_Y) at height $0.3h_u$ (height of measured peak Δ_Y) at the west end. **(c)** West end vertical reinforcement strains for cycle 1 of large amplitude positive peak drift ratios (Θ_{pk}). 117

Figure 4.14. Contours of the BTM for Case of Study 2 – RWL. **(a)** Out-of-plane displacement ratio Δ_Y/t_w. **(b)** Minimum principal strains ε_2 in the compression face. **(c)** Vertical strains ε_z in the axis of the wall. 118

Figure 4.15. Case Study 3 − Wall2: (a) Description of the test specimen; (b) Description of the Beam-Truss Model; (c) Material properties..... 120

Figure 4.16. Results of the BTM for Case Study 3 − Wall2. **(a)** Base moment − top displacement. **(b)** Out-of-plane displacement (Δ_Y) at height $0.53h_u$ (height of

computed peak Δ_Y) at the east end. **(c)** East end vertical reinforcement strains for cycle 2, large amplitude negative peak drift ratios (Θ_{pk}). 122

Figure 4.17. Measured vs. Computed out-of-plane displacement history for Wall2 at a height equal to $0.6h_u$ (Level 1) and $0.3h_u$ (Level 2) at the east end. 124

Figure 4.18. Contours of the BTM for Case of Study 3 − Wall2. **(a)** Out-of-plane displacement ratio Δ_Y/t_w. **(b)** Minimum principal strains ε_2 in the compression face at the peak out-of-plane displacement (Δ_Y). 124

Figure 4.19. Contours of the BTM for Case of Study 3 − Wall2. Vertical strains ε_z in the axis of the wall at the peak drift prior to the peak Δ_Y. 125

Figure 5.1. Core Wall case study building – Geometry..... 139

Figure 5.2. (a) ETABS model of case study. **(b)** Mode shape 1 in EW, T_{1X} = 1.39 sec. **(c)** Mode shape 2 in EW, T_{2X} = 0.35 sec. **(d)** Mode shape 1 in NS, T_{1Y} = 1.49 sec. **(e)** Mode shape 2 in NS, T_{2Y} = 0.29 sec. 142

Figure 5.3. Core Wall case study building – Structure. 144

Figure 5.4. Description of the Hybrid Fiber-Section – Enhanced Beam-Truss Model. 147

Figure 5.5. Constitutive material stress-strain relations. **(a)** Stress-strain relationship for ConcretewBeta. **(b)** Concrete compressive strength reduction factor β. **(c)** Stress-strain relationship for SteelDRC. 151

Figure 5.6. Out-of-plane shear response modeling. 153

Figure 5.7. Stress-strain relation for *PinHardwP* material. 153

Figure 5.8. Core Wall case study building, Hybrid Fiber-Section – Enhanced Beam-Truss Model..... 157

Figure 5.9. (a) Comparison of base shear force – top displacement for the Fiber Model. **(b)** Decomposition of base shear force for *Fiber-Model-1/3-X*. 160

Figure 5.10. Decomposition of base shear force. **(a)** *HyBTM-1st-X*. **(b)** *HyBTM-1st-Y*. 162

Figure 5.11. Decomposition of base shear force. **(a)** *HyBTM-1/3-X*. **(b)** *HyBTM-1/3-Y*. 162

Figure 5.12. Decomposition of base shear force. **(a)** *HyEBTM10-1st-X*. **(b)** *HyEBTM10-1st-Y*. 165

Figure 5.13. Decomposition of base shear force. **(a)** *HyEBTM10-1/3-X*. **(b)** *HyEBTM10-1/3-Y*. 166

Figure 5.14. Decomposition of base shear force. **(a)** *HyEBTM15-1/3-X*. **(b)** *HyEBTM15-1/3-Y*. 170

Figure 5.15. Base shear force apportioning for *HyEBTM15-1/3-X*. **(a)** Flanges. **(b)** Webs. 174

Figure 5.16. Base shear force apportioning for *HyEBTM15-1/3-Y*. **(a)** Flanges. **(b)** Webs. 175

Figure 5.17. Deformed shape for *HyEBTM15-1/3-X* at $\Theta = 3.6\%$ (1x, inches). **(a)** General View. **(b)** Close up. 176

Figure 5.18. Comparison of base shear force – top displacement for Fiber Model, HyBTM and HyEBTM, 1st mode shape load pattern. **(a)** X-direction. **(b)** Y-direction. 179

Figure 5.19. Comparison of base shear force – top displacement for Fiber Model, HyBTM and HyEBTM, triangular load pattern. **(a)** X-direction. **(b)** Y-direction. 183

Figure 5.20. Comparison of inter-story drift ratios for Fiber Model, HyBTM and HyEBTM, X-direction. **(a)** 1st mode shape load patter, $\Theta = 4.9\%$. **(b)** Triangular load pattern, $\Theta = 1.4\%$. 184

LIST OF TABLES

Table 2-1. Properties of reinforcement used in the wall piers. 18

Table 2-2. Properties of reinforcement used in conventionally reinforced coupling beams of Wall A. 19

Table 2-3. Properties of reinforcement used in diagonally reinforced coupling beams of Wall B..... 19

Table 3-1. Reinforcement used in the wall piers of both specimens..... 44

Table 3-2. Specimen Wall A coupling beam reinforcing details. 44

Table 3-3. Specimen Wall B coupling beam reinforcing details. 45

Table 3-4. Comparison of the coupling efficiency coefficients computed for the EBTM and the NTM. 73

Table 3-5. EBTM and NTM computed wall pier base moments at peak base shear and apportioning base shear factors computed using Paulay and Priestley (Paulay & Priestley, 1992). 80

Table 4-1. Summary of properties of the test specimens and results of the BTM. 100

Table 4-2. Summary of parametric studies. 102

Table 5-1. Seismic design criteria for Core Wall case study building (Chapter 11, ASCE 7-16)..... 141

Table 5-2. Calculation of the design base shear for Core Wall case study building (ASCE 7-16, Chapter 12)..... 143

Table 5-3. Nonlinear static analysis cases..... 159

ACKNOWLEDGMENTS

I would like to thank, first and foremost, my advisor Professor José I. Restrepo; without his support, this work simply could not have been possible. Also, I sincerely thank the other members of my committee, the Professors, Joel P. Conte, Veronica Eliasson, Yuri Fialko, and Sashi Kunnath, for the time they dedicated and for providing valuable feedback to my work.

My deepest gratitude to Dr. Marios Panagiotou, from whom I have learned a lot, by co-authoring my research. Also, I would like to thank other co-authors, Professor Ramalingam Santhakumar, M.S. Sergio Godínez and Professor Felipe Pérez, for their collaboration, and other important contributors, Dr. Rodrigo Carreño, Dr. Massimo Petracca, and Professor Guido Camata for their help.

Very special thanks to my wife, Thelma López, not only for being an important collaborator by formatting this dissertation but for supporting me throughout this work in so many other different ways.

Thanks to my fellow graduate student Manuel Vega for his guidance and more important for his friendship these years.

Also, I express my gratitude to other people that with their exemplary professionalism made possible this achievement; thanks to the SE department staff, especially Yvonne Wollman, Julie Storing, Lindsay Walton and, Joana Halnez; thanks to the UC MEXUS – CONACYT staff, especially Susana Hidalgo and Veronica Sandoval; and thanks to the Fulbright – COMEXUS staff especially Savitri Arvey and Enrique Romero.

Finally, thanks to the *Consejo Nacional de Ciencia y Tecnología* (CONACYT), the *California Institute for Mexico and the United States* (UC MEXUS), the program *Becas Fulbright - García Robles* (COMEXUS) and the Department of Structural Engineering at UCSD, which provided financial support to pursue my doctoral studies.

Chapter 2, in part, is a reprint of the material as it appears in *Nonlinear Cyclic Truss Model for Analysis of Reinforced Concrete Coupled Structural Walls*. Bulletin of Earthquake Engineering, Special Issue: Nonlinear Modeling of Reinforced Concrete Structural Walls and Wall Systems, https://doi.org/10.1007/s10518-019-00639-8, 2019. Alvarez, Rodolfo; Restrepo, Jose I.; Panagiotou, Marios; and Santhakumar, A. Ramalingam. The dissertation author was the primary investigator and author of this paper.

Chapter 3, in part, is a reprint of the material as it appears in *Analysis of Reinforced Concrete Coupled Structural Walls Via the Beam-Truss Model.* Engineering Structures, 2020, https://doi.org/10.1016/j.engstruct.2020.111005. Alvarez, Rodolfo; Restrepo, Jose I.; Panagiotou, Marios; and Godinez, Sergio E. The dissertation author was the primary investigator and author of this paper.

Chapter 4, in part, is a reprint of the material as it appears in *RC Wall Plastic Hinge Out-of-Plane Buckling - Analysis Using the Nonlinear Beam-Truss Model*. Journal of Structural Engineering, 2020, https://ascelibrary.org/doi/abs/ 10.1061/(ASCE)ST.1943-541X.0000687. Alvarez, Rodolfo; Restrepo, Jose I.; and Panagiotou, Marios. The dissertation author was the primary investigator and author of this paper.

Chapter 5, in part, is currently being prepared for submission for publication of the material. Alvarez, Rodolfo; Restrepo, Jose I.; and Panagiotou, Marios. The dissertation author was the primary investigator and author of this paper.

VITA

2020 Doctor of Philosophy in Structural Engineering.

University of California San Diego.

2018-2020 Teacher Assistant.

Department of Structural Engineering, University of California San Diego.

2005-2015 Project Engineer.

Operadora STII S.A. Mexicali, Baja California, México.

2008-2014 Adjunct Professor.

Universidad Autónoma de Baja California, Mexicali, Baja California México.

2004-2005 Project Engineer.

Estructure S. de R.L. de C.V., Mexicali, Baja California, México.

2004 Master of Science in Structural Engineering.

Universidad de Guadalajara, Guadalajara, Jalisco, México.

1999 Civil Engineering.

Instituto Tecnológico de Tepic, Tepic, Nayarit, México.

PUBLICATIONS

Mavros, M., Panagiotou, M., Koutromanos, I., **Alvarez, R.**, & Restrepo, J. I. (in preparation). Advanced Cyclic Analysis of a 14-Story RC Core Wall Building System Using the BTM-Shell Methodology.

Alvarez, R., Restrepo, J. I., & Panagiotou, M. (in preparation). Enhanced Beam-Truss Model for Nonlinear Analysis of RC Core Walls.

Alvarez, R., Restrepo, J. I., & Panagiotou, M. (2020). RC Wall Plastic Hinge Out-of-Plane Buckling - Analysis Using the Nonlinear Beam-Truss Model. *Journal of Structural*

Engineering. https://ascelibrary.org/doi/abs/ 10.1061/(ASCE)ST.1943-541X.0000687

Alvarez, R., Restrepo, J. I., Panagiotou, M., & Godinez, S. E. (2020). Analysis of Reinforced Concrete Coupled Structural Walls Via the Beam-Truss Model. *Engineering Structures*. https://doi.org/10.1016/j.engstruct.2020.111005.

Godínez, S. E, **Álvarez, R.**, & Restrepo, J. I. (2019). Simulación de Muros de Concreto Reforzado Basada en GiD+OpenSees Usando "Beam-Truss Model". *Memorias Técnicas, XXII Congreso Nacional de Ingeniería Sísmica*. Monterrey, Nuevo León, México.

Alvarez, R., Restrepo, J. I., & Panagiotou, M. (2019). Nonlinear Cyclic Beam Truss Model for Analysis of Reinforced Concrete Coupled Structural Walls. *Bulletin of Earthquake Engineering*, Special Issue: Nonlinear Modeling of Reinforced Concrete Structural Walls and Wall Systems. https://doi.org/10.1007/s10518-019-00639-8.

Álvarez-Sánchez, R., & Restrepo, J. I. (2017). Plataforma para Simulación de Muros de Concreto Reforzado Basada en OpenSees-MATLAB usando Beam-Truss Model. *Memorias Técnicas, XXI Congreso Nacional de Ingeniería Sísmica*. Guadalajara, Jalisco, México.

Álvarez-Sánchez, R., Vega, M., Restrepo, J. I., & Pérez, F. P. (2017). Simulación Híbrida Virtual Basada en una Plataforma OpenSees/Abaqus de Edificio para Estacionamiento Ubicado en la Ciudad de Mexicali B.C. *Memorias Técnicas, XXI Congreso Nacional de Ingeniería Sísmica*. Guadalajara, Jalisco, México.

Álvarez, R., Martínez, J., & Trujillo, R. (2013). Revisión del Factor de Reducción Q' adoptado en las NTC del Municipio de Mexicali Utilizando Registros Locales. *Memorias Técnicas, XIX Congreso Nacional de Ingeniería Sísmica.* Boca del Río, Veracruz, México.

Trujillo, R., & **Álvarez, R.** (2013). Identificación del Mecanismo de Colapso de un Edificio de Concreto para Estacionamiento en Etapa de Construcción en Mexicali, B.C., debido al Sismo el Mayor-Cucapah. *Memorias Técnicas XIX Congreso Nacional de Ingeniería Sísmica*. Boca del Río, Veracruz, México.

Álvarez, R., Leyva, L., & Urzúa, D. (2003). Software para el Cálculo de Respuestas No Lineales de Sistemas de Un Grado de Libertad con Modelos Degradantes para Mampostería. *Memorias Técnicas XIV Congreso Nacional de Ingeniería Sísmica*. León, Guanajuato, México.

ABSTRACT OF THE DISSERTATION

Seismic Response Verification of Reinforced Concrete Structural Wall Systems

by

Rodolfo Alvarez Sanchez

Doctor of Philosophy in Structural Engineering

University of California San Diego, 2020

Professor José I. Restrepo, Chair

Reinforced concrete structural walls are frequently used as the main lateral load resisting system in multi-story buildings. The seismic response of buildings with such a lateral load system has been traditionally labeled as excellent, but damage observed in walls in recent earthquakes has prompted the need to look into behavioral modes not considered before in design and to look into the response of walls into the softening range. This dissertation focuses on enhanced numerical methodologies for the verification of the

seismic response, including softening, of reinforced concrete structural wall systems.

First, a Truss Model for reinforced concrete coupled structural walls is developed. Bar bond-slip, dowel action, and confining effect of the foundation are considered. Two cyclic tests, on scaled seven-story coupled walls (from literature), are used for validation. It is shown that the compressed wall piers resist most of the base shear force and that the coupling beams at lower levels develop the largest shear forces.

Second, using the same benchmark test specimens, two models for the nonlinear cyclic analysis of reinforced concrete coupled walls are developed, i.e., Modified Beam-Truss Model and Enhanced Beam-Truss Model. The role of the strain penetration in diagonally reinforced coupling beams on the hysteretic energy dissipated is studied. It is verified that the computational-efficient proposed models predict well the overall response and the sliding shear failures of coupling beams.

Third, the Beam-Truss Model developed in a previous study for the nonlinear cyclic analysis of reinforced concrete components is extended to compute out-of-plane buckling in structural walls. The novel Beam-Truss Model computes accurately the force – displacement responses and the buckling behavior of three test specimens reported in literature used for validation.

Finally, the Beam-Truss Model is enhanced to compute the out-of-plane nonlinear shear response of wall piers in the analysis of Core-Wall-Building systems. Using the proposed model and pushover analyses, a comprehensive study on a 14-story archetype Core-Wall building is carried out. It is shown that the in-plane shear response has a large influence on the lateral strength and displacement capacity, whereas the out-of-plane shear response mainly influences the displacement capacity.

Chapter 1. Introduction

1.1 Motivation

In buildings of all heights, it is common that reinforced concrete (RC) structural walls form the lateral load resisting system. Traditionally these systems have been considered to exhibit excellent seismic performance; however, in relatively recent high-intensity earthquakes, i.e., Maule 2010 and Christchurch 2011, some buildings with structural walls exhibited an unexpected behavior (Wallace et al. 2012, NEHRP 2014, Dashti et al. 2015). Extensive concrete crushing, bar buckling and fracture, shear failures of vertical and horizontal wall segments, and out-of-plane wall buckling were observed.

The expectations of society in the face of an earthquake scenario are changing. More buildings' owners want existing and new structures to meet performance tailored to their necessities. It has been possible with the arrival of the Performance-Based Design (PBD) (ASCE 41-17 2017, LATBSDC-17 2017, TBI-17 2017). The structural engineers identify, according to the owner's requirements, objectives for serviceability and resistance, and execute the projects to achieve the desired performance. Results of nonlinear analyses are used to support the design.

In PBD, the Fiber Model is the most commonly used methodology to simulate RC structural walls, whereas in general, nonlinear shear springs are used to model coupling beams (Naish et al. 2013, ASCE 41-17 2017). These modeling techniques have some limitations since nonlinear flexure-shear interaction, and actual kinematics of the coupling beams are not accounted for, which could lead to inaccuracies, especially when short coupling beams are included in coupled walls and core walls (Lu and Panagiotou 2016).

Moreover, it has been observed that for nonlinear time history analysis, the Fiber Models could compute larger shear force demands than the models including flexure-shear interaction (Mehmood et al. 2017). Not to mention that by definition, the Fiber Models cannot capture out-of-plane wall buckling.

Modeling the nonlinear shear response (including shear failure) and out-of-plane buckling (including softening) is especially important because current conventional design and PBD rely on prescribed limits based on scarce experimental evidence, (ACI 318-14 2014, ACI 318-19 2019).

Flexure-shear interaction in RC structural walls can be computed by several advanced finite element models (e.g., Gormak 1974, Zhao et al. 2004, Mohr et al. 2007, Kono et al. 2011, Constantin and Beyer 2012, Mihaylov and Franssen 2017, Wang et al. 2017, Hoult et al. 2018). However, only two numerical studies have been carried out to compute buckling in structural walls (Parra 2015, Dashti 2017), which also used the finite element method. In all these cases, the associated computational cost hampers their application to nonlinear time history analysis of building systems.

On the other hand, more computationally efficient macro models, which consider flexure-shear interaction, have been developed, e.g., Multiple-Vertical-Line-Element-Model (Kolozvari et al. 2019, Isakovic and Fischinger 2019), Truss Model and Beam-Truss Model (Panagiotou et al. 2012, Lu et al. 2014).

The Truss Model and the Beam-Truss Model have been extensively validated using RC test specimens that exhibited flexural and shear failures (Panagiotou et al. 2012, Moharrami et al. 2015, Lu et al. 2016, Lu and Panagiotou 2016, Alvarez et al. 2019).

Moreover, the Beam-Truss Model has successfully calculated the seismic response of buildings (Lu 2014, Zhang et al. 2017).

1.2 Objectives and scope

The research work presented herein focuses on enhanced practicing engineering-oriented methodologies for the numerical verification of the seismic response of reinforced concrete (RC) structural wall systems, including softening.

The first objective was to enhance the simple and computationally efficient Truss Model (Panagiotou et al. 2012) and Beam-Truss Model (Lu et al. 2014), for the simulation of RC coupled walls incorporating conventionally and diagonally reinforced coupling beams.

The nonlinear cyclic Truss Model was validated for RC coupled walls, after some additions were implemented (Alvarez et al. 2019). These additions included modeling: (i) the strain penetration of beam's reinforcement protruding into the wall piers (Zhao and Sritharan 2007), (ii) the dowel action of the longitudinal reinforcement of wall piers and coupling beams, and (iii) the confining effect of the foundation on the base of the wall piers (Presland 1999). The proposed Truss Model used the element *Truss2*, and material *ConcretewBeta*, as these implemented in OpenSees (OS, McKenna 2018) by Lu and Panagiotou (2013). The validation of the model was carried out comparing computed and measured overall and local responses for two 1:4 scale seven-story coupled wall specimens reported by Santhakumar (1974). One test specimen incorporated conventionally reinforced coupling beams, which exhibited sliding shear failure, whereas the other specimen incorporated diagonally reinforced coupling beams and had a highly-ductile

response. Key responses that can be only computed were also studied to characterize the seismic response of the RC coupled walls, i.e., the base shear force apportioning, the coupling efficiency coefficients (Paulay and Priestley 1992), and the shear forces in the coupling beams.

Then, using the same test specimens for validation (Santhakumar 1974), and building on the Beam-Truss Model, two computationally efficient models were proposed, i.e., the Modified Beam-Truss Model (MBTM) and the Enhanced Beam-Truss Model (EBTM). The grid and diagonals of the MBTM used truss elements except for the boundary elements, where displacement-based elements were used. The EBTM was an extension of the MBTM, which incorporated the strain penetration in the reinforcement of the coupling beams. The effect of the strain penetration on the hysteretic energy dissipated was investigated. Results obtained with these models were validated and compared with the results computed by the Truss Model (Alvarez et al. 2019).

The second objective of this work was to extend the Beam-Truss Model developed by Lu et al. (2014) for nonlinear cyclic analysis of RC components, to compute the out-of-plane buckling response of structural walls. This was achieved by using a grid of displacement-based elements, and diagonal truss elements with nonlinear geometric transformation. Strain penetration of the longitudinal reinforcement at the base of the walls was included. The novel Beam-Truss Model was validated using three test specimens, whose response exhibited degradation because of out-of-plane buckling, i.e., TW1 (Almeida et al. 2017), RWL (Dashti 2017), and Wall2 (Goodsir 1985). Unsupported height to wall thickness ratio of the test specimens ranged from 10-25. Computed and measured lateral force-displacement responses, out-of-plane displacements, and strains were

compared. The influence of key aspects of the modeling on the overall response, e.g., the grid size and torsional rigidity of the elements, was studied by means of parametric analyses.

The final objective was to develop a model for the nonlinear analysis of Core-Wall-Building systems, including the out-of-plane shear response of the walls piers. To achieve this, the Beam-Truss Model developed by Lu et al. (2014), which considers in-plane nonlinear shear response and nonlinear flexural warping, was enhanced using shear springs to model the nonlinear out-of-plane shear response. The response of the shear springs was made axial-force dependent via a built in-house material, i.e., *PinHardwP*, implemented in OS. The model used a hybrid approach to improve the computational economy (Arteta et al. 2019), i.e., the lower stories of the Core Wall were modeled with the novel Beam-Truss Model, whereas the upper stories adopted Fiber-Section Model. Nonlinear geometric transformation was used. An archetype 14-story Core Wall building assumed located in downtown Los Angeles was modeled using the hybrid Beam-Truss Model, and carrying out a series of pushover analyses with 1st mode shape and triangular load patterns, its overall and local responses were characterized.

1.3 Outline

A short description of the five chapters included in this dissertation is presented below:

- Chapter 1: Introduction

  In this chapter, the motivation, objectives, and scope, including the outline of the content, are presented.

- Chapter 2: Nonlinear Cyclic Truss Model for Analysis of Reinforced Concrete Coupled Structural Walls

  This chapter presents a Truss Model for the simulation of reinforced concrete coupled structural walls. Models for conventionally reinforced and diagonally reinforced coupling beams are discussed.

- Chapter 3: Analysis of Reinforced Concrete Coupled Structural Walls Via the Beam-Truss Model

  Two computationally economic approaches for the nonlinear cyclic analysis of reinforced concrete coupled walls, i.e., Modified Beam-Truss Model and Enhanced Beam-Truss Model, are presented in this chapter. The effect of modeling the bar-bond slip in the coupling beams is studied.

- Chapter 4: RC Wall Plastic Hinge Out-of-Plane Buckling – Analysis Using the Nonlinear Beam-Truss Model

  In this chapter, the Beam-Truss Model developed to compute the nonlinear cyclic response of concrete components is extended to consider out-of-plane buckling in structural walls. The role played by the strain penetration of the longitudinal reinforcement at the base of the walls on the out-of-plane displacements is investigated.

- Chapter 5: Enhanced Beam-Truss Model for Nonlinear Analysis of RC Core Walls

  The Beam-Truss Model for nonlinear analysis of reinforced concrete structures is enhanced to compute the out-of-plane nonlinear shear response of the wall pier

in the analysis of Core-Wall. Using the novel model, a comprehensive study on a 14-story Core-Wall building is carried out.

Chapter 2. Nonlinear Cyclic Truss Model for Analysis of Reinforced Concrete Coupled Structural Walls

2.1 Abstract

This paper discusses the Truss Model proposed by Panagiotou et al. (2012) for modeling reinforced concrete coupled structural walls. The model is validated with the landmark seismic testing of two 1:4 scale seven-story test specimens reported in Santhakumar (1974) and in Paulay and Santhakumar (1976). The first specimen, Wall A, incorporated conventionally reinforced coupling beams, whereas the second specimen, Wall B, incorporated diagonally reinforced coupling beams. These two specimens attained roof drift ratios of at least 1.7% before the initiation of lateral strength degradation. Coupling beams in specimen Wall A exhibited significant strength degradation due to sliding shear, whereas coupling beams in specimen Wall B maintained the capacity throughout.

We compare key overall and local responses reported for the two specimens with those computed with the Truss Models, as well as responses that could be only computed. In the latter, we show that when the beams effectively coupled the walls, the shear force at the wall base was mainly resisted by the wall being compressed. Moreover, the analysis shows that the first level coupling beams develop greater shear forces than the other beams despite all beams were identically reinforced. This is caused by the restraint provided by the fixed-base walls and by the kinematics of the strongly coupled walls. The Truss Model captures these responses because it explicitly considers the axial-flexure-shear interaction of RC walls and beams.

2.2 Introduction

A lateral load resisting system of choice in mid-to high-rise buildings are reinforced concrete coupled structural walls, termed coupled walls thereafter in this paper. Strongly coupled walls are characterized by the significant variation of axial forces in the walls when subjected to lateral loading. Such variation affects the distribution of internal forces as well as the deformation capacity and damage patterns. Coupling beams are key elements in coupled walls. Conventionally reinforced squat coupling beams have exhibited shear failures in buildings subjected to strong intensity earthquakes Paulay (1969). For these reasons, codes prescriptive dimensional limits for the use of squat conventionally reinforced coupling beams (ACI 318-14 2014).

In current U.S. practice and for RC wall buildings lower than 73 m, coupled walls are typically modeled using linear shell elements, and the results of the linear analysis are used to support the design. For taller buildings, and occasionally for buildings of less than 73 m high, the performance-based design is used, and the performance of the different elements is assessed via nonlinear time-history analysis (LATBSDC-17 2017). In design offices, walls are typically modeled for nonlinear analysis with fiber-section nonlinear beam elements and coupling beams with ad hoc shear springs or with calibrated beam elements with non-physical moment hinges (Naish et al. 2013, ASCE 2017).

Various modeling techniques able of capturing axial-flexure-shear interaction in the nonlinear reversed cyclic analysis of structural walls and elements have been reported by several researchers (Panagiotou et al. 2012, Lu and Panagiotou 2013, Toprak et al. 2015, Dashti et al. 2017, Rajapakse et al. 2019). These models can be grouped in four main

categories: (a) models that use empirically calibrated shear springs which are uncoupled from the flexural modeling of the component (Vulcano 1992, Fischinger et al. 1992, Naish et al. 2013); (b) macro models that use multiple vertical lines of elements to model the nonlinear behavior in flexure, coupled with specific assumptions with elements modeling the nonlinear behavior in shear (Fischinger et al. 2012, Kolozvari et al. 2015); (c) nonlinear Truss or Beam-Truss Models (Panagiotou et al. 2012, Lu et al. 2016); (d) and finite element models using smeared-crack, plasticity approach (Mohr et al. 2007) or fiber force-based elements (Rajapakse et al. 2019). This paper focuses on the nonlinear cyclic Truss Model and Beam-Truss Model which have been validated for RC walls (Panagiotou et al. 2012, Lu et al. 2016), columns (Moharrami et al. 2015), and slabs (Lu and Panagiotou 2016) as well as for entire RC buildings (Lu 2014, Zhang et al. 2017).

Coupled RC walls have been modeled by Panagiotou et al. (2012), and by Lu and Panagiotou (2016) using either a Truss or a Beam-Truss Model, respectively. In both cases, diagonal shear failures were reported in the wall piers. Mihaylov and Franssen (2017) modeled 24 coupling beam tests using FEM (smeared rotating crack model); displacements were increased monotonically to capture sliding shear and diagonal compression failures of the coupling beams. The failure of coupling beams due to sliding shear in coupled RC walls in reversed cyclic loading tests has not been explicitly computed before, to the best of our knowledge.

The objective of this paper is to validate the Truss Model for coupled walls incorporating conventionally and diagonally reinforced coupling beams. The validation is achieved by computing the complete response, including failure, of the two landmark tests on coupled structural walls reported by Santhakumar (1974) and Paulay and Santhakumar

(1976). The seven-story test specimens were built at a 1:4 scale. Specimen Wall A incorporated conventionally reinforced coupling beams, whereas Wall B incorporated diagonal reinforced coupling beams. Wall A exhibited sliding shear of the coupling beams resulting in degradation of the overall response at 1.7% roof drift ratio. Wall B demonstrated a highly-ductile response up to a 3.6% roof drift ratio; after that, it experienced buckling of the wall longitudinal reinforcement and toe crushing of one of the wall piers.

The 2D analysis used a Truss Model based on the Beam-Truss Model method (Lu et al. 2014), and the corresponding elements and materials as these implemented in OpenSees (OS) (McKenna 2018) by Lu and Panagiotou (2013). The vertical and horizontal elements were trusses in the Truss Model instead of force-based beam elements used in the Beam-Truss Model, Lu et al. (2016).

2.3 Description of the Truss Model

2.3.1 Components and geometry

Figure 2.1 depicts two wall piers connected through coupling beams and the suggested 2D Truss Model. In Lu et al. (2014), nonlinear fiber-section beam elements model the concrete and reinforcing steel of the section sub-areas in the vertical and horizontal direction; the elements are pinned in the plane except the confined boundary elements. In the 2D model (Figure 2.1), all vertical and horizontal elements are nonlinear trusses, except for some elements at the base of boundaries and ends of coupling beams where beams (displacement-based elements) were used. The beams are used to model only the reinforcement in those specific locations and to consider dowel action. The diagonal

elements are truss elements modeling the diagonal compression field of concrete, including biaxial effects.

For all the nodes, where only truss elements are interconnected, the rotational DOFs are restrained. All the elements at the base of the wall piers are fixed. Biaxial behavior of concrete (Vecchio and Collins 1986), as adjusted for mesh objectivity by Panagiotou et al. (2012), is considered in the diagonal trusses using *Truss2* elements and the *ConcretewBeta* uniaxial material (Lu and Panagiotou 2013). These truss elements are defined using four nodes, two of them for element length and others for transverse gage length. The area of diagonals is defined based on the thickness of the panel and effective width $b_{eff} = a \sin(\theta_d)$ (Figure 2.1). Lu et al. (2016) include recommendations about geometry definition and angle of inclination of diagonals θ_d in coupled walls.

2.3.2 Materials

The Truss Model uses constitutive stress-strain relationships for the materials available in the OS: *ConcretewBeta*, and *SteelDRC*. The former is a routine developed for concrete subjected to a biaxial strain field (Lu and Panagiotou 2013), and the latter is an in-house written routine for reinforcing steel, based on the model proposed by Dodd and Restrepo-Posada (1995).

Lu et al. (2016), use zero tensile strength for concrete in diagonal and horizontal wall elements (vertical coupling beam elements). Stress at the closure of cracks is a function of cracking strength in the *ConcretewBeta* material. To improve the calculation of hysteretic behavior, in terms of pinching, a small tensile strength and a scaled *alpha* parameter were used. Parameter *alpha* controls the path of unloading from tensile strain

(McKenna 2018). Tensile strength in diagonals was $f_{td} = 0.01f_t$, whereas $alpha = 0.03f'_c/f_{td}$ (where f_t and f'_c are defined in the next paragraph).

The parameters for unconfined concrete material were calculated according to Lu and Panagiotou (2013), see Figure 2.2a. The compressive strength f'_c occurs at the strain $\varepsilon_o = -0.002$ and the crushing at strain $\varepsilon_{cu} = -0.004$, whereas the modulus of elasticity is $E_c = 5000\sqrt{f'_c}$ (MPa). Tensile strength of concrete f_t was calculated according to the Eq. 2.1 (Collins and Mitchell 1997),

$$f_t = 0.55f_r \tag{2.1}$$

Where f_r is the modulus of rupture of concrete. For the case of confined concrete, Lu and Panagiotou (2013) recommend define the peak compressive stress f_{cc} and strain ε_{co}, according to Mander et al. (1988), see Figure 2a. In this model, the onset of softening strain ε_{cs} was,

$$\varepsilon_{cs} = -0.002 - k_e {}^{f_l}/_{9f'_c} \tag{2.2}$$

Where k_e is the confinement efficiency coefficient, and f_l is the confining stress. The regularized strain at crushing (or residual strength) was calculated according to Lu and Panagiotou (2013) using a maximum value $\varepsilon_{cu} = \varepsilon_{cs} - 0.002$. Ideally, the crushing strength should be set equal to zero, but for enhanced numerical robustness, a residual compressive strength $f_{cu} = -0.2f'_c$ was used.

Whenever the response of a material includes perfectly plastic or softening behavior, the objectivity of the model in the nonlinear analysis could be lost (Coleman and Spacone 2001). Here, the regularization of the concrete stress-strain relationship was, according to Lu et al. (2014). For concrete in tension, a distinction was made: while

unreinforced concrete considers tension softening and regularization (Rokugo et al. 1989), reinforced concrete considers tension stiffening (Stevens et al. 1991) and no regularization was carried out.

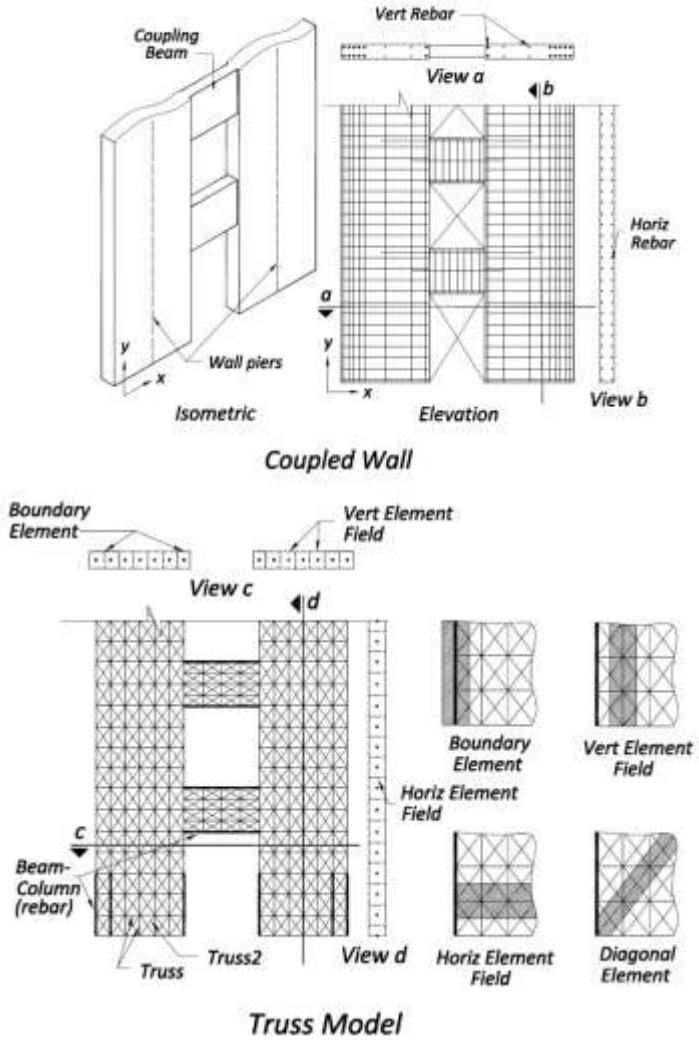

Figure 2.1. Determination of components geometry for the 2D version of the Truss Model methodology.

The steel reinforcement material constitutive model *SteelDRC* (Carreño 2018) depicted in Figure 2.2b and available in OS was used. This material makes use of tensile test parameters to model the yield plateau and kinematic hardening and bar fracture.

SteelDRC includes ultimate strain ε_u as a parameter; because of that, no calibration is needed using parallel materials to include a cap for the strength. The Bauschinger effect is represented by the parameter *OmegaFac*, which could be used to heuristically account for bar bond-slip (Rashid et al. 2000).

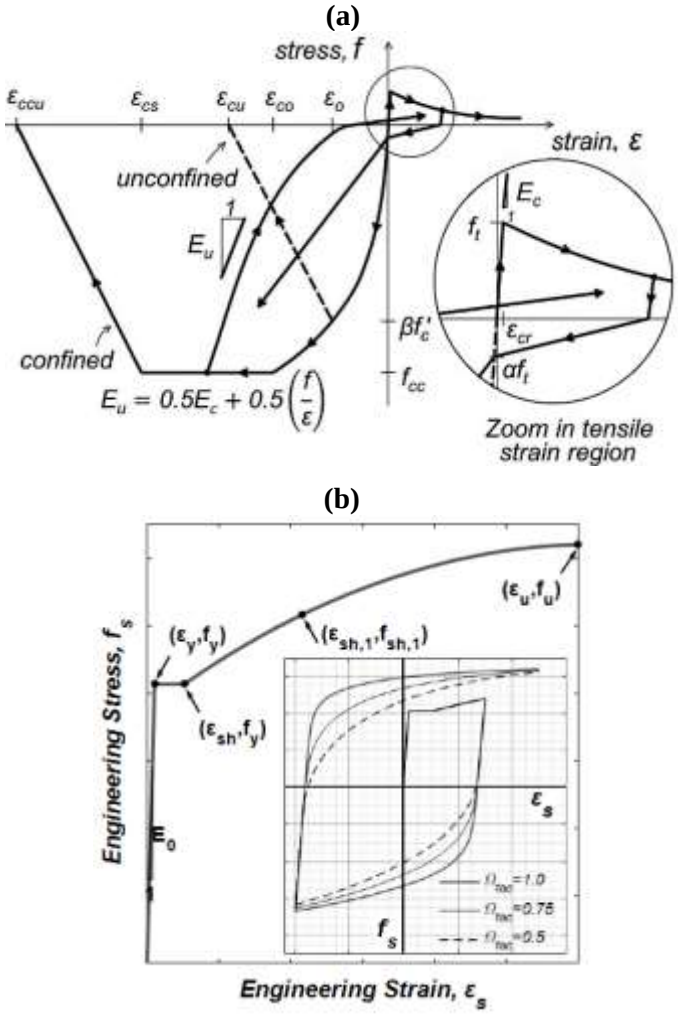

Figure 2.2. Uniaxial materials used in the Truss Model. **(a)** Strain-stress relationship for *ConcretewBeta* (Lu and Panagiotou 2013). **(b)** Model parameters for material *SteelDRC* (Carreño 2018).

2.4 Case studies

2.4.1 Description of test units

This section describes the seven-story coupled wall test specimens reported by Santhakumar (1974). The two specimens, Wall A and Wall B, had identical geometry and reinforcement, except for the reinforcement in the coupling beams, see Figure 2.3. The 100 mm thick walls were 5.49 m high by 1.60 m long. The 76 mm thick coupling beams were 0.38 m long by 0.31 m deep, resulting in an aspect ratio l_c/h = 1.25. Each specimen was cast flat in a single operation and with the same concrete batch. The concrete mechanical properties at the day of testing were f'_c = 31.6 MPa and f_r = 2.9 MPa for Wall A and f'_c = 30.0 MPa and f_r = 2.7 MPa for Wall B.

Table 2-1 lists the main mechanical properties of the reinforcement. The walls were reinforced longitudinally with 5/8 in. diameter deformed bars (nominally 16 mm diameter bars & labeled D16 in Table 2-1) and transversely with 1/4 in. diameter deformed bars (nominally 6 mm diameter bars & labeled D6 in Table 2-1). Tables 2-2 and 2-3 list the mechanical properties of the reinforcement used in the coupling beams of Wall A and Wall B, respectively. The coupling beams in specimen Wall A were reinforced longitudinally with 3/8 in. diameter deformed bars (nominally 10 mm diameter bars & labeled D10 in Table 2-2) and transversely with 1/4 in. diameter bars (nominally 6 mm diameter bars & labeled D6 in Table 2-2).

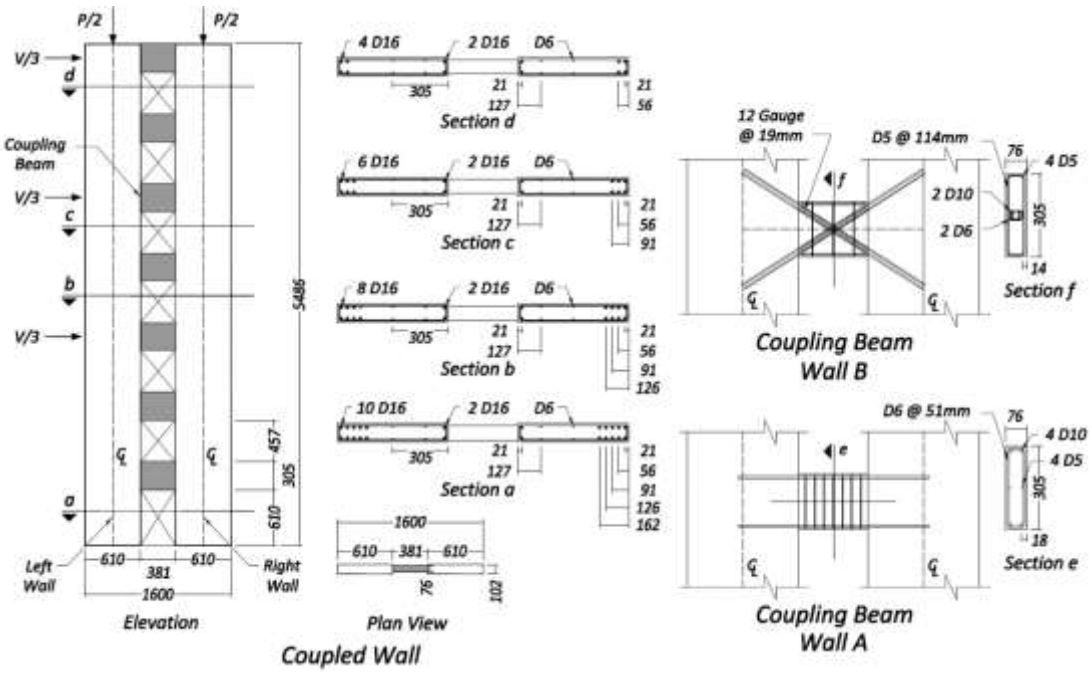

Figure 2.3. Dimensions and reinforcement details for wall piers and coupling beams of Wall A and Wall B.

The coupling beams in specimen Wall B were diagonally reinforced with 3/8 in. diameter deformed bars (D10) and longitudinally with 3/16 in. diameter bars (nominally 5 mm diameter bars & labeled D5 in Table 2-3), and the transverse reinforcement consisted of 3/16 in. diameter bars (D5).

The reinforcement of the wall specimens was defined according to the design of the seven-story prototypes considering five tributary bays (20'x30') and lateral load equal to $0.1W_t$ (where W_t is the seismic weight), in accordance with the seismic design knowledge of the 1970s. The design resulted in a large amount of longitudinal reinforcement at the boundaries and relatively large longitudinal bar sizes, see Table 2-1.

Table 2-1. Properties of reinforcement used in the wall piers.

Story	Flexural (vert) f_y = 305 MPa f_u = 472 MPa						Secondary (vert) f_y = 343 MPa f_u = 487 MPa		Stirrup (horiz) f_y = 352 MPa f_u = 498 MPa	
	Outer	(%)		Inner	(%)					
	bar	ρ_s	ρ_s *	bar	ρ_s	ρ_s *	Bar	ρ_s (%)	Bar	ρ_s (%)
1	10 D16	3.49	10.6	2 D16	0.70	2.13	2 D6	0.26	2 D6@76	0.88
2	10 D16	3.49	10.6	2 D16	0.70	2.13	2 D6	0.26	2 D6@76	0.88
3	10 D16	3.49	10.6	2 D16	0.70	2.13	2 D6	0.26	2 D6@76	0.88
4	8 D16	2.79	8.52	2 D16	0.70	2.13	2 D6	0.25	2 D6@102	0.67
5	6 D16	2.79	6.39	2 D16	0.70	2.13	2 D6	0.24	2 D6@102	0.67
6	4 D16	1.39	4.26	2 D16	0.70	2.13	2 D6	0.23	2 D6@152	0.44
7	4 D16	1.39	4.26	2 D16	0.70	2.13	2 D6	0.23	2 D6@152	0.44

*, percentage of the reinforcement with respect to the maximum area of the outer boundary element.

Contribution of concrete to shear resistance was ignored, and excess stirrups were provided. This allowed the development of very large yielding flexural strains. A large amount of shear reinforcement in the coupling beams of the Wall A allowed yielding of the flexural reinforcement and prevented shear diagonal failures, but the stirrups were ineffective controlling sliding shear. At this stage, dowel action played an important role in the coupling beams. Dowel action also was important at the failure of Wall A, failure initiated in the trailing walls, having a narrow area in compression, the transmission of shear by dowel action was significant. Moreover, Santhakumar (1974) estimated that more than 30% of the base shear in Wall B was carried by mechanisms other than stirrups, such as dowel action and aggregate interlock.

Because of height limitations, the specimens were tested in the horizontal position using a double cantilever loading frame with forces applied manually using single-acting prestressing jacks. The dead load was simulated by applying a compressive force of 111 kN on each wall pier using a prestressing system that ran the entire height of the specimen (wall height + foundation block depth). The vertical loads applied to the specimens were

selected to generated equal stresses as those expected in the prototype. In non-dimensional terms, the applied prestressing load was $N/f'_cA_g = 0.057$ for Wall A and $N/f'_cA_g = 0.06$ for Wall B. The specimens were subjected to reversed cyclic loading by quasi-statically applying identical lateral forces on Levels 3, 5 and 7. The load pattern of the applied lateral forces was chosen to mimic the shear and moment distribution that results in the application of the inverted triangular pattern in the New Zealand code (NZSS 1900).

The axial force in the tendons was adjusted during the loading and unloading phase of tests to keep it reasonably constant. Displacements on the loading frame and specimens were recorded using a theodolite, while strains in the walls and coupling beams were measured with DEMEC gages (CCA 2018).

Table 2-2. Properties of reinforcement used in conventionally reinforced coupling beams of Wall A.

Flexural (long)		Secondary (long)		Stirrup (transv)	
f_y = 315 MPa		f_y = 230 MPa		f_y = 346 Mpa	
f_u = 431 MPa		f_u = 339 MPa		f_u = 487 Mpa	
Bar	ρ_s (%)	Bar	ρ_s (%)	Bar	ρ_s (%)
2 D10	0.62	2 D 5	0.14	2 D6 @ 51	1.76

Table 2-3. Properties of reinforcement used in diagonally reinforced coupling beams of Wall B.

Main (diag)		Secondary (vert)		Confining	
f_y = 315 MPa / 346 MPa		f_y = 230 MPa		f_y = 381 MPa	
f_u = 431 MPa / 487 MPa		f_u = 339 MPa		f_u = 478 MPa	
Bar	ρ_s (%)	Bar	ρ_s (%)	Bar	ρ_s (%)
2 D10 + 2 D6	1.12	2 D 5 @ 114	0.35	12 Gauge @ 19	4.00

2.4.2 Truss Models of the two specimens

All the models described here were developed using the 64-bit open-source computer program OpenSees Version 2.5.0 rev 6248 (McKenna 2018). This version was compiled, including the in-house routine *SteelDRC* written by Carreño (2018) and *HDF5* libraries to run a beta version of the OS postprocessor STKO (Petracca et al. 2017b,

Petracca et al. 2017a). The models were generated from TCL scripts without any preprocessor.

The definition of the geometry of the vertical elements accounted for the asymmetry of the wall longitudinal reinforcement. Each wall had a concentration of longitudinal reinforcement at one of the ends, where a boundary element would typically be detailed nowadays. For this reason, in this paper, the term “boundary” will be used thereafter. However, the walls had no confinement reinforcement. Based on the formulation of Lu et al. (2014), vertical end beams use in-plane flexural rigidity only for confined regions. Here, with the exception of the elements modeling reinforcement to consider dowel action, the end elements were modeled without in-plane flexural rigidity because of the absence of confinement. This prevented a spurious delay in the computation of shear failures.

The mesh layout size was selected to result in six identical quadrilaterals. The exterior boundary at the base had 10 D16 bars (Figure 2.4); this section was modeled with two vertical lines of elements. Truss elements represented reinforcement and concrete, with the exception of the first three levels of the grid (Figure 2.4), where circular fiber-section beams modeled the bars in order to capture the effect of dowel action at the regions of the wall where the peak sliding deformations occur.

The rest of the sections of the exterior boundary (Figure 2.3) were modeled using only truss elements. The interior boundary had 2 D16 bars in all its elevation (Figure 2.3), and the section was modeled in a similar way with one vertical line of elements. Areas of concrete and reinforcement of the remaining four field vertical lines (trusses) were adjusted to obtain agreement between model and test centroidal axes.

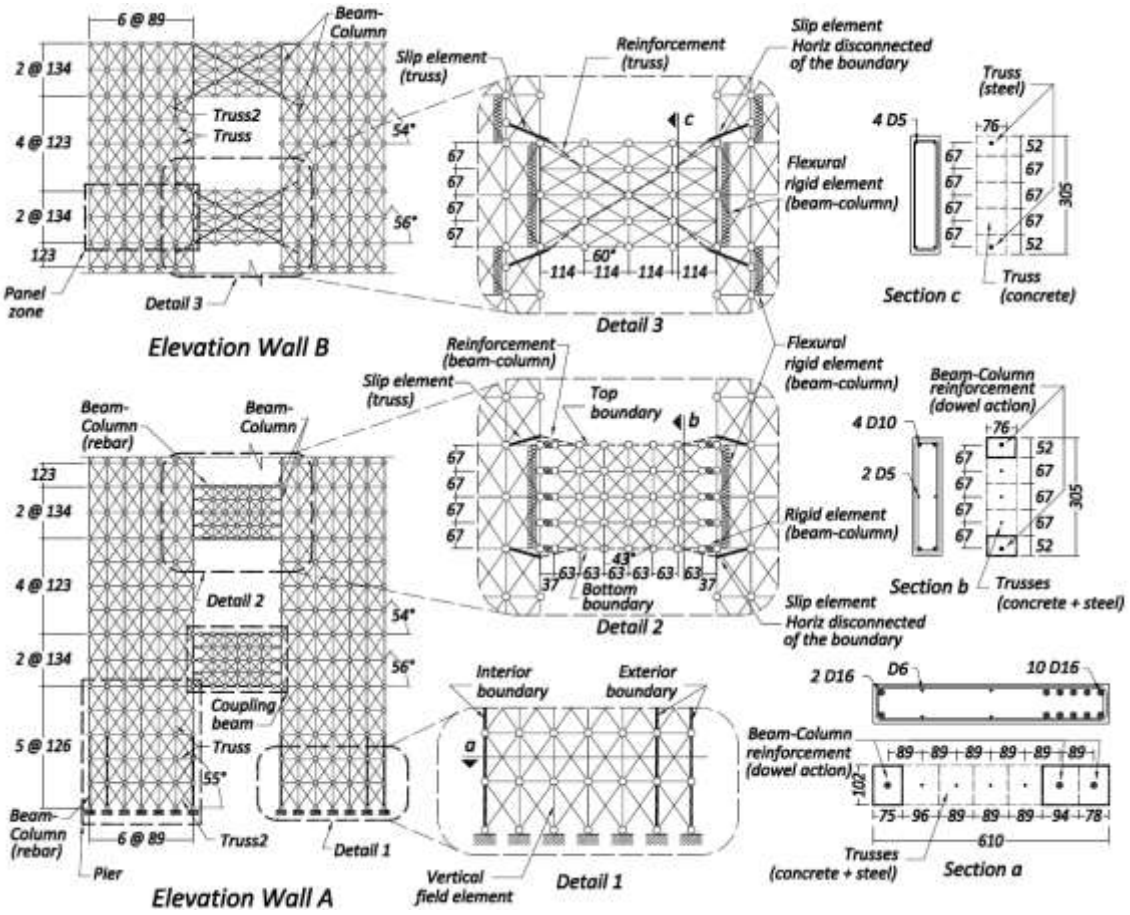

Figure 2.4. Description of the Truss Models of Walls A and B.

For the case of study, the inclinations of diagonals were proposed according to the recommendation of Lu et al. (2014) and the general crack pattern observed. Four angles resulted in each wall, corresponding to four zones (Figure 2.4): pier of the first level, pier above the first level, coupling beams, and panel zones. The selected inclination of diagonals in the wall piers was 55° in the first level and 54° above the first level, whereas, in the panel zones, it was 56°. In the coupling beams, the inclination of the diagonal was 47° and 30° in the Wall A and Wall B, respectively. The inclination of the diagonals in the panel zones (56°) was the result of the grid formed by the vertical and horizontal elements. If the wall piers are considered as individual cantilever walls, the inclination of diagonals,

according to Lu et al. (2014) would have been 56° and 60° in Wall A and Wall B, respectively, whereas the inclination in coupling beams would have been 45°. Although shear failures in the wall piers were not reported during the tests, the definition of these angles is very important because in-plane pure Truss Models are quite sensitive to the inclination of the diagonals for a response that involves diagonal failure (especially diagonal tension failure).

The coupling beams in Wall A used seven vertical and five horizontal lines. The reinforcement and concrete were represented with truss elements except for the top and bottom bars that were modeled using circular fiber-section beams to capture dowel action in this critical region of the walls. The mesh of coupling beams was more refined than those of the piers to capture sliding shear. Additional rigid elements were used to generate offsets and consider the real length of the coupling beams, with the objective of moving the localization of the sliding shear out of the wall piers (Figure 2.4). The coupling beams of Wall B used five vertical and five horizontal lines, and all the elements were trusses modeling reinforcement and concrete.

The protruding length of the horizontal and diagonal bars of the coupling beams into the wall piers were modeled with truss elements (slip elements, Figure 2.4). The anchorage length of these elements was adjusted close to the physical length of the bar minus one half of their development length. To simulate the pinched hysteretic behavior typical of bond-slip, the slip elements used *Hysteretic* material of OS calibrated according to the properties of the steel and pinching parameters 0.60 and 0.15. The stress-strain envelopes were adjusted to generate force-displacement curves corresponding to the length recommended by Zhao and Sritharan (2007), in this case, about twenty bar diameters. In

the slip elements, the horizontal DOFs in the nodes of the boundaries were released to avoid restrictions of the wall piers reinforcement on the debonded elements. For both models, a parametric study using larger anchorage lengths showed similar overall responses.

Presland (1999) noted that the foundation adjacent to members under compression provides additional confinement in the critical section at the base. Without modeling the confinement provided from the foundation, degradation due to premature sliding shear failure at the base of the Wall A and Wall B occurs at 2.7% and 1.5% drift ratios, respectively. To consider the influence of the foundation on the base of the Wall B, the concrete of vertical and diagonal trusses of the first two levels of the grid was considered as well-confined by the foundation beam. This height is approximately equal to the length of the compression zone of the wall pier under the maximum compressive load (Presland 1999). The first level was considered under triaxial confinement (Mander et al. 1988), with lateral stresses f_2 and f_3 chosen ad hoc and made equal to $0.3f_1$ (where f_1 is the maximum vertical stress). Trial runs were made using lower confinement, but the analysis showed the crushing of the concrete at the wall base, which was not observed during testing. The second level was confined to the average of unconfinement state and the maximum confinement. This resulted in confined compressive strength f_{cc} equal to $-1.86f'_c$ and $-1.43f'_c$ for the first and the second grid-level, respectively. At the base of the piers and the elements adjacent to the piers in the coupling beams of the Wall A, a similar calibration of the properties of the concrete was carried out. For the case of the beams, this resulted in f_{cc} equal to $-1.1f'_c$.

OpenSees includes the uniaxial material *ReinforcingSteel*, which allows the use of two different approaches to consider bar buckling in the fiber section level: Gomes and Appleton (1997) and Dhakal and Maekawa (2002). These models for bar buckling are calibrated in terms of the slenderness ratio $l_{SR} = L_u/d_b$ (where L_u is the unsupported length and d_b equal to the bar diameter). In the boundary elements of the test specimens, only the most exterior bars could be considered latterly supported; because of that the definition of L_u is not straightforward for the rest of the bars. For this reason, the bar buckling was kept out of the scope of this work.

The nonlinear fiber-section beam elements (DBE) used three integration points. Linear geometry was used for the analysis. Lateral loads were applied using displacement control.

2.5 Comparison of responses

This section compares key test responses with those computed using the Truss Models for the two specimens. Figure 2.5 depicts the overall hysteretic response for specimens Wall A and Wall B (in grey). Specimen Wall A showed a pinched response caused by sliding shear in the coupling beams. The peak base shear force in this specimen was reached at a 1.7% roof drift ratio. Thereafter, gradual softening occurred. Specimen Wall B showed a stable hysteretic response with minimal degradation to a 3.6% roof drift ratio. Santhakumar (1974) reported that at this drift ratio, “the kink at the junction of the wall and the base block caused the compression wall to buckle”. This failure mode could be cataloged today as buckling of the reinforcement in the wall boundary element, followed by the crushing of the unconfined concrete core.

The models resulted in larger initial stiffness due to the overlapping areas of the elements (Lu et al. 2014). The model of Wall A, computed with a very good level of accuracy the peak lateral forces at each of the loading cycles (i.e., within ±8%), except for the peaks of the semi-cycles 1, 2 and 12 where the Truss Model predicts the lateral force with a maximum error of 24% (see Figure 2.5a). The model captures very well the sliding shear in the coupling beams in this specimen, compare Figure 2.6a and Figure 2.6b. Santhakumar states that during a semi-cycle with large lateral displacement (maximum drift ratio equal to 2.4%), the inner wall boundary element reinforcement buckled. The Truss Model cannot capture the buckling of the wall longitudinal reinforcement since bar buckling is not considered. However, the contour of the minimum principal strains ε_2 of the Wall A at maximum drift suggests that the model is capable of capture the damage pattern at the base, compare Figure 2.7a and Figure 2.7b.

A comparison of the experimentally measured and computed hysteretic responses for Wall A indicates that the Truss Model overpredicts the hysteretic energy dissipated. The authors note that the hysteretic response recorded for specimen Wall A shows an unusual ‘banana’ shape and recentering during the unloading phases (i.e., unloading in double curvature). Without any further evidence, we judge this to be caused by the presence of the prestressing tendons providing axial force in the walls. The tendon acts unintendedly as a recentering mechanism if it remains linear (Restrepo and Rahman 2007).

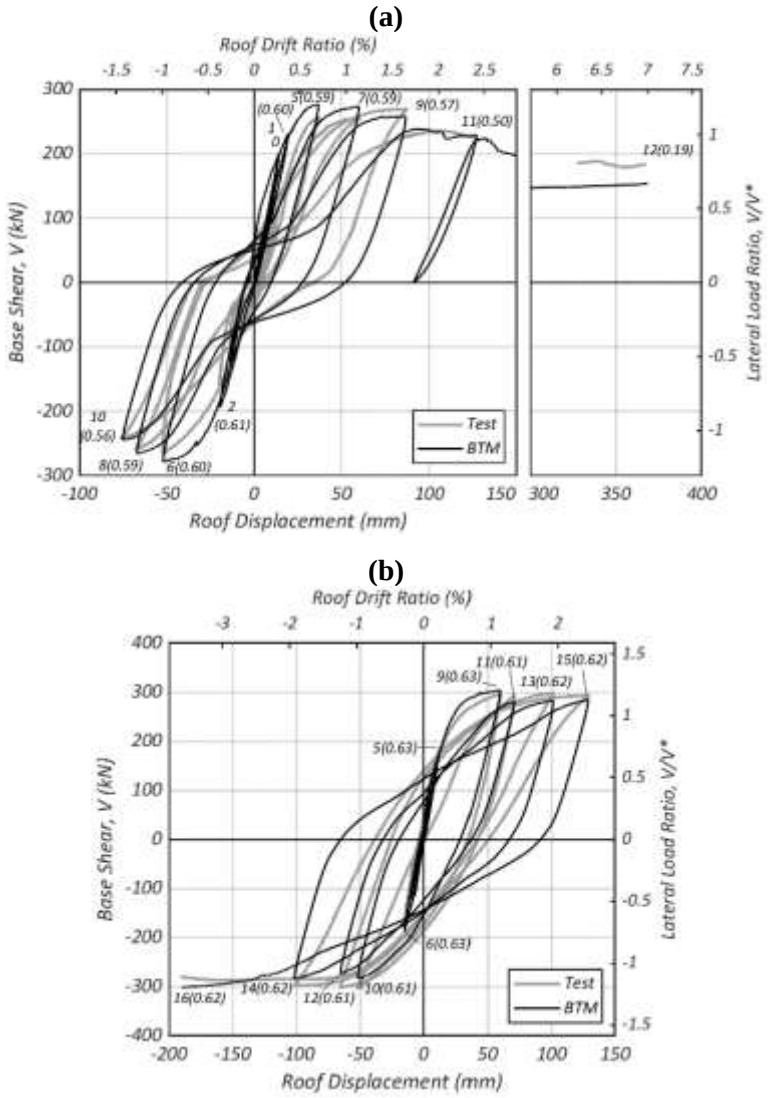

Figure 2.5. Comparison of Truss Models and test results: base shear – roof displacement. **(a)** Wall A. **(b)** Wall B (theoretical ultimate base shear in Wall A $V^* = 230$ kN and Wall B $V^* = 252$ kN). The coupling efficiency coefficient (Paulay and Priestley 1992) calculated at the specific displacement in the response is shown in parenthesis.

For the specimen Wall B, the Truss Model computes the peak lateral force accurately in all semi-cycles with a maximum error of 10%, as well as the response envelope up to 3.6% roof drift ratio, see Figure 2.5b. However, the model significantly overpredicts the hysteretic energy dissipation and the unloading stiffness throughout all the cycles. The 'banana' shape and recentering unloading response are also present for Wall

B. Local responses provide an insight into the response of the different members in the system. The tests described by Santhakumar (1974) were densely instrumented. However, the tests were carried out in the early days of experimental earthquake engineering, where the emphasis in the presentation of the data was given to the applied forces, and not to forces and displacements. Unfortunately, the step number or applied lateral displacement are not given in the report.

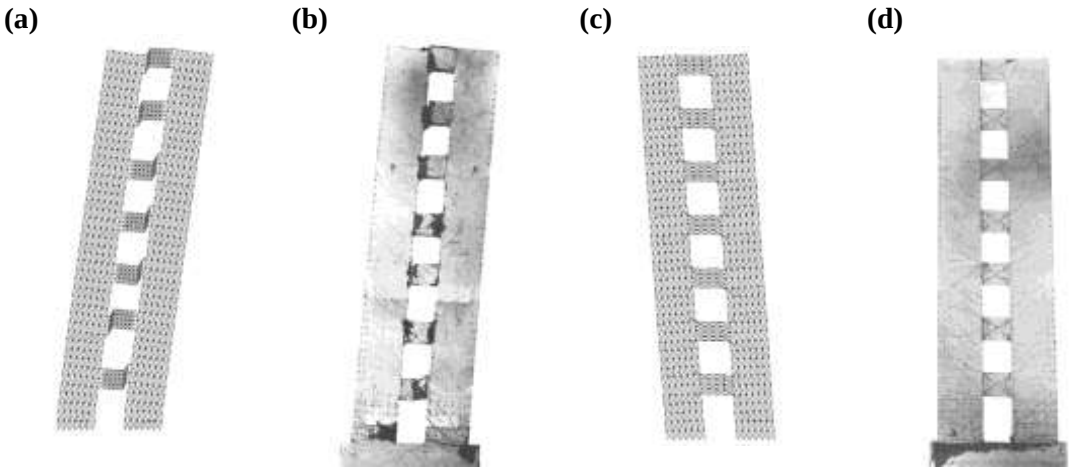

Figure 2.6. (a) Deformed shape of model Wall A at maximum displacement (2x). **(b)** Wall A after the test. **(c)** Deformed shape of model Wall B at maximum displacement (2x). **(d)** Wall B after the test. Deformed shapes generated using STKO (Petracca et al. 2017a, Petracca et al. 2017b) and pictures from Santhakumar (1974).

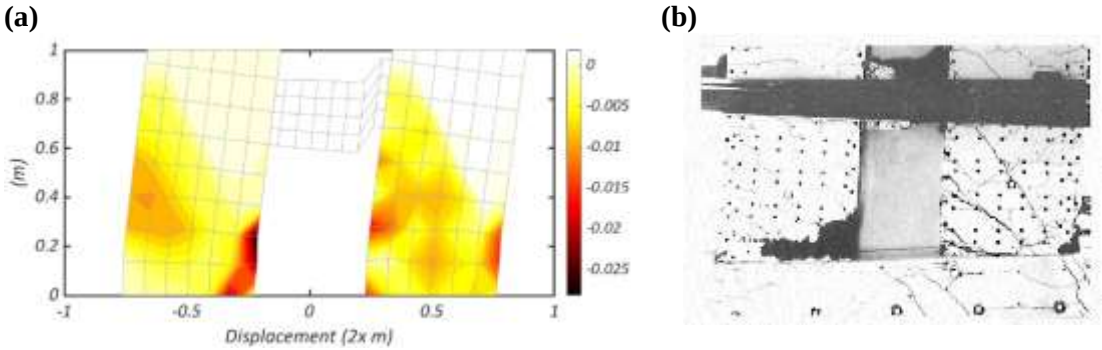

Figure 2.7. (a) Minimum principal strains ε_2 at maximum drift in Wall A (strains calculated according to Zhang et al. 2017). **(b)** Cracks formed in the Wall A at the base in the semi-cycle 12 (pictures from Santhakumar 1974).

Instead, and as it was customary in the early days of experimental earthquake engineering, the researchers used the ratio of the base shear at which the response is presented to the theoretical ultimate base shear (V/V^*).

The use of such a ratio leads to significant uncertainty in the definition of the lateral displacement when the tangent stiffness is small and makes the comparison of model and specimen results difficult. Nevertheless, we consider the test results to be valuable and to give insight into the behavior. For this reason, the results of the models are compared with test results reported for the two specimens.

Figure 2.8a and Figure 2.8b compare the measured and computed reinforcing strains for the coupling beams in specimens Wall A and Wall B, respectively. The strains computed from the Truss Models were calculated from the nodal displacements. Although the magnitude of the bar strains computed from the models and those recorded in the experiments differ as much as 300%, the Truss Model strains do, in general, follow similar trends.

An aspect that is often overlooked in simplified models of coupled shear walls is the coupling between the axial and flexure degrees of freedoms in the coupling beams. Coupling beams, whether these beams are conventionally or diagonally reinforced and are part of coupling walls or tube-like frames, lengthen and result in the development of yield lines in the slabs (Fleischman et al. 2014).

Santhakumar measured the dilatation at discrete locations between the longitudinal axes of the leading and trailing walls in both specimens, see Figure 2.9a and Figure 2.9b, respectively.

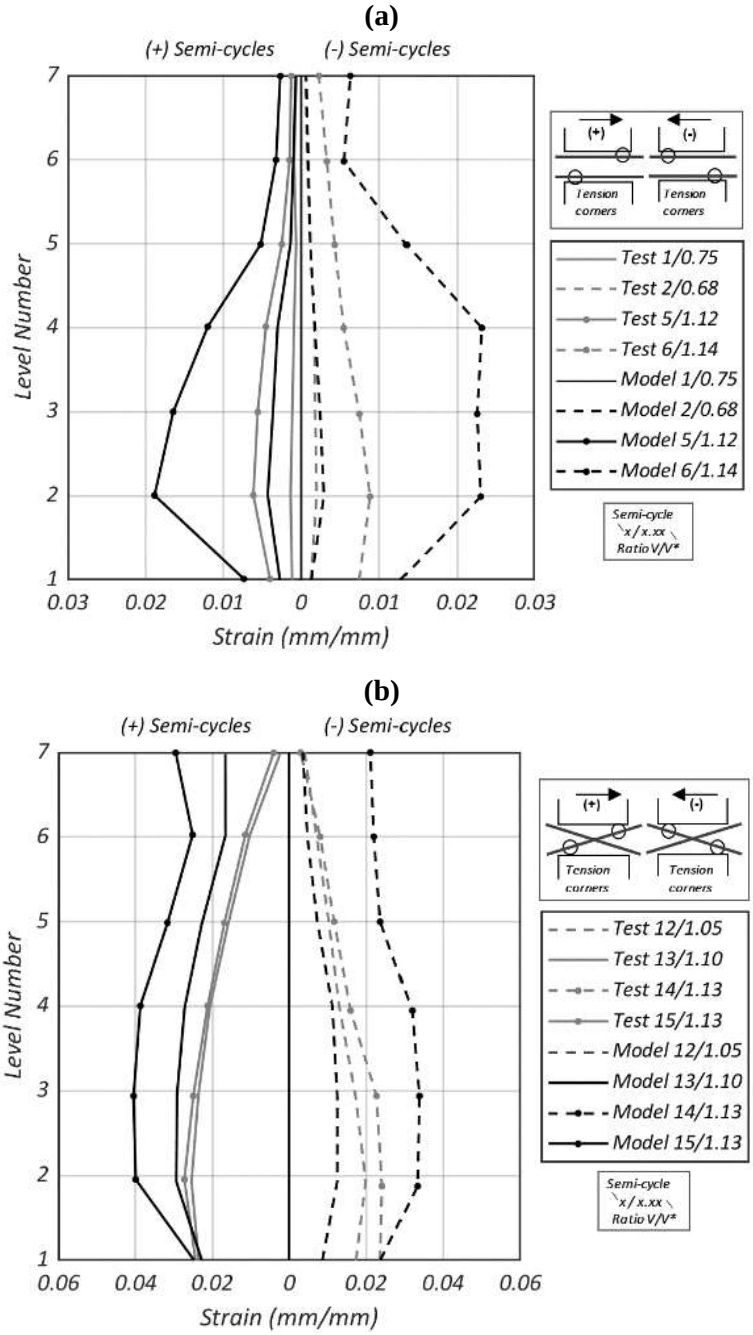

Figure 2.8. (a) Average strains in flexural reinforcement of tension corners in coupling beams of Wall A. **(b)** Average strains of diagonal reinforcement in tension for coupling beams of Wall B.

Past 1.25% roof drift ratio (i.e., semi-cycle 9 and greater for specimen Wall A, and semi-cycle 13 and greater for specimen Wall B), the dilatation is rather uniform throughout

the wall height, except below the lowest most coupling beam, where it is significantly smaller. This is because of the restraint provided by the foundation block.

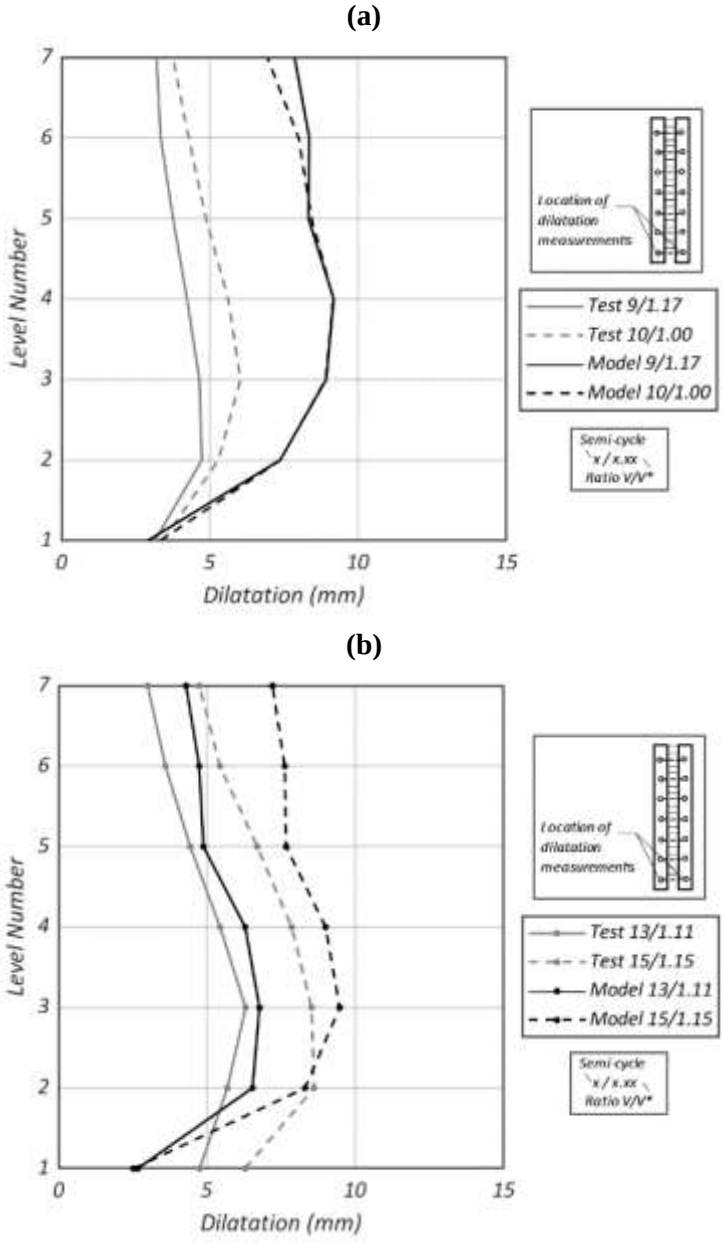

Figure 2.9. Dilatation of coupled walls last cycles. **(a)** Wall A. **(b)** Wall B.

Dilations computed from the Truss Models follow similar trends, though the dilations computed for specimen Wall A are greater than those recorded for this test. The

magnitude of the recorded and computed dilations in specimen Wall B are in reasonable agreement.

2.6 Evaluation of computed responses not measured in the tests

This section discusses responses that could not be recorded during the tests, due to the degree of internal indeterminacy, but that can easily be extracted from the analyses. These responses provide significant insight into the behavior of coupled walls. Figure 2.10 shows the variation of axial forces of specimens Walls A and B as predicted by the Truss Models. Axial forces of alternating sign develop in the walls of these specimens because of coupling. In these walls, the theoretical coupling efficiency coefficient, as defined by Paulay and Priestley (1992), calculated at the peak of various semi-cycles are depicted in Figure 2.5 next to the semi-cycle number (number inside parentheses). In specimen Wall A, the model indicates that the coupling efficiency coefficient decreases once the peak base shear force has been reached. The decrease in the coupling efficiency is also manifested in the amplitude of the wall axial forces, which also decreased after semi-cycle 9, see Figure 2.10a. According to the model, the decrease in the coupling was caused by degradation in the response of the coupling beams, see Figure 2.11a. In contrast, the coupling efficiency coefficient remained approximately constant with the progression of the test on specimen Wall B. Figure 2.10b shows that the magnitude of the maximum and minimum axial forces at the peak in every semi cycle remained very similar.

The hysteretic shear force - shear strain responses of Level 1 and Level 7 beams given by the Truss Models are shown in Figure 2.11 for the beams of specimens Wall A and Wall B. Figure 2.11 also shows the theoretical shear force calculated in accordance

with ACI-318 (2014) but using measured material properties and considering zero axial force. The theoretical shear strength of the conventionally reinforced coupling beams of specimen Wall A was 58% of the limit prescribed in ACI 318-14 of $0.83\sqrt{f'_c}\,A_g$ (MPa). For the diagonally reinforced coupling beams of specimen Wall B, the theoretical shear force was 81% of the limit prescribed in ACI 318-14. A comparison of the hysteretic responses of Level 1 and Level 7 beams reveal some distinct behavior. In both specimens, Level 1 coupling beams develop significant overstrength (70% and 63% greater strengths than the theoretical strength). In contrast, Level 7 beams develop low to moderate overstrength (25% and 8% greater strengths than the theoretical strength for the beams in Wall A and Wall B, respectively). The reason for the excess in capacity in Level 1 beams is the presence of axial compression force in the beams. When unrestrained, deep conventionally and diagonally reinforced beams elongate significantly if subjected to large chord rotations (Restrepo-Posada 1993). However, the presence of stiff walls connected to a foundation and framing into these beams, constrain the elongation of the beams, see Figure 2.9, resulting in the development of compressive forces, which redistribute the shear force from the trailing (decompressing or tensioning) wall to the leading (compressed) wall. The compressive force results in an increase of the capacity of the beams, and in the case of the beams in these two specimens, it decreases the shear strain at the onset of softening. The restraint on the coupling beams caused by the foundation and stiff walls gradually vanishes with height. Thus, coupling beams in Level 7, experienced small axial forces and the capacity was well predicted by conventional methods.

Figure 2.12 shows the distribution of the base shear in specimens Wall A and Wall B at various drift ratios. For specimen Wall A, the model indicates that at the wall base,

the leading wall resists between 67% and 84% of the base shear force. The maximum force resisted by the leading wall (shown as "Comp" in Figure 2.12) was 80% of the limit prescribed in ACI-318 (2014) of $0.83\sqrt{f'_c}\,A_g$ (MPa).

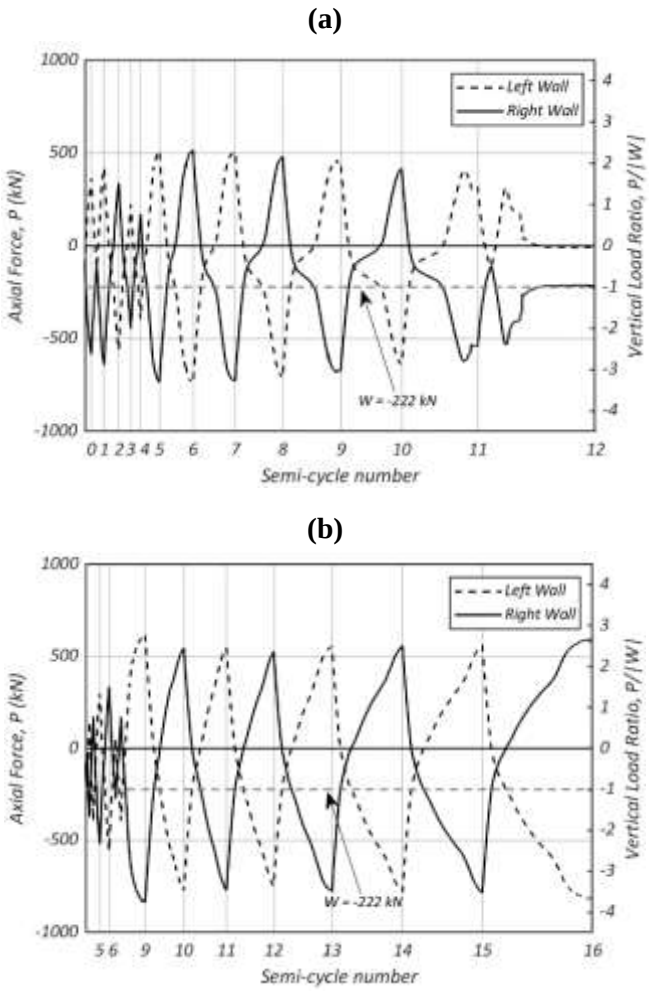

Figure 2.10. (a) History of axial force distribution in Wall A. **(b)** History of axial force distribution in Wall B (simulated gravitational force W = -222 kN).

Only at the end of testing (i.e., at 7.01% roof drift ratio), when the coupling provided by the beams had degraded because of sliding shear, the trailing wall resisted a significant percentage of the base shear.

(a)

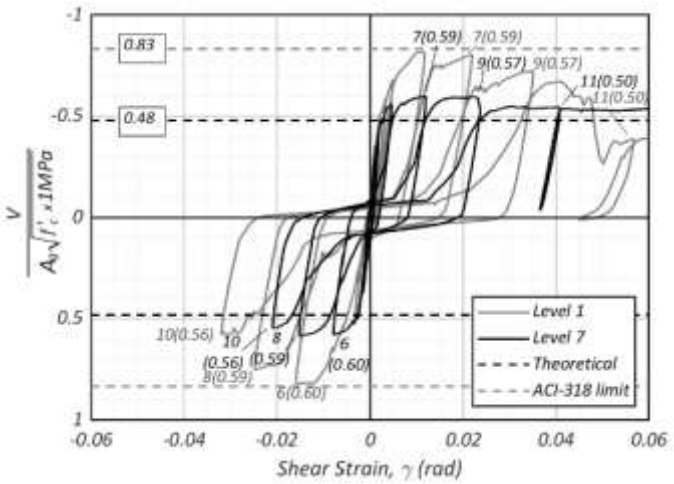

(b)

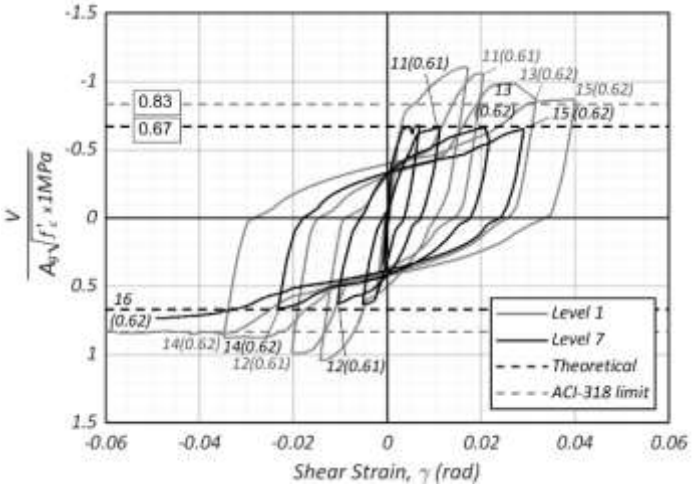

Figure 2.11. Normalized shear force - shear strain relationships computed for the first-level coupling beam and for the roof coupling beam. **(a)** Wall A. **(b)** Wall B. The theoretical capacity in Wall A and Wall B beams was predicted using measured material properties. The coupling efficiency coefficient (Paulay and Priestley 1992) calculated at the specific displacement in the response is shown in parenthesis.

For specimen Wall B, the model indicates that at the wall base, the leading wall resisted between 81% and 91% of the base shear force. The maximum force resisted by the leading wall 96% of the limit prescribed in ACI-318 (2014) of $0.83\sqrt{f'_c}\,A_g$ (MPa). We note that apportioning of the shear force between leading and trailing walls should not be

computed by linear analysis tools often used in design practice, unless different ad hoc stiffness modifiers are used for the leading and trailing wall in the linear model.

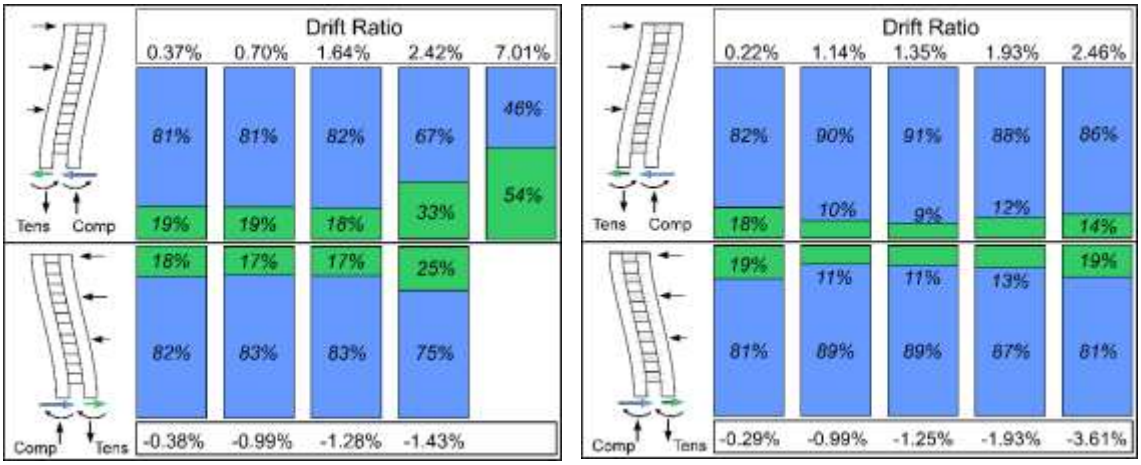

Figure 2.12. Distribution of base shear in the left wall and right wall for peaks of semi-cycles (blue color indicates the wall is in compression while green corresponds to the wall in tension). **(a)** Wall A. **(b)** Wall B.

2.7 Conclusions

This paper compared the response of a landmark test on two 1:4 scale seven-story coupled walls (Santhakumar 1974) with the response calculated using the Truss Model. The model was developed using the opensource nonlinear analysis program OpenSees. Specimen Wall A used conventionally reinforced beams with a theoretical shear force capacity of 58% of the maximum permitted in ACI-318 (2014). The peak lateral force in this specimen was attained at a 1.7% roof drift ratio. Gradual softening in the overall response occurred thereafter and was associated with significant sliding shear in all the coupling beams. Specimen Wall B was built incorporating diagonally reinforced beams with a theoretical shear force capacity of 81% of the maximum permitted in ACI 318-14. This specimen exhibited stable response with minimum degradation and attained a roof

drift ratio of 3.6% when the longitudinal reinforcement in a wall toe buckled and the concrete there crushed.

Truss Models of both specimens capture well key aspects of the response: the response envelope of both specimens and sliding shear of the beams in specimen Wall A. The models overpredict the hysteretic energy dissipation compared with the observed test response. It seems plausible that the unloading part of the experimentally measured hysteretic responses, and the recentering observed could be due to the presence of the elastic tendons used to provide axial force. The tests incorporated a mechanism to manually control the axial force in the tendons during the loading and unloading phase of the tests. In broader terms, and because the methodology used in this system test in the early days of experimental earthquake engineering gave emphasis on reporting results as a function of force ratios, and not force and drift ratios, a comparison of test and model results is made difficult. Nevertheless, model and test results show similar trends in the strains in the coupling beam reinforcement and in the dilatation between the wall axes caused by the lengthening of the coupling beams.

Important responses that cannot be recorded in a test, were computed with the Truss Model. The model shows the effect that the restraint provided by the foundation to the walls also restrains the lower level coupling beams. As a result, these beams develop axial compression and higher overstrength that beams on other levels. Finally, the Truss Models showed that for the two test specimens, the wall being compressed (leading wall) carries more than 67% of the shear force. This apportioning of the shear force between leading and trailing walls cannot be computed by linear analysis tools unless different ad hoc stiffness modifiers are used for the leading and trailing wall in the linear model.

2.8 Acknowledgements

Chapter 2, in part, is a reprint of the material as it appears in *Nonlinear Cyclic Truss Model for Analysis of Reinforced Concrete Coupled Structural Walls*. Bulletin of Earthquake Engineering, Special Issue: Nonlinear Modeling of Reinforced Concrete Structural Walls and Wall Systems, https://doi.org/10.1007/s10518-019-00639-8, 2019. Alvarez, Rodolfo; Restrepo, Jose I.; Panagiotou, Marios; and Santhakumar, A. Ramalingam. The dissertation author was the primary investigator and author of this paper.

We acknowledge to the CONACYT, UC MEXUS, and COMEXUS for providing financial support.

Chapter 3. Analysis of Reinforced Concrete Coupled Structural Walls Via the Beam-Truss Model

3.1 Abstract

The use of an enhanced version of the Beam-Truss Model proposed in a previous study to compute the nonlinear response of reinforced concrete coupled walls is discussed in this paper. The results of the cyclic tests of two seven-story one-quarter scale coupled walls tested in New Zealand are used for model validation. Except for the coupling beams, the specimens were identical. One of the specimens (Wall A) had a conventional arrangement of reinforcement in the coupling beams, whereas the other (Wall B) had beams with diagonal bars. Specimen Wall A showed lateral force-displacement response degradation after reaching a 1.6% roof drift ratio. The degradation in specimen Wall A was due to the sliding shear of the beams. Specimen Wall B exhibited stable hysteretic response throughout the test.

The authors use two kinds of Beam-Truss Models and compare computed and measured key responses in these tests. Computed responses, measured and not measured in the tests, are also compared with the results of Nonlinear Truss Models reported in the literature.

This paper shows that the relatively simple and computational-efficient Beam-Truss Models predicted well important aspects of the response, such as the lateral force-displacement envelope, the sliding shear of the coupling beams in specimen Wall A and the ductile behavior of specimen Wall B.

3.2 Introduction

Reinforced concrete coupled structural walls or core walls incorporating two wall piers interconnected with a series of coupling beams are a commonly used lateral system in buildings. Walls can be coupled with conventionally reinforced or diagonally reinforced beams. However, shear failures observed in stout conventionally reinforced coupling beams in buildings exposed to strong ground motions and in a testing (Boroschek et al. 2014, Paulay and Santhakumar 1976) have led to geometrical and shear stress limits for the use of these two types of coupling beams. For example, in ACI 318-14 (2014), coupling beams with an aspect ratio $l_n/h < 2$ (where l_n is the length of the clear span measured face-to-face of supports, and h is the depth of the coupling beam) and $V_u \geq 4\sqrt{f'_c}\, A_{cw}$ (where V_u is the factored shear force in lb, f'_c is the compressive strength of concrete in psi, and A_{cw} is the area of the concrete section in in^2) shall be diagonally reinforced, and if $l_n/h \geq 4$ the coupling beams shall be designed as beams of special moment frames. In any case, V_n shall not be taken greater than $10\, A_{cw} \sqrt{f'_c}$ (where V_n is the nominal strength in lb). The coupling beams are key components for the seismic response of coupled walls; these have a significant influence in the axial and shear force demands in the framing wall piers (Alvarez et al. 2019).

In current practice, it is common to use linear analysis (either equivalent static or modal response spectrum) to obtain section demands in support of the design. It is well known that demands calculated from the linear analysis can significantly underestimate the shear force demands in the wall piers (Boroschek et al. 2014, Panagiotou et al. 2011, Panagiotou and Restrepo 2011, Panagiotou and Restrepo 2009). An important disadvantage of the linear analysis is the use of prescriptive element effective stiffness to

account for cracking, which hampers the use of redistribution concepts and, more importantly, it results in irrational shear and flexure demands in coupled walls (Alvarez et al. 2019). Such irrational demands can cause difficulties in the implementation of the capacity design. For buildings, the performance-based design is desired to use nonlinear time-history analysis (TBI 17 2017). In this situation, the most popular solution to model the walls is using Euler-Bernoulli beams with fiber-sections and uniaxial materials, whereas in general, the coupling beams are modeled using shear springs (Naish et al. 2013, ASCE 41-13 2013). These modeling techniques have their own limitations as nonlinear flexure-shear interaction cannot be accounted for.

The correct simulation of coupled walls with short coupling beams is especially difficult because it is necessary to consider flexure-shear interaction (Lu and Panagiotou 2016). Reinforced concrete structural walls can be modeled using either micro or macro models (Lu and Panagiotou 2013, Toprak et al. 2015, Dashti et al. 2017a), which consider the flexure-shear interaction. The micro models relay on the detailed interpretation of the local behavior of specimen walls, whereas the macro models focus on capturing practically and efficiently the overall wall response with reasonable accuracy. Smeared-crack or plasticity-based finite elements (Gormak 1974, Zhao et al. 2004, Mohr et al. 2007, Mihaylov and Franssen 2017) are examples of micro models. On the other hand, empirically calibrated shear springs (Naish et al. 2013, Vulcano 1992, Fischinger et al. 1992); multiple vertical line models (Fischinger et al. 2012, Kolozvari and Wallace 2016); truss models and beam-truss models (Lu et al. 2016, Lu and Panagiotou 2013, Panagiotou et al. 2012) are macro model examples.

This paper mainly focuses on the Beam-Truss Model (BTM) methodology proposed by Lu et al. (2016). The BTM had its origin in the 2D Truss Model developed by Panagiotou et al. (2012), which incorporated the biaxial behavior of concrete proposed by Vecchio and Collins (1986). The Truss Model implements a truss analogy capable of capturing flexure-shear interaction in 2D walls. Barbosa (2011) extended the Truss Model to 3D by considering out-of-plane bending in the model. Lu and Panagiotou (2013) developed a model similar to BTM, which included mainly truss action in-plane and beam-like action out-of-plane; in this methodology, all the vertical elements incorporated the in-plane flexural rigidity. Lu et al. (2016) developed the BTM from the former model (Lu and Panagiotou 2013), making all the elements to work as truss elements in-plane, except for those representing confined concrete (e.g., boundary elements), which included in-plane flexural rigidity. The BTM naturally considers the flexure-shear interaction and warping associated with multi-axial stress states in nonplanar elements, which allows to model not only walls but slabs and core walls. Furthermore, the BTM has been used to compute the seismic response of complete buildings with nonlinear time-history analysis (Lu 2014, Zhang et al. 2017).

This paper applies, with some differences, the BTM methodology to the computation of the nonlinear cyclic response of two pioneering tests on reinforced concrete coupled walls. The tests, reported by Santhakumar (1974), consisted of two one-quarter scale seven-story coupled walls that were subjected to quasi-static reversed cyclic loading. Except for the coupling beams, the specimens (Wall A and Wall B) were equal. Specimen Wall A was reinforced with longitudinal bars and stirrups in the beams. This specimen exhibited degradation of its response after reaching a 1.6% roof drift ratio. Sliding shear

failure occurred in the beams that resulted in overall degradation. Specimen Wall B incorporated diagonally reinforced coupling beams and exhibited ductile and stable hysteretic behavior up to a roof drift ratio equal to 3.6% when a wall pier buckled above the foundation.

Two computational models of the specimens Wall A and Wall B were created in OpenSees (OS) (McKenna 2019) with different variants of the BTM developed by Lu et al. (2016). The first BTM used in this paper included truss elements to represent vertical and horizontal elements, except for the modeling the boundary elements, where displacement-based elements (DBE) were the preferred choice; whereas Lu et al. (2016) exclusively used force-based elements (FBE) in all vertical and horizontal elements. This model will be termed here Modified Beam-Truss Model (MBTM). The second BTM, termed the Enhanced Beam-Truss Model (EBTM), was an extension of the MBTM that incorporated the bar-bond slip of the reinforcement anchored beyond the coupling beam ends. In the case of specimen Wall A, the EBTM also incorporated the dowel action of the longitudinal reinforcement of the coupling beams. This paper discusses key results obtained with each of these two models and makes a comparison with responses reported by Santhakumar (1974). Furthermore, responses computed with the EBTM are compared with those computed using the Nonlinear Truss Model (NTM) developed by Alvarez et al. (2019) for the same specimens. Element responses that are relevant to the practicing engineering community, which could not be measured in these two tests, are discussed in this paper.

3.3 Description of specimens

The MBTM and EBTM are validated with the landmark reversed cyclic loading tests of two specimens reported by Santhakumar (1974), Paulay and Santhakumar (1976). The geometry and reinforcement of the two one-quarter scale specimens, Wall A and Wall B, corresponded to the design of building prototypes with seven stories. The tributary area of the coupled walls in the prototype buildings was 6.10 m by 9.10 m, and the corresponding lateral loading was 10% of the seismic weight (NZSS-1900 1965).

The specimens were identical except for the reinforcement of the coupling beams (see Figure 3.1). The coupling beams in specimen Wall A had conventional longitudinal and transversal reinforcement, and those in specimen Wall B had diagonal bars. The geometry of the coupled walls and coupling beams is displayed in Figure 3.1. The aspect ratio of the beams resulted in length/depth = 1.25. The specimens were cast in a horizontal position without cold joints. The reinforcement properties used in the wall piers of the specimens are listed in Table 3-1. The compressive strength of the concrete was f'_c = 31.6 MPa, whereas the modulus of rupture was f_r = 2.9 MPa in specimen Wall A; in specimen Wall B, these were 30.0 MPa and 2.7 MPa, respectively.

The longitudinal bars sizes at base of the wall piers were #5 (16 mm) at the edges, and #2 (6.35 mm) in between edges, see Figure 3.1. The walls piers were transversely reinforced using #2 stirrups. Table 3-2 and Table 3-3 list the characteristics of the reinforcement of the beams in both specimens. Longitudinal bars #3 and transversal bars #2 were used to reinforce the coupling beams of specimen Wall A. The beams in specimen Wall B had diagonal #3 bars and longitudinal 3/16” (4.8 mm) diameter bars.

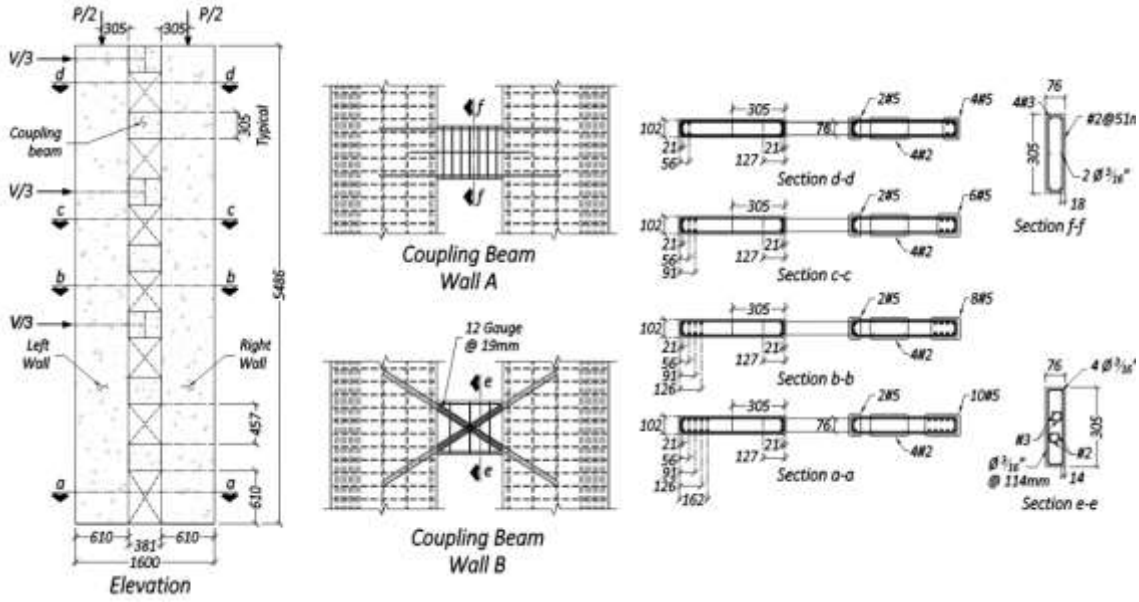

Figure 3.1. Geometry and reinforcement details of specimens Wall A and B.

Table 3-1. Reinforcement used in the wall piers of both specimens.

Level	Vertical Reinforcement						Horizontal Reinforcement	
	Outer boundary		Inner boundary				Stirrups	
	Steel ratio	Bar	Steel ratio	Bar	Steel ratio	Bar	Steel ratio	Bar
1	0.1060	10 #5	0.0213	2 #5	0.0026	2 #2	0.0088	2 #2@76
2	0.1060	10 #5	0.0213	2 #5	0.0026	2 #2	0.0088	2 #2@76
3	0.1060	10 #5	0.0213	2 #5	0.0026	2 #2	0.0088	2 #2@76
4	0.0852	8 #5	0.0213	2 #5	0.0025	2 #2	0.0067	2 #2@102
5	0.0639	6 #5	0.0213	2 #5	0.0024	2 #2	0.0067	2 #2@102
6	0.0426	4 #5	0.0213	2 #5	0.0023	2 #2	0.0044	2 #2@152
7	0.0426	4 #5	0.0213	2 #5	0.0023	2 #2	0.0044	2 #2@152
	f_y = 3.05 GPa				f_y = 3.43 GPa		f_y = 3.43 GPa	
	f_u = 4.72 GPa				f_u = 4.87 GPa		f_u = 4.87 GPa	

Table 3-2. Specimen Wall A coupling beam reinforcing details.

Main Reinforcement				Secondary Reinforcement	
Longitudinal		Transverse		Longitudinal	
Steel ratio	Bar	Steel ratio	Bar	Steel	Bar
0.0062	2 #3	0.0176	2 #2 @ 51	0.0014	2 ϕ 3/16”
f_y = 3.15 GPa		f_y = 3.46 GPa		f_y = 2.30 GPa	
f_u = 4.31 GPa		f_u = 4.87 GPa		f_u = 3.39 GPa	

Table 3-3. Specimen Wall B coupling beam reinforcing details.

Main Reinforcement				Secondary Reinforcement	
Diagonal		Confining of diagonal		Vertical	
Steel ratio	Bar	Steel	Bar	Steel	Bar
0.0112	2 #3 + 2 #2	0.0400	12 Gauge @ 19 mm	0.0035	2 ϕ 3/16″ @ 114 mm
f_y = 3.15 – 3.46 GPa		f_y = 3.81 GPa		f_y = 2.30 GPa	
f_u = 4.31 – 4.87 GPa		f_u = 4.78 GPa		f_u = 3.39 GPa	

In the case of the conventionally reinforced coupling beams incorporated in specimen Wall A, a large amount of transverse reinforcement was used (see Table 3-2), which in turn was effective delaying shear diagonal failures but ineffective preventing sliding shear. Due to the relatively large size of the longitudinal reinforcement of the coupling beams, dowel action played an important role during the sliding shear. A large amount of longitudinal reinforcement was placed at the wall pier ends too (see Table 3-1), where relatively large diameter bars were detailed. Therefore, dowel action was also important in this case. For specimen Wall B, Santhakumar (1974) estimated that mechanisms such as dowel action and aggregate interlock carried more than 30% of the base shear.

To simulate the vertical load, the specimens were subjected to compressive forces of 111 kN at the wall piers (N/f'_cA_g = 0.06), which resulted in similar axial stresses as in the walls of the prototype buildings. These forces were applied with prestressing tendons at the centroid of the wall piers, along with the height. The specimens were also subjected to forced-controlled quasi-static reversed cyclic loading with equal loads at the 3rd, 5th, and 7th level; the lateral load pattern was chosen according to the NZSS-1900 (1965). The test control method employed by Santhakumar (1974) differs from the nowadays used displacement-controlled, which can maintain adequate control near the peak load and the softening response. The forces were applied using single-acting jacks. To keep the vertical

load constant during the lateral loading and unloading, the tensile force in the tendons was manually controlled.

3.4 Description of the modified Beam-Truss Model

3.4.1 Model components

The BTM, as developed by Lu et al. (2016) is a 3D methodology used to compute the response of planar (e.g., coupled walls) and non-planar (e.g., core walls) reinforced concrete elements and structures subjected to quasi-static monotonic or reversed cyclic loading and to earthquake input ground motions. The concrete and reinforcement in the vertical and horizontal directions are modeled using FBE with fiber-sections according to their tributary areas. The grid formed by the vertical and horizontal elements has out-of-plane flexural rigidity, which allows the BTM to capture warping. In-plane rigidity is only used in the confined elements (e.g., boundary elements). The diagonal compression field of the concrete is modeled using *Truss2* elements with sections also according to their tributary areas.

The specimens Wall A and Wall B were planar, loaded only in-plane, and no warping was expected to occur. Due to this, to reduce the number of DOF, the models were implemented using a 2D version of the BTM described above. In this modified BTM (termed thereafter MBTM), the vertical and horizontal elements, instead of being FBE, are chosen truss elements. Additionally, to enhance convergence, the boundary elements of the MBTM use DBE (including in-plane flexural rigidity) instead of FBE. *Truss2* elements for diagonals and *ConcretewBeta* material, as implemented by (Lu and Panagiotou 2013) in OpenSees (McKenna 2019), are also adopted for the MBTM.

When *ConcretewBeta* is used in the definition of a *Truss2* element, the material considers the influence of the biaxial field of strains in the compressive strength of the concrete via the compressive strength reduction factor β (Vecchio and Collins 1986). The *Truss2* element defines a dummy perpendicular element as gage; then, the *ConcretewBeta* material monitors the strains and adjusts the compressive strength of the *Truss2* element accordingly. This adjustment in the compressive strength is a key aspect to consider for the correct computation of shear failures in concrete elements. The calibration of the input parameters that control the factor β (i.e., *bint*, *ebint*, *bres* and *ebres*), is in accordance with Lu et al. (2014).

The geometry and definition of the elements of the MBTM are shown in Figure 3.2. The inclination of the diagonal elements is proposed according to Lu et al. (2014) as, $\theta_d = tan^{-1} (V_{max}/(f_{y,t}\ \rho_t\ t_w\ d_{vl})) \leq 65\ °$, where V_{max} is the peak lateral force, $f_{y,t}$ the yield strength of the transversal reinforcement, ρ_t is the steel ratio of the transversal reinforcement, t_w the wall thickness and d_{vl} the width of the grid in the direction of loading. The areas of concrete and reinforcement in the truss elements and fiber-section beams are also defined in Figure 3.2. The effective width of the diagonal elements is $b_{eff} = a\ sin\ (\theta_d)$, where *a* is the spacing between the vertical elements. Additional recommendations about the geometric definition of the elements and the angle of inclination of the diagonals can be found in Lu et al. (2014). In the MBTM, all the DOF of the nodes are fixed at the walls piers' base; and where only truss elements are connected to a single node, the in-plane rotational DOF of the node is restrained to avoid ill-conditioning.

3.4.2 Constitutive stress-strain relationships

The reinforcing steel is modeled with the uniaxial material *SteelDRC* (Carreño 2018), which is an in-house OpenSees implementation of the model developed by Dodd and Restrepo-Posada (1995) (Figure 3.3a). This constitutive material stress-strain relationship is calibrated using tensile test parameters, and because this explicitly simulates the yield plateau, the kinematic hardening, and the point of ultimate strength (ε_u, f_u), further calibrations are not needed to set a cap in the strength. *SteelDRC* also considers the Bauschinger effect, which is controlled by the parameter *OmegaFact.* This parameter is calibrated according to the carbon content of the steel (Carreño 2018).

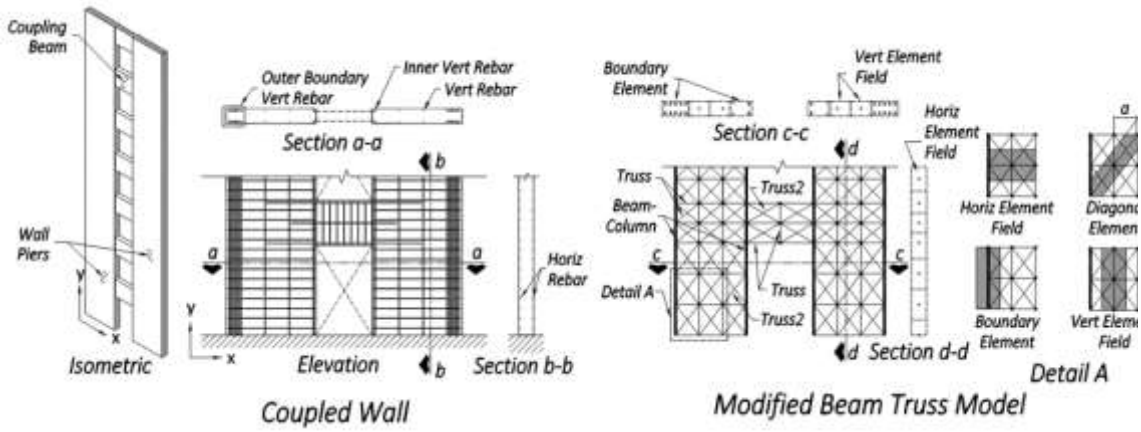

Figure 3.2. Description of the geometry and the type of elements used in the MBTM.

The MBTM uses *ConcretewBeta* material in all concrete components. The calibration of the constitutive stress-strain relationships of the *ConcretewBeta* (see Figure 3.3b) was similar to that described in Alvarez et al. (2019) and repeated here for convenience. The Young's modulus of concrete is $E_c = 5000\sqrt{f'_c}$ (MPa), whereas the strain at the compressive strength f'_c and the strain at crushing f_{cu} are $\varepsilon_o = -0.002$ and $\varepsilon_{cu} = -0.004$ respectively (Lu and Panagiotou 2013). The direct tensile strength in terms of the modulus of rupture f_r is $f_t = 0.55 f_r$ (Collins and Mitchell 1997). The confined compressive strength

f_{cc} and the corresponding strain ε_{co} were calculated according to Mander et al. (1988). The strain at the softening onset was defined as $\varepsilon_{cs} = -(0.002 + k_e \cdot f_l/(9f'_c))$, where f_l is the confining stress and k_e the efficiency coefficient (Alvarez et al. 2019). Zero tensile strength f_t was assumed in all diagonal elements, horizontal wall pier elements, and vertical elements of the coupling beams (Lu et al. 2016). The compressive stress at the closure of cracks in the diagonal elements was made equal to $-0.03f'_c$ (Alvarez et al. 2019). To enhance convergence, the compressive residual strength of the concrete after crushing is equal to $-0.2f'_c$.

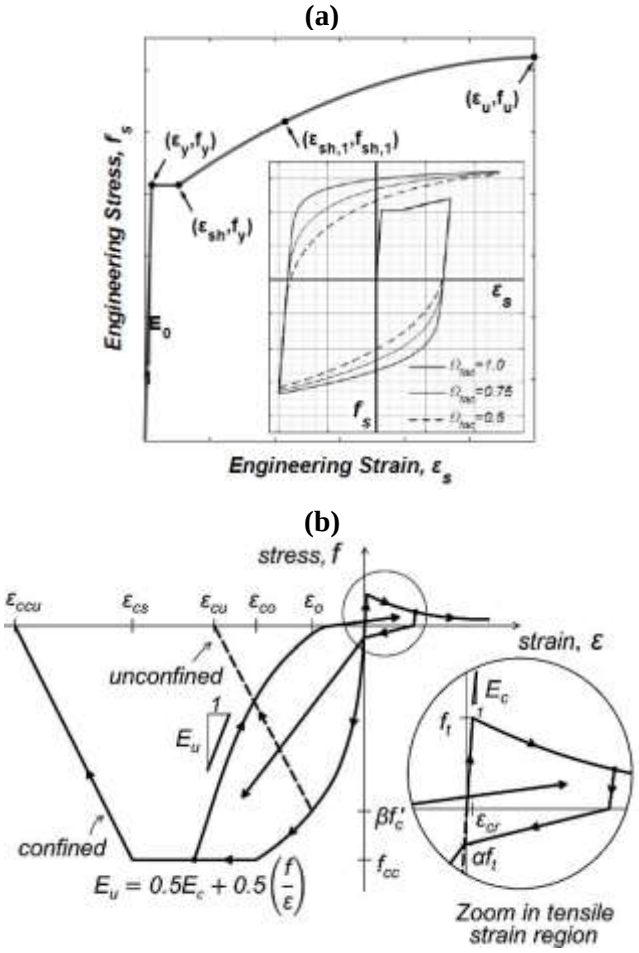

Figure 3.3. Uniaxial constitutive material stress-strain relationships. **(a)** Stress-strain relationship for *SteelDRC*, figure courtesy of Carreño (2018). **(b)** Stress-strain relationship for *ConcretewBeta*, figure courtesy of Lu and Panagiotou (2013).

To preserve the mesh objectivity of the models (Coleman and Spacone 2001), the constitutive stress-strain relationships used for concrete are regularized in compression following Lu and Panagiotou (2013), whereas the regularization of the factor β is carried out as in Lu et al. (2014).

3.4.3 Specific details of the models

A built in-house 64-bit executable of the program OpenSees (McKenna 2019) is used to develop the models in this paper. The executable includes the classes corresponding to the material *SteelDRC* (Carreño 2018) and the postprocessing libraries of the program *STKO* (Petracca et al. 2017a, Petracca et al. 2017b).

The wall pier toes had concentrations of longitudinal reinforcement (Figure 3.1). Here, these regions are designated "boundary elements", as in modern codes, although they were not detailed to confine the concrete and delay the buckling of the reinforcement. Due to the asymmetry of the longitudinal reinforcement in the wall piers, the geometric definition of vertical elements is challenging. Three equal horizontal quadrilaterals are proposed for the grid (Figure 3.4). The boundaries are modeled with beam elements including in-plane flexural rigidity. It is considered that any spurious delay of shear failures in the wall piers due to the use of beam elements in the boundaries does not affect the conclusions because indeed, shear failures were not observed in the wall piers of the specimens.

Section "a" (see Figure 3.1) had 2 #5 + 2 #2 bars at the interior boundary element and 10 #5 bars at the exterior boundary, and each bar is represented in the model by one fiber of steel. The concrete is modeled with 15 layers in the interior boundary element (0.148 m x 0.102 m) and 18 layers in the exterior boundary (0.183 m x 0.102 m). The two

remaining vertical lines use truss elements, and the corresponding areas are adjusted, so the test and model centroids coincide. The rest of the sections ("b" to "d", see Figure 3.1) are defined in a similar way.

Lu et al. (2016) proposed a methodology to calculate the inclination of the diagonals in their BTM. Assuming the wall piers are two independent cantilever walls, this procedure results in inclinations of the diagonals equal to 60° and 63° in specimens Wall A and Wall B, respectively. However, because the wall piers of the specimens did not fail in shear and the diagonals only play an important role in such a situation, in this paper, the methodology of Lu et al. (2016) is not used. Instead, the inclination of the diagonals of the MBTM is proposed according to the crack pattern observed in the specimens. The inclination in the wall piers at Level 1 and the wall piers above the Level 1 results in 53° and 46°, respectively. The inclination of the diagonal reinforcement in the specimen Wall B defines the grids of the coupling beams, resulting in the inclination of the diagonals trusses equal to 60°. To capture sliding shear in the coupling beams of the MBTM, the grids of beams are finer than those in the wall piers (four by four quadrilaterals, see Figure 3.4). Finally, the slope of the diagonals in the panels is 40°, as a result of the grid set by vertical elements in the wall piers and horizontal elements in the beams.

The flexure reinforcement of the coupling beams in specimen Wall A and the diagonal reinforcement of the beams in specimen Wall B are anchored in the MBTM using truss elements (Figure 3.4). The length of these truss elements is proposed to be equal to the physical anchorage length minus one half the corresponding development length.

The element state-determination of the fiber-section beams adopts three Gauss-Lobatto integration points; all the elements in the MBTM use linear coordinate

transformation. The vertical loads and the lateral loading protocol are applied through force control and displacement control integrator, respectively. As mentioned before, the vertical loads were simulated in the specimens by applying forces with prestressing tendons at the centroid wall piers. It is possible to model the tendons in the MBTM using truss elements along the height wall piers. The truss elements should be connected at the top wall piers, and the tendons' nodes at the base should be the loading and control nodes to introduce the prestressing forces using displacement control analysis. The main side effect of using tendons to simulate vertical loads is the additional stiffness introduced in the system if the prestressing forces are not controlled as the coupled wall experiences lateral deformations.

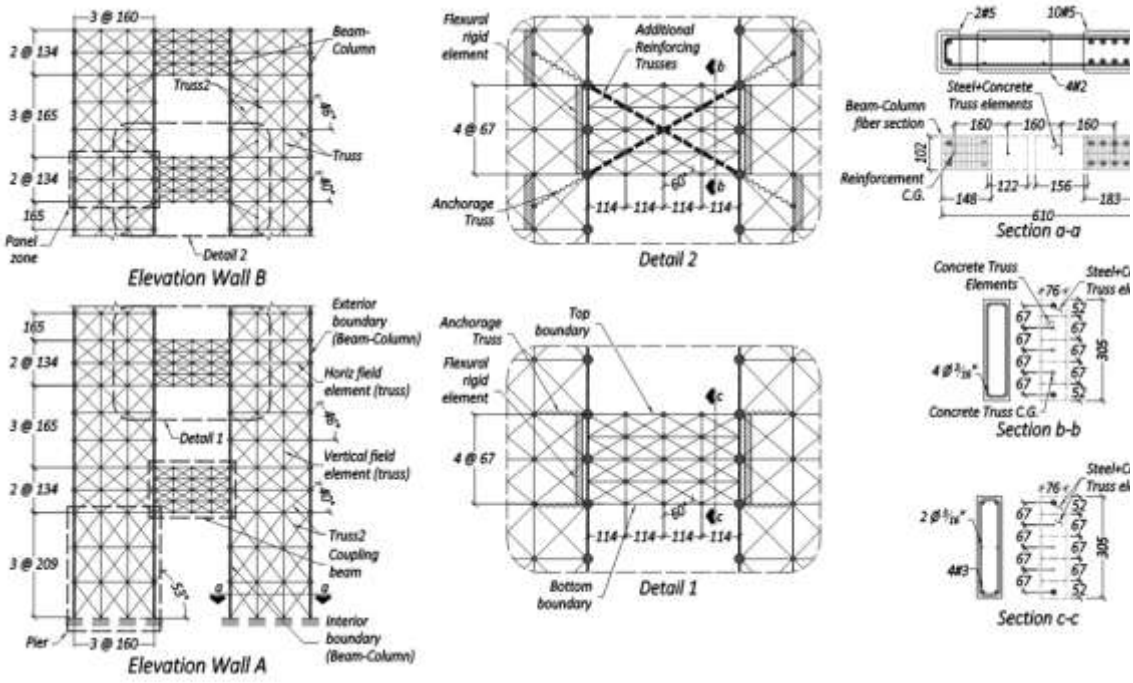

Figure 3.4. Specific details of the MBTM of the specimens Wall A and Wall B.

The force in the tendons was manually controlled in the tests, and because of that in the MBTM the vertical loads were applied directly at top nodes using simple force control analysis.

3.5 Description of the Enhanced Beam-Truss Model

The Enhanced Beam-Truss Model (EBTM), was mainly an extension of the MBTM described above. The EBTM uses the same model components and constitutive stress-strain relationships as the MBTM, and the modeling of the wall piers is identical, but some improvements to the modeling of the coupling beams were implemented. The EBTM incorporates the bar-bond slip of the reinforcement anchored beyond the coupling beam-ends, and for specimen Wall A, it also incorporates the dowel action of the longitudinal reinforcement of the coupling beams. A detailed description of these enhancements is given below.

In the models developed for the two coupled wall specimens, the coupling beams are modeled using only truss elements (i.e., Truss Model). For responses that exhibit shear failures, which is the case of the beams of specimen Wall A, the Truss Models are rather dependent on the slope of diagonal elements (Panagiotou et al. 2012). In the EBTM of specimen Wall A, the angle of inclination of the diagonal elements of the coupling beams is defined according to the methodology proposed for specimen walls by Lu et al. (2016), which results in 45°. This angle agrees with the general crack pattern observed. The grid of the coupling beams of the EBTM of specimen Wall A has six horizontal quadrilaterals by four vertical quadrilaterals (Figure 3.5a). Truss elements are used to represent the reinforcement and the concrete, except for the flexure reinforcing steel at the top and bottom of the beams. In such locations, to better compute the sliding shear response exhibited in this specimen, dowel action is captured modeling the reinforcement with fiber-section beams. Additional rigid elements are used to locate sliding shear failure outside the

wall piers. The grid of the coupling beams of the EBTM of specimen Wall B is identical to the grid of the MBTM.

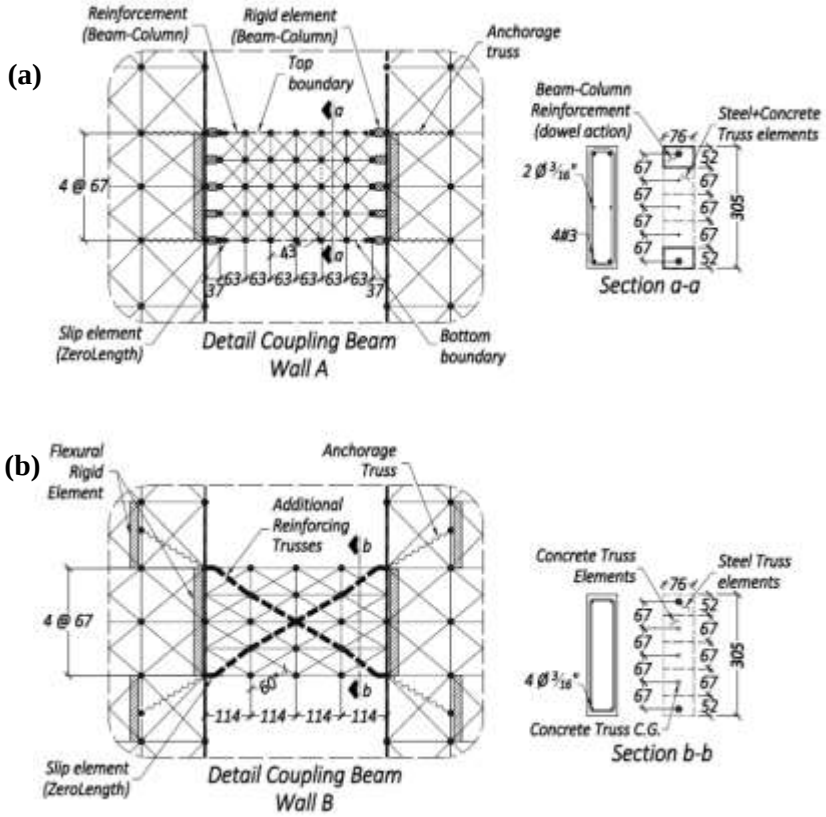

Figure 3.5. Coupling beam modeling details used in the EBTM. **(a)** Specimen Wall A. **(b)** Specimen Wall B.

To better compute the hysteretic energy dissipated, the coupling beams of the EBTM include the bond-slip of the longitudinal reinforcement anchored in the wall piers in specimen Wall A (Figure 3.5a) and of the diagonal bars in specimen Wall B (Figure 3.5b). A parametric study indicated that when in-plane flexural rigidity is used in the beams to represent the boundary elements, the modeling of the anchorage of the flexure reinforcement and diagonal bars does not affect the computed responses significantly. This is because the end beam elements locally stiffen the behavior and redistribute the forces eliminating the effect of the anchorage. Therefore, the bar bond-slip is modeled using

zeroLength elements with horizontal DOF in the interface of the coupling beams and the wall piers, see Figure 3.5. The pinched hysteretic behavior typical of bar bond-slip is simulated using the uniaxial material *Hysteretic* in the *zeroLength* elements, see Figure 3.6. This material used pinching parameters *pinchx = 0.40* and *pinchy = 0.20* (Lu et al. 2014), and it was calibrated with the properties of the reinforcement that represents. The force-displacement curves of the *zeroLength* elements mimic truss elements with area equal to the anchor reinforcement and length L_b defined using the methodology proposed by Zhao and Sritharan (2007). The different lengths L_b result in about twenty bar diameters for the case studies. The envelope of the *Hysteretic* material is defined as depicted in Figure 3.6. In the case of specimen Wall B, the force-displacement envelope of the diagonal anchorage is transformed to the horizontal DOF of the *zeroLength* element in terms of the inclination of the diagonal θ_d as follows:

$$e_1 = \varepsilon_y L_b / \sin \theta_d, \qquad s_1 = A_s f_y \sin \theta_d \tag{3.1}$$

$$e_2 = 0.5\varepsilon_u L_b / \sin \theta_d, \quad s_2 = A_s f_u \sin \theta_d \tag{3.2}$$

$$e_3 = \varepsilon_u L_b / \sin \theta_d, \qquad s_3 = A_s f_u \sin \theta_d \tag{3.3}$$

To avoid deformations in compression in the *zeroLength* elements, the *Hysteretic* material runs in parallel with the no-tension uniaxial material *ENT* calibrated to be rigid in compression. In the EBTM, fiber-section beam elements in specimen Wall A and truss elements in specimen Wall B are used to model longitudinal and diagonal bars in the coupling beams, respectively. The beams and trusses representing the reinforcement are connected to the boundary elements through z*eroLength* elements, whereas the truss elements representing the concrete areas are connected directly to the boundaries (Figure 3.5).

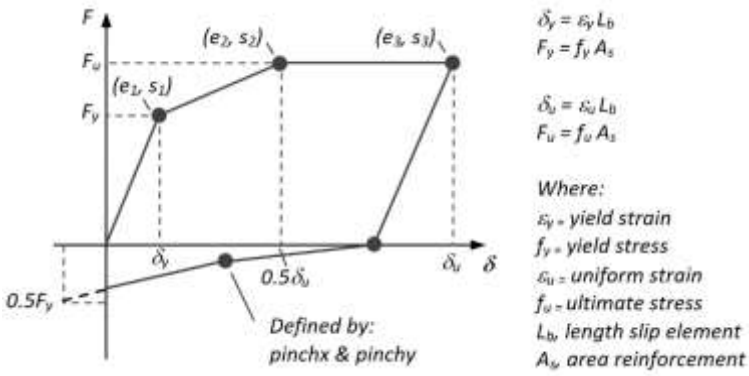

Figure 3.6. Calibration of the Hysteretic Material for bond-slip of the reinforcement of the coupling beams.

3.6 Model validation

3.6.1 Validation of the Modified Beam-Truss Models

Key aspects of the experimentally measured overall responses for both specimens, and corresponding predicted responses using the MBTM are compared in this section. The measured and computed base shear - roof displacement relationship responses for the specimens are shown in Figure 3.7.

Specimen Wall A exhibited sliding shear failure in the beams and crushing at the base, which caused the pinched overall response depicted in Figure 3.7a. This specimen attained the peak base shear at the roof drift ratio equal to 1.6%; after that, the specimen Wall A displayed progressive softening. On the other hand, a stable hysteretic response was exhibited by specimen Wall B up to the roof drift ratio of 3.6%. At this drift, a misalignment of the specimen caused plastic hinge wall buckling at the wall pier assuming the largest compressive force of the two wall piers (Santhakumar 1974).

The MBTM predicts an initial stiffness twice as large as the values reported for the tests, which is expected because of the overlapping areas of the elements (Lu et al. 2014). For specimen Wall A the model underpredicts the peak forces of the base shear, except for

the first cycles (Figure 3.7a). The maximum error was 26% and occurred at the peak of the semi-cycle 1. During the semi-cycle 11 (with maximum drift ratio 2.4%), specimen Wall A exhibited bar buckling at the base of the inner boundary of the wall pier in tension (Santhakumar 1974). This local response is not captured by the models because these do not explicitly consider bar buckling.

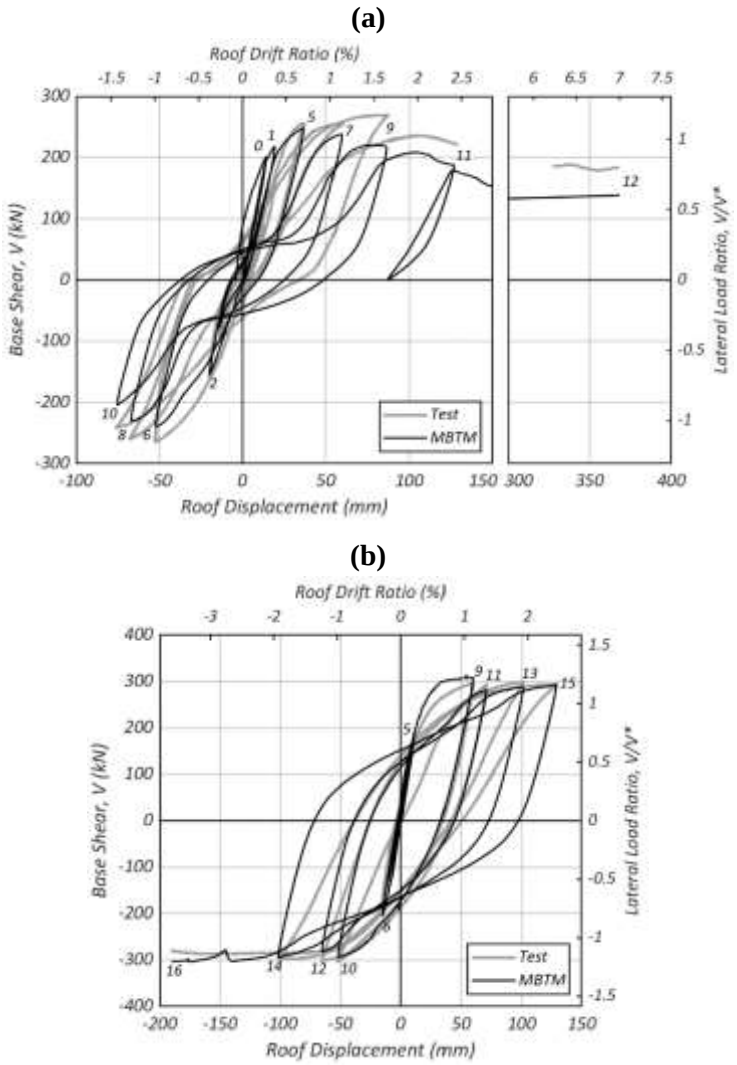

Figure 3.7. MBTM computed and measured the base shear - drift ratio. **(a)** Specimen Wall A. **(b)** Specimen Wall B. Where the code-calculated ultimate base shear, V^*, is 230 kN for specimen Wall A and 252 kN for specimen Wall B.

For specimen Wall A, a comparison of the measured and computed base shear - roof displacement relationship responses (Figure 3.7a) reveals that the hysteretic energy dissipated is greatly overestimated by the MBTM. The measured hysteretic response exhibits unusual behavior (i.e., unloading in double curvature). The unloading branches, exhibit small stiffness in comparison with the initial stiffness and then stiffens upon further unloading. The opposite was expected; that is, close to the reversals, unloading branches with stiffness like the initial and then gradual softening. The authors believe that such unexpected behavior is likely caused by the manual control of the load in the prestressing in the tendons (used to simulate the vertical loading in the specimens) during lateral unloading (Restrepo and Rahman, 2007).

The envelope of the hysteretic response of specimen Wall B computed by the MBTM is in good agreement with the measured response, see Figure 3.7b. The maximum error is 19% and occurs at the peak of the semi-cycle 6; for the rest of the lateral loading, the peaks of base shear are calculated within an error of 8.4%. However, significant differences exist in the prediction of the overall hysteretic energy dissipation with the MBTM. This is visually explicit when comparing the measured and computed hysteretic responses in Figure 3.7b. The authors note that the unloading response of specimen Wall B also exhibits an unusual double curvature and recentering, which greatly affects the energy dissipated per cycle. The lack of the explicit consideration of the bond-slip of the diagonal reinforcement in the coupling beams may have also contributed to the overestimation of the hysteretic energy dissipated.

3.6.2 Validation of the Enhanced Beam-Truss Models

To validate the EBTM, key experimentally measured and numerically computed responses are compared in this section. Figure 3.8a compares the measured and computed base shear - roof displacement relationship responses for the specimen Wall A and Figure 3.8b displays the corresponding information for specimen Wall B. The EBTM of specimen Wall A, in general, computes with a good level of accuracy the peak base shears of the semi-cycles, except for the first cycles. In the first two cycles, the maximum error is 42%; and for the rest of the lateral loading, the maximum error occurred at the peak of the semi-cycle 12, where the computed base shear is 14% less than the measured response. As the computed base shear - roof displacement response depicted in Figure 3.5a, the hysteretic response calculated for the EBTM of specimen Wall A (Figure 3.8a) overestimates the hysteretic energy dissipated. Thus, no effect of the explicit consideration of bond-slip in the flexure reinforcement of the coupling beams is observed. The EBTM captures the observed sliding shear failure of beams in specimen Wall A remarkably well, see Figure 3.9a and Figure 3.9b.

The envelope of the hysteretic response for the Wall B computed by the EBTM is in excellent agreement with the measured response (Figure 3.8b). The maximum error is 8% and occurs at the peak of the semi-cycle 6. As in Figure 3.5b, the experimentally measured, and the calculated unloading response using the EBTM for the Wall B differ, see Figure 3.8b. The enhanced model still overestimates the hysteretic energy dissipated, but the explicit consideration of bar bond-slip in the diagonal reinforcement of the coupling beams clearly has a positive effect on the prediction. The ductile behavior of the specimen Wall B is well-captured by the EBTM, compare Figure 3.9c and Figure 3.9d.

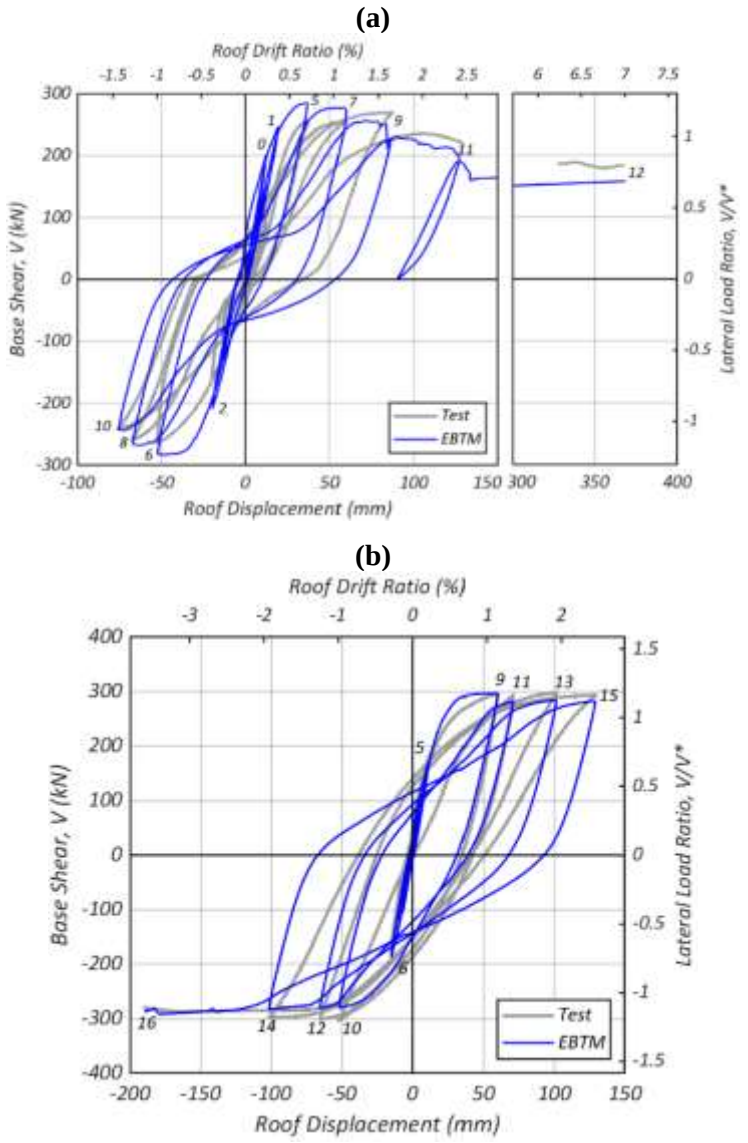

Figure 3.8. EBTM computed and measured the base shear - drift ratio. **(a)** Specimen Wall A. **(b)** Specimen Wall B. Where the code-calculated ultimate base shear, V^*, is 230 kN for specimen Wall A and 252 kN for specimen Wall B.

A deeper understanding of the behavior of the coupled walls as a system is gained through the study of the local responses. Specimens Wall A and Wall B were densely instrumented (Santhakumar 1974). However, the measured local responses were reported for lateral force levels, which was typical in the early experiments in the field, and not for

lateral displacement levels, as it is widely accepted today, because the latter can be used effectively to capture responses near or past the peak load.

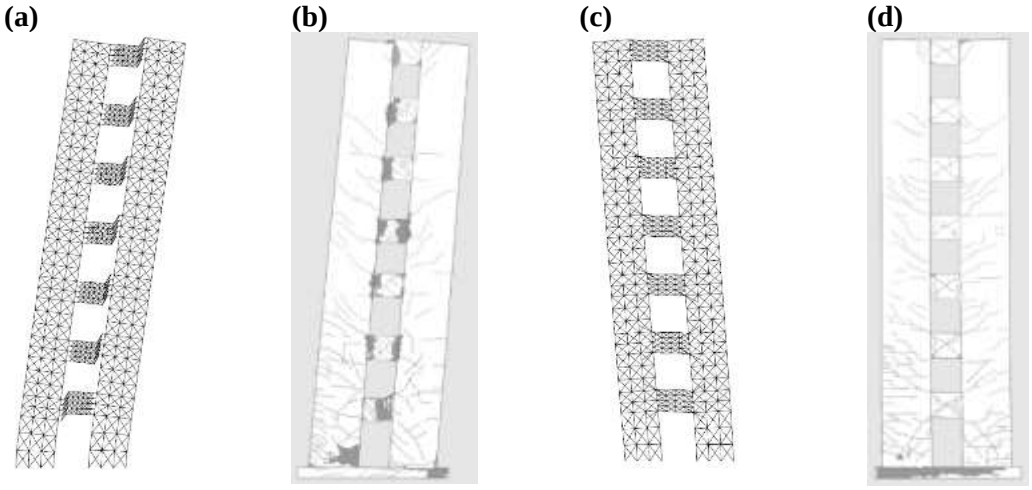

Figure 3.9. (a) EBTM deformed the shape of specimen Wall A at maximum drift ratio (2x). **(b)** Specimen Wall A at the end of the test. **(c)** EBTM deformed the shape of specimen Wall B at maximum drift ratio (2x). **(d)** Specimen Wall B at the end of the test. The images of the model were created with the program STKO (Petracca et al. 2017a, Petracca et al. 2017b).

Therefore, results are labeled using the ratio of the base shear (when the response occurs) to the code-calculated ultimate base shear, V/V^*. When the stiffness of the specimen is small, the definition of the lateral displacement at which a specific response occurred is uncertain if the ratio V/V^* is used. This makes the comparison of the experimentally measured and numerically calculated local responses difficult. Nevertheless, in this paper, the results of tests and models are compared, because the authors consider that such comparison is still valuable for the qualitative validation of the models.

Measured and computed average tensile strains at the corners of the coupling beams are depicted in Figure 3.10. Figure 3.10a compares the strains of the flexure reinforcement of the coupling beams of specimen Wall A, whereas Figure 3.10b compares the strains of the diagonal reinforcement of the beams of specimen Wall B. To compute the strains, the truss elements closest to the locations of the instrumentation in the specimens are used. The

magnitude of the average tensile strains calculated using the EBTM differs from those measured in the tests. However, in general, the computed values follow similar trends to the experimentally measured responses. Additionally, to the particular reasons that make challenging the prediction of strains for these tests, in general, the approximation of the strains in finite element models is coarser than for displacements because strains are computed as derivatives of displacements. Moreover, although the regularization of the concrete stress-strain relationships (Dashti et al. 2017a) achieves the overall objectivity of the models, meaning that the base shear - roof displacement relationship response is essentially independent of the grid size, such methodology makes the response to lose objectivity at the section level.

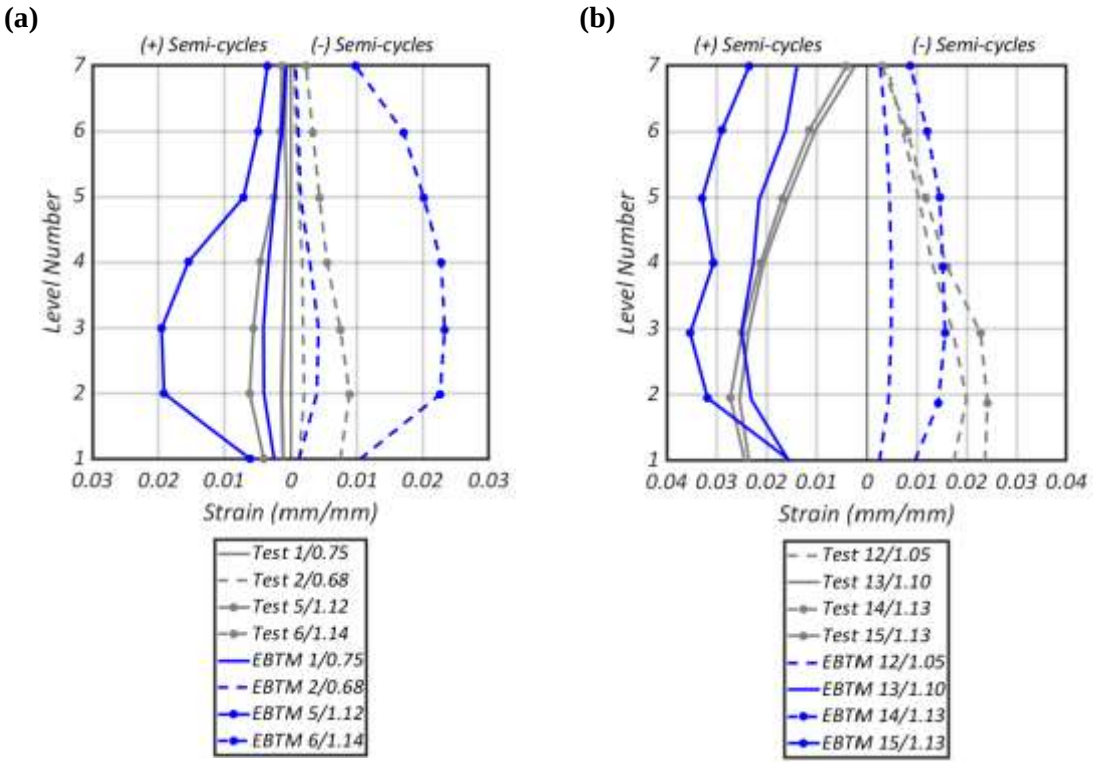

Figure 3.10. EBTM computed and measured strains of the reinforcement at the tension corners of the coupling beams. **(a)** Specimen Wall A. **(b)** Specimen Wall B. Where x / x.xx = Semi-cycle / Ratio V/V^*.

Therefore, the stress-strain curves are grid-dependent, and the prediction of the local responses becomes especially challenging when localization occurs.

Coupling beams tend to lengthen significantly after yielding, regardless of whether these beams incorporate conventional or diagonal reinforcement (Restrepo-Posada 1993), and yield lines can result in the slabs connected to the beams because of such lengthening (Fleischman et al. 2014, Paulay and Priestley 1992). Dilatation between the center lines of the leading and trailing wall piers was measured in both specimens to study the lengthening of the coupling beams (Santhakumar 1974). Figure 3.11a and Figure 3.11b compare the computed and measured dilatations for the Wall A and Wall B, respectively; the computed dilatations were derived from nodal displacements. According to Figure 3.11, the dilatation remains quite uniform along the wall height for roof drift ratios larger than 1.3% (9th and 11th semi-cycle in specimens Wall A and Wall B, respectively), except for the Level 1. In that location, the dilatation of the coupled walls is significantly smaller. This is because the foundation restrains the coupling beams from lengthening. Computed dilatations from the EBTM exhibit similar trends than those measured. However, whereas for specimen Wall B measured and calculated dilatations are in good agreement, for specimen Wall A the dilatations are generally overpredicted.

Figure 3.12a and Figure 3.12b compare the measured and computed strains of the outermost longitudinal reinforcement at the left wall piers (bars F) in the Wall A and Wall B, respectively. The average strains of the first and third integration points of the fiber-sections beams representing the boundaries are used to compute the strains at the gage location. The EBTM computes the longitudinal strains with a reasonable level of accuracy.

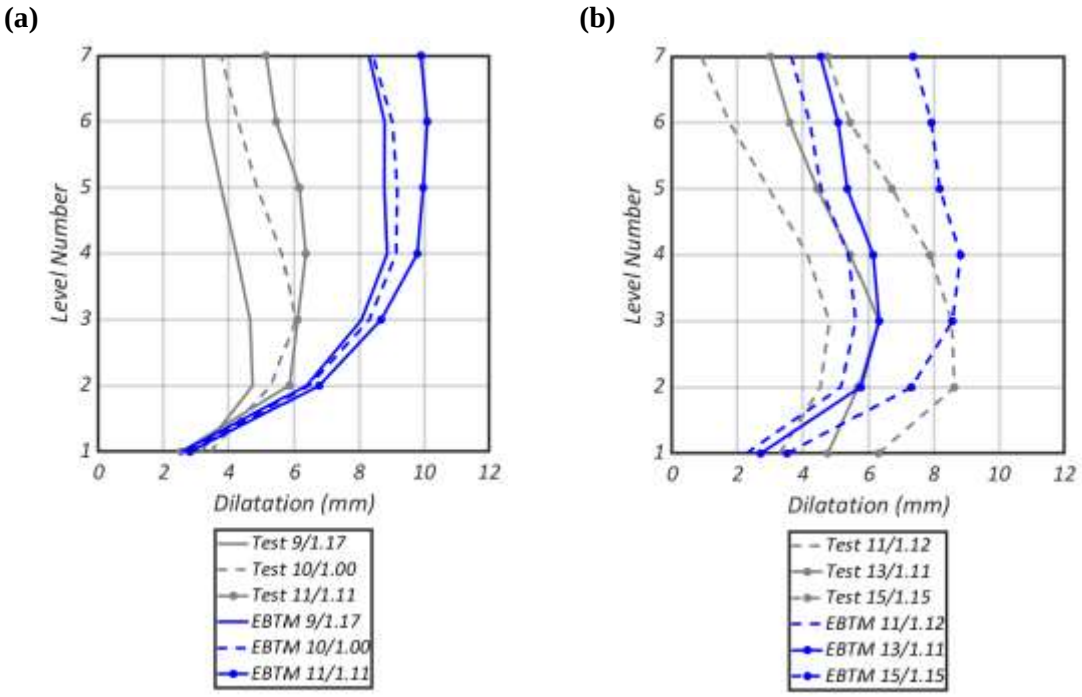

Figure 3.11. EBTM computed and measured specimen dilatations. **(a)** Specimen Wall A. **(b)** Specimen Wall B. Where x / x.xx = Semi-cycle / Ratio V/V^*.

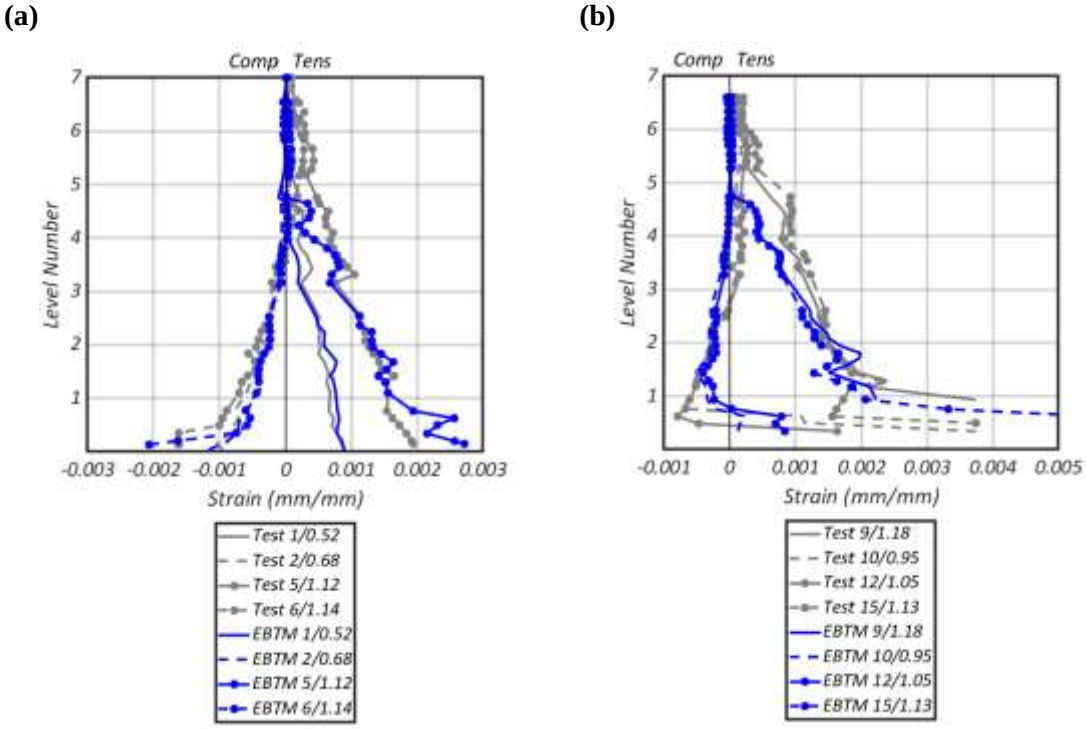

Figure 3.12. EBTM computed and measured strains at the outermost longitudinal reinforcement of the left wall pier (Bars F). **(a)** Specimen Wall A. **(b)** Specimen Wall B. Where x / x.xx = Semi-cycle / Ratio V/V^*.

A similar comparison for the innermost longitudinal reinforcement at the left wall pier (bars D) of specimen Wall A and Wall B is shown in Figure 3.13a and Figure 3.13b, respectively. Even though the longitudinal strains calculated by the EBTM differ with those measured, the computed strains follow similar trends.

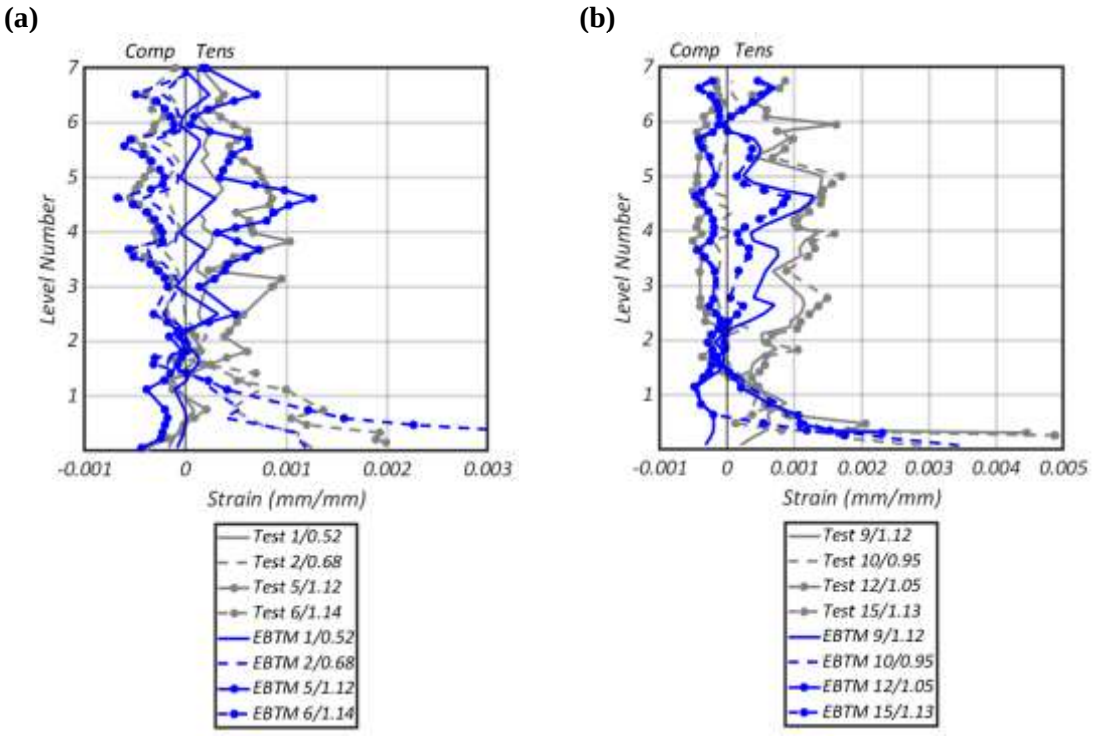

Figure 3.13. EBTM computed and measured strains at the innermost longitudinal reinforcement of the left wall pier (Bars D). **(a)** Specimen Wall A. **(b)** Specimen Wall B. Where x / x.xx = Semi-cycle / Ratio V/V^*.

3.6.3 Strain contours computed from the Enhanced Beam-Truss Models

To get additional insight into the local behavior of lateral systems based on coupled walls, contours of strains for the EBTM of specimen Wall B were created (Figure 3.14 and Figure 3.15). For each node, rosettes of strains are formed using the horizontal, diagonal, and vertical elements of the quadrilaterals concurring the node (Alvarez-Sanchez and Restrepo 2017, Zhang et al. 2017). The strains of the horizontal, diagonal, and vertical

elements of the rosettes (ε_x, ε_{x1}, ε_y, respectively) are calculated from nodal displacements. Then, these strains are used to define the shear strain γ_{xy}, maximum principal strain ε_1, minimum principal strain ε_2, and maximum shear strain γ_{max} as follows:

$$\gamma_{xy} = \frac{2\varepsilon_{x1} - \varepsilon_x - \varepsilon_y - (\varepsilon_x - \varepsilon_y)\cos 2\theta_d}{\sin 2\theta_d} \tag{3.4}$$

$$\varepsilon\varepsilon_1 = \frac{\varepsilon_x + \varepsilon_y}{2} + \sqrt{\left(\frac{\varepsilon_x - \varepsilon_y}{2}\right)^2 + \left(\frac{\gamma_{xy}}{2}\right)^2} \tag{3.5}$$

$$\varepsilon\varepsilon_2 = \frac{\varepsilon_x + \varepsilon_y}{2} - \sqrt{\left(\frac{\varepsilon_x - \varepsilon_y}{2}\right)^2 + \left(\frac{\gamma_{xy}}{2}\right)^2} \tag{3.6}$$

$$\varepsilon\gamma_{max} = 2 \cdot \sqrt{\left(\frac{\varepsilon_x - \varepsilon_y}{2}\right)^2 + \left(\frac{\gamma_{xy}}{2}\right)^2} \tag{3.7}$$

Where θ_d is the inclination of the diagonal. The results of the rosettes concurring in each node are averaged to calculate the nodal strains. The contours are generated from the interpolation of the nodal strains. For convenience, the rectangular components of the coupled wall (i.e., wall piers and coupled walls) are assumed isolated for calculating nodal strains. To generate strain contours, strains are averaged at the boundaries of the components. This procedure was implemented in the GUI *StrainContour1.m* developed in-house using MATLAB (MathWorks 2018).

Figure 3.14a shows the contour of computed vertical strains ε_y for specimen Wall B at the peak of the semi-cycle 15 (drift ratio 2.5%). The maximum computed strain ε_y is 0.045, and it occurs in the compression diagonal of the coupling beam in Level 1.

(a) ε_y **(b)** ε_2

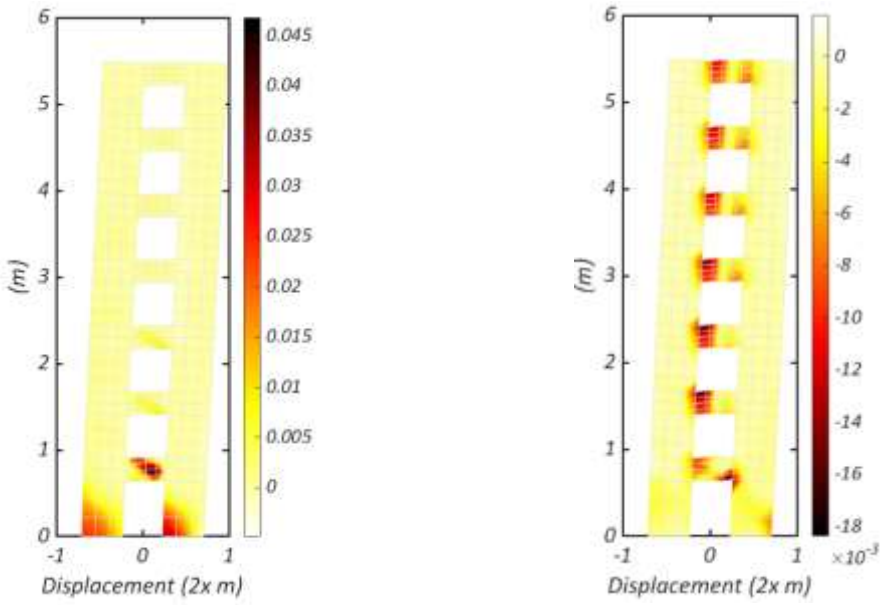

Figure 3.14. Strain color plots calculated using the EBTM of specimen Wall B at the peak of the semi-cycle 15 (drift ratio 2.5%). **(a)** Vertical strains ε_y. **(b)** Minimum principal strains ε_2.

Large strains ε_y are also observed at the walls' bases concentrated toward the boundary elements in tension. Minimum principal strains ε_2 for the same peak are depicted in Figure 3.14b. The strains ε_2 are concentrated at the compression corners of the coupling beams, the smallest computed value occurs in Level 1, and it is equal to -0.018. The magnitude of the minimum strains ε_2 in the coupling beams increases towards the Level 7 (roof level). Close-ups of the contours of computed strains in Level 1 for specimen Wall B at the peak of the semi-cycle 15 (drift ratio 2.5%) are shown in Figure 3.15. Horizontal strains ε_x larger than 0.03 are reported at the tension corners of the coupling beam (see Figure 3.15a). Figure 3.15b and Figure 3.15d present similar distribution for the vertical strains ε_y and maximum principal strain ε_1, which indicates that the largest tensile strains occur in the vertical direction close to the boundary elements in tension. Shear strains γ_{xy} and maximum shear strains γ_{max} larger than 0.04 are observed in the joints of the coupling

beam and the walls piers (see Figure 3.15c and Figure 3.15f). Finally, Figure 3.15e shows that the minimum principal strains ε_2 at the base of specimen Wall B occurs in the boundary element in compression of the wall pier in compression.

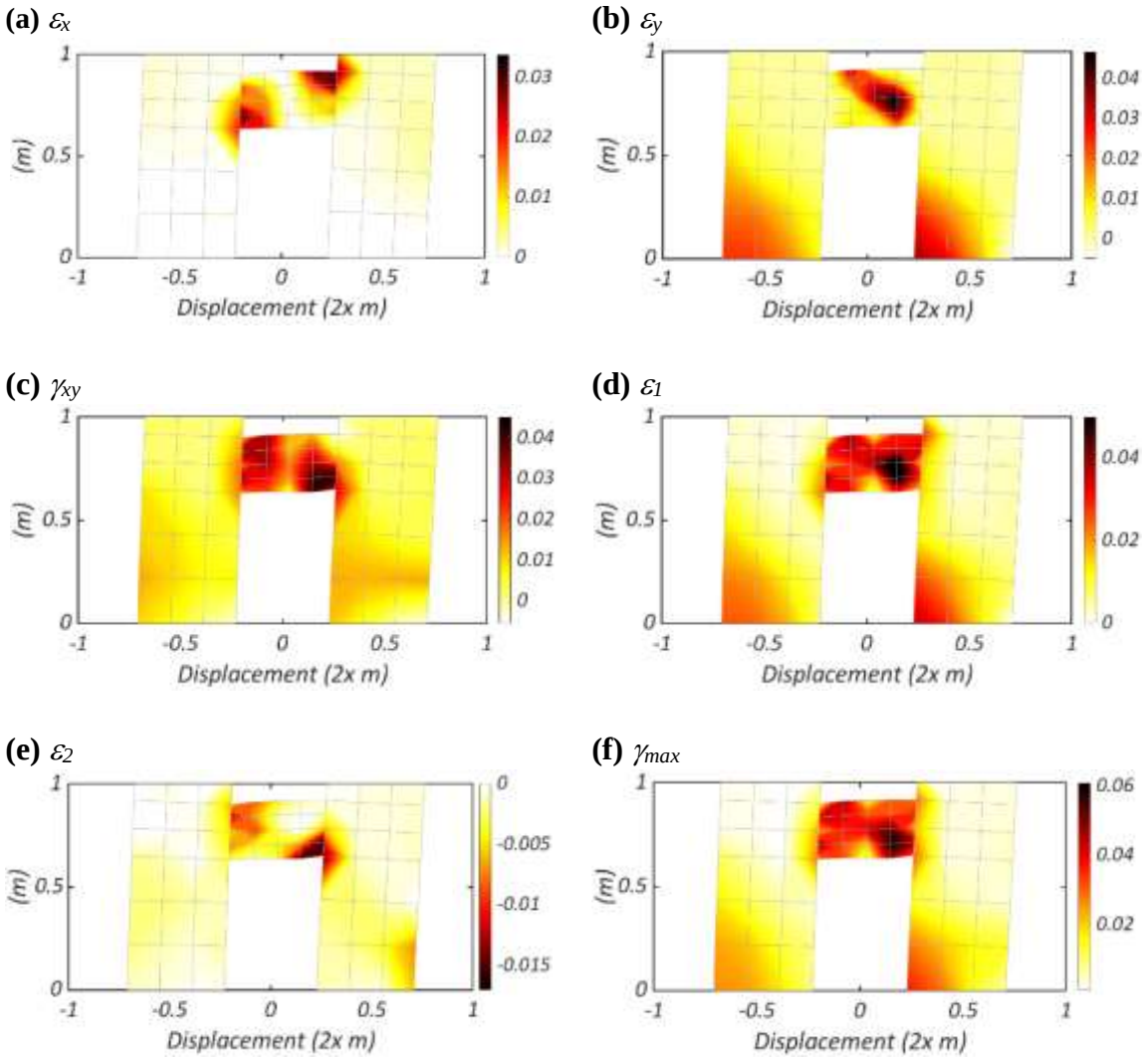

Figure 3.15. Strain color plots calculated using the EBTM at the base of specimen Wall B at the peak of the semi-cycle 15 (drift ratio 2.5%). **(a)** Horizontal strains ε_x. **(b)** Vertical strains ε_y. **(c)** Shear strains γ_{xy}. **(d)** Maximum principal strains ε_1. **(e)** Minimum principal strains ε_2. **(f)** Maximum shear strains γ_{max}.

3.6.4 Comparison of EBTM with a Nonlinear Truss Model

This section compares some overall and local responses computed using the EBTM with responses reported by Alvarez et al. (2019) for specimens Wall A and Wall B computed using a Nonlinear Truss Model (NTM). The NTM used only truss elements, except for some fiber-section beam elements used to simulate dowel action at the base of the walls and the ends of the coupling beams. The wall piers in the NTM had grids of 6 by 43 quadrilaterals, whereas in the EBTM, they have 3 by 35 quadrilaterals. Finer grids were used in the NTM to simulate the boundaries with two vertical lines of truss elements instead of one line of beams as in the EBTM. The grids and bond-slip considerations of the coupling beams in the NTM were similar to the proposed for the EBTM. Additionally, the NTM included the effect of the confinement that the foundation provides to the base of specimen wall piers (Presland 1999); for specimen Wall A, this confining effect was also included in the elements of coupling beams adjacent to the wall piers. According to Alvarez et al. (2019), without the confining of the foundation, the NTM predicted sliding shear failures at the base of the specimen walls, when in reality, this behavior was not reported in the tests. No sliding shear at the base of the wall piers was observed for the EBTM; therefore, the confining effect is not included here.

The EBTM and the NTM were run using a computer with a dual-processor Intel Xeon Gold 6136, 64 GB of RAM, and the same version of the OpenSees [2.5.0 (rev 6248) 64 Bit]. The runtimes for the specimen Wall A were 2.8 and 4.2 hours for the EBTM and NTM, respectively; whereas, for the specimen Wall B, the corresponding times were 1.7 and 2.2 hours, respectively.

Figure 3.16a and Figure 3.16b compare the computed base shear - roof displacement relationship responses calculated using the EBTM and the NTM for the specimen Wall A and Wall B, respectively. The measured responses (gray lines) are shown as a reference.

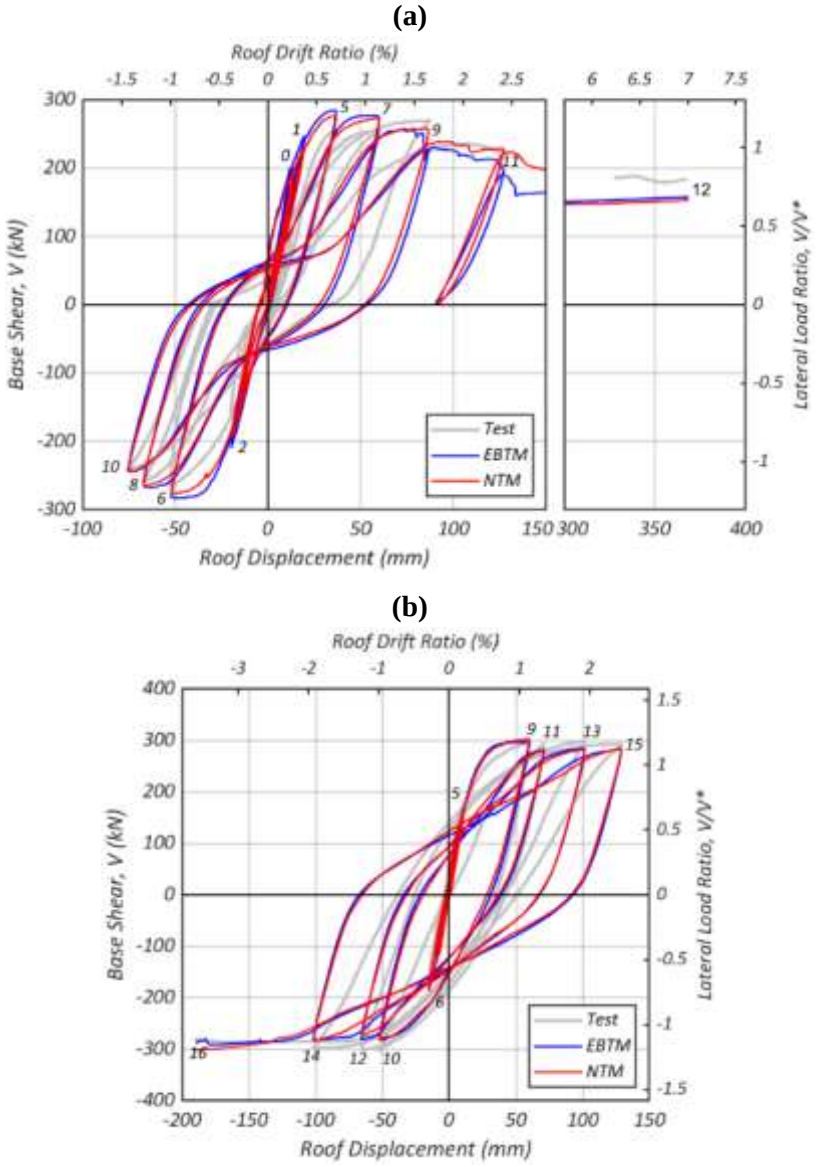

Figure 3.16. EBTM and NTM computed base shear - drift ratio. **(a)** Specimen Wall A. **(b)** Specimen Wall B. Where the code-calculated ultimate base shear, V^*, is 230 kN for specimen Wall A and 252 kN for specimen Wall B.

The EBTM and the NTM of specimen Wall A predict similar shear strengths and hysteretic responses (Figure 3.16a). The shear strength calculated using the EBTM is 3.3% greater than the shear strength calculated with the NTM. However, the EBTM exhibits a higher rate of degradation than the NTM; see, for example, the peak of the semi-cycle 11 (drift ratio 2.4%), at that point, the base shear is 16% smaller than the value predicted for the NTM. The difference in the rate of degradation is attributed to the fact that the EBTM does not consider the confining effect of the wall piers on the coupling beam ends, whereas this effect is included in the NTM.

For specimen Wall B, the EBTM and the NTM computed very similar base shear - roof displacement hysteretic responses, see Figure 3.16b. The NTM considered the bond-slip of the diagonal reinforcement of the coupling beams using the material *Hysteretic* in the anchor truss elements (Alvarez et al. 2019), whereas the EBTM concentrated the bond-slip behavior in *zeroLength* elements put in series with the anchor truss elements. The practically overlapping computed responses (Figure 3.16b) prove that the beams used to model the interior boundary elements in the EBTM cut-off the work in series (*zeroLength*-*Truss*), preventing any double-counting of bond-slip.

The average tensile strains at the corners of the coupling beams computed using the EBTM and the NTM are compared with the measured responses (in gray) in Figure 3.17a and Figure 3.17b for specimens Wall A and B, respectively. The measured average tensile strains and those computed with the EBTM and NTM are generally in poor agreement. Nevertheless, the general trends are similar, being the results more consistent for the NTM.

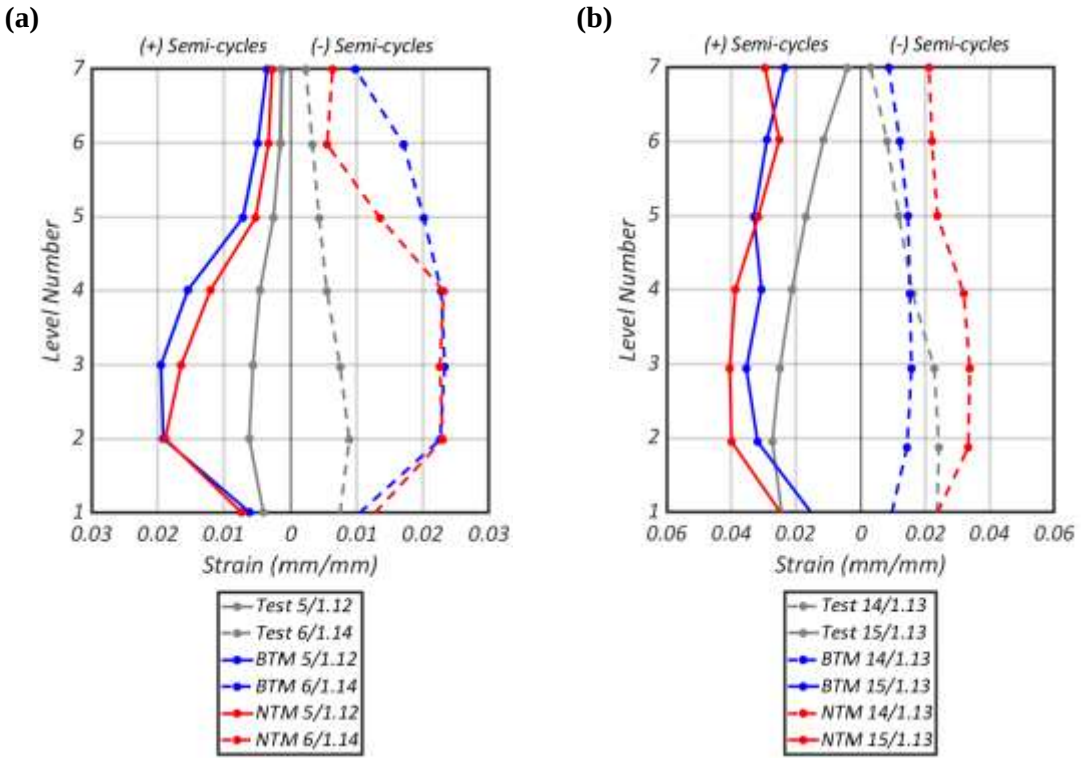

Figure 3.17. EBTM and NTM computed reinforcement tensile strains at the coupling beam corners. **(a)** Specimen Wall A. **(b)** Specimen Wall B. Where x / x.xx = Semi-cycle / Ratio V/V^*.

Table 3-4 compares the coupling efficiency coefficients (CEC) computed for different peaks of the semi-cycles in the Wall A and Wall B responses using the EBTM and NTM. The CEC is defined as $1 - |(M_a + M_b)/M_{OT}|$, where M_a and M_b are the base moments of wall piers, and M_{OT} is the overturning moment (Paulay and Priestley 1992). The maximum possible value for CEC is one, which corresponds to idealized wall piers pinned at the base with base moments equal to zero. As the stiffness of the coupling beams decreases relative to the stiffness of the wall piers, CEC decreases towards zero, that is, the wall piers gradually decouple. The values of the CEC calculated using the EBTM (CEC_{EBTM}) are slightly smaller than the corresponding values for the NTM (CEC_{TM}). For specimen Wall A, the CEC consistently decreases after the response has reached the lateral

strength at the peak of the semi-cycle 5 (drift ratio 0.7%). From this point onwards, coefficient CEC_{EBTM} decreases to only 16%, and CEC_{TM} drops to 19%, indicating severe decoupling, which resulted from the softening and eventual failure of the coupling beams, see Figure 3.19a and 3.19b. In contrast, the CEC_{EBTM} and CEC_{TM} computed for specimen Wall B remain relatively constant throughout, see Table 3-4.

Table 3-4. Comparison of the coupling efficiency coefficients computed for the EBTM and the NTM.

Wall A				Wall B			
Semi-cycle	Drift Ratio	CEC_{EBTM}*	CEC_{TM}**	Semi-cycle	Drift Ratio	CEC_{EBTM}*	CEC_{TM}**
1	0.37	0.57	0.60	5	0.22	0.59	0.63
2	-0.38	0.57	0.61	6	-0.29	0.58	0.63
5	0.70	0.55	0.60	9	1.14	0.58	0.63
6	-0.99	0.55	0.60	10	-0.99	0.56	0.61
8	-1.28	0.53	0.59	11	1.35	0.56	0.62
9	1.64	0.47	0.57	12	-1.25	0.56	0.61
10	-1.43	0.49	0.56	13	1.93	0.57	0.62
11	2.42	0.36	0.50	14	-1.93	0.56	0.62
12	7.01	0.16	0.19	15	2.46	0.57	0.62
				16	-3.61	0.57	0.62

*, coupling efficiency coefficients calculated using the EBTM.
**, coupling efficiency coefficients calculated using the NTM.

In coupled walls, the base shear is the sum of the base shear forces carried by the leading wall pier (that is, the pier being compressed), and trailing wall pier (that is, the pier being decompressed). The proportion in which the wall piers carry the shear force is of interest from the point of view of design. Both the EBTM and the NTM indicate that for specimens Wall A and B, the leading wall carried a significant percentage of the applied shear force while the coupling between the wall piers was maintained, see Figure 3.18a and Figure 3.18b. At the peak applied lateral force at 0.70% drift ratio, the leading wall pier carried 81% of the lateral force applied to specimen Wall A according to both models. At larger drifts, when the coupling beams softened and eventually failed, the leading and

trailing wall piers had more even participation in the shear resistance, see the participation at 2.42% and 7.01% drift ratios. For specimen Wall B, the models indicate that the leading wall pier carried between 90% and 93% of the peak applied lateral force, which occurred at a 1.14% drift ratio, and such large participation was largely maintained throughout testing.

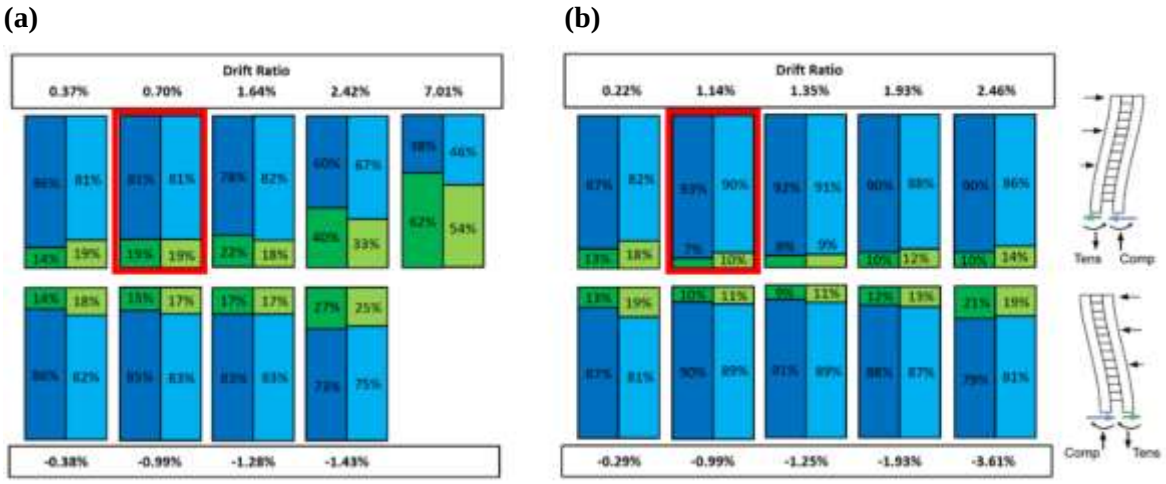

Figure 3.18. Base shear distribution in the wall piers for semi-cycles peaks computed using EBTM and NTM. Blue color indicates compression in the wall pier (leading wall pier), whereas green indicates tension (trailing wall pier); the darker colors show the results computed by the EBTM, and the clearer colors show the results computed by the NTM. **(a)** Specimen Wall A. **(b)** Specimen Wall B. The red rectangles indicate the base shear distribution at the peak base shear resisted by each specimen.

The overall response of specimen Wall B did not exhibit degradation, and the uneven distribution of shear force between the trailing and leading wall piers was observed during the complete test, in the EBTM and NTM. The maximum shear force predicted in the two models was at least 109% the limit in the ACI 318-14 (2014).

Figures 3.19 and 3.20 compares the hysteretic shear force - shear strain responses computed with the EBTM and the NTM for Level 1 and Level 7 coupling beams, respectively, of specimens Wall A and Wall B.

The shear strain was calculated from nodal points at the corners using the following equation,

$$\text{g}\,\gamma = \gamma_1 + \gamma_2 = \frac{\varepsilon_{jm} - \varepsilon_{il}}{2}\left(\tan\theta + {}^{1}/_{\tan\theta}\right) \tag{3.8}$$

Where:

γ, shear strain of the coupling beam

θ, inclination of the diagonals

ε_{jm}, ε_{il}, strains of the diagonals

γ_1, γ_2, inclination of vertical and horizontal sections of the coupling beams after the shear deformation, respectively.

The equation assumes the entire deformation in the panel defined by the four points is caused by shear, see Figure 3.21. This assumption is deemed acceptable for the coupling beams in these two specimens, given their small aspect ratio.

The code-calculated shear strength of the coupling beams (calculated using measured material properties), and the maximum shear strength allowed by ACI 318-14 (2014) for these beams of $0.83\sqrt{f'_c}\,A_g$ (MPa) are also plotted in Figures 3.19 and 3.20. The EBTM and NTM compute for Level 1 beams for both specimens, a peak shear force well-above code-calculated shear strength. Whereas for Level 7, the code-calculated shear strength and the peak shear forces predicted by the models are closer. Despite the coupling beams in specimen Wall A were identical, the EBTM and NTM predict that Level 1 beam resisted 19% and 37% greater shear force than Level 7 beam. Similarly, the two models indicate that in specimen Wall B, Level 1 beam resisted 41% and 49% greater shear force than Level 7 in spite, also, that these two beams were identical. The reason for this

difference is chiefly due to the development of significant axial compression in the lower level beams in both specimens.

(a) *Wall A, Level 7*

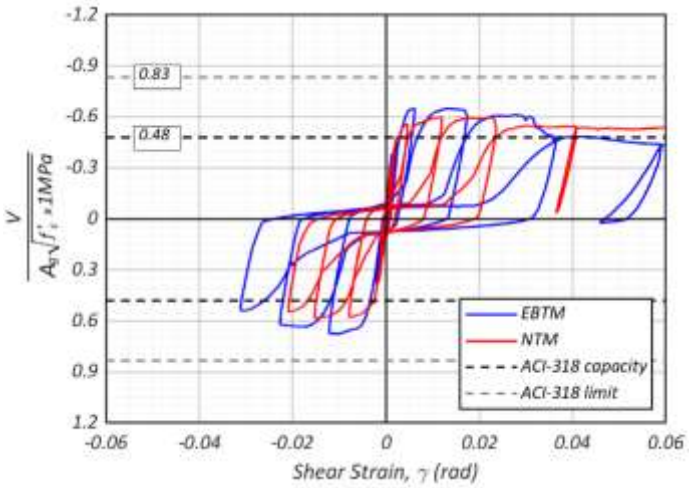

(b) *Wall A, Level 1*

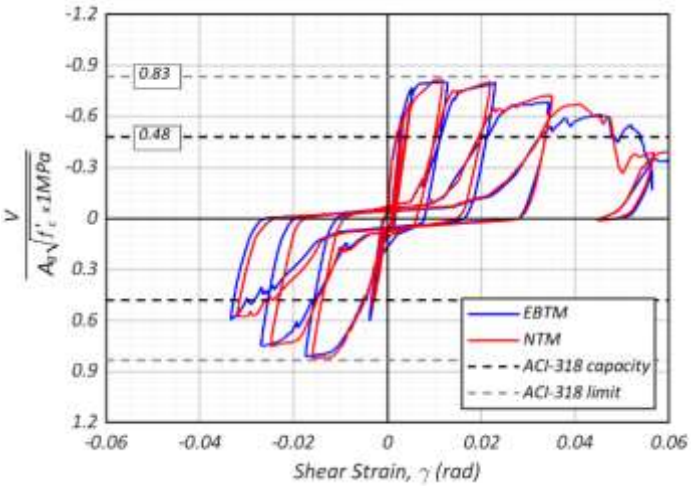

Figure 3.19. EBTM and NTM computed shear force - shear strain in coupling beams of Wall A. **(a)** Level 7. **(b)** Level 1. The code-calculated capacity was computed using measured material properties.

As these beams try to lengthen, the restraint provided by the walls, which are themselves restrained from sliding by the footing, results in the development of axial compression, and in a redistribution of the shear force in the trailing wall pier into the leading wall pier.

(a) *Wall B, Level 7*

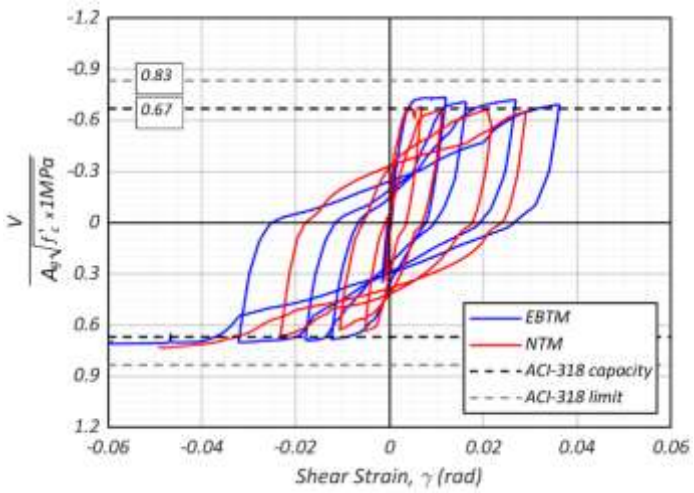

(b) *Wall B, Level 1*

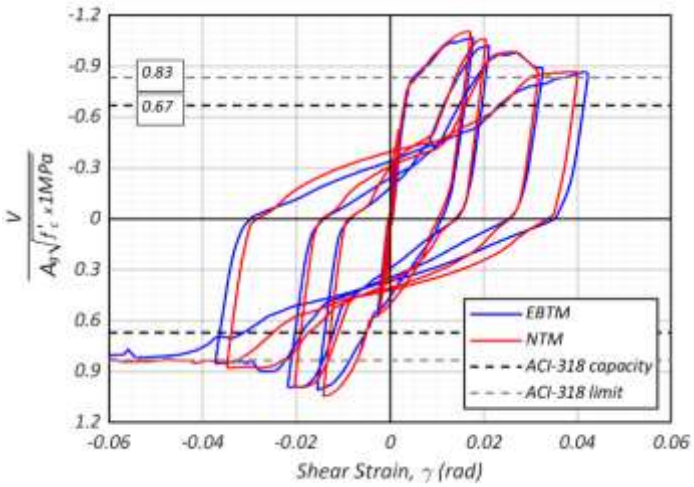

Figure 3.20. EBTM and NTM computed shear force - shear strain in coupling beams of Wall B. **(a)** Level 7. **(b)** Level 1. The code-calculated capacity was computed using measured material properties.

The axial force levels $N/(A_g f'_c)$ computed at the peak base shear force for specimen Wall A Level 1 coupling beam were -0.008 and -0.009, according to the EBTM and NTM. For specimen Wall B, the axial compression force levels computed at the peak base shear for Level 1 beam were -0.015 and -0.017 to the EBTM and NTM. In contrast, at the peak base shear, the computed axial compressions in Level 7 beam were -0.005 and -0.007 for specimen Wall A, and -0.006 and -0.004 for specimen Wall B according to the EBTM and NTM.

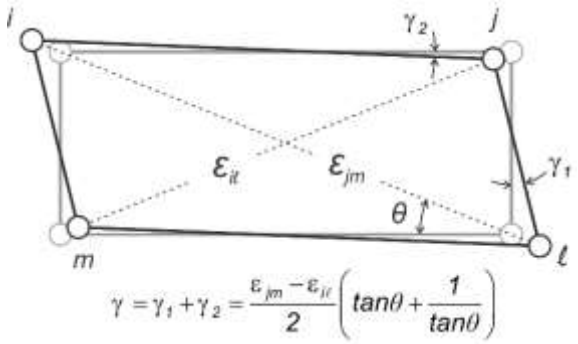

Figure 3.21. Computation of shear strain (γ) in a coupling beam.

3.7 Impact of findings on current practice.

Current practice to support the design of building systems incorporating reinforced concrete coupled structural walls, planar or configured in core walls, is divided into two main groups: (i) those who use the code prescriptive methods and use linear analysis tools together with stiffness modifiers to heuristically account for cracking and (ii) those who take a further step and carry a nonlinear design verification via a set of multi-axis input ground motions.

The uneven apportioning of base shear between the wall piers, predicted by the EBTM and the NTM at drifts approaching the peak base shear, cannot be captured with linear analysis when stiffness modifiers in the trailing and leading wall piers are made equal, as recommended in codes and design standards, nor by methods that apportion the shear force in proportion to the overstrength moment as recommended by Paulay and Priestley (1992). For identical trailing and leading wall piers, the use of identical stiffness modifiers for the leading and trailing wall piers would result in equal design shear forces in both wall piers, which, as shown in Figure 3.18, would grossly underestimate the design shear force demands. A small improvement is attained if the shear force is apportioned in proportion to the overstrength moments. Table 3-5 indicates that if the base shear is

apportioned in proportion to the overstrength moments, the leading wall pier will assume between 58% and 67% of this force, whereas the nonlinear analysis indicates the leading wall piers in Specimens A and B resisted 81% and 90% to 93% of the applied base shear, respectively, see these ratios in the bars marked with red boxes in Figure 3.18. If only a linear analysis were to be used to support the design of such coupled walls, the stiffness modifier for the lead wall pier should be significantly greater than that for the trailing wall pier. Judgment should be exercised in the selection of the stiffness modifiers in each case due to the inherent nonlinear nature of the response of these lateral systems, but the analysis of specimens Wall A and Wall B presented in the previous section seems to suggest a design where each wall pier is detailed to resist the entire base shear force.

Those in practice that make use of nonlinear analysis tools to validate the response of a preliminary design often model the nonlinear response of diagonally reinforced coupling beams with one DOF vertical shear springs. These simple models have shown the ability to reproduce the measured response of such beams (Naish et al. 2013, ASCE 41-13 2013). However, such a model ignores any axial-flexure-shear coupling, which will preclude the coupling beams from assuming axial load caused by the restraint of the wall piers. The axial load itself in the coupling is not as important as it is the additional redistribution of the shear force from the trailing to the leading wall pier, indicating that nonlinear analysis using simple vertical shear elements to represent the coupling beams will also underestimate the shear force demand in the wall piers, particularly near the base of the walls where the foundation provides the most considerable restraint to the wall piers and, hence, to the coupling beams. Modeling diagonally reinforced coupling beams with a model similar to that used in the MBTM is simple enough for use in practice.

Table 3-5. EBTM and NTM computed wall pier base moments at peak base shear and apportioning base shear factors computed using Paulay and Priestley (Paulay & Priestley, 1992).

	Wall A				Wall B			
Model	M_a kN-m	M_b kN-m	DF_a	DF_b	M_a kN-m	M_b kN-m	DF_a	DF_b
EBTM	256	184	0.58	0.42	269	171	0.61	0.39
NTM	260	167	0.61	0.39	286	143	0.67	0.33

M_a, base moment in leading wall pier
M_b, base moment in trailing wall pier
DF_a, distribution factor for leading wall pier, $M_a/(M_a+M_b)$
DF_b, distribution factor for trailing wall pier, $M_b/(M_a+M_b)$

3.8 Conclusions

This paper uses two versions of the Beam-Truss Model, termed the Modified Beam-Truss Model (MBTM) and the Enhanced Beam-Truss Model (EBTM), to compute key response parameters of two one-quarter scale seven-story coupled structural walls tested by Santhakumar (1974). Specimens Wall A and Wall B were identical except for the type of the coupling beams. Specimen Wall A was built incorporating conventional coupling beams, whereas Specimen Wall B had diagonally reinforced coupling beams. In Specimen Wall A, sliding shear of the coupling beams and crushing at the base caused degradation of the lateral load capacity at 1.6% roof drift ratio. Specimen Wall B had a stable response up to a 3.6% roof drift ratio when the wall pier in compression exhibited local buckling at the wall base.

The MBTM was a variation of the model developed by Lu et al. (2016); the former used a combination of truss and displacement-based elements in vertical and horizontal members as opposed to the latter, which just used force-based elements. The EBTM was identical to the MBTM except that it incorporated the bar-bond slip of the reinforcement anchored beyond the coupling beam ends.

The overall lateral load-displacement responses computed using the MBTM exhibited a very good agreement with the responses reported for the two specimens, including the softening in the response of Specimen Wall A. However, it was evident that this model overpredicts the hysteretic energy dissipated by the specimens. Like the MBTM, the lateral load-displacement response computed with the EBTM also showed very good agreement with the measured responses for both specimens. The inclusion of a bond-slip relationship in the EBTM resulted in a closer prediction of the overall specimens' hysteretic responses.

The EBTM was used to predict local responses like (i) strains of the reinforcement at the tension corners of the coupling beams, (ii) dilatation of the coupled walls, and (iii) strains of the longitudinal reinforcement of the boundary elements. All the predicted responses were in fair agreement with those reported. Similar responses were also attained with the Nonlinear Truss Model (NTM) described by Alvarez et al. (2019).

The degree of coupling provided for the beams was studied using the coupling efficiency coefficients (Paulay and Priestley 1992). For the EBTM of Wall A, the coefficients decrease after the response reaches the peak base shear, whereas, for Wall B, the coefficients remain approximately constant during the entire test. The EBTM also shows that the foundation restrains the lengthening of the coupling beams at the first level, which generates axial compression and, consequently, large overstrength in these beams. Similar results were obtained using the NTM.

From the point of view of professional practice, the EBTM has clearly indicated that the lead wall pier in the coupled walls tested assumed a very high proportion of the applied base shear. This contrasts with the equal shear force design stemming from the use

of equal stiffness modifiers in linear analysis of such walls, or from apportioning the base shear in the leading and trailing wall piers in proportion to the overstrength moments. A recommendation is to design each wall pier for the entire shear force.

The MBTM and EBTM are alternative methodologies to model coupled walls that overcomes some limitations of the beam elements and calibrated shear springs commonly used in practice to model wall piers and coupling beams, respectively. The models can adequately compute lengthening of the coupling beams and naturally capture the axial load exerted on them by the restraint imposed for the coupled walls in the proximity of the foundation, this is not achieved by calibrated shear springs. It was also verified that the EBTM computes a rational apportioning of base shear between the trailing and the leading wall piers, which is not possible to compute using linear analysis and code-prescribed stiffness modifiers, as commonly done in practice. Softening and shear failures in the coupling beams are also well- captured by the models, and with relative simplicity, the EBTM can include bond-slip and dowel action in the coupling beams.

3.9 Acknowledgements

Chapter 3, in part, is a reprint of the material as it appears in *Analysis of Reinforced Concrete Coupled Structural Walls Via the Beam-Truss Model.* Engineering Structures, 2020, https://doi.org/10.1016/j.engstruct.2020.111005. Alvarez, Rodolfo; Restrepo, Jose I.; Panagiotou, Marios; and Godinez, Sergio E. The dissertation author was the primary investigator and author of this paper.

The authors would like to acknowledge the Mexican Government for providing financial support through the *Consejo Nacional de Ciencia y Tecnología* (CONACYT).

This work was also supported by the *University of California Institute for Mexico and the United States* (UC MEXUS) and the program *Becas Fulbright - García Robles* (COMEXUS).

Chapter 4. RC Wall Plastic Hinge Out-of-Plane Buckling – Analysis Using the Nonlinear Beam-Truss Model

4.1 Abstract

The Beam-Truss Model (BTM), developed for the nonlinear cyclic analysis of reinforced concrete components including softening, is extended to compute the out-of-plane buckling observed in plastic hinges of various slender structural walls. This is achieved by using fiber-section displacement-based elements with PDelta geometric transformation and truss-elements with Corotational transformation. The BTM is enhanced by considering strain penetration at the base of the walls. This paper discusses the BTM for three test specimens that exhibited out-of-plane buckling and whose response softened as a result of this phenomenon. The test specimens' unsupported height to wall thickness ratio ranged between 10 and 25. Using the same calibration of the modeling parameters for the development of the three models, the BTM is validated by comparing measured and computed lateral force− displacement responses, out-of-plane displacements, and local strain responses. The BTM computes accurately the force – displacement responses as well as out-of-plane displacements of the test specimens and the buckling behavior.

4.2 Introduction

Reinforced concrete (RC) structural walls are commonly used as a seismic load-resisting system in buildings of all heights. The response of structural walls to earthquakes has often been branded as excellent. Despite this, the performance of structural walls in some of the buildings affected by the strong-intensity 2010 M_w = 8.8 Maule and 2011 M_w

= 6.2 Christchurch earthquakes was somewhat unexpected (where M_w is moment magnitude). Out-of-plane buckling observations in the plastic hinge regions of well-detailed structural walls raised concerns (Dashti et al. 2015) and indicated design deficiencies requiring further research.

Out-of-plane buckling, termed "buckling" thereafter, is a response mode manifested by a significant out-of-plane deformation in the compression zone in the plastic hinge region of the walls. This mode of response occurs after a large in-plane curvature reversal (Rosso et al. 2016) and is caused by a number of factors, e.g., (i) residual tensile strains in the longitudinal reinforcement after a large inelastic excursion (Paulay and Goodsir 1985, Paulay and Priestley 1993), (ii) wall height to thickness ratio (i.e., slenderness), (iii) loss of concrete cover when responding in flexure, (iv) crushing of the concrete at the wall toe, which can also result in local buckling of the reinforcement.

Contrary to the definition of buckling used here, which implies out-of-plane deformations of a large portion of the wall, local buckling, as defined by Rosso et al. (2016) is a localized phenomenon which involves out-of-plane deformations mainly related with compression failure. The local buckling is out of the scope of this paper.

Buckling reduces the lateral deformation capacity of a structural wall, and hence, this mode of response should be studied, and appropriate design provisions should be incorporated into design codes and guidelines.

Large residual out-of-plane deformations observed in building walls in the aftermath of the Chile 2010 and New Zealand 2011 earthquakes, resulted in changes of the slenderness limits of structural walls in codes as the ACI-318 (2014 and 2019), requiring a minimum thickness for special boundary elements equal to $h_u/16$ (where h_u is the laterally

unsupported height). For the case where $c/l_w \geq 3/8$ (where c is the length of the compression zone, and l_w is equal to the length of the wall), the thickness of the boundary shall be greater than or equal to 12 in.

In the current performance-based design (PBD) practice (e.g., LATBSDC 2017), structural walls are typically modeled using nonlinear fiber-section beam-elements or similar. However, such modeling techniques, by definition, cannot capture buckling. Hence, the stability performance of the walls is limited to meet prescriptive code requirements (e.g., ACI 2019).

The nonlinear cyclic Beam-Truss Model (BTM) (Lu et al. 2014) is a modeling methodology for RC walls, beams, and slabs that explicitly represents flexure-shear interaction and it efficiently models both planar and flanged walls. The BTM has been shown to compute accurately the response of various structural wall and coupling beam specimens that exhibit various failure modes, including diagonal tension, diagonal compression, and sliding shear failures (Lu et al. 2016, Lu and Panagiotou 2016, Alvarez et al. 2019). This methodology has successfully calculated the seismic response of buildings (Lu 2014), including the collapse simulation of the structurally complex 15-story Alto Rio building (Zhang et al. 2017).

To the best of our knowledge, only two numerical studies have been carried out to compute buckling in structural walls (Parra 2015, Dashti 2017). In those, a detailed nonlinear finite element method (FEM) was used with an associated computational cost that hampers the application of such a modeling approach in the nonlinear time-history analysis of buildings systems. BTM, the approach presented here, is a simple but robust methodology that can be easily incorporated in the analysis of buildings. In this paper, the

BTM is extended to include the buckling of structural walls subjected to reversed in-plane cyclic loading. Three test specimens are studied: TW1 (Almeida et al. 2017), RWL (Dashti 2017), and Wall2 (Goodsir 1985). The test specimens RWL and Wall2 had a rectangular section and incorporated two curtains of longitudinal and transverse reinforcement, whereas the test specimen TW1 was a short-flange T-shaped section wall and had a single curtain of longitudinal and transverse reinforcement. The three test specimens exhibited buckling during testing. Buckling resulted in the softening of the in-plane lateral force − wall top displacement (F−D) response. The peak drift ratios attained by the test specimens before the degradation occurred were $|\Theta_{pk}| \geq 2.5\%$ (where $\Theta_{pk} = \Delta_p/h_c$, Δ_p is the peak in-plane lateral displacement of a cycle at the control point and h_c is the height of the control point), with exception of the test specimen TW1 which degraded after a $\Theta_{pk} = 1.0\%$.

This study builds on the BTM methodology described by Lu et al. (2014). To compute buckling, instead of using the Linear geometric transformation and force-based elements (FBE) as Lu et al. (2014, 2016), PDelta transformation and displacement-based elements (DBE) are used. Another difference with the BTM described by Lu et al. (2014, 2016) is the incorporation of strain penetration at the base of the walls, which was found to have an important effect on the response of walls exhibiting buckling.

4.3 Literature review

Prior to the earthquakes of Chile (2010) and New Zealand (2011), buckling in structural walls had been observed in quasi-static reversed load testing as an unintended behavior (e.g., Oesterle et al. 1976, Vallenas et al. 1979, Thomsen and Wallace 1995). One of the earliest studies focusing on this response mode was that reported by Goodsir (1985),

who observed buckling in the test specimen Wall2. Buckling occurred in the compression zone of the wall after unloading from Θ_{pk} = -2.3%, where large tensile strains had been imposed in the longitudinal reinforcement in the boundary region of the wall, which buckled. Another pioneering experimental study was conducted by Chai and Elayer (1999). They tested fourteen prisms simulating wall boundary elements. These prisms had ratios h_u/t_w between 12 and 18 (where t_w is the thickness of the wall) and were subjected to large amplitude cyclic axial loading to demonstrate the influence of the maximum tensile strain on the prisms' lateral stability.

In the experimental study at the E-Defense Shaking table on a four-story building designed with modern code provisions, buckling of walls was observed. In this test, the buckling of the compression zones was accompanied by spalling and crushing (Tuna et al. 2012, Wallace 2012).

Most recent experimental testing studies on buckling of RC vertical components have used isolated boundary elements (e.g., Moehle et al. 2010, Chrysanidis and Tegos 2012, Arteta et al. 2014, Massone et al. 2014, Taleb et al. 2016, Haro et al. 2018). Experimental studies on buckling of RC walls are found in Beattie (2004), Johnson (2010), Almeida et al. (2017), and Dashti et al. (2017). Beattie (2004) tested a slender structural wall, whereas Johnson (2010) tested an asymmetrically reinforced planar wall. In both cases, the walls exhibited small out-of-plane displacements (Δ_Y), and small strength degradation up to $|\Theta_{pk}|$ = 2%. Almeida et al. (2017) investigated the behavior of short-flange T-shaped walls. Two test specimens, TW1 and TW4, with a single curtain of longitudinal reinforcement, were subjected to in-plane and biaxial loading, respectively. The test specimens exhibited buckling that ultimately triggered the in-plane failure of the

walls after $|\Theta_{pk}|$ = 0.75%. Dashti et al. (2017) tested uniaxially a planar wall (RWL) that exhibited buckling failure after $|\Theta_{pk}|$ = 3%. Buckling failure occurred in the wall when the out-of-plane displacements generated instability.

Some phenomenological models for buckling of RC prisms have been developed (Paulay and Priestley 1993, Chai and Elayer 1999, Parra-Torres 2015, Haro et al. 2019). these models calculate values of the maximum tensile strain capacities prior to the buckling failure. Moreover, numerical simulations have been carried out to reproduce buckling in prisms. For example, Parra et al. (2015) used FEM (smeared crack) to reproduce the prisms tested by Chai and Elayer (1999), whereas Parra and Moehle (2017) simulated the same series of tests using nonlinear fiber-section Corotational beam-elements. A limitation of the tests and models of prisms, when they are used to simulate buckling of walls, is that prisms are subjected to curvature only about the horizontal axes, whereas in walls exhibiting buckling curvature is present about vertical and horizontal axes.

Archetype models of RC walls with ratios h_u/l_w between 1 and 3 were used in Parra (2015) to study the influence of strain gradients along with the wall height and length on the out-of-plane displacements. The models used four-node isoparametric curved shell elements with Total Lagrangian description for geometric nonlinearity. The number of FEM simulations to capture the buckling phenomena in structural walls described herein is limited. Parra (2015) modeled the specimen R2 tested by Oesterle et al. (1976) using curved shell elements with embedded reinforcement and total strain crack model for concrete. The analysis was conducted up to Θ_{pk} = ±2.2% cycle, at which lateral bracing was added in the test. There was good agreement between the measured and computed F−D responses. The peak $|\Delta_Y|$ computed by this researcher was 50% larger than that

measured. Dashti (2017) used the same FEM formulation than Parra (2015) and modeled the test specimens: R2 (Oesterle et al. 1976), Specimen 3 (Beattie 2004), RWN (Johnson 2010), RWL (Dashti et al. 2017), and TW1 (Almeida et al. 2017). The computed F−D response of the test specimen R2 exhibited good agreement with the reported up to the second cycle with Θ_{pk} = ±2.2%, whereas the computed peak $|\Delta_Y|$ was 64% larger than the measured value. The simulation was continued without considering the lateral bracing added during the test; softening in the F−D response was computed at Θ_{pk} = 3% before it occurred in the test. Specimen R2 exhibited bar fracture, which was not modeled. For Specimen 3 and RWN, the F−D responses, in general, were reasonably predicted. However, in Specimen 3 at a cycle with Θ_{pk} = ±2%, the computed peak $|\Delta_Y|$ was 70% larger than that measured, and ultimately the model became unstable before reaching Θ_{pk} = -2.5%, which was not observed in the test. The F−D response of RWL was well predicted up to Θ_{pk} = 3%, but the model did not capture the strength degradation associated with Δ_Y as the wall approached to Θ_{pk} = -3%. The computed peak $|\Delta_Y|$ after Θ_{pk} = 3% was 93% smaller than the measured. Dashti (2017) also carried out the blind prediction of TW1. In this case, the computed F−D response up to Θ_{pk} = 1% exhibited more degradation than the observed in the test. The test specimen failed at peak displacement Θ_{pk} = -1%, because of the large $|\Delta_Y|$ during that semi-cycle; however, the model did not.

4.4 Description of the analysis methodology

4.4.1 Elements and geometry definition

Figure 4.1 and 4.2 depicts the typical BTM layout of an RC wall developed to capture buckling. This methodology is based on the elements (*CorotTruss2*) and materials

(*ConcretewBeta*) as implemented in the program OpenSees (OS) (McKenna 2019) by Lu and Panagiotou (2013). The BTM has three spatial dimensions; and six degrees of freedom (DOF): three translations (U_x, U_y, and U_z) and three rotations (R_x, R_y, and R_z) in each node (see Figure 4.2a). The areas of concrete and reinforcement, as well as the inclination of diagonals (θ_d), follow the recommendations given by Lu et al. (2014) (Figure 4.1 and Figure 4.2a). In the BTM, the concrete and reinforcement are modeled using nonlinear Bernoulli fiber-section beam-elements in the vertical and horizontal directions, whereas truss-elements are used in the diagonals. All beam-elements have in-plane rotational (DOF R_y) releases at the nodes, except for those at the confined boundaries, as described by Lu et al. (2014). The BTM, as presented here, differs from that described by Lu et al. (2014) in that in the unconfined compression zones in the wall's boundaries, the beam-elements also have in-plane flexural rigidity when a single vertical beam-element is used to model the compression zone.

To compute the out-of-plane buckling response mode, truss-elements use the Corotational geometric transformation (*element CorotTruss2*), and beam-elements use the PDelta transformation (*geomTransf PDelta*). The only option for geometric nonlinearity in OS truss-elements is the Corotational transformation. Corotational transformation and PDelta transformation can be used with beam-elements. PDelta transformation uses small-angle approximation for the rotation of the cords and considers shear forces to act in the undeformed configuration. Since out-of-plane buckling in these walls is primarily governed by the axial forces acting in the beam-elements, the latter constraint did not affect the analysis.

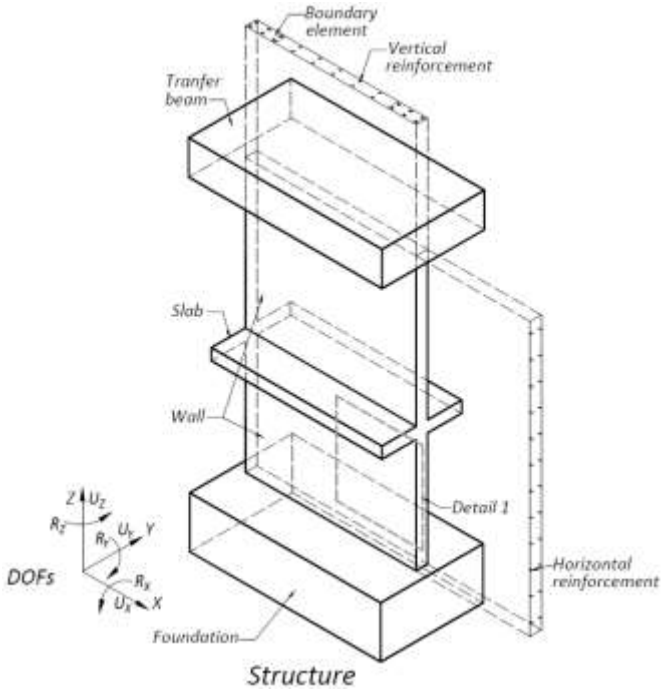

Figure 4.1. Description of the Beam-Truss Model – Structural component.

These simplifications render a reduced number of nonconstant terms in the local transformation matrix and the local stiffness matrix. The PDelta transformation was found to be more robust than the Corotational transformation, and the former was the preferred choice in the analysis. The model does not require any eccentricity to compute buckling. However, to trigger buckling in the same direction as observed in the test, an eccentricity in the reinforcement equal to $0.01t_w$ is used. This eccentricity affects neither the F−D response nor the magnitude of the out-of-plane displacements; similar results can be obtained with no eccentricity.

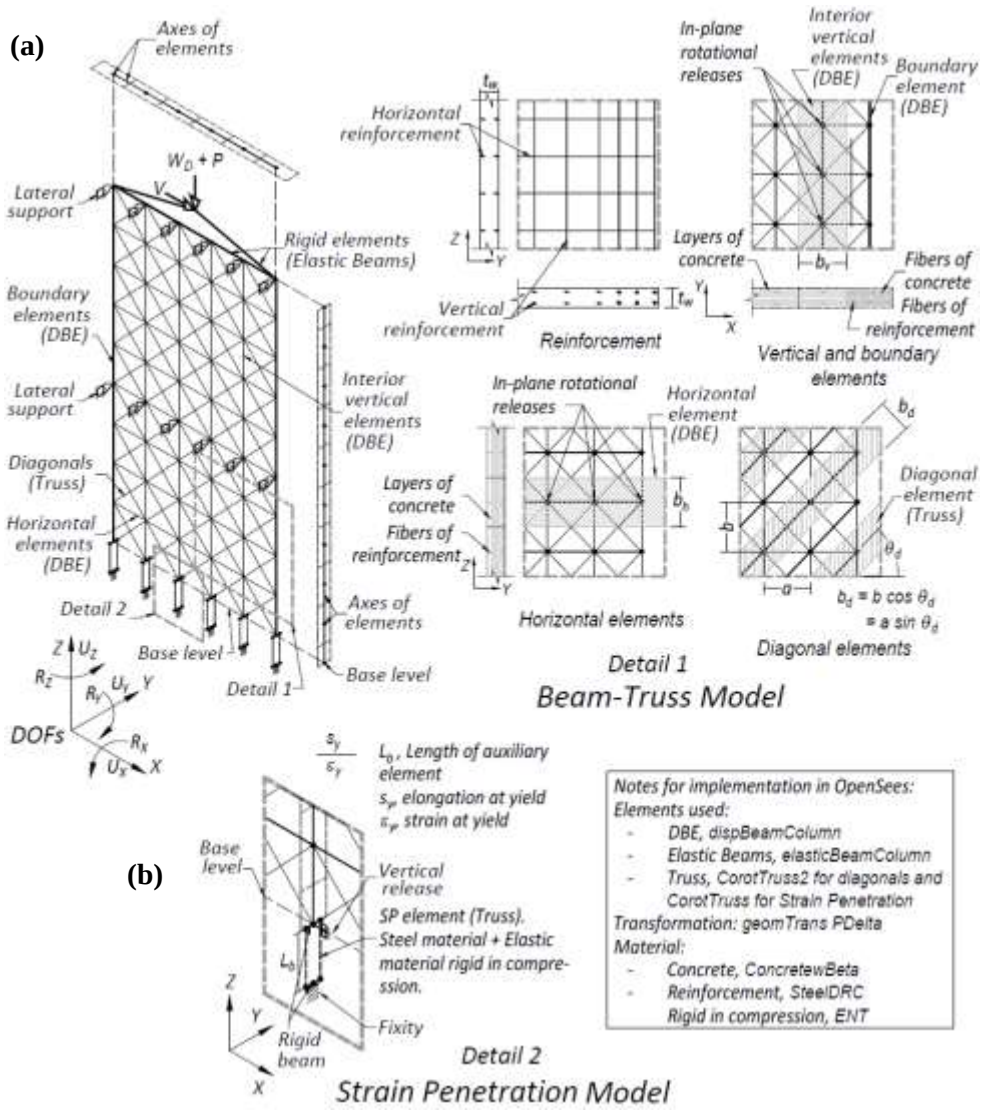

Figure 4.2. Description of the Beam-Truss Model. **(a)** Definition of the geometry and type of elements used. **(b)** Approach for modeling strain penetration.

The nonlinear fiber-section beam-elements chosen in OS are *dispBeamColumn* (DBE), and the truss-elements in the diagonals are *CorotTruss2* elements (Lu and Panagiotou 2013). DBE were preferred because the FBE need to iterate at the element level in each analysis step. With the additional lack of guarantee of convergence at the element level, the robustness of FBE, in general, is expected to be inferior to that of DBE (Koutromanos and Bowers 2016). Three Gauss-Lobatto integration points are used for the beam-elements. The torsional rigidity of the beam-elements was found to have an

important effect on the buckling, as it will be discussed below. The optimum value for the torsional rigidity found from a sensitivity study was *0.02GJ* (see section "Parametric Studies"), where $G = 0.38E_c$ is the shear modulus of the concrete, E_c is the concrete Young's modulus, and J the torsional constant of the beam-element gross-section.

Elastic beam-elements (*elasticBeamColumn*) are used to model auxiliary rigid elements such as the transfer beams at the top of the test specimens (Figure 4.2a).

The solution strategy included the integrators *LoadControl* and *DisplacementControl* for the application of the vertical forces and the lateral displacements, respectively. A TCL script to change the solution algorithm, number maximum of iterations, error tolerance, and increment of force and displacement for the *LoadControl* and the *DisplacementControl* integrator, respectively, was developed to control the iterative computation. The default option for the solution algorithm was *Newton*, which was changed for *ModifiedNewton*, *NewtonWithLineSearch*, and *KrylovNewton* until attaining convergence. The maximum number of iterations for the solution algorithm varied from 100 to 1000 before moving to the next algorithm. To check for convergence was used the test *EnergyIncr*, with error tolerance ranging from 1e-7 to 1e-2 N-m (1e-6 to 1e-1 kip-in). The solver and method to impose constraints were *SparseSYM* and *Transformation*, respectively.

The nodes at laterally supported levels are considered restrained in the DOF U_y, which is the translation perpendicular to the plane of the walls (Y-axis) (Figure 4.2a). All the DOFs of the nodes at the base level of the walls are fixed, with the exception of the vertical translation U_z, to allow for the strain penetration modeling (Figure 4.2b), described next.

As it is shown in the section "Parametric Studies", the strain penetration was also found to significantly affect the wall buckling. The strain penetration is modeled using auxiliary vertical truss-elements *corotTruss* (termed "SP-elements" thereafter) to represent the reinforcement protruding towards the foundation (Figure 4.2b). The length of the SP-element (L_b) was calculated conforming to the type of steel and bar diameter (d_b) that the element represents as well as the compressive strength of the concrete (f'_c) (Moharrami et al. 2015). In particular, L_b is equal to s_y/ε_y, where s_y is the elongation at the yield (bond-slip) and ε_y the strain at the yield. The value of s_y was defined in accordance with Zhao and Sritharan (2007). The constitutive stress-strain relation used for the simulation of the strain penetration is *SteelDRC* (Carreño 2018), described in the following section. This material model was run in parallel with the elastic-no-tension material *ENT* to prevent compressive strains in the SP- elements.

Additional information about the elements and geometry definition of the BTM is available in Lu et al. (2014).

4.4.2 Material modeling

To model unconfined and confined concrete, the BTM uses the *ConcretewBeta* (Lu and Panagiotou 2013) (Figure 4.3a) material model. When used with *CorotTruss2* elements, the *ConcretewBeta* material incorporates the effect of the biaxial strain field on the compressive behavior of concrete (Vecchio and Collins 1986). This material uses the tensile strain perpendicular to the compression field measured by a dummy gauge-element defined in the *CorotTruss2* elements, whose instantaneous strain is used to modify the uniaxial compressive stress-strain behavior of the concrete through the compressive

strength reduction factor β (Vecchio and Collins 1986) (Figure 4.3b). The calibration of the concrete materials is explained in the following paragraphs.

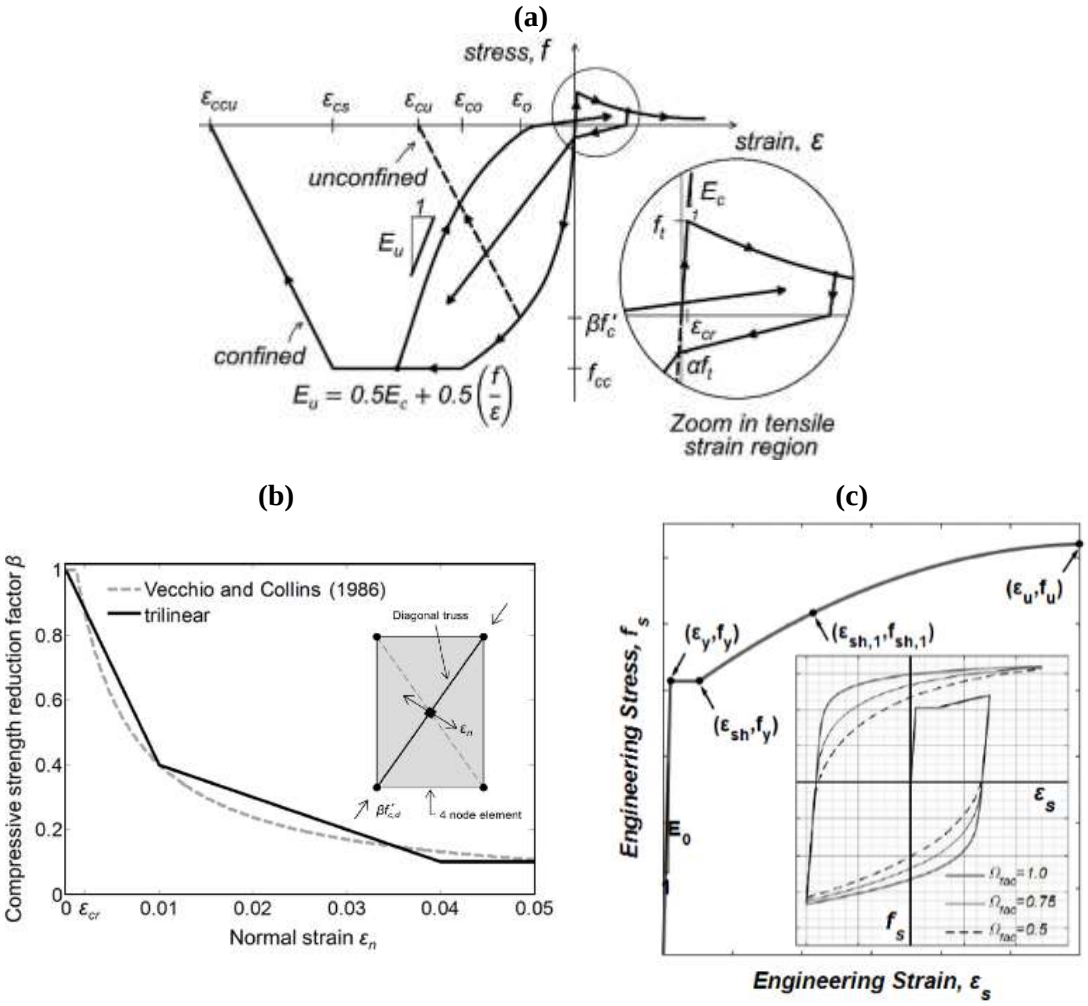

Figure 4.3. Materials used in the Beam-Truss Model. **(a)** Stress-strain relationship for *ConcretewBeta* (reprinted from Lu and Panagiotou 2013,©ASCE). **(b)** Compressive strength reduction factor β (Lu et al. 2014). **(c)** Stress-strain relationship for *SteelDRC* (adapted from Carreño 2018).

Unless the key parameters defining the stress-strain response of unconfined concrete are known, the strain at the compressive strength of the concrete is assumed ε_o = -0.002, the strain at crushing is assumed ε_{cu} = -0.004 (Figure 4.3a), and E_c is assumed $5000\sqrt{f'_c}$ (MPa) (Lu and Panagiotou 2013). As in Lu et al. (2014, 2016), the direct tensile

strength of the concrete f_t is made equal to zero in the diagonal and horizontal elements, whereas for the vertical concrete elements $f_t = 0.55f_r$ (Collins and Mitchell 1997) if the modulus of rupture f_r is known, or $f_t = 0.33\sqrt{f'_c}$ (MPa) (Lu and Panagiotou 2013) if f_r is unknown. In the BTM, the tension stiffening is computed activating the *ConcretewBeta* tension-stiffening option based on Stevens et al. (1991). The compressive strength of the confined concrete f_{cc} and the corresponding strain ε_{co} (Figure 4.3a) are defined according to Mander et al. (1988). The strain at the onset of softening is $\varepsilon_{cs} = -(0.002 + k_e \cdot f_l/(9f'_c))$, where k_e is the coefficient of efficiency of the confinement and f_l is the confining stress (Alvarez et al. 2019). The stress at the closure of the cracks in the diagonal elements is considered $-0.01f'_c$, which improves the calculation of pinching in the hysteretic responses.

The stress-strain relation of the *ConcretewBeta* is regularized, adjusting the strains at crushing, based on the fracture energy in compression (Lu et al. 2014). Additionally, β is regularized based on Lu et al. (2014). To improve the numerical robustness of the models, a residual compressive strength $f_{cu} = -0.2f'_c$ is used (Alvarez et al. 2019).

Reinforcing steel is modeled with the *SteelDRC* material (Carreño 2018) (Figure 4.3c), which is an in-house OS implementation based on the model proposed by Dodd and Restrepo-Posada (1995). *SteelDRC* simulates the yield plateau, the Bauschinger effect, strain hardening, the ultimate strength point (ε_u, f_u), and bar fracture. In this paper, the monotonic stress-strain constitutive relationships were calibrated using the available experimental coupon tests. The parameter *OmegaFact*, which controls the curvature of the Bauschinger effect, was calibrated based on the type of steel (Carreño 2018).

4.4.3 Implementation of the BTM

The models described in this paper were developed using a built in-house 64-bit executable of the open-source code OpenSees Version 2.5.0 rev 6248 (OS) (McKenna 2019). The executable included the *uniaxialMaterial* class *SteelDRC* and the HDF5 libraries to run a beta version of the graphical user interface STKO (Petracca et al. 2017). All the models were created from TCL scripts and post-processed using STKO and MATLAB (2018). To run the models was used a workstation fitted with Dual 3.00-GHz Intel Xeon Gold 6136 CPU and 64GB of RAM.

An adequate cross-section discretization is important to compute buckling response mode. Interior vertical elements and horizontal elements must have out-of-plane flexural rigidity and in-plane rotational releases at the nodes (Figure 4.2a). It is not possible explicitly to model nodal releases in OpenSees. To introduce the in-plane rotational release at the nodes of the beam-elements, the fiber-sections are discretized, as shown in Figure 4.4.

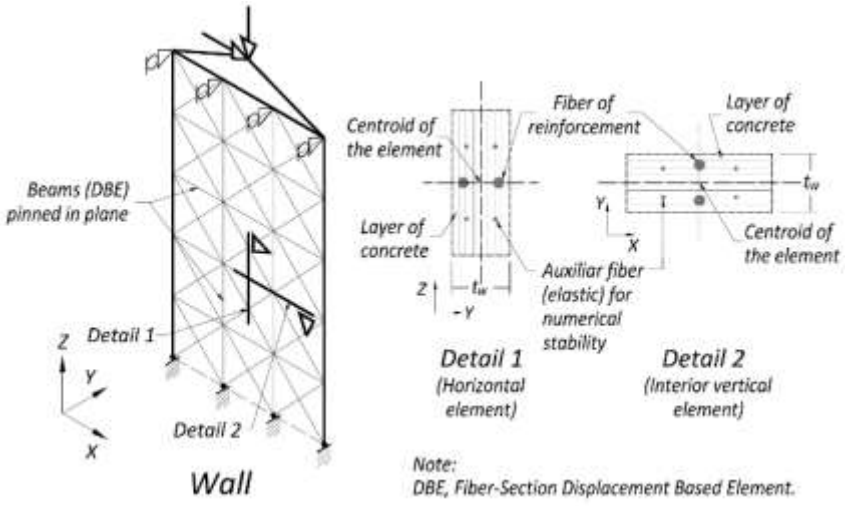

Figure 4.4. Implementation of the Beam-Truss Model in OpenSees using displacement-based elements and fiber-section with layers.

The concrete is modeled here with at least eight layers perpendicular to the axis released in rotation (i.e., Y-axis), whereas the reinforcement corresponding to each curtain is discretized in fibers over the released axis. This arrangement of fibers creates zero flexural rigidity at the section level in the plane of the wall, which generates numerical instability. To avoid numerical instability of the section and allow in-plane rotational release at the nodes of the elements, four auxiliary elastic fibers with very low-stiffness are used. This fibers have a modulus of elasticity equal to 200 GPa and area equal to the area of the section times $1 \times 10^{-12.}$

4.5 Parametric studies

The BTM described in this paper was validated by comparing the measured and computed responses of three test specimens: TW1 (Almeida et al. 2017), RWL (Dashti 2017), and Wall2 (Goodsir 1985). Relevant information on the test specimens and models is listed in Table 4-1. The failure modes of the test specimens are depicted in Figure 4.5. Using the default methods and values stated above, the comparison between model and test specimen key responses of the three case studies is presented in detail in the following section.

The response of the test specimens was computed using the same set of values for the empirical parameters, i.e., eccentricity in the reinforcement to control the direction of buckling, the torsional rigidity of beam-elements, and area of auxiliary fibers to avoid numerical instability, set forth above. The selection of such values was supported by a series of parametric analyses.

Table 4-1. Summary of properties of the test specimens and results of the BTM.

Test	l_w (mm)	t_w (mm)	ρ_l (%)	$\frac{h_u}{t_w}$	$\frac{N}{f'_c A_g}$	$\frac{M}{Vl_w}$	$\frac{V_{max}}{V_{ACI\ limit}}$	Θ_{pp} (%)	ε_{tb} (%)	$\frac{\Delta'_{Yp}}{t_w}$	Computed Failure (Reported Failure)
TW1	2700	80	0.67	25	0.043	3.7	0.16	1.0	1.6	-0.6	B (OCB)
RWL	1600	125	2.29	16	0.06	3.75	0.24	3.0	4.1	0.6	B (B)
Wall2	1500	100	1.73	10	0.04–0.16	–	0.51	-2.3	3.0	-0.4	OU (B)

Notes:

l_w, length of the wall

t_w, thickness of the wall

ρ_l, average vertical steel ratio

h_u/t_w, where h_u is the laterally unsupported height

N/f'_cA_g, axial load ratio, where N is the total vertical load (N), f'_c is the compressive strength of concrete (MPa), and A_g is the gross area of the wall (mm^2)

M/Vl_w, shear span ratio, where M is the base bending moment, V is the base shear

$V_{max}/V_{ACI\ limit}$, where V_{max} is the computed peak base shear (N) and $V_{ACI\ limit} = 0.83A_{cv}\sqrt{f'_c}$ (MPa) [$10A_{cv}\sqrt{f'_c}$ (psi)], A_{cv} is the area considered for shear (mm^2)

Θ_{pp}, peak drift ratio prior to the computed peak out-of-plane displacement

ε_{tb}, maximum computed tension strain in reinforcement prior to the peak out-of-plane displacement

Δ'_{Yp}, peak measured out-of-plane displacements

B = buckling failure; OCB = out-of-plane displacement triggered crushing and bar buckling; OU = out-of-plane displacements without failure.

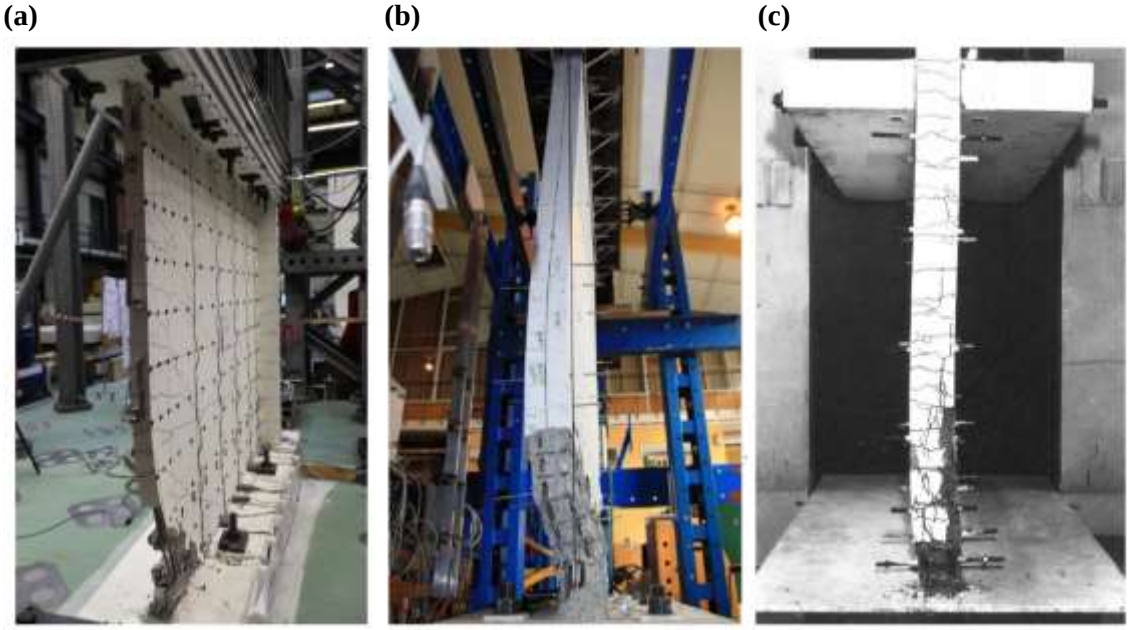

Figure 4.5. (a) Case Study 1 − TW1, south end at the end of the test after failure (Almeida et al. 2017). **(b)** Case Study 2 − RWL, west end out-of-plane instability (Dashti 2017). **(c)** Case Study 3 – Wall2, east end showing buckling to the south (Goodsir 1985).

The grid size initially was proposed to meet, as close as possible, different requirements such as the inclination of the diagonals, location of the out-of-plane restrains, distribution of the properties of concrete and reinforcement, and geometry of the boundary elements. The use of at least four vertical elements in the unsupported height was deemed as suitable to compute out-of-plane buckling response mode. The most appropriate grid size was found by examining two models of each test specimen. One model had a fine-grid (default method used in the case studies to be described later), whereas the other had a coarse-grid. The ratios l_v/h_u (where l_v is the length of the vertical elements) in the fine-grid models were 0.1, 0.08, and 0.13 for test specimens TW1, RWL, and Wall2, respectively. The coarse-grid models had grids with l_v/h_u ratios of about double those used in the fine-grid models. While the mesh refinement, in general, did not affect the F−D responses, the coarse-grid models predicted about 20% smaller $|\Delta_Y|$ than those computed with the fine-grid models. Which for the case study, RWL delayed the buckling failure in the coarse-grid model until the second cycle with Θ_{pk} = 3%, whereas in the fine-grid model, as in the test, buckling failure occurred during the first cycle. For test specimen TW1, both the model with coarse-grid and the model with fine-grid computed softening in the F−D responses in the semi-cycle reported in the test. Neither the fine-grid model nor the coarse-grid model of Wall 2 computed buckling failure, and the use of coarse-grid did not significantly modify the load step at which the peak Δ_Y was computed.

The effect of using beam-elements with in-plane flexural rigidity in the compression zones in the wall's boundaries was studied with three models, termed "in-plane truss models" (ITM), corresponding to the case studies (see Table 4-2). The ITM are similar to the BTM with the difference that the former had no flexural rigidity in all the

elements. For the test specimen TW1, the ITM computed peak lateral strength and $|\Delta_Y|$ at the onset of the buckling failure 10% and 30% smaller than the corresponding values computed by the BTM (the onset of the buckling failure or instability is defined as the point after which the increments of $|\Delta_Y|$ consistently grow for constant increments of in-plane lateral drift Θ). For RWL, the ITM computed similar peak strength and $|\Delta_Y|$ at the onset of the instability than the values computed by the BTM; however, the ITM exhibited excessive pinching. The ITM of the test specimen Wall2 did not converge due to early strength degradation in the F−D response. Degradation in the ITM of Wall2 occurred during the first cycle with Θ_{pk} = -1.6%, whereas the test exhibited degradation after reaching Θ_{pk} = -2.3%.

Table 4-2. Summary of parametric studies.

Test	Default BTM	No Strain Penetration	No in-plane flexural rigidity for the boundaries (ITM)	Torsional Rigidity *0.1GJ*
TW1	Buckling failure	Premature buckling failure	Buckling failure	Δ_Y without buckling failure
RWL	Buckling failure	Δ_Y without buckling failure	Buckling failure	Δ_Y without buckling failure
Wall2	Δ_Y without buckling failure	Δ_Y without buckling failure	M−D degradation at Θ = 1.3% and non-convergence	Δ_Y without buckling failure

A number of parametric analyses carried out in this investigation indicate that the strain penetration has a small influence on the F−D response prior to the buckling failure, but in general, it affects the computed out-of-plane displacements (Table 4-2). Models of test specimens TW1, RWL, and Wall2 where strain penetration was not considered resulted in 15%, 93%, and 27% smaller peak $|\Delta_Y|$ (respectively) than the models including strain penetration (default method used in the case studies). The model of test specimen TW1 without strain penetration computed softening in the F−D response during the cycle with

Θ_{pk} = 0.75%, whereas the test exhibited degradation after reaching Θ_{pk} = 1%. In the model of test specimen RWL the reduction of $|\Delta_Y|$ prevented the buckling failure observed in the test. In test specimens TW1 and RWL, the consideration of strain penetration allowed to capture softening in the F−D responses in the same semi-cycles as in the corresponding tests.

The effect of using Linear geometric transformation instead of nonlinear transformation (default method used in the case studies) was also studied. Three models for the case studies were created using the Linear transformation (BTM-LG). For the test specimens TW1 and RWL, the BTM-LG and BTM F–D responses were similar up to the onset of the buckling failure. Furthermore, the BTM-LG and BTM of the Wall2 computed a similar base moment − top displacement relationship response (M−D). No noticeable out-of-plane displacements were computed by the BTM-LG; even in the test specimen TW1, where its single curtain of reinforcement was placed with a small eccentricity (see Figure 4.9a).

The torsional rigidity of the beam-elements was found to play an important role in the prediction of the out-of-plane displacements. Values of torsional rigidity equal to *0.02GJ* (default value used in the case studies), *0.05GJ*, and *0.1GJ* (Table 4-2) were studied. The $|\Delta_Y|$, in general, decreased as the torsional rigidity increased. For the test specimen TW1, the models with torsional rigidity *0.05GJ* and *0.02GJ* accurately computed softening in the F−D responses, whereas the torsional rigidity equal to *0.1GJ* prevented buckling failure (Figure 4.6a). For test specimen RWL, buckling failure did not occur when the torsional rigidity was made equal to *0.05GJ* and to *0.1GJ* (Figure 4.6b). The F−D responses for Wall2 computed with torsional rigidities *0.02GJ, 0.05GJ,* and *0.1GJ* were all

very similar (Figure 4.6c). The sensitivity study led to an optimum torsional rigidity equal to *0.02GJ* for vertical and horizontal beam-elements.

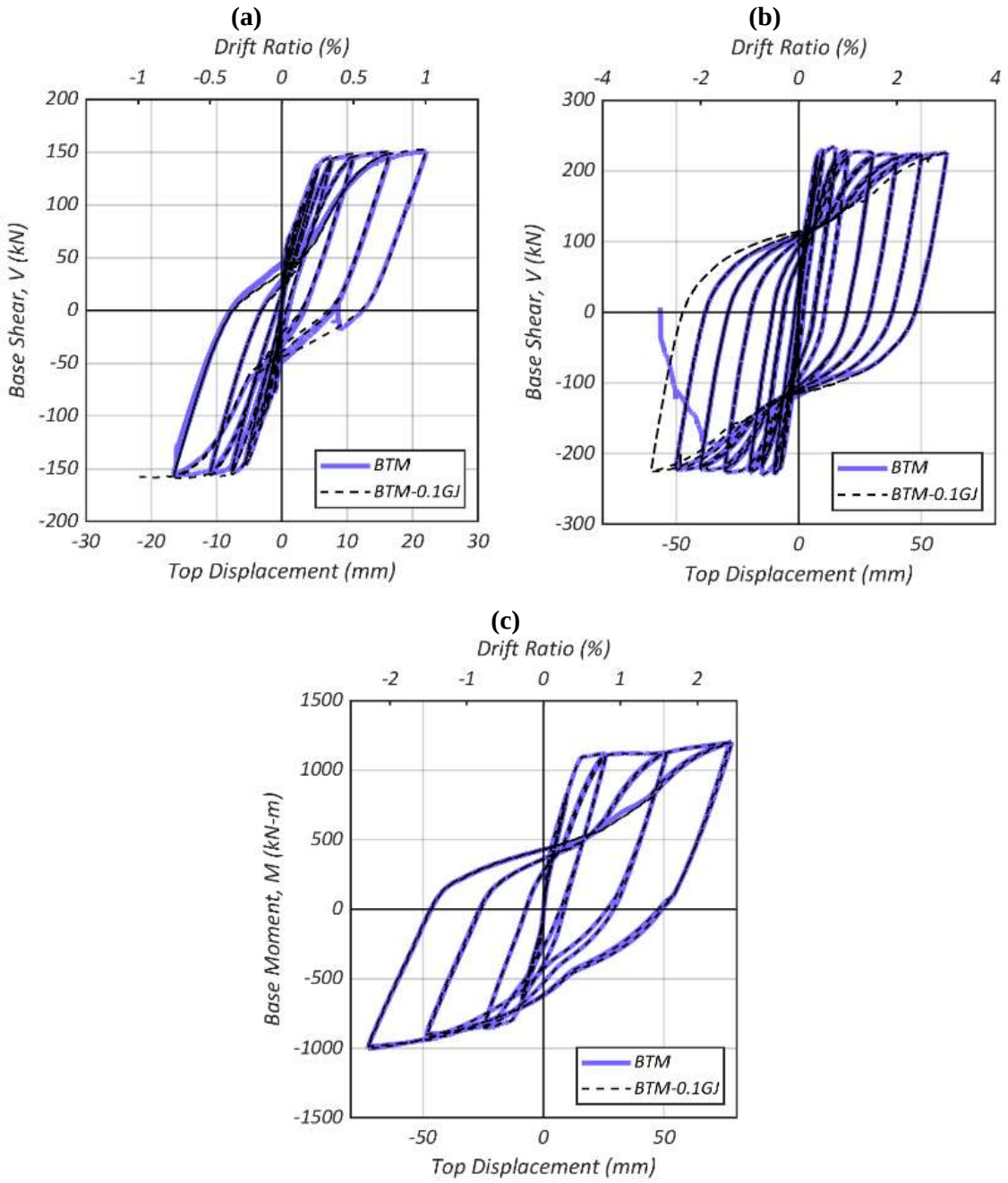

Figure 4.6. Comparison of base shear force − top displacement computed using torsional rigidity equal to *0.02GJ* (BTM) and *0.1GJ*. **(a)** Case Study 1 − TW1. **(b)** Case Study 2 – RWL. **(c)** Case Study 3 – Wall2.

Bar buckling did not trigger plastic hinge out-of-plane buckling in any of the three test specimens; therefore, this response mode was not included in the BTM. However, to study the role played by bar buckling on the overall out-of-plane buckling response mode of the walls, an alternative model for test specimen Wall2, termed "BTM-Cages", was created (Figure 4.7).

This model was identical to the default BTM, except for explicitly including the reinforcement cages of the boundary elements. The concrete at boundary elements was modeled using a single vertical line of fiber-section beam-elements (Plain-Concrete-Elements), from the base to the intermediate support level (Figure 4.7), whereas the bars were modeled using multiple lines of beam-elements (Bar-Elements).

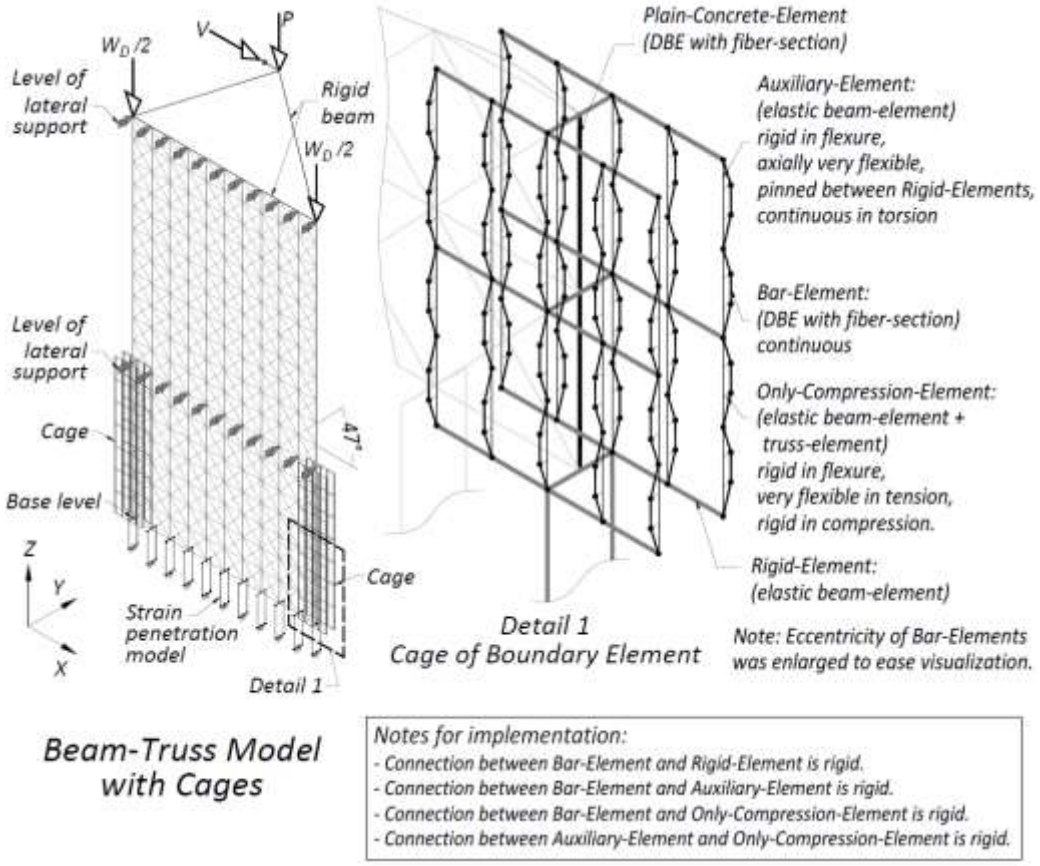

Figure 4.7. Description of the Beam-Truss Model with Cages for Case Study 3 − Wall2.

The Bar-Elements had circular fiber-sections (3 fibers in the radius by 12 fibers in the circumference) and used PDelta geometric transformation, similar to the formulation developed by (Carreño 2018). Rigid-Elements connected the Bar-Elements to the Plain-Concrete-Elements. The lateral support provided by stirrups to bars was modeled using the Auxiliary-Elements, which were elastic beam-elements rigid in flexure and axially very flexible. Additionally, to prevent bar buckling inwards of the confined concrete core were used Only-Compression-Elements. These elements resulted from the aggregation of elastic beam-elements and truss-elements (Figure 4.7).

To trigger the bar buckling outwards, the bars were modeled with eccentricity between stirrups equal to $0.001s$, where s is the spacing of the stirrups. This eccentricity was small enough to do not affect the results.

Figure 4.8a compares the M−D responses computed by the BTM and BTM-Cages for test specimen Wall2. The models compute very similar overall responses, the maximum difference, which occurs at the peak base moment (Θ_{pk} = 2.5%), is equal to 6.2%.

Figure 4.8b compares the out-of-plane displacement histories computed with both models at the location of the peak Δ_Y (height $0.53h_u$, east end). In general, the BTM-Cages computes slightly smaller out-of-plane displacements with a very similar shape than the BTM, the difference for the peak Δ_Y (Θ = 0.7%) is 5.9%.

Deformed shapes computed by both models are also very similar (see Figure 4.8c and Figure 4.18a). The plastic buckling of the reinforcement was found not to play an important role in the out-of-plane buckling response, even in the post-buckling behavior.

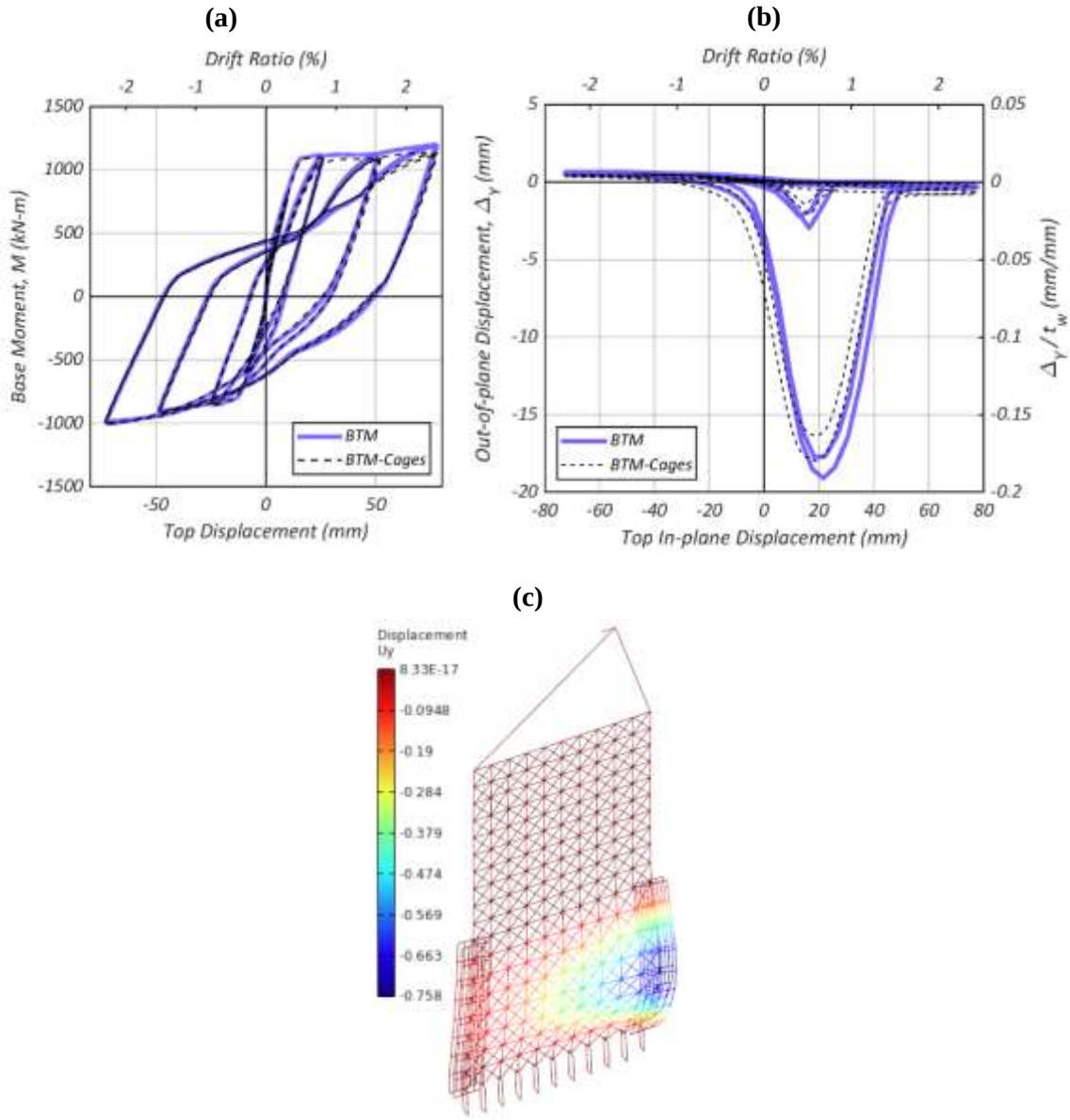

Figure 4.8. BTM-Cages responses, Case Study 3 – Wall2. **(a)** Base moment − top displacement. **(b)** Out-of-plane displacement (Δ_Y) at height $0.53h_u$ (height of computed peak Δ_Y) at the east end. **(c)** Line color map at peak out-of-plane displacement (inches, 10x).

4.6 Model validation

A comparison of measured and computed F−D responses, out-of-plane displacements, and wall longitudinal reinforcement strains is used herein to validate the BTM. Additionally, to gain insight into the buckling behavior of the BTM, contours of

strains are computed using a methodology similar to the described by Álvarez-Sánchez and Restrepo (2017). Displacement fields for planes at different locations along the wall thickness are obtained from the nodal displacements and rotations of the BTM, and using strain rosettes are computed the nodal strains and contours for ε_z (vertical) and ε_2 (minimum principal strain). This procedure was implemented in the GUI StrainContour3D.m developed in-house with MATLAB (2018).

4.6.1 Case Study 1 − Specimen TW1 (Almeida et al. 2017)

Case Study 1 is the short-flange T-shaped structural wall specimen TW1 built at full-scale and reported by Almeida et al. (2017), see Figure 4.9. This test specimen was designed following the current practice for residential buildings in Colombia (NSR-10 2010). The shear span ratio was M/Vl_w = 3.7 (where M is the base bending moment, and V is the base shear) and the axial load ratio N/f'_cA_g = 0.043 (where N is the total vertical load including self-weight and A_g is the gross area of the wall), which was maintained constant throughout the test. The test specimen was tested to Θ_{pk} = ±1%. Two cycles were applied at each displacement level. The lengths of the web and the flange were 2620 mm and 440 mm respectively, whereas the thickness in both cases was 80 mm; the ratio h_u/t_w was equal to 25. TW1 had a single curtain of reinforcement; the average vertical steel ratio was ρ_l = 0.67%, and the horizontal steel ratio ρ_h = 0.18%. No confining reinforcement was provided at the wall boundaries. The material properties for the test specimen are listed in Figure 4.9c.

The measured and computed F−D responses for TW1 are depicted in Figure 4.10a. Stable hysteretic behavior was observed up to Θ_{pk} = 1%.

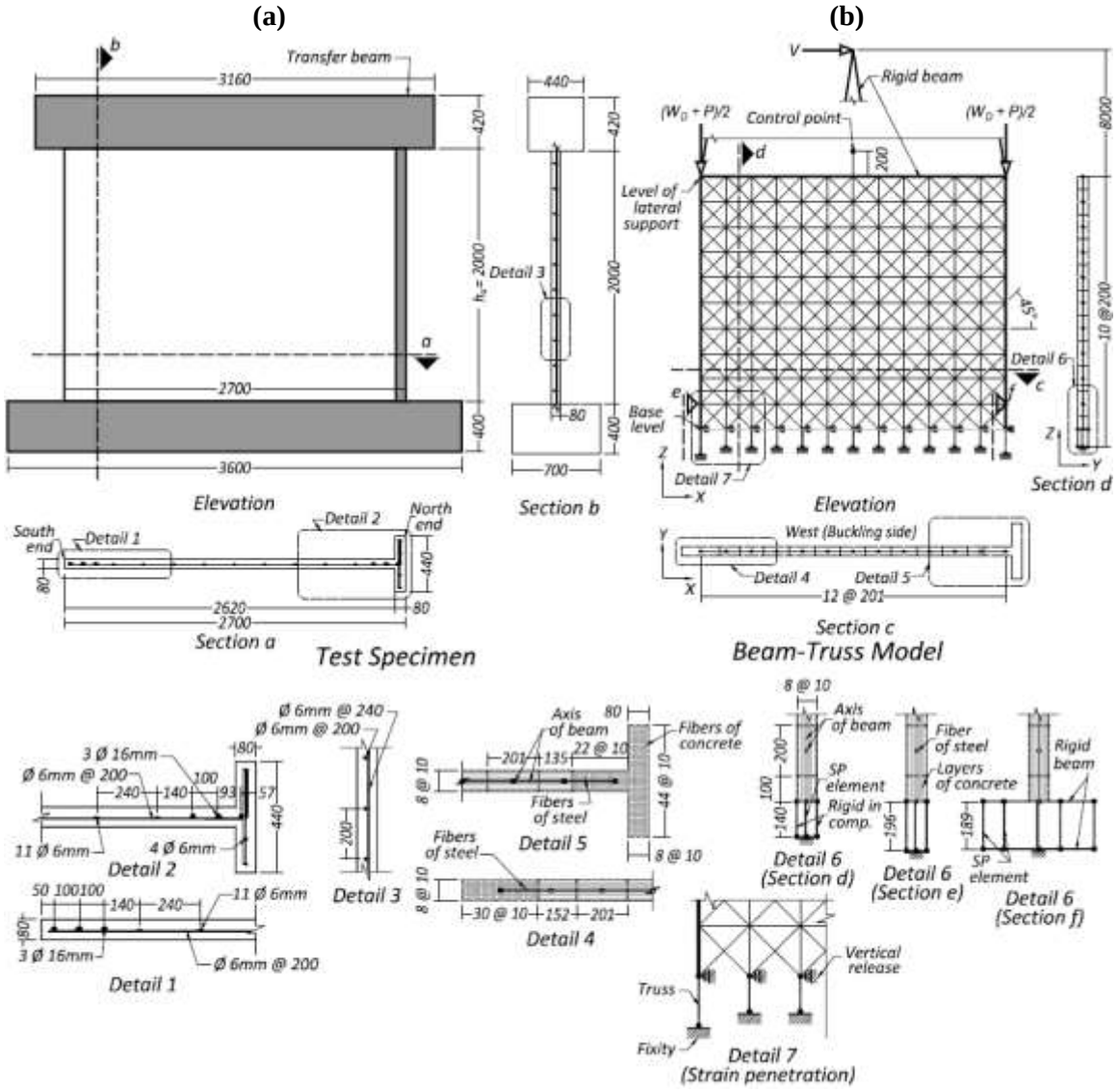

(c)

Summary of properties:

Height	*2 m*
Length	*2.7 m*
Width	*80 mm*
Shear span	*10 m*
$P/(f'_c A_g)$	*0.043*
Web rebar, ρ_w	*0.15 %*
Boundary rebar, ρ_b	*2.63 %*
Horizontal rebar, ρ_h	*0.18 %*

Concrete:

Compressive strength, f'_c	*28.8 MPa*
Modulus of elasticity, E_c	*25.3 GPa*
Strain at f'_c, ε_o	*-0.002*
Tensile strength, f_t	*2.2 MPa*

Note: Dimensions in mm
W_D, selft weight
ϕ, bar diameter (d_b)
h_w, unsupported height

Reinforcing steel:

Bar	*f_y (MPa)*	*f_u (MPa)*	*E_s (GPa)*	*ε_y (%)*	*ε_{sh} (%)*	*ε_u (%)*
ϕ 6 mm	*460*	*625*	*184*	*0.25*	*0.25*	*9.9*
ϕ 16 mm	*565*	*650*	*209*	*0.27*	*2.7*	*14.1*

f_y, yield strength; f_u, ultimate strength; E_s, modulus of elasticity; ε_y, yield strain; ε_{sh}, hardening strain; ε_u, ultimate strain

Figure 4.9. Case Study 1 − TW1. **(a)** Description of the test specimen. **(b)** Description of the Beam-Truss Model. **(c)** Material properties.

The peak base shear measured for this wall was $\hat{V}_{max} = 0.15A_{cv}\sqrt{f'_c}$ (MPa) [$1.8A_{cv}\sqrt{f'_c}$ (psi)] (where A_{cv} is the area considered for shear). The ratio $\hat{V}_{max}/V_{ACI\ limit}$ was equal to 0.18, where $V_{ACI\ limit} = 0.83A_{cv}\sqrt{f'_c}$ (MPa) [$10A_{cv}\sqrt{f'_c}$ (psi).

During the reloading towards Θ_{pk} = -1%, near-zero Θ, the test specimen exhibited the largest peak $|\Delta_Y|$ (south end deformed towards the west side, see Figure 4.9b), followed by strength degradation in-plane and failure of the wall due to concrete crushing and bar buckling (Figure 4.5a).

Figure 4.9b shows the BTM for test specimen TW1 with θ_d equal to 45°. Twelve quadrilaterals in the horizontal direction and ten in the vertical were formed by the grid of beam-elements with l_v/h_u = 0.1. The length of the SP-elements for bars with d_b = 16 mm was $L_b = 12d_b$, and for bars with d_b = 6 mm it was $L_b = 23d_b$. In this case, because the wall had a single curtain of reinforcement, auxiliary elements, rigid in compression, represented the interface between the wall's concrete and the foundation (Figure 4.9b). The nodes at the laterally supported level (top of the grid) were restrained to the rotation about the X-axis, according to the boundary condition in the test. The BTM had 1267 DOFs and required 98 minutes to run the total cumulative displacement equal to 415 mm using increments of 0.03 mm.

The BTM computes the overall hysteretic response very satisfactorily, see Figure 4.10a. The computed peak base shear V_{max} is 10% smaller than that recorded in the test. The maximum |error| in the computation of the peak forces, at any cycle, is 14%.

The peak Δ_Y was measured at the south web end at a distance measured from the wall base equal to $0.4h_u$. The computed out-of-plane response, at the location where the measured out-of-plane response was reported, was obtained using linear interpolation of

the out-of-plane displacements of the nodes. A similar procedure was used in the other two case studies. In general, the BTM of TW1 computes the out-of-plane displacement history satisfactorily at that location (Figure 4.10b).

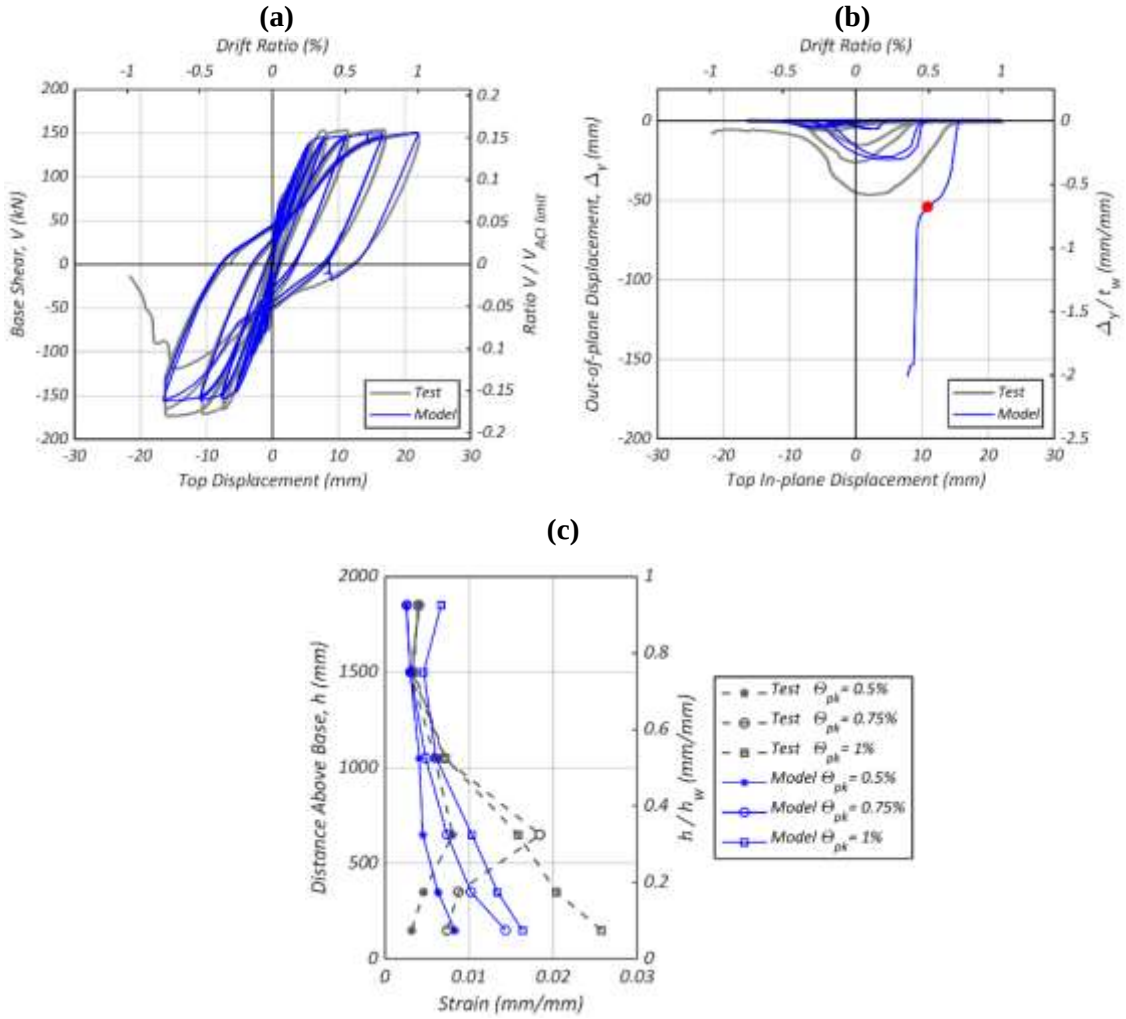

Figure 4.10. Results of the BTM for Case Study 1 − TW1. **(a)** Base shear force − top displacement. **(b)** Out-of-plane displacement (Δ_Y) at height $0.4h_u$ (height of measured peak Δ_Y) at the south end. **(c)** South end vertical reinforcement strains for cycle 1 of large amplitude positive peak drift ratios (Θ_{pk}).

Just like in the test, the BTM computes peaks Δ_Y at near-zero lateral drift, in reasonable agreement with the test. The maximum |error| for the computed peaks of Δ_Y is 48%, with the exception of peak Δ_Y in the last semi-cycle (from 1% to -1% drift ratio).

After partially recovering from buckling by the end of the last-semi-cycle, the test specimen exhibited failure in-plane (concrete crushing and bar buckling, see Figure 4.10a and Figure 4.5a). The failure in-plane was triggered by the large prior peak Δ_Y. As in the test, softening in the F−D response is computed by the BTM in the last semi-cycle; however, it is associated with the onset of buckling failure (Figure 4.10b).

Figure 4.10c compares the measured and computed strains of the outer vertical bar at the web end of the test specimen TW1. The comparison considers the strains corresponding to the positive Θ_{pk} in the first cycle of the three largest amplitudes tested (0.5%, 0.75%, and 1% drift ratios). The measured strains were reduced from six external LVDTs placed along with the height of the south face. The LVDTs were supposed to be attached to the outer vertical bar of the wall's boundary. The computed strains at the center of the bar at the location of the LVDTs (mid-height of the supports) were calculated by linear interpolation of the strains computed by the model at the location of the first and last integration point of the Bernoulli beam-elements at the boundary. Neither the measured nor computed bar axial strain immediately above the foundation included strain penetration. A similar procedure for the computation of bar strains was used in the other two case studies. The strains computed for the bar of this test specimen do not compare closely with those reported at the lower end of the wall where plasticity developed, and the |error| in the computed peak strain is 37%. The regularization of the concrete constitutive stress-strain relationships achieves the overall objectivity of the BTM. However, it results in the loss of objectivity at the section level if plasticity is present. Therefore, the stress-strain curves are grid-dependent, and the prediction of the strains becomes challenging.

Figure 4.11a displays the contour of the out-of-plane displacement ratio Δ_Y/t_w at the onset of the buckling failure predicted by the model.

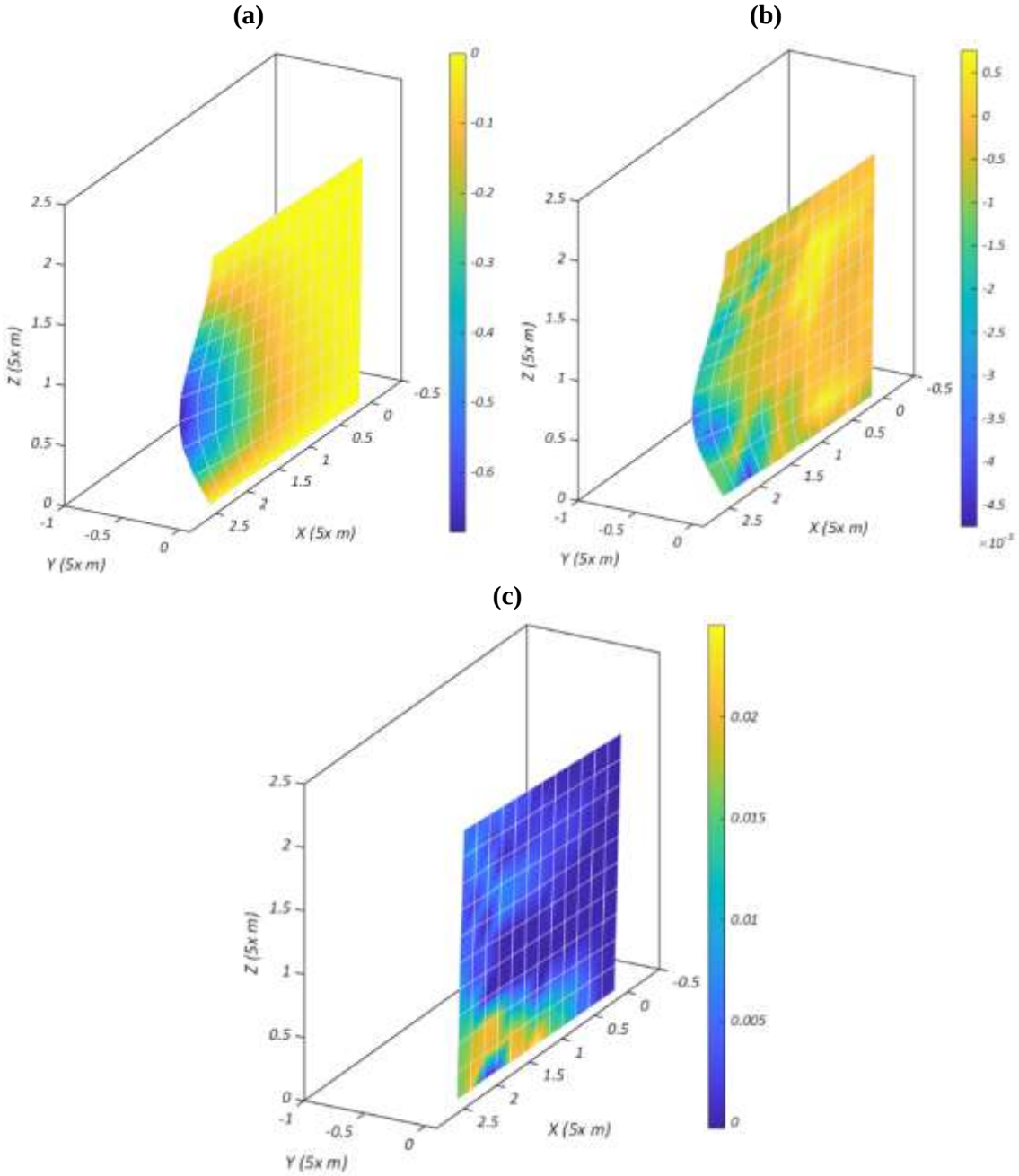

Figure 4.11. Contours of the BTM for Case of Study 1 − TW1. **(a)** Out-of-plane displacement ratio Δ_Y/t_w at the onset of the instability. **(b)** Minimum principal strains ε_2 in the compression face at the onset of the instability. **(c)** Vertical strains ε_z in the axis of the wall at the peak drift prior to the peak out-of-plane displacement.

Instability begins after reaching the Θ_{pk} = 1% at Θ = 0.49% (see Figure 4.11a and dot in Figure 4.10b), with $|\Delta_Y|$ equal to $0.69t_w$, which is 16% larger than the measured peak $|\Delta_Y|$. The computed peak Δ_Y occurs as in the test at the web end (south end) but at a height equal to $0.3h_u$, 25% lower than the measured height. The contour of ε_2 in the compression face (east side) at the same drift is depicted in Figure 4.11b. The peak ε_2 occurs in the region of peak Δ_Y and is equal to -0.0035, which indicates degradation of the cover; however, no spalling was observed in the test in that location. Figure 4.11c displays the contour of ε_z in the wall axis at the prior peak displacement (Θ_{pk} = 1%). Strains ε_z are large, ranging from 0.018 at the base to 0.012 at the height of the computed peak Δ_Y.

4.6.2 Case Study 2 − Specimen RWL (Dashti 2017)

Case Study 2 refers to the half-scale test specimen RWL reported by Dashti (2017). This planar wall, see Figure 4.12a, represented the base story of a four-story prototype building designed in accordance with NZS 3101 (2006). The wall-length l_w and thickness t_w were 1600 mm and 125 mm, respectively, and the ratio h_u/t_w was equal to 16. The reinforcement ratios were ρ_l = 2.29% and ρ_h = 0.84%. Two curtains of reinforcing steel, and confining reinforcement in the boundaries were incorporated in this test specimen. Figure 4.12c lists the material properties. The shear span and axial load ratio were M/Vl_w = 3.75 and N/f'_cA_g = 0.06, respectively. The lateral loading protocol included three cycles for each displacement level, except for the last two increments where two cycles were applied. This wall was tested to Θ_{pk} = -2.5% − 3%.

Figure 4.13a compares the measured and predicted F−D responses for this test. Force $\hat{V}_{max} = 0.22A_{cv}\sqrt{f'_c}$ (MPa) [$2.6A_{cv}\sqrt{f'_c}$ (psi)], and $\hat{V}_{max}/V_{ACI\ limit}$ = 0.26.

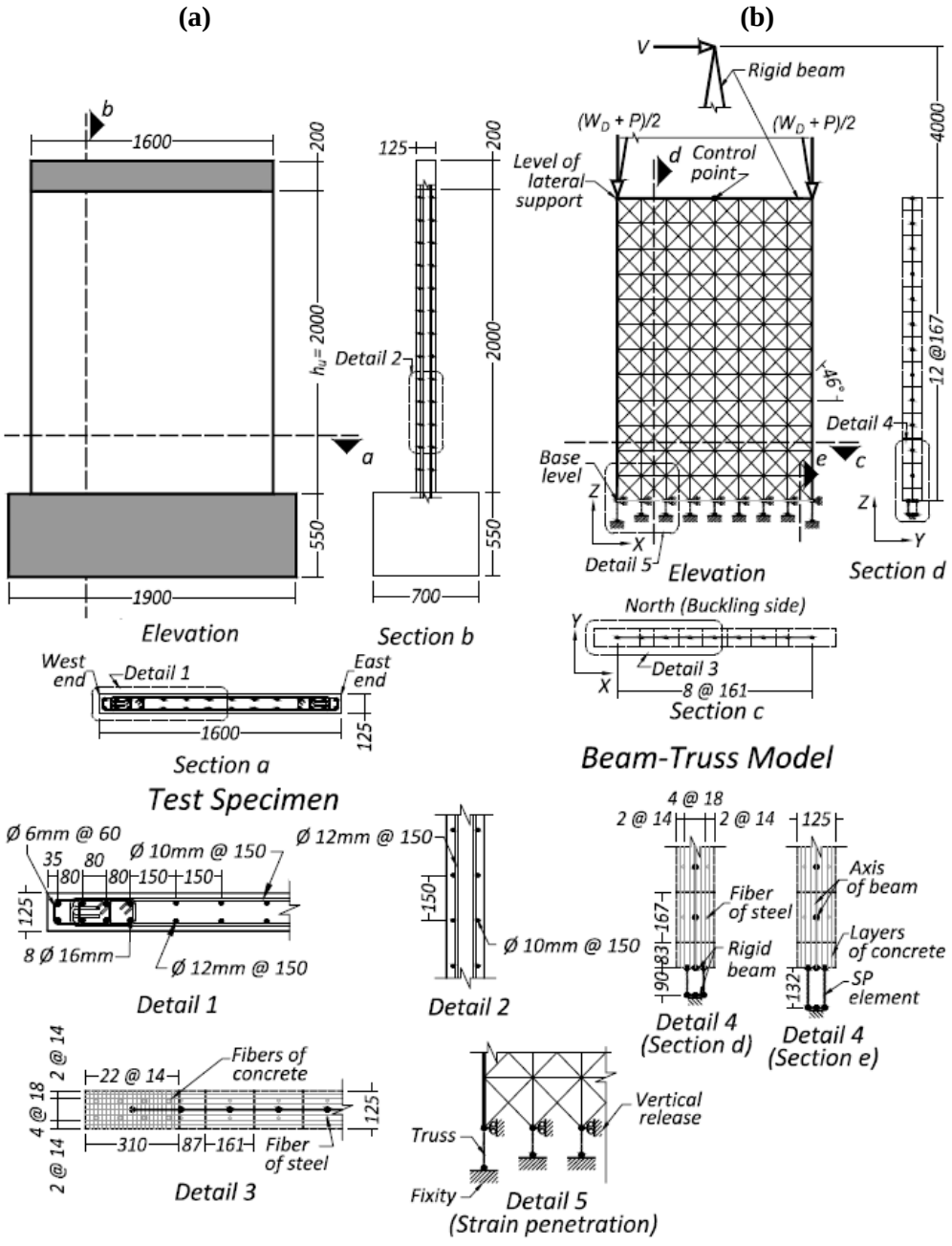

(c)

Summary of properties:

Height	2 m
Length	1.6 m
Width	125 mm
Shear span	6 m
$P/(f'_c A_g)$	0.06
Web rebar, ρ_w	1.1 %
Boundary rebar, ρ_b	4.2 %
Horizontal rebar, ρ_h	0.84 %

Concrete:

Compressive strength, f'_c	34.8 MPa
Modulus of elasticity, E_c	29.5 GPa
Strain at f'_c, ε_o	-0.002
Tensile strength, f_t	1.95 MPa

Note: Dimensions in mm
W_D selft weight
ϕ, bar diameter (d_b)
h_u, unsupported height

Reinforcing steel:

Bar	f_y (MPa)	f_u (MPa)	E_s (GPa)	ε_y (%)	ε_{sh} (%)	ε_u (%)
ϕ 6 mm	411	-	-	-	-	-
ϕ 10 mm	330	460	229	0.2	1.1	20
ϕ 12 mm	334	509	170	0.3	1.9	19
ϕ 16 mm	366	478	168	0.28	1.57	18.5

f_y, yield strength; f_u, ultimate strength; E_s, modulus of elasticity; ε_y, yield strain; ε_{sh}, hardening strain; ε_u, ultimate strain

Figure 4.12. Case Study 2 – RWL. **(a)** Description of the test specimen. **(b)** Description of the Beam-Truss Model. **(c)** Material properties.

Noticeable out-of-plane displacements began when the test specimen was unloaded from Θ_{pk} = 1.5% (west end deformed to the north side, see Figure 4.12b). For this semi-cycle, the peak Δ_Y recovered completely. As $|\Theta_{pk}|$ increased, the residual $|\Delta_Y|$ also increased. The hysteretic response was stable up to Θ_{pk} = 3%. However, during the unloading from that drift, the wall exhibited buckling failure (Figure 4.5b). Neither bar buckling nor bar fracture was observed in the test.

The BTM, shown in Figure 4.12b, used a grid of 8 by 12 quadrilaterals with l_v/h_u = 0.08 and θ_d = 46°. The SP-elements for d_b = 16 mm (boundary elements) had $L_b = 11d_b$, and for bars with d_b = 12 mm (interior vertical beam-elements) had $L_b = 15d_b$.

The rotations about X-axis were released at the laterally supported level (top of the grid; see Figure 4.12b). The model had 875 DOFs and completed 2101 mm of total cumulative displacement in 46 minutes with increments of 0.13 mm.

The F–D response of this test specimen is accurately computed by the BTM, see Figure 4.13a. V_{max} is within 8% of the measured peak force. The maximum |error| for the computed peak lateral forces at each of the loading cycles with $|\Theta_{pk}| \geq 0.5\%$ is less than 14%. The model also accurately computes the abrupt strength degradation due to buckling failure after reaching Θ_{pk} = 3%, as occurred in the test.

Figure 4.13b compares the measured and computed out-of-plane displacement versus top in-plane displacement response at the location of peak Δ_Y. The measured peak Δ_Y occurred at a distance measured from the wall base equal to $0.3h_u$ at the west end. Despite that the maximum |error| for the computed peaks Δ_Y is 63%, the buckling histories follow similar patterns, both the west and the east ends develop peaks Δ_Y near-zero Θ.

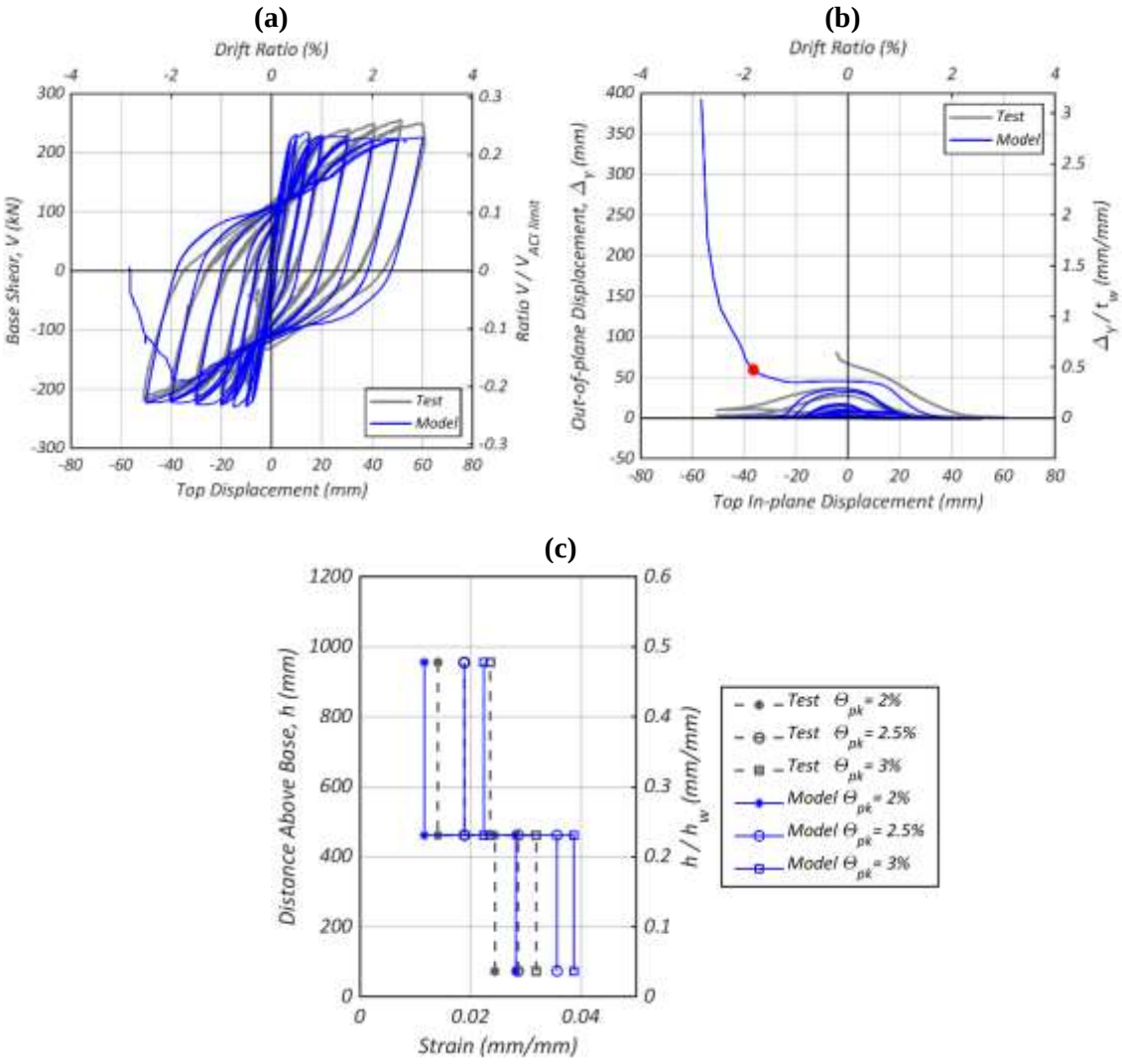

Figure 4.13. Results of the BTM for Case Study 2 – RWL. **(a)** Base shear force − top displacement. **(b)** Out-of-plane displacement (Δ_Y) at height $0.3h_u$ (height of measured peak Δ_Y) at the west end. **(c)** West end vertical reinforcement strains for cycle 1 of large amplitude positive peak drift ratios (Θ_{pk}).

The measured and computed strains of the outer vertical bar at the south face at the west end of test specimen RWL are compared in Figure 4.13c. In this case, the measured strains were computed from two externally placed linear potentiometers attached to the extreme end reinforcement of the test specimen. The strains in the first cycles with Θ_{pk} = 2%, 2.5%, and 3% are compared. The BTM predicts the strains with maximum |error| equal to 25%.

Figure 4.14a depicts the contour of Δ_Y/t_w computed at Θ = -1.8% after reaching Θ_{pk} = 3%. This is the drift where the onset of buckling is predicted (see the dot in Figure 4.13b).

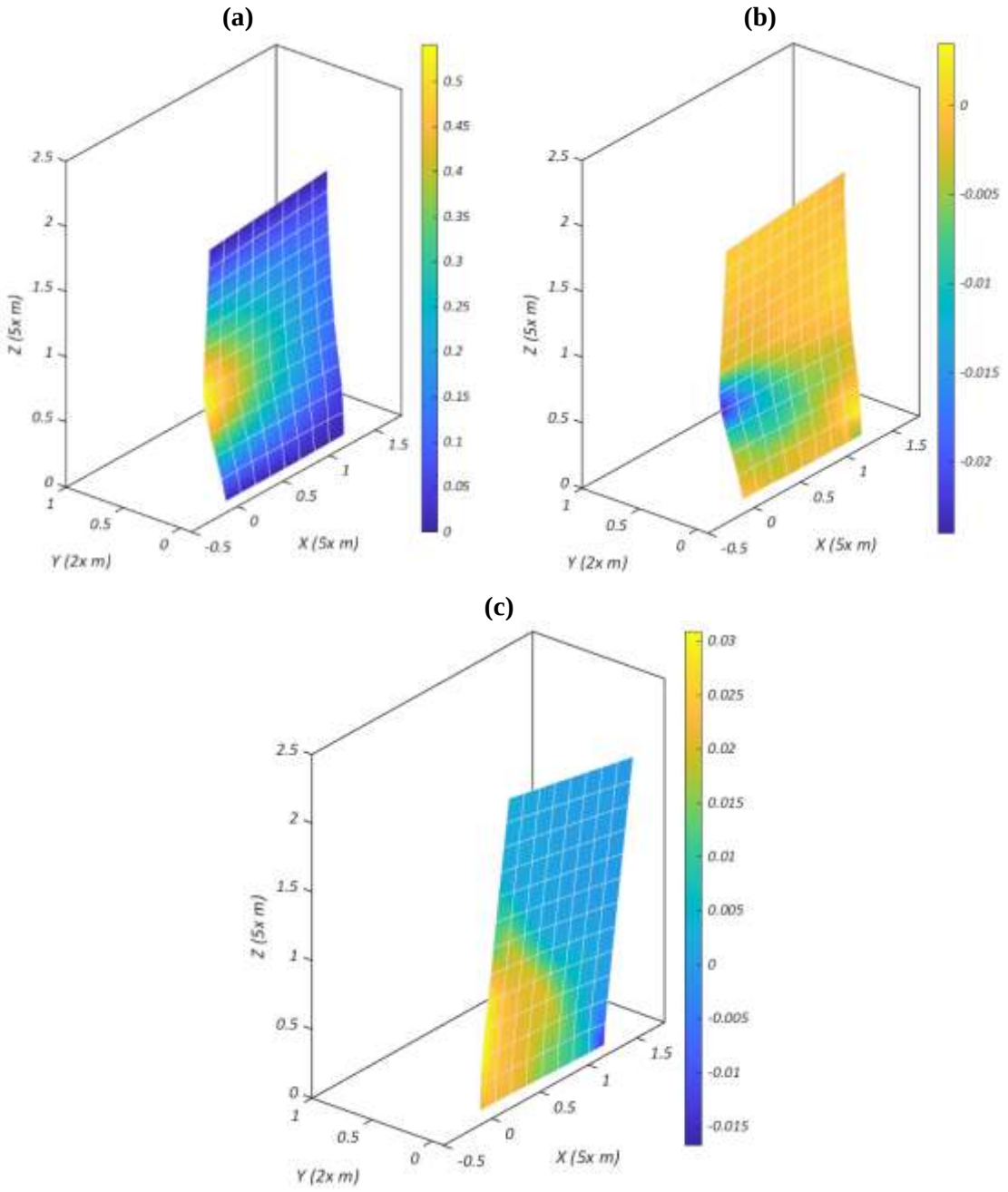

Figure 4.14. Contours of the BTM for Case of Study 2 – RWL. **(a)** Out-of-plane displacement ratio Δ_Y/t_w at the onset of the instability. **(b)** Minimum principal strains ε_2 in the compression face at the onset of the instability. **(c)** Vertical strains ε_z in the axis of the wall at the peak drift prior to the peak out-of-plane displacement.

The computed peak Δ_Y occurs, as in the test, at the west end, but at a height equal to $0.42h_u$ ($0.3h$ in the test). The computed $|\Delta_Y|$ at the onset of buckling is $0.54t_w$, whereas the corresponding measured $|\Delta_Y|$ was $0.58t_w$. Figure 4.14b shows the contour of ε_2 in the compression face (south side) at the onset of the instability. The peak ε_2 is -0.024 and occurs in the region of peak Δ_Y. The strain in the reinforcing bar at the side of compression (south side) is ε_z = -0.02, whereas the corresponding strain in the side of tension (north side) is ε_z = 0.035. The strain difference indicates the localization due to the onset of the buckling failure. Figure 4.14c shows the contour of ε_z in the axis of the wall at Θ_{pk} = 3% (the peak drift prior to the peak Δ_Y). At that drift, the computed peak of tensile strains at the west end (at the height of peak Δ_Y) is very large (ε_z = 0.025), which points out the importance of the residual reinforcing steel strains on the buckling failure.

4.6.3 Case Study 3 − Specimen Wall2 (Goodsir 1985)

Case Study 3 is the 1:4 scale planar test specimen Wall2 described by Goodsir (1985). This test specimen was designed per NZS 3101 (1982) to represent the first two stories of a mid-rise building (Figure 4.15a). The application of an eccentric and variable vertical force P caused the shear span ratio M/Vl_w to vary during the test (Figure 4.15b), P was applied with eccentricity equal to $0.25l_w$ (Figure 4.15a). N/f'_cA_g varied between 0.04 and 0.16, and the shear span was 3180 mm. Two cycles were applied for increasing displacement levels up to Θ_{pk} = -2.3% − 2.5%. The l_w and t_w of the wall were 1500 mm and 100 mm, respectively. A concrete slab, connected to the bracing steel structure, was placed close to the middle height of the wall, resulting in h_u/t_w = 10 for the lower vertical span (Pour 1, see Figure 4.15a).

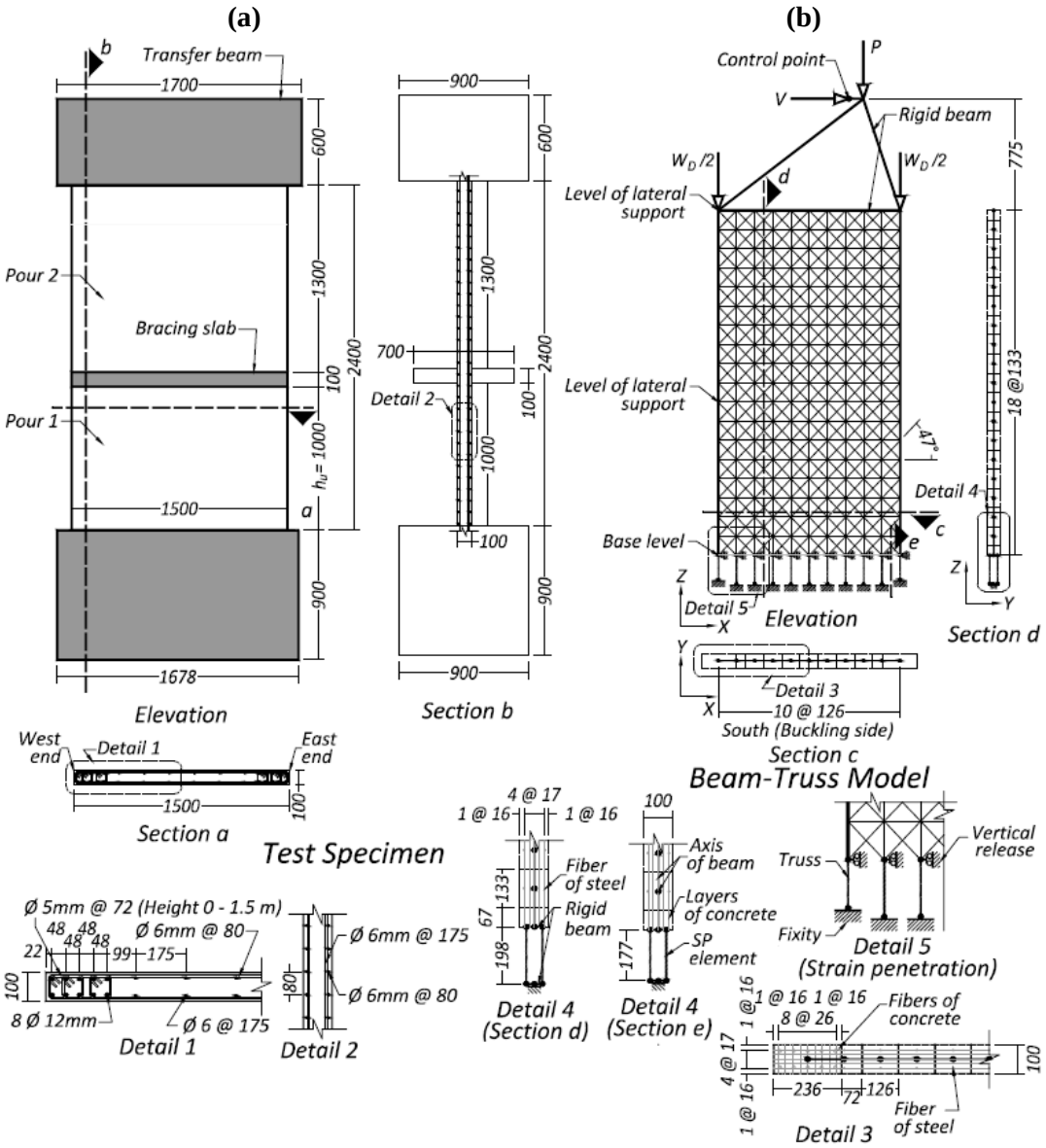

(c)

Summary of properties:

Height	2.4 m
Length	1.5 m
Width	100 mm
Shear span	3.18 m
$P/(f'_c A_g)$	0.05 - 0.26
Web rebar, ρ_w	0.32 %
Boundary rebar, ρ_b	4.71 %
Horizontal rebar, ρ_h	0.71 %

Note: Dimensions in mm
W_D, selft weight
ϕ, bar diameter (d_b)
h_u, unsupported height

Reinforcing steel:

Bar	f_y (MPa)	f_u (MPa)	E_s (GPa)	ε_y (%)	ε_{sh} (%)	ε_u (%)
ϕ 5 mm	290	-	-	-	-	-
ϕ 6 mm	360	497	206	0.18	0.7	10
ϕ 12 mm	450	692	196	0.23	1.15	12

f_y, yield strength; f_u, ultimate strength; E_s, modulus of elasticity; ε_y, yield strain; ε_{sh}, hardening strain; ε_u, ultimate strain

Concrete - Pour 1:

Compressive strength, f'_c	25.3 MPa
Modulus of elasticity, E_c	25.1 GPa
Strain at f'_c, ε_o	-0.002
Tensile strength, f_t	1.66 MPa

Concrete - Pour 2:

Compressive strength, f'_c	34.3 MPa
Modulus of elasticity, E_c	29.3 GPa
Strain at f'_c, ε_o	-0.002
Tensile strength, f_t	1.93 MPa

Figure 4.15. Case Study 3 − Wall2: (a) Description of the test specimen; (b) Description of the Beam-Truss Model; (c) Material properties.

This wall had steel ratios ρ_l = 1.73% and ρ_h = 0.96% and incorporated two curtains of reinforcement with confinement in the wall's boundaries. The material properties of the test specimen are listed in Figure 4.15c.

The measured base bending moment − wall top displacement relationship response (M−D) is shown in Figure 4.16a. The $V_{max} = 0.42A_{cv}\sqrt{f'_c}$ (MPa) [$5.1A_{cv}\sqrt{f'_c}$ (psi)], and $V_{max}/V_{ACI\,limit}$ is equal to 0.51. In this test, the $\hat{V}_{max}$ cannot be compared with $V_{ACI\,limit}$ because such value was not reported. During the reloading from Θ_{pk} = -2.3% to the third Θ_{pk} = 2.5%, softening in the measured M−D response initiated at $\Theta = -1\%$ due to buckling failure (east end deformed to the south side, Figure 4.15b), the test was stopped at Θ = 1.1%. Test specimen Wall2 did not exhibit bar buckling or bar fracture (Figure 4.5c).

The BTM had a grid of 10 by 18 quadrilaterals with θ_d = 47° and l_v/h_u = 0.13 (Figure 4.15b). The lengths of the SP- elements were $L_b = 14d_b$ for bars with d_b = 12 mm (boundary elements), and $L_b = 33d_b$ for d_b = 6 mm (interior vertical beam-elements). Nodal rotations about X-axis were released at levels of lateral support (the bottom of the transfer beam and the bracing slab). The bracing slab was modeled using truss-elements and elastic material with a modulus of elasticity equal to $0.35E_c$. The cyclic analysis, with a cumulative displacement of 1351 mm, took 159 minutes for this 1472 DOFs model. The displacement increment used was 0.38 mm; between each of these increments, a series of force increments adjusted the vertical load P.

The BTM accurately computes the overall hysteretic response of Wall2, with the exception of the last semi-cycle, where the degradation exhibited in the test is underestimated by the model (Figure 4.16a). At each of the loading cycles, the peaks of the computed base moments are also well predicted, the maximum |error| is 5.4%, except for

the first two cycles where this is 9.2%. The test was stopped during the last semi-cycle at Θ = 1.1% because the wall exhibited instability, and the actuator's stroke limit was reached.

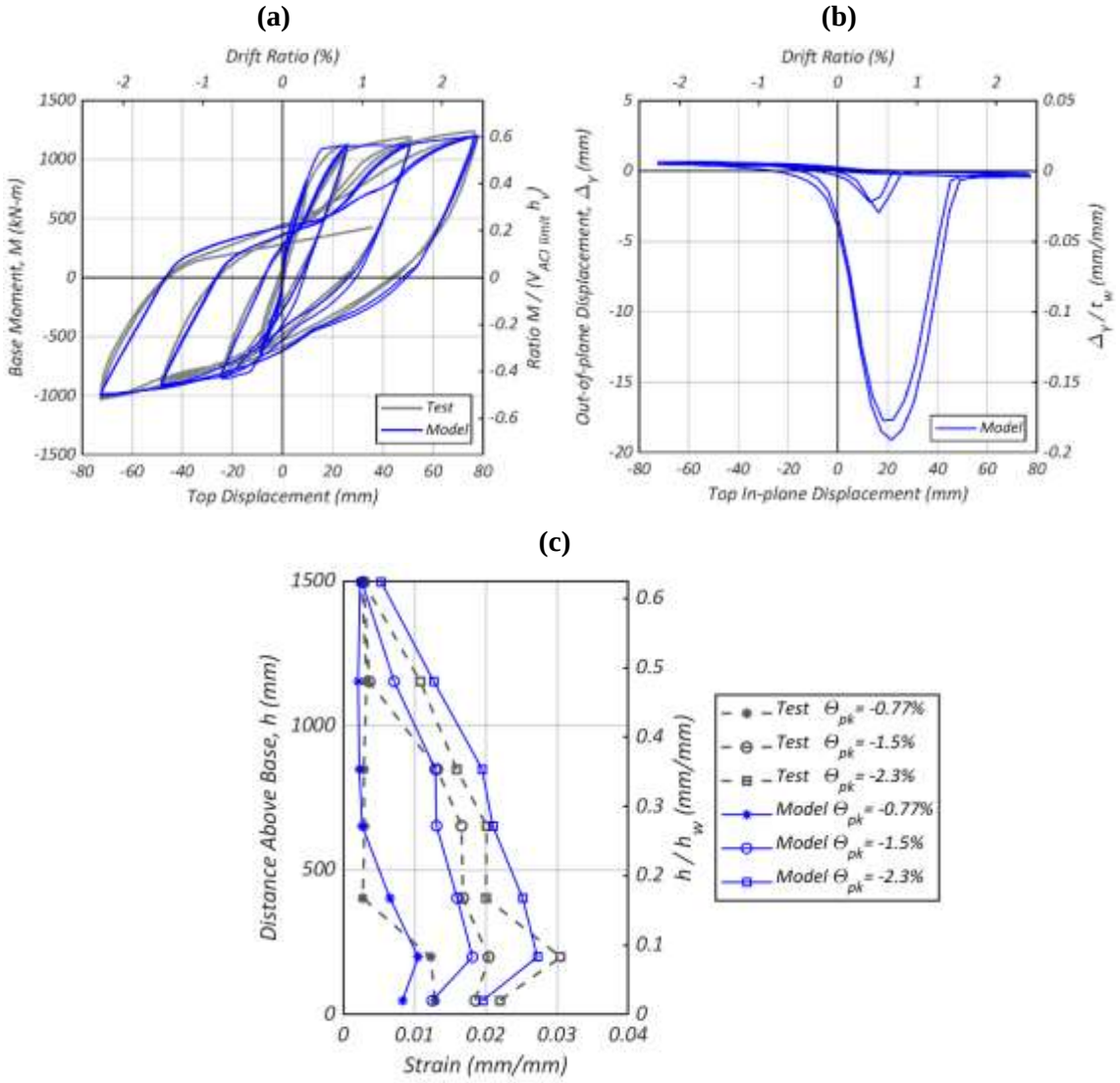

Figure 4.16. Results of the BTM for Case Study 3 − Wall2. **(a)** Base moment − top displacement. **(b)** Out-of-plane displacement (Δ_Y) at height $0.53h_u$ (height of computed peak Δ_Y) at the east end. **(c)** East end vertical reinforcement strains for cycle 2, large amplitude negative peak drift ratios (Θ_{pk}).

Although the numerical simulation reaches Θ_{pk} = 2.5% without exhibiting as much degradation as occurred in the test, the buckling response mode is well captured by the

model (Figure 4.17). Figure 4.16b displays the computed out-of-plane displacements − top in-plane displacements relationship response at the location of the computed peak Δ_Y. The BTM captures the peaks of Δ_Y near-zero Θ, which was the typical behavior of the test specimen. Measured Δ_Y at the onset of buckling failure was not reported, the measured peak $|\Delta_Y|$ was $0.4t_w$ (when the test was stopped because buckling failure) whereas the computed peak $|\Delta_Y|$ is $0.2t_w$, which is consistent with the fact that smaller degradation occurred in the model than in the test.

Figure 4.16c displays the strains of the outer vertical bar at the northeast end; the measured and computed strains at the second peak of the cycles with Θ_{pk} = -0.77%, -1.5% and -2.5% are compared. Eight strain gauges attached to the bar were used to calculate the strains along with the height of the test specimen. As in the previous case studies, the computed strains were interpolated from strains at the location of the integration points. In this case, the measured and computed bar strains follow very similar trends, and the peak bar strain is computed with |error| equal to 11%.

Figure 4.17 displays a comparison of the measured and computed histories of Δ_Y at the east end at $0.6h_u$ (Level 1) and $0.3h_u$ (Level 2). The BTM computes quite accurately the load steps where the peaks of Δ_Y occurred in each cycle.

Figure 4.18a shows the contour of Δ_Y/t_w at the drift where the peak Δ_Y is computed in the last semi-cycle (Θ = 0.68%). The contour indicates that peak Δ_Y occurs at the east end at a height equal to $0.53h_u$, whereas in the test, the peak was reported at $0.4h_u$. Figure 4.18b displays the contour of ε_2 computed at the same Θ for the north side (compression face).

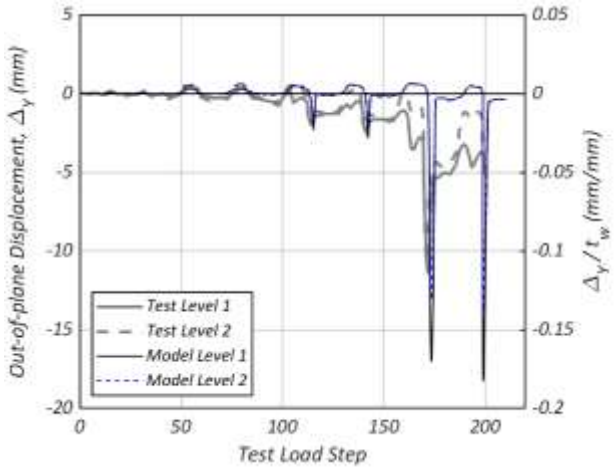

Figure 4.17. Measured vs. Computed out-of-plane displacement history for Wall2 at a height equal to $0.6h_u$ (Level 1) and $0.3h_u$ (Level 2) at the east end.

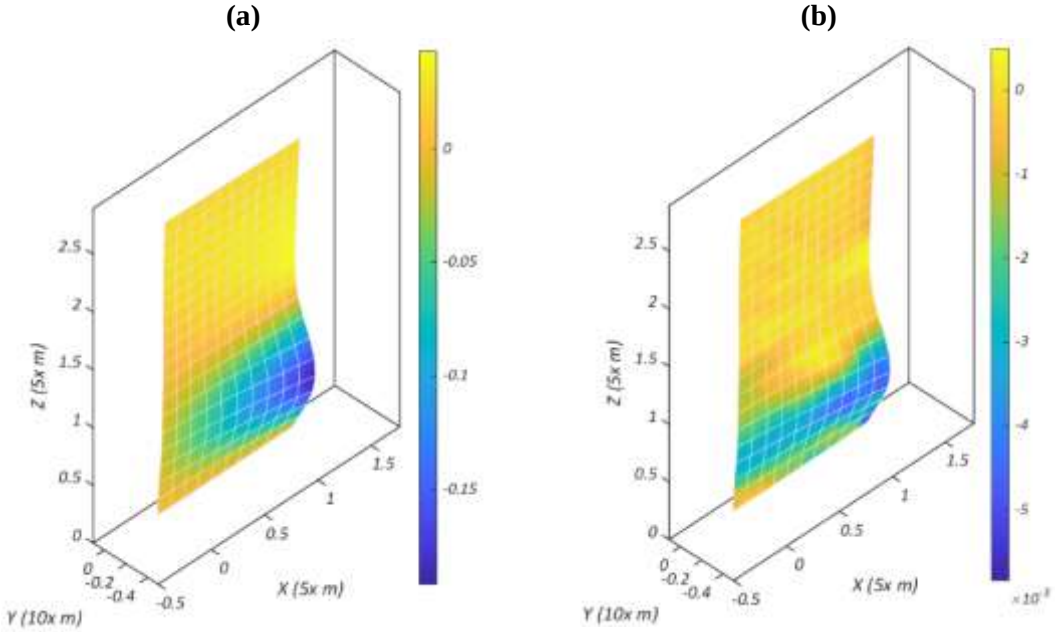

Figure 4.18. Contours of the BTM for Case of Study 3 − Wall2. **(a)** Out-of-plane displacement ratio Δ_Y/t_w. **(b)** Minimum principal strains ε_2 in the compression face at the peak out-of-plane displacement (Δ_Y).

The ε_2 in the location of the peak Δ_Y is -0.0045, whereas the peak ε_2, which occurs at the base, is equal to -0.0058. This is consistent with the damage pattern observed in the test specimen (Figure 4.5c).

The contour of ε_z at the prior cycle with Θ_{pk} = -2.3% is depicted in Figure 4.19. The peak vertical strain ε_z occurs at the east end at the region of the peak Δ_Y, and it is 0.022, a large value as in the previous case studies.

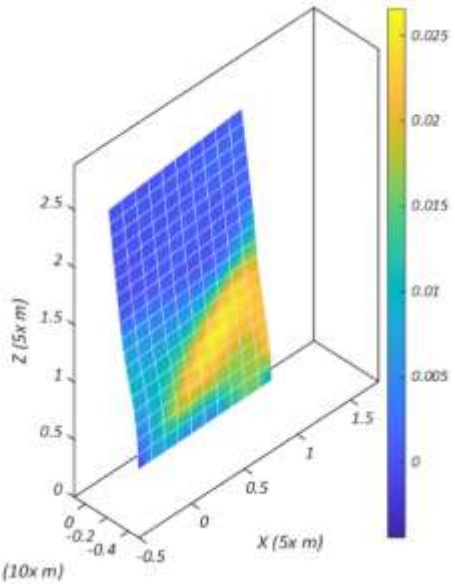

Figure 4.19. Contours of the BTM for Case of Study 3 − Wall2. Vertical strains ε_z in the axis of the wall at the peak drift prior to the peak Δ_Y.

4.7 Conclusions

This paper extended the previously developed Beam-Truss Model (BTM) without geometric nonlinearities for analysis of RC walls, including softening, to plastic hinge out-of-plane buckling analysis using nonlinear-geometry. The model uses a grid of nonlinear fiber-section displacement-based elements with PDelta geometric transformation and diagonal nonlinear Corotational truss-elements. All the beam-elements have an in-plane rotational release at the nodes, except for outer vertical elements representing the compression zones at the wall's boundaries. The BTM was further enhanced by modeling the strain penetration of the reinforcing steel at the base of the walls, which was found to play an important role in the accurate calculation of out-of-plane buckling. This is because

modeling of strain penetration affects the boundary condition as well as the magnitude of strains, both having an important effect for computing buckling. Important for the accurate computation of buckling was also the use of in-plane flexural rigidity at the end vertical beam-elements (representing the compression zones) for both cases of confined and unconfined wall's boundaries.

The BTM model for buckling analysis was validated by comparing the experimentally measured and computed responses of three large-scale test specimens subjected to in-plane uniaxial loading: TW1, RWL, and Wall2 with slenderness ratios ranging between 10 and 25. The comparisons included the overall lateral force – displacement, the out-of-plane displacement, and the local strain responses. TW1 is a short-flange T-shaped wall with a single curtain of reinforcement, whereas RWL and Wall2 are planar walls with two curtains of reinforcement. The walls had strength degradation because of buckling. TW1 exhibited softening in the F−D response after drift ratio Θ_{pk} = 1%, whereas the planar walls reached $|\Theta_{pk}| \geq 2.5\%$ before buckling failure. The models were developed using the open-source nonlinear analysis program OpenSees (McKenna 2019). The following conclusions are drawn:

- In general, the BTM computes the F−D responses of the walls TW1 and RWL very satisfactorily, and the M−D response of Wall2, with 10% maximum |error| of the peak base shear or base moment. The models also computed similar strength degradation of the walls TW1 and RWL at the same semi-cycle with the tests. The model of Wall2 did not capture as much degradation in the last semi-cycle as that observed in the test.

- In all models, the out-of-plane buckling response mode was computed very satisfactorily. The peaks Δ_Y were computed, in agreement with the tests, at relatively small $|\Theta|$. The maximum |error| for the computed peaks Δ_Y is 63%. The location of peak out-of-plane displacements differed no more than 40% in elevation between the models and the tests.
- Vertical strains at the bars of the wall's boundaries for Θ_{pk} prior to the onset of buckling failure in TW1 and RWL, and peak out-of-plane displacement in Wall2, were computed. In general, the measured and computed bar strains followed similar trends, and the peak bar strains at the wall's boundaries were computed with maximum |error| equal to 37%.
- Computed vertical strains ε_z corroborated the importance of residual tensile strains for out-of-plane buckling. The maximum ε_z ranged from 0.018 to 0.025 for the Θ_{pk} prior to the onset of buckling failure (TW1 and RWL) or peak out-of-plane displacement (Wall2).
- The computation of buckling was found to be sensitive to the effective torsional rigidity of the beam-elements. While the default BTM with *0.02GJ* in general computed the buckling behavior accurately, models with *0.1GJ* did not capture buckling failure.

4.8 Acknowledgments

Chapter 4, in part, is a reprint of the material as it appears in *RC Wall Plastic Hinge Out-of-Plane Buckling - Analysis Using the Nonlinear Beam-Truss Model*. Journal of Structural Engineering, 2020, https://ascelibrary.org/doi/abs/ 10.1061/(ASCE)ST.1943-

541X.0000687. Alvarez, Rodolfo; Restrepo, Jose I.; and Panagiotou, Marios. The dissertation author was the primary investigator and author of this paper.

This work was funded by the *Consejo Nacional de Ciencia y Tecnología* (CONACYT), the *University of California Institute for Mexico and the United States* (UC MEXUS), and the program *Becas Fulbright - García Robles* (COMEXUS).

Chapter 5. Enhanced Beam-Truss Model for Nonlinear Analysis of RC Core Walls

5.1 Abstract

The three-dimensional Beam-Truss Model for nonlinear analysis of reinforced concrete structures, including degradation due to in-plane shear response, is enhanced to compute out-of-plane nonlinear shear response in the analysis of Core-Wall-Building systems. This Enhanced Beam-Truss Model considers nonlinear axial-flexure-shear interaction in-plane and nonlinear warping, including out-of-plane flexural and shear responses. The latter is archived via nonlinear shear springs, which use a built in-house material to compute shear response dependent on axial forces.

To improve the computational economy, the model combines in series using a hybrid approach, the Enhanced Beam-Truss Model with a Fiber-Section Model. Displacement-based elements and truss-elements with nonlinear geometric transformation are used.

Using the novel Hybrid Fiber-Section – Enhanced Beam-Truss Model, a comprehensive study on a 14-story archetype Core-Wall building is carried out. The responses of monotonic pushover analyses with 1st mode shape load pattern and triangular load pattern (resultant at 1/3 height), in two orthogonal directions, are studied. Fiber-Section Model and Hybrid Fiber-Section – Beam-Truss Model are used as benchmarks.

Influence of the in-plane shear deformations on the overall response was found for both load patterns. The models that considered in-plane shear response computed smaller lateral strengths than the models that did not. For 1st mode shape load pattern, the in-plane

shear response did not affect the displacement capacity, and the influence of the out-of-plane shear response on the overall and local responses was limited. However, for the triangular load pattern, the in-plane shear response had a large influence on the lateral strength and displacement capacity, whereas the out-of-plane shear response exhibited limited influence on the lateral strength and large influence in the displacement capacity.

5.2 Introduction

Reinforced concrete (RC) walls are commonly used as part of the lateral system of buildings in earthquake-prone regions. Due to its low cost, fast construction, and open architecture, the RC Core-Wall-Building system has become the choice in mid-rise (30-50 m tall) and high-rise constructions (more than 50 m tall). In these buildings, a central Core Wall is the primary lateral system, whereas post-tensioned RC slabs and peripheral columns constitute the gravity system. The Core Wall is formed by coupled walls in one direction and cantilever walls in the orthogonal direction, i.e., two coupled C-shaped walls.

Even though the seismic response of RC wall buildings is labeled as excellent, some gaps of knowledge have been pointed out, since unexpected damage in mid-rise and high-rise RC wall buildings has been observed in past earthquakes, e.g., M_w 6.2, 2011 Christchurch, New Zealand (Kam et al. 2011) (where M_w is moment magnitude).

Moreover, in recent years, with the increase in the use of Performance-Based Design (PBD), e.g., LATBSDC-17 (2017), and Nonlinear Response History Analysis (NLRHA), it has been observed that the Modal Response Spectrum Analysis (MRSA), commonly used in conventional design, e.g., ASCE 7-16 (2016), can underestimate the seismic shear force demands in mid-rise and high-rise Core Walls (Zekioglu et al. 2007,

Fry et al. 2010). The source of this underestimation may be attributed to the lower level of nonlinearity exhibited by the higher vibration modes. Therefore, to use the same response modification coefficient, *R*, in the MRSA, to account for the demand contributions of all modes may be inappropriate (Panagiotou 2017, Mehmood et al. 2017, Najam 2018).

Several linear and nonlinear methods of analysis suitable for RC Core-Wall-Building systems have been developed. The linear methods are used for conventional design, e.g., Equivalent Lateral Force (ELF) procedure and MRSA, whereas the nonlinear methods are used in PBD and research. The analysis of Core Walls requires to model wall piers and coupling beams.

The methods available to model wall piers can be grouped into four main categories: (i) Wide-Column-Frame analogy. In this method, the wall piers of each C-shaped wall are modeled using beam-elements connected to each other with rigid links. Euler-Bernoulli linear beam-elements and nonlinear fiber-section beam-elements (Fiber-Section Model or for simplicity Fiber Model, which is commonly used in PBD) are used. These elements account for axial-flexure interaction and assume plane sections and zero shear deformations (Kwan 1993, Arabzadeh and Galal 2018, Arteta et al. 2019). (ii) Multiple-Vertical-Line-Element-Model (MVLEM). Here, the wall piers are modeled using four-node macro elements. These macro elements have internal vertical line elements and shear springs, which model nonlinear axial-flexure-shear behavior assuming plane sections. The in-plane and out-of-plane behavior are uncoupled; and, whereas the in-plane response is nonlinear, the out-of-plane response is linear (Kolozvari et al. 2019, Isakovic and Fischinger 2019). (iii) Beam-Truss Models (BTM) (Lu et al. 2014, Lu et al. 2016, Lu and Panagiotou 2016). In this method, a grid of nonlinear fiber-section beam-elements and

diagonal truss-elements is used to model the wall piers. The BTM explicitly considers axial-flexure-shear interaction and coupled in-plane and out-of-plane axial-flexure behavior. The out-of-plane flexural response is nonlinear, whereas zero out-of-plane shear deformations are assumed. (iv) Finite Element Method (FEM). Linear shell elements are the most commonly used elements to model wall piers when ELF procedure or MRSA is prescribed. For PBD, NLRHA is required, and nonlinear shell elements are also used. The most popular nonlinear shells are rectangular elements, where separate layers account for vertical nonlinear axial-flexure interaction and in-plane horizontal shear forces, whereas out-of-plane flexure and shear responses are linear (Zekioglu et al. 2007, Fry et al. 2010, Ugalde et al. 2019). Other more sophisticated 4-node shells and 8-node solid-elements based on the Modified-Compression-Field-Theory (MCFT) are available to model Core Walls in research applications (Wang et al. 2017, Mehmood et al. 2017).

Coupling beams are modeled in the linear applications, e.g., ELF procedure and MRSA, using beam-elements or shell elements. In the nonlinear analysis, e.g., NLRHA, the most common methodologies used to model coupling beams are based on calibrated nonlinear shear springs or beam-elements with nonlinear rotational springs (Naish et al. 2013b, ASCE 41-17 2017).

For some years, it has been known that the shear force demands computed using NLRHA could be higher than the shear forces computed using MRSA (Zekioglu et al. 2007, Fry et al. 2010). However, recently, it was observed that the Fiber Models, the most common approach used in nonlinear analysis applied to PBD, exhibit higher amplification than FEM models, including axial-flexure-shear interaction (Mehmood et al. 2017). This difference in the shear force demands occurs because of the inability of the Fiber Models

to take into account the nonlinear shear response, which indicates the importance of the axial-flexure-shear interaction in the modeling of RC-Core-Wall building systems. Additionally, modeling the nonlinear shear response, including shear failure, of Core Walls is especially important because currently conventional design and PBD, rely on prescribed limits for shear strength capacity based on scarce experimental evidence (ACI 318-14 2014).

Built on the BTM methodology described by Lu et al. (2014), this paper develops an enhanced OpenSees (OS) (McKenna 2019) framework for the nonlinear analysis of RC Core-Wall-Building systems. The novel model combines in series an enhanced version of the BTM, termed thereafter Enhanced Beam-Truss Model (EBTM) with a conventional Fiber Model, upgrading the two-dimensional hybrid approach used by Arteta et al. (2019) to three-dimensional analysis. In the resulting model, termed thereafter Hybrid Fiber-Section – Enhanced Beam-Truss Model (HyEBTM), the lower stories of the Core Walls are modeled using EBTM, whereas the upper levels use Fiber Model.

Like the BTM, the HyEBTM includes axial-flexure-shear interaction in-plane and nonlinear warping, however, whereas the BTM considers zero shear deformations for warping, the HyEBTM is extended to include an out-of-plane nonlinear shear response. Additionally, the proposed model improves the computational economy by applying a hybrid approach. The HyEBTM uses the special material ConcretewBeta and element Truss2 as coded by Lu and Panagiotou (2013) in OS for the implementation of BTM; also, it uses the built in-house materials SteelDRC and PinHardwP, the latter developed for the implementation of RC shear response dependent on axial force.

5.3 Literature review

Most of the experimental information related to the behavior of RC Core-Wall-Building systems comes from studies focused on individual walls, e.g., (Oesterle et al. 1976, Thomsen and Wallace 1995, Thomsen and Wallace 2004, Tran et al. 2017), and coupling beams, e.g., (Binney 1972, Galano and Vignoli 2000, Naish et al. 2013a, Poudel et al. 2018). Some other studies on planar RC coupled wall systems, more relevant for the study of Core Walls, are also available (Santhakumar 1974, Shiu et al. 1981, Ozselcuk 1989, Lequesne et al. 2010, Lehman et al. 2013). However, except for the test reported by Lehman et al. (2013), these studies do not fully represent the geometry and loading conditions of modern coupled walls. Lehman et al. (2013) tested a 1:3 scale 3-story coupled wall specimen, which simulated the lowest part of a 10-story building by considering the vertical and lateral load demands from upper stories. Damage in the test specimen progressed from yielding in the coupling beams to yielding and spalling in the wall piers. Sudden loss of lateral and vertical load resisting capacity occurred at 2.3% drift ratio, because of concrete crushing and bar buckling in the compressed wall pier.

Experimental studies focused on RC Core-Wall-Building systems are scarce (Nakachi et al. 1996, Adebar et al. 2008, Inada et al. 2008, Constantin and Beyer 2016, Menegon et al. 2017). Nakachi et al. (1996) conducted the static lateral loading test of four 1:8 scale L-shaped wall specimens to simulate the response of multistory Core Walls. The effect of the size of the confinement area and the amount of confining steel, on the lateral displacement capacity of the Core Walls, was studied. The influence of cracking on the effective stiffness of multistory buildings was studied by Adebar et al. (2008). They tested, under static lateral loading, a large-scale flanged-section wall specimen with aspect ratio

h_w/l_w = 7.2 (where h_w and l_w are height and length, respectively), low vertical steel ratio ρ_s = 0.0045, and constant vertical load ratio $N/(f'_cA_g)$ = 0.1 (where N is the compressive load, f'_c is the compressive strength of the concrete, and A_g is the gross area of the section). The damage progressed from concrete spalling to bar buckling and bar fracture at 2.4% drift ratio. Inada et al. (2008) tested three 1:4.5 scale L-shaped wall specimens under static lateral loading, up to 1.5% drift ratio, to simulate the corners of Core Walls. The first test specimen, an equilateral L-shaped wall, was loaded parallel to one of its wall piers, whereas the second and third test specimens, equilateral and inequilateral L-shaped walls, respectively, were loaded diagonally. After a 0.5% drift ratio, it was observed that plane sections did not remain plane; this due to local crushing of concrete. The first test specimen exhibited sudden out-of-plane shear failure of the wall pier perpendicular to the direction of loading, and the other two test specimens failed when the concrete at unconfined regions crushed. Constantin and Beyer (2016) investigated the response of two 1:2 scale C-shaped wall specimens under bidirectional and diagonal static lateral loading. The test specimens were subjected to vertical load ratios of 0.06 and 0.15. The failure mode in both test specimens was related to concrete crushing in unconfined regions. The displacement capacity of the walls decreased as the vertical load ratio increased; hence the first test specimen failed at a 3.0% drift ratio, whereas the second failed at a 1.5% drift ratio. The major findings were: (i) plane sections do not remain plane under diagonal loading, (ii) large compression depth in the flange ends can generate large compressive strains in unconfined regions, and (iii) out-of-plane buckling can occur because of the strain gradient across the wall pier width. Menegon et al. (2017) tested a 1:1.5 scale 1-story C-shaped wall specimen (box-shaped building core) under static lateral loading up to 4% drift ratio. The

test specimen represented the ground story of a 4-story Core Wall, and it was detailed to match typical practice in low seismicity regions. Relatively good displacement capacity was attained given the type of detailing used.

Testing on complete Core Wall sections, i.e., two coupled C-Shaped walls, are even scarcer. To the best of our knowledge, only two experimental studies have been carried out in this fashion, (Barbachyn et al. 2015, Wang et al. 2017), and these studies were focused on novel multistory Core-Wall-Building systems. Barbachyn et al. (2015) investigated the lateral response of two 1:2.5 scale 3-story coupled shear wall specimens with post-tensioned coupling beams; whereas Wang et al. (2017) tested two 1:5 scale 5-story Core Wall specimens, one steel reinforced concrete (SRC) Core Wall and the other Core Wall with embedded steel trusses (STRC).

On the other hand, several numerical studies related to RC Core-Wall-Building systems have been carried out. Some of these studies used the BTM methodology. Lu et al. (2014) modeled a C-shaped wall specimen reported by Constantin and Beyer (2016), which was subjected to multidirectional static lateral loading. Computed and measured force – displacement responses exhibited excellent agreement, except for diagonal loading. In this case, the response was underestimated. Diagonal concrete crushing was computed by the BTM, as reported for the test. Lu and Panagiotou (2015) modeled three 20-story archetype buildings located in a near-fault region. One building had a conventional fixed-base Core Wall. Another building had post-tensioned rocking Core Wall, and the last one was an isolated building with post-tensioned rocking Core Wall. Modeling scheme, i.e., BTM, explicitly accounted for flexure-shear interaction in walls and slabs. The conventional building exhibited diagonal concrete crushing at a 2.3% drift ratio. Arteta et

al. (2019) developed a hybrid model formed by BTM and nonlinear fiber-section force-based elements (FBE) connected in series. The lower levels of the walls, where flexure-shear interaction could play a role, are modeled using BTM, whereas the upper levels, where the behavior is flexure-dominated, are modeled using FBE. The methodology was validated using three wall specimens with aspect ratios h_w/l_w = 1.5, 2.3, and 3.1. Finally, an 8-story non-ductile frame-wall archetype building was simulated.

Other studies on Core Walls, using more sophisticated models based on FEM, have also been done. Kono et al. (2011) simulated two L-shaped wall specimens (Inada et al. 2008) using rectangular nonlinear shell elements with ten layers. Computed and measured force – displacement responses exhibited fair agreement, whereas the extension and intensity of the damage were well captured. Constantin and Beyer (2012) modeled a C-shaped wall specimen (Constantin and Beyer 2016) using eight-layered rectangular nonlinear shell elements. A smeared rotating crack formulation based on the MCFT was employed, and out-of-plane shear behavior was considered. Two C-shaped wall specimens (Constantin and Beyer 2016, Menegon et al. 2017) were modeled by Hoult et al. (2018) to study the plastic hinge length in walls with low longitudinal steel ratios. RC three-dimensional solid-elements that uses the Disturbed-Stress-Field-Model (DSFM) were employed. Wang et al. (2017) simulated two Core Wall specimens (Wang et al. 2017), one SRC, and other STRC. The FEM models used 8-node solid-elements with three translational degrees of freedom (DOF) per node to simulate concrete. Initial stiffness was overestimated in both models, and the lateral force – displacement response was predicted with reasonable accuracy.

As mentioned before, recent studies have observed that shear forces used in the conventional design of mid-rise and high-rise Core Walls could be unconservative. For this reason, using mostly high-rise buildings case studies, several other numerical studies have been focused on evaluating and improving the code prescription of the RC Core-Wall-Building systems (Boivin and Paultre 2010, Munir and Warnitchai 2012, Leng et al. 2014, Panagiotou 2017, Mehmood et al. 2017).

5.4 Core wall case study building

5.4.1 Building description

This paper studies a 14-story RC Core-Wall building assumed located in downtown Los Angeles, California (34.05° N, 118.26° W). The building was proportioned to be representative of a typical residential tower. Figure 5.1 shows the geometry of the building. The floor to floor height is 3.66 m for all stories, the total building height is 51.21 m, and the plan area is 28.14 m x 28.14 m. A central Core Wall composed of two C-shaped coupled walls is used as the lateral force-resisting system. In the X-direction, the centerline length of the walls is 3.2 m, whereas, in the Y-direction, it is 7.32 m, with a wall thickness of 610 mm at Story 1-5 and 508 mm at Story 6-14. Coupling beams span 2.13 m between the C-shaped walls in the X-direction, the beams are 1016 mm deep with the same width of the walls. This configuration results in a coupled wall system in the X-direction and in a cantilever wall system in the Y-direction. The gravity system consists of post-tensioned RC flat slabs, 203 mm thick, which are supported by 711 mm square columns at the perimeter, and the Core Wall at the center.

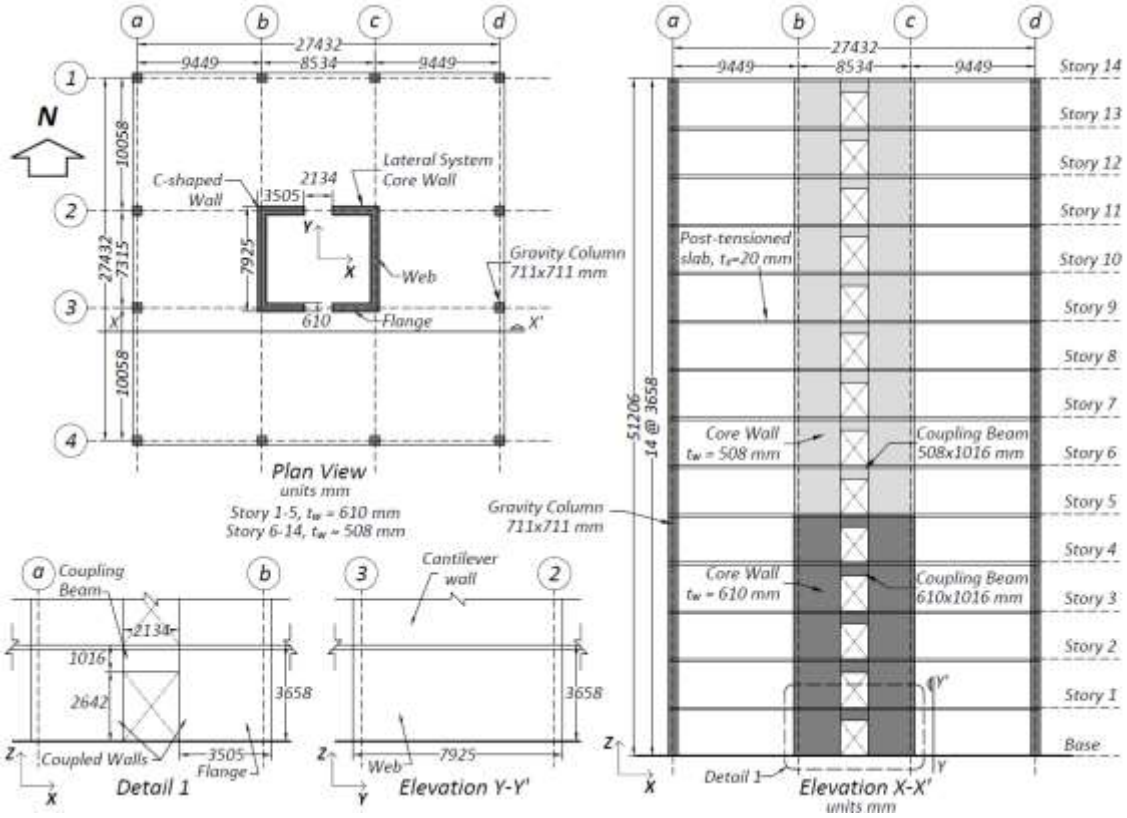

Figure 5.1. Core Wall case study building – Geometry.

5.4.2 Building design

The gravity and seismic design loads were in accordance with the minimum loads prescribed in the ASCE 7-16 (2016), whereas the reinforced concrete elements were proportioned to meet the provisions of the ACI 318-14 (2014). Consistent with residential use, Live load equal to 1.92 kPa and Superimposed Dead load also 1.92 kPa, were considered on all floors. Normal-density concrete (2400 kg/m^3) with nominal compressive strength f'_c = 48.3 MPa, and reinforcing steel ASTM 615 with nominal yield strength f_y = 414 MPa (Grade 60), were used for design.

The building was located in a high seismic hazard area with PGA = 0.52 g, on-site class D (Stiff soil). Modal Response Spectrum Analysis (MRSA) was adopted to compute the seismic-demands. The total Dead load, this is, structure self-weight plus superimposed

dead load, constituted 100% the seismic weight (94,600 kN). The seismic design criteria are listed in Table 5-1.

A linear model developed in ETABS Ultimate 18.0.2 (CSI 2018) was used for the MRSA (Figure 5.2a). The computer model included the structure above the ground, which was considered fixed at the base. Walls and slabs were simulated using Shell-Thin elements, whereas columns and coupling beams were modeled using Frame elements. Following the guidance of ACI 318-14, the effective moment of inertia of the walls was $0.5I_g$ (where I_g is the inertia of the gross section). For the coupling beams, the effective moment of inertia was assumed $0.3I_g$, which is the upper limit prescribed in LATBSDC-17 (2017). Additionally, the flexural rigidity of columns and slabs was artificially decreased to make the Core Wall resisting the total lateral loads.

The same linear model was used to perform a modal analysis (Figure 5.2a). The overall seismic response was dominated by translational modes, instead of torsional modes, due to the symmetry of the masses and the lateral force-resisting system. Periods of the first translational modes in the X-direction (coupled walls) and Y-direction (cantilever walls) are T_{1X} = 1.39 sec and T_{1Y} = 1.49 sec, respectively. Modal mass ratios for the first translational modes are $M_{e\text{-}1X}$ = 0.63 and $M_{e\text{-}1Y}$ = 0.67, whereas modal height ratios are $H_{e\text{-}1X}$ = 0.74 and $H_{e\text{-}1Y}$ = 0.73. The mode shapes of the first and second translations modes are shown in Figure 5.2b-5.2e.

The ASCE 7-16 design-basis earthquake response spectrum, with damping ratio ξ = 5%, was used in the MRSA. Modal decomposition included 30 modes, which accounted for modal mass participation of 99% the actual mass in all directions, well above the 90% participation required by the code (ASCE 7-16, 12.9.1.1).

Table 5-1. Seismic design criteria for Core Wall case study building (Chapter 11, ASCE 7-16).

Parameter	Value
Risk category (Table 1.5-1)	II
Seismic importance factor, I_e (Table 1.5-2)	1.0
Site class (Table 20.3-1)	D
Design spectral response accelerations:	
Mapped spectral response accelerations short period, S_s (Figure 22-1)	1.97 g
Mapped spectral response accelerations 1-s period, S_1 (Figure 22-2)	0.70 g
Short period site coefficient, F_a (Table 11.4-1)	1.0
1-s period site coefficient, F_v (Table 11.4-2)	1.7
MCE_R spectral response accelerations short period, S_{MS} (Eq. 11.4-1)	1.97 g
MCE_R spectral response accelerations 1-s period, S_{M1} (Eq. 11.4-2)	1.19 g
Design spectral response accelerations short period, S_{DS} (Eq. 11.4-3)	1.31 g
Design spectral response accelerations 1-s period, S_{D1} (Eq. 11.4-4)	0.79 g
Design response spectrum:	
$T_o = 0.2(S_{D1}/S_{DS})$	0.12 s
$T_s = S_{D1}/S_{DS}$	0.61 s
Long-period, T_L	8.0 s
Seismic design category (Table 11.6-1 & 11.6-2)	D

The total lateral responses were obtained, combining the spectral responses using the CQC combination method. The reduction response modification coefficient, $R = 6$, was used since the Core Wall was intended to be designed as a special RC walls system (ASCE-14, table 12.2-1). To compute the MRSA demands, an amplification redundancy factor $\rho = 1.3$ was also considered. Finally, the design seismic-demands were calculated, scaling up the MRSA base shear in the X and Y-direction to make them equal to the corresponding shears calculated using the Equivalent Lateral Force (ELF) procedure. Seismic design parameters used in the MRSA and the details of the calculation of design base shear are shown in Table 5-2.

The estimated inter-story drift ratios (Θ_s) were computed using MRSA demands, with the elastic displacements scaled by $C_d/\rho = 5/1.3 = 3.8$. Maximum drift ratio in X and Y-direction were $\Theta_{s\text{-}x} = 0.008$ and $\Theta_{s\text{-}y} = 0.01$, respectively, well below the code limit, i.e., $\Theta_{s\text{-}max} = 0.02$ (ASCE 7-16, Table 12.12-1).

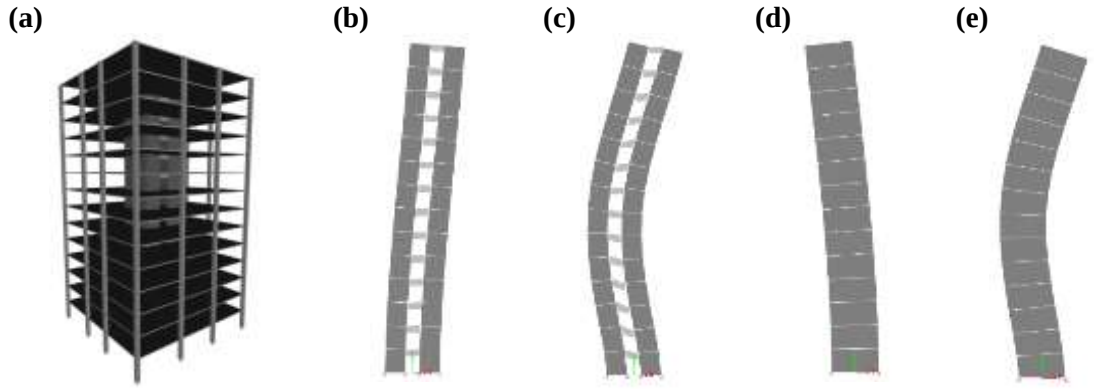

Figure 5.2. (a) ETABS model of case study. **(b)** Mode shape 1 in EW, T_{1X} = 1.39 sec. **(c)** Mode shape 2 in EW, T_{2X} = 0.35 sec. **(d)** Mode shape 1 in NS, T_{1Y} = 1.49 sec. **(e)** Mode shape 2 in NS, T_{2Y} = 0.29 sec.

The design seismic-demands were combined with the gravity demands using ASCE 7-16 load combinations rules (ASCE 7-16, 2.3.1), which resulted in factored axial forces, shear forces, and moments. These design demands were used to proportion the wall piers and coupling beams of the Core-Wall (Figure 5.3).

A single-base plastic-hinge design was adopted, consistent with the uniform structural configuration of the Core-Wall. Axial-flexure design of the Core Wall was controlled by load combinations with primary action in the X- direction, which generated tensile axial forces in the decompressed C-shaped wall. The Core Wall was divided into three portions, along with the height for longitudinal reinforcement proportioning. The lower portion, i.e., Story 1-5 (Figure 5.3, Sec-1a, 1b), was 610 mm thick and had a longitudinal steel ratio ρ_l = 1.57%. The middle and upper portion, i.e., Story 6-8 (Figure 5.3, Sec-2), and Story 9-14 (Figure 5.3, Sec-3), respectively, were 508 mm thick; however, the middle portion had ρ_l = 1.53%, whereas the upper portion had ρ_l = 1.21%. The sections were tension controlled, and a strength reduction factor ϕ = 0.9 was used for the calculation of the design flexural strength. The amount of longitudinal reinforcement at the Core Wall

base was determined such that its design flexural strength was approximately equal to the design base moment. In other levels, longitudinal reinforcement in excess was provided to avoid the formation of plastic-hinges in unintended locations.

Table 5-2. Calculation of the design base shear for Core Wall case study building (ASCE 7-16, Chapter 12).

Parameter	Value
Structural system selection (Table 12.2-1):	
Seismic force-resisting system	Special RC shear walls
Response modification coefficient, R	6.0
Overstrength factor, Ω_o	2.5
Deflection amplification factor, C_d	5.0
Height limit, h_n	48.8 m
Horizontal structural irregularities (Table 12.3-1)	1a Torsional
Vertical structural irregularities (Table 12.3-2)	None
Redundancy factor, ρ (12.3.4)	1.3
Period determination (12.8.2):	
Parameter for calculation of T_a, C_t	0.02
Parameter for calculation of T_a, x	0.75
Approximate fundamental period, $T_a = C_t\, h_n^x$ (Eq. 12.8-7)	0.93 s
Coefficient for the upper limit, C_u (Table 12.8-2)	1.4
Upper limit period, $T_{max} = C_u\,(T_a)$	1.31 s
Period of 1st translational mode X-direction, T_{1X}	1.39 s
Period of 1st translational mode Y-direction, T_{1Y}	1.49 s
Period for scaling forces in X and Y-direction, T_X, T_Y (12.9.1.4.1)	1.31 s
Base shear:	
Effective seismic weight, W (12.7.2)	94,600 kN
Upper limit seismic response coefficient, $C_{S\text{-}2} = S_{DS}/(R/I_e)$ (Eq. 12.8-2)	0.218
Seismic response coefficient for $T \leq T_L$, $C_{S\text{-}3} = S_{D1}/(T \cdot R/I_e)$ (Eq. 12.8-3)	0.101
Seismic response coefficient $C_s = min(C_{S\text{-}2}, C_{S\text{-}3})$	0.101
Base shear of Equivalent Lateral Force procedure, $V_{ELF} = \rho \cdot C_s \cdot W$	12,400 kN
Base shear of MRSA, without scaling, in X-direction, $V_{X\,MRSA}$	95,60 kN
Base shear of MRSA, without scaling, in Y-direction, $V_{Y\,MRSA}$	92,70 kN
Scaling force factor in X-direction, SFF_X	1.3
Scaling force factor in Y-direction, SFF_Y	1.34
Base shear in X and Y-directions, V_X, V_Y	12,400 kN

Compression zones in the Core Wall were checked for special boundary requirements using the neutral axis depth calculated for all load combinations (ACI 318-14, 18.10.6.2). Special boundaries were required only in the toes of the C-shaped walls

(Figure 5.3, Sec-1a, and Detail 1a); however, alternate anti-buckling ties (#3 @ 203 mm) were provided in the complete section at Story 1, which is a common practice.

Design shear demands in the wall piers were relatively low. In the X and Y-direction, the maximum shear force were $0.21A_{cv}\sqrt{f'_c}$ (MPa) and $0.18A_{cv}\sqrt{f'_c}$ (MPa), respectively, whereas the maximum shear force allowed by the ACI 318-14 is $\phi \cdot 0.83A_{cv}\sqrt{f'_c}$ (MPa), where f'_c is the compressive strength of concrete, and A_{cv} is the area consider for shear (mm^2). The design shear strength was calculated using $\phi = 0.6$ since the nominal shear strength was not verified to be larger than the shear demands developed by the nominal moment strength of the wall (ACI 318-14, 21.2.4). The horizontal steel ratio provided in the X-direction in all stories was $\rho_h = 0.37\%$. In the Y-direction, the minimum steel ratio prescribed in the code controlled the design, $\rho_h = 0.25\%$ was provided.

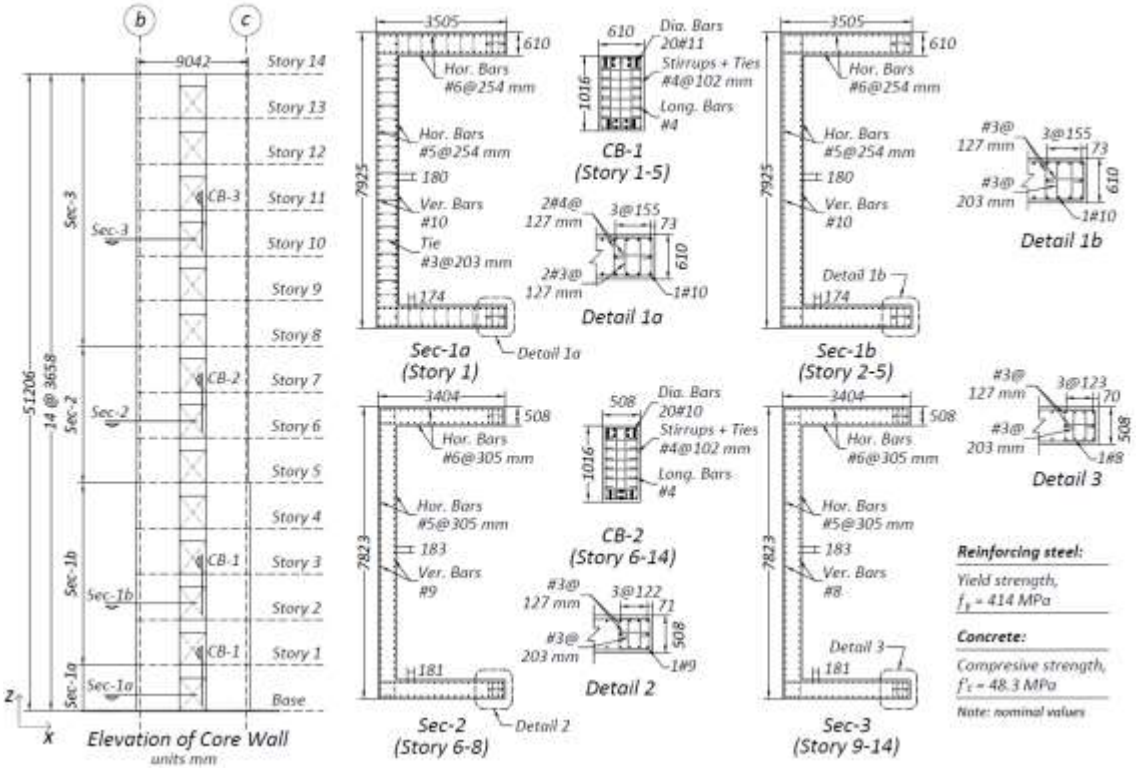

Figure 5.3. Core Wall case study building – Structure.

Two groups of coupling beams were designed, the first group included beams in Story 1-5 (Figure 5.3, CB-1) and the second group beams in Story 6-14 (Figure 5.3, CB-2). Diagonal reinforcement in the coupling beams was determined such that their design shear strengths (calculated using ϕ = 0.85) were approximately equal to the maximum design shear force in each group. The shear demands were relatively high; the maximum shear force was $0.57A_{cv}\sqrt{f'_c}$, which is 81% the maximum allowed by the code. Coupling beams in Story 1-5 were diagonally reinforced with a total of 20 bars # 11, and in Story 6-14, they were reinforced with a total of 20 bars # 10. Full confinement of the diagonally reinforced coupling beams was used (ACI 318-14, 18.10.7.4d).

5.5 Hybrid Fiber-Section – Enhanced Beam-Truss Model

5.5.1 Geometry and components of the model

Figure 5.4 shows a typical Core Wall formed by two coupled C-shaped walls, and the corresponding OS Hybrid Fiber-Section – Enhanced Beam-Truss Model (HyEBTM). Three spatial dimensions; and six DOF, i.e., translations U_x, U_y, U_z, and rotations R_x, R_y, R_z, are activated in each node. HyEBTM uses OS stock materials and elements as well as other built in-house components, as it is described below.

The lower portion of the Core Wall, where axial-flexure-shear interaction can be important, is modeled using Enhanced Beam-Truss Model (EBTM) (Figure 5.4, Detail 1), whereas upper portion, where behavior is controlled by axial-flexure interaction, is modeled using conventional Fiber Model (Figure 5.4, Detail 2). The two parts of HyEBTM are connected using rigid beam-elements (*elasticBeamColumn*) (Figure 5.4, Detail 3). The

EBTM portion height is $h_{EBTM} \geq 6l_w/5 - h_v/3$, where l_w is the length of the wall, and h_v is the shear span, (Arteta et al. 2019).

The EBTM is an enhanced version of the BTM methodology described by Lu et al. (2014), which includes out-of-plane nonlinear shear response (see section "Out-of-plane shear response modeling"). Nonlinear fiber-section beam-elements are used to model reinforced concrete in vertical and horizontal directions. Unlike the BTM (Lu et al. 2014), which uses force-based elements (FBE, *forceBeamColumn*), the EBTM uses displacement-based elements (DBE, *dispBeamColumn*), since the numerical robustness of DBE, in general, is expected to be superior to that of FBE (Koutromanos and Bowers 2016). Except for the nodes of vertical beam-elements at boundary elements and corners, the nodes of all DBE have in-plane rotational releases, i.e., nodes in webs are released in R_x and nodes in flanges, and coupling beams are released in R_y. The nodal releases are modeled using the procedure proposed in Chapter 4, i.e., the reinforcement of each curtain is concentrated in corresponding fibers along the axis released in rotation, whereas the concrete is discretized in several perpendicular layers. *Truss2* elements are used to model the diagonal compression field of concrete. Sections of concrete and reinforcement in beam-elements and truss-elements are defined according to their tributary areas, (Lu et al. 2014), as shown in Figure 5.4, Detail 1. The inclination of diagonals is $\theta_d = tan^{-1}\,(V_{max}/(f_{y,t}\,\rho_t\,t_w\,d_{vl})) \leq 65°$, where V_{max} is the maximum resisted lateral force, $f_{y,t}$ is the yield stress of the transversal reinforcement, ρ_t is the transversal steel ratio, t_w is the thickness of the wall, and d_{vl} is the distance between the vertical outer lines in the EBTM, (Lu et al. 2014).

In the Fiber Model portion of the HyEBTM, each of the C-shaped walls is modeled using a single vertical line of nonlinear fiber-section beam-elements (stick-model). DBE

are also used in this case. The sections of the beam-elements are discretized in multiple fibers of confined and unconfined concrete, and reinforcement, according to the structural layout. The torsional rigidity of the stick-model is *0.1GJ*, $G = 0.38E_c$ is the shear modulus of the concrete, E_c is corresponding Young's modulus, and J is the torsional constant of the gross section. Rigid beam-elements (*elasticBeamColumn*) connect the stick-models at floor levels with the model of the coupling beams, which in turn connect both stick-models (Figure 5.4, Detail 3).

The coupling beams in the EBTM and the Fiber Model portions are modeled based on the Truss Model developed by Alvarez et al. (2019) (see section "HyEBTM for Case Study"). Slabs framing C-shaped walls and coupling beams are modeled at floor levels using elastic beam-elements (*elasticBeamColumn*).

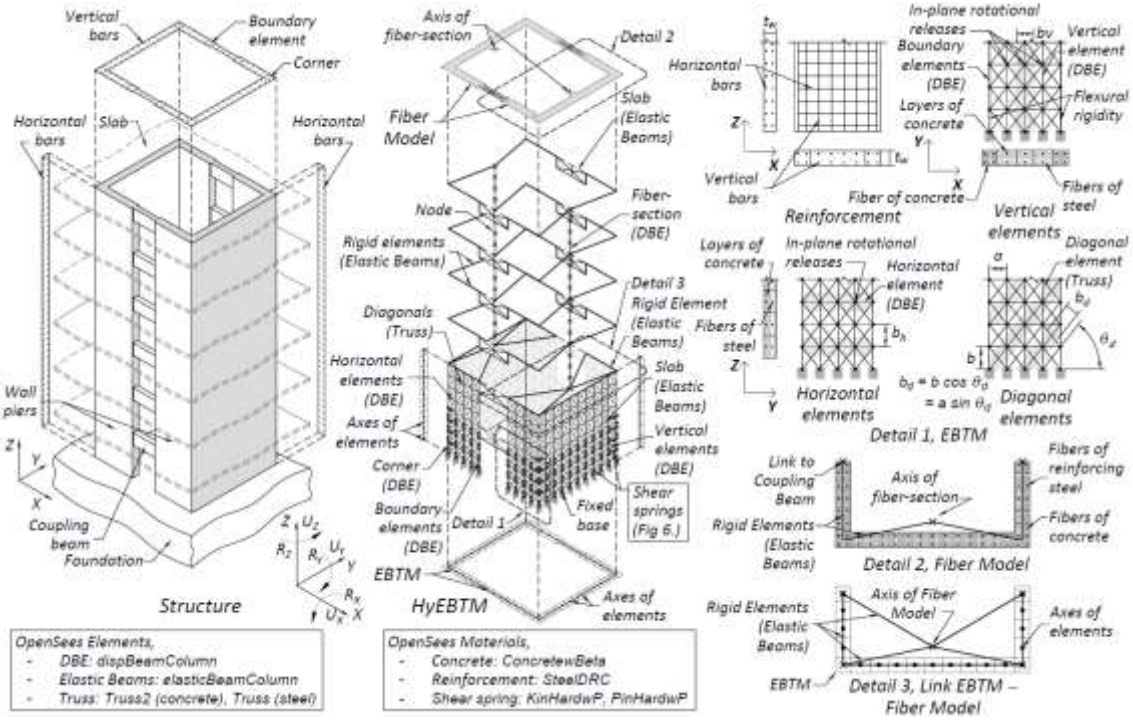

Figure 5.4. Description of the Hybrid Fiber-Section – Enhanced Beam-Truss Model.

The geometric properties of these elastic beam-elements are calculated using the tributary slab width. Axial rigidity is A_gE_c, where A_g is the gross area, in-plane flexural rigidity is $0.7E_cI_z$, out-of-plane flexure rigidity E_cI_y is assumed zero, and the torsional rigidity is $0.1GJ$.

All nodes at the HyEBTM base are fixed. Corotational geometric transformation is used in the truss-elements (*CorotTruss* and *CorotTruss2*), whereas PDelta transformation is used in the beam-elements (*geomTransf PDelta*). Two Gauss-Lobatto integration points are used in all DBE.

5.5.2 Material modeling

Concrete

The material *ConcretewBeta*, developed by Lu and Panagiotou (2013), is used to model unconfined and confined concrete in HyEBTM (Figure 5.5a). If the *ConcretewBeta* parameters are unknown, the stress-strain relations of the concrete materials are calibrated as follows.

Young's modulus of concrete is $E_c = 3220\sqrt{f'_c} + 6900$ (MPa), and strain at the compressive strength of the concrete is $\varepsilon_o = 0.0008k_3 - 0.0028$, where k_3 is $40/f'_c$ (MPA), as proposed by Razvi and Saatcioglu (1999). The strain at crushing is,

$$\varepsilon_{cu} = {}^{0.8f'_c}\!/_{E_c} + \varepsilon_o - {}^{G_{fc}}\!/_{0.6f'_c L_e} \leq 3\varepsilon_o \tag{5.1}$$

Which is a regularized value dependent on the length of the element L_e (mm) and the fracture energy in compression G_{fc} (N/mm), as proposed by Coleman and Spacone (2001). G_{fc} is 87.6 N/mm (Ugalde et al. 2019). Maximum $\varepsilon_{cu} = 3\varepsilon_o$ (Arteta et al. 2019) is set to avoid an excessive steep slope for the degrading branch.

In the vertical beam-elements of wall piers, the direct tensile strength of the concrete f_t is $0.55f_r$, where f_r is the modulus of rupture (Collins and Mitchell 1997). If the f_r is unknow, f_t is assumed $0.33\sqrt{f'_c}$ (MPa) (Lu and Panagiotou, 2013). *ConcretewBeta* option to calculate tension stiffening with the model developed by Stevens et al. (1991) is used. In the horizontal beam-elements of wall piers, vertical beam-elements of coupling beams, and diagonal truss-elements, the direct tensile strength of concrete is assumed zero according to Lu et al. (2014), a dummy value of $f_{td} = 0.01f_t$ is used here; in other locations $f_{td} = f_t$. The parameter *alpha*, which controls the path of unloading from tensile strain, is $0.045f'_c/f_{td}$.

The compressive strength of the confined concrete f_{cc} (MPa) and the corresponding strain ε_{co} are defined as proposed by Razvi and Saatcioglu (1999). The strain at the onset of softening is $\varepsilon_{cs} = \varepsilon_o - k_e f_l/9f'_c$, where k_e is the coefficient of efficiency of the confinement and f_l is the confining stress (Alvarez et al. 2019). The strain at the crushing of confined concrete is,

$$\varepsilon_{ccu} = {0.8f'_{cc}}/{E_c} + \varepsilon_{co} - {G_{fcc}}/{0.6f'_{cc}L_e} \leq \varepsilon_{cs} + 2\varepsilon_{co} \tag{5.2}$$

Where corresponding fracture energy in compression is $G_{fcc} = 87.6 \leq (f_{cc}/f'_c - 0.85) \leq 219$ (N/mm) (Ugalde et al. 2019). A limit for ε_{ccu}, i.e., $\varepsilon_{cs}+2\varepsilon_{co}$, is used to increase numerical robustness.

In the EBTM portion and the coupling beams, *ConcretewBeta* is used along with *Truss2* elements to model the effect of the biaxial strains field on the compressive stresses of the concrete in the diagonal directions (Vecchio and Collins 1986, Hsu and Mo 2010). A gauge-element, defined with each *Truss2* element, measures the perpendicular strains ε_n

(Figure 5.5b). Current strains are used to modify the compressive stresses of the concrete via the compressive strength reduction factor β. For $\varepsilon_n \leq 0$ β is 1, and for $\varepsilon_n > 0$, a trilinear relation $\beta - \varepsilon_n$ is used. Intermediate and residual β values are chosen similar to test values reported by Hsu and Mo (2010), i.e., $\beta_{int} = 0.45f_2$, and $\beta_{res} = 0.25f_2$, respectively, where $f_2 = 5.8\sqrt{f'_c}$ (MPa). Corresponding perpendicular tensile strains are $\varepsilon_{bint} = 0.01L_r/L_g$, and $\varepsilon_{bres} = 0.035L_r/L_g$, which are regularized values, as proposed by Panagiotou et al. (2012), dependent on the truss-element length L_g (mm), where the reference length L_r (test gauge-length) is 1500 mm (Hsu and Mo 2010). The numerical robustness of the models is enhanced using residual compressive strength, which for unconfined concrete is $-0.2f'_c$ and for confined concrete is $-0.2f'_{cc}$ (Alvarez et al. 2019).

Reinforcement

The uniaxial material *SteelDRC*, developed by Carreño (2018), is used to model the reinforcement. This material is an in-house OS implementation of the model proposed by Dodd and Restrepo-Posada (1995). *SteelDRC* explicitly models the yield plateau, the kinematic hardening, and the bar fracture. Coupon-test parameter values are used to calibrate the constitutive stress-strain relation, i.e., yield point (ε_y, f_y), point of onset of hardening (ε_{sh}, f_{sh}), point in hardening branch ($\varepsilon_{sh,1}$, $f_{sh,1}$), and point of ultimate strength (ε_u, f_u) (Figure 5.5c). When experimental information is not available, the constitutive stress-strain relation can be calibrated using recommended values, e.g., for steel ASTM A615, Young's modulus E_s = 200 GPa, yield stress f_y = 478 MPa, strain at the onset of hardening ε_{sh} = 0.011, ultimate strain in tension ε_u = 0.106, ultimate strength f_u = 769 MPa, and exponent of power function for hardening P_{sh} = 3.5 (Carreño 2018). *SteelDRC* also models the Bauschinger effect, which is controlled by the parameter Ω_{fac}. This parameter is

calibrated according to the carbon content of the steel; the recommended value for steel ASTM A615 is 0.83 (Carreño 2018).

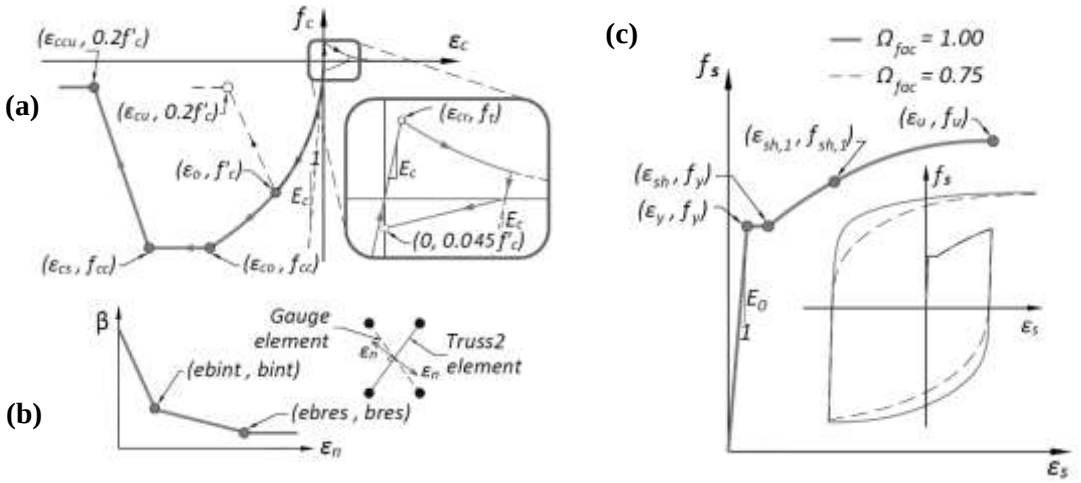

Figure 5.5. Constitutive material stress-strain relations. **(a)** Stress-strain relationship for *ConcretewBeta*. **(b)** Concrete compressive strength reduction factor β. **(c)** Stress-strain relationship for *SteelDRC*.

5.5.3 Out-of-plane shear response modeling

The out-of-plane nonlinear shear response of the wall piers is modeled via shear springs. Figure 5.6 shows a typical layout, including shear springs. Vertical beam-elements in the boundary elements and corners have bidirectional shear springs, with active DOF in U_x and U_y directions (Figure 5.6, Details 1, 2). Other vertical beam-element and horizontal beam-elements at the corners, only have out-of-plane shear springs, with active DOF in U_x and U_y directions, in webs and flanges, respectively (Figure 5.6, Details 3-5). The nodes at shear spring locations are connected through *zeroLength* elements. These elements use rigid materials (*Elastic*) in all directions except for those directions specified for the shear springs, which use *PinHardwP* material.

Uniaxial material *PinHardwP* is an in-house OS implementation developed to model nonlinear shear response dependent on axial force using shear springs. The axial

force in a control element (see the note in Figure 5.6) is monitored by the spring material to define the shear strength and the residual strength in the spring. Three branches form the backbone curve of *PinHardwP*, i.e., Elastic branch, Softening branch, and Residual branch. The backbone curve and hysteretic behavior of the material are shown in Figure 5.7. Stress-strain relations of the concrete materials are calibrated as follows.

The stiffness of the elastic branch, K_o, is GA_g/L_c, where G (MPa) is the shear modulus of the concrete (as calculated above), A_g is the gross area of the cross-section of the control element (mm^2), L_c is tributary length (mm), as proposed by LeBorgne (2012). Ultimate shear strength V_o is $f_{Vo} \cdot V_n$, where f_{Vo} is assumed 1.5 (Ugalde et al. 2019), and the nominal shear strength V_n is calculated adapting ACI 318-19 (2019) equations,

$$V_n = f_{Vc}\left(0.66\lambda_s \rho_w^{1/3} \sqrt{f'_c}\ (\text{MPa}) + {}^{N_u}\!/_{6A_g}\right) b_w d + f_{Vs} V_s \qquad (5.3)$$

Where the size effect modification factor λ_s is $\sqrt{2/(1 + 0.004d)} \leq 1$, if the area of transverse reinforcement A_v (mm^2) is larger than the minimum specified $A_{v,min}$ (ACI 318-19, 9.6.3.4), and $\lambda_s = 1$, if it is not, ρ_w is the longitudinal steel ratio, N_u is the axial load (N), b_w is the width of the cross-section (mm), and d is the effective depth (mm). f_{Vc} is a factor ≤ 1, which considers the interaction of shear forces acting in-plane and out-of-plane on the shear strength contribution of concrete. For unidirectional lateral loading, e.g., monotonic or cyclic pushover analysis, f_{Vc} is assumed 1, whereas in multidirectional lateral loading, e.g., NLRHA, f_{Vc} is assumed 0.5.

Shear reinforcement strength, V_s, is $A_v f_{y,t} d/s$, where $f_{y,t}$ is the yield strength of transverse reinforcement (MPa), and s is the spacing of the transverse reinforcement.

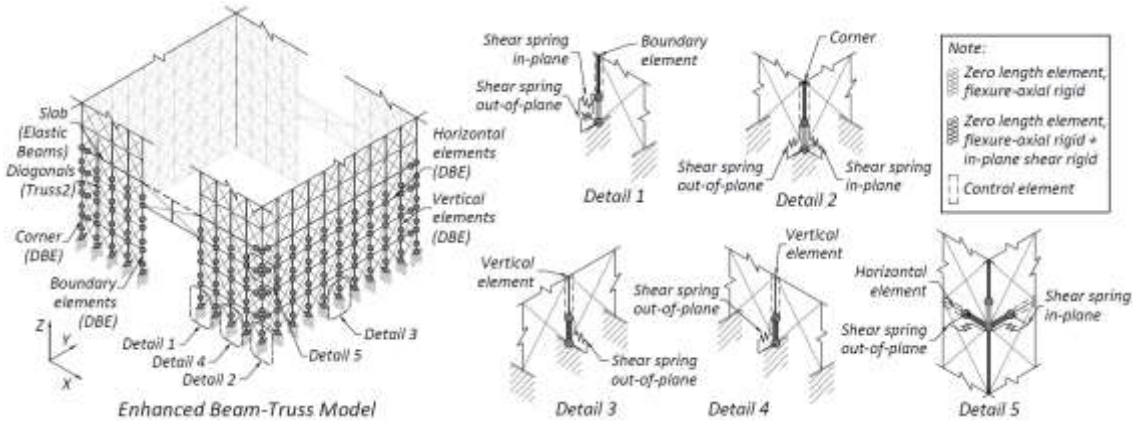

Figure 5.6. Out-of-plane shear response modeling.

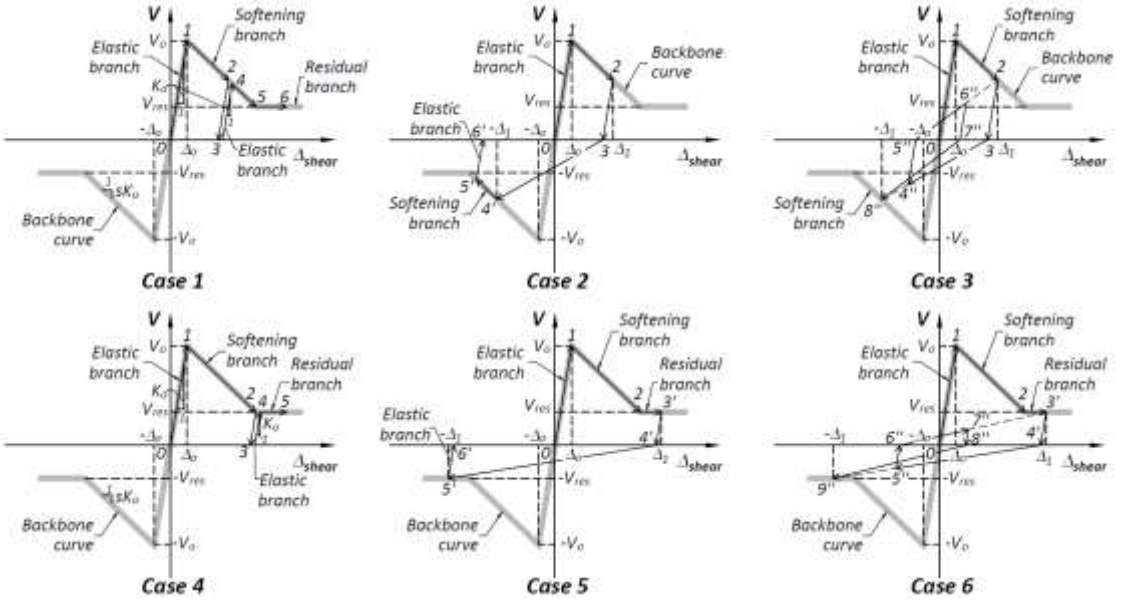

Figure 5.7. Stress-strain relation for *PinHardwP* material.

f_{Vs} is a factor ≤ 1, which considers the efficiency of shear reinforcement; f_{Vs} is assumed 0.75. The minimum shear strength is $V_{n\ min} = f_{Vs} \cdot V_s$, whereas maximum shear strength $V_{n\ max}$ is $f_{Vc} \cdot V_{c\ max} + f_{Vs} \cdot V_s$, where $V_{c\ max}$ is the minimum of $f_{Vc} \cdot (0.42\sqrt{f'_c}\ (\text{MPa})) \cdot b_w\ d$ and $f_{Vc} \cdot (0.66\lambda_s \rho_w^{1/3} \sqrt{f'_c} (\text{MPa}) + 0.05 f'_c) \cdot b_w\ d$, (ACI 318-19 2019).

Calibration parameters for the softening and the residual branches are calculated according to LeBorgne (2012). The slope of the softening branch is $sK_o = -V_o/\Delta_r$, the residual deformation Δ_r (mm) is,

$$\Delta_r = \left(-0.16 - 15.4\rho_t - {0.009l_d}/{d_b} + {0.7A_{cc}}/{A_g} + {0.58f_yA_s}/{f'_cA_g}\right)L \geq 0.02L \quad (5.4)$$

Where ρ_t is the transversal steel ratio, l_d is the development length of the longitudinal reinforcement, d_b is the corresponding bar diameter, A_{cc} is the confined area, and L is the wall pier span (mm). Finally, the residual shear strength, V_{res}, is $(0.36 - 0.17s/d)\cdot V_o$.

5.6 Hybrid Fiber-Section – Enhanced Beam-Truss Model for case study

A built in-house executable of the open-source FEM program OpenSees 2.5.0 64-bit (OS) (McKenna 2019) was used to develop the HyEBTM of the case study. Uniaxial materials *SteelDRC* (Carreño 2018) and *PinHardwP*, as well as HDF5 libraries of the GUI STKO (Petracca et al. 2017a, Petracca et al. 2017b), were included in the executable. OS input was created semi-automatically from TCL scripts, whereas the output was post-processed using MATLAB (MathWorks 2018) and STKO. A workstation fitted with dual CPU Intel Xeon Gold 6136 and 64GB RAM was used to run the model.

The HyEBTM included only the Core Wall of the case study building, and it was assumed that the gravity system, not included in the model, resists by itself the PDelta effect of its tributary vertical load. Figure 5.8 shows the layout of the HyEBTM and the key material properties of the concrete and reinforcing steel used. The first three stories in

the HyEBTM are modeled using EBTM, and the rest of the stories are modeled using Fiber Model.

Grid size in the EBTM portion is selected to satisfy, as close as possible, the required inclination of the diagonal truss-elements (Lu et al. 2014), and the geometry of boundary elements and couplings beams. The grid of the webs forms 15 equal horizontal quadrilaterals (Figure 5.8, Elevation West), whereas the grid of flanges forms 6 equal horizontal quadrilaterals (Figure 5.8, Elevation South). Each story has 4 equal quadrilaterals in the vertical direction. This results in inclinations of the diagonal truss-elements equal to 62° in flanges and webs.

Vertical beam-elements at boundary elements and corners have biaxial flexural rigidity, the sections of these beam-elements are discretized using 10 by 10 concrete fibers and 10 steel fibers in the actual location of longitudinal bars. The rest of beam-elements only have out-of-plane flexural rigidity, which is accomplished in the vertical beam-elements with sections using 10 layers of the concrete perpendicular to the out-of-plane direction and 2 steel fibers on the centroidal axis parallel to the out-of-plane direction (Figure 5.8, Sec-1a, 1b). A similar discretization is used in the sections of horizontal beam-elements (Figure 5.8, Sec-vx, vy).

The out-of-plane nonlinear shear response is modeled in the first story in vertical beam-elements and horizontal beam-elements at the corners (Figure 5.8, Elevation West, and South), as described in the previous section.

The coupling beams in the HyEBTM are modeled using BTM, similar to Alvarez et al. (2019). Grid size in the coupling beams is selected according to the inclination of actual diagonal reinforcement and grid size of the panel zone of the wall piers in the EBTM.

This results in a grid of 2 by 2 quadrilaterals and inclination of the diagonal truss-elements equal to 65°, which is the upper bound for θ_d (Lu et al. 2014). Concrete in the diagonal direction is modeled using *Truss2* elements, whereas the diagonal reinforcement is modeled using *Truss* elements. Rigid offsets are used, in the EBTM, to adjust the beam span of the model to the actual length of the coupling beam. The protruding diagonal reinforcement is anchored in the grid of the wall piers using rigid beam-elements (*elasticBeamColumn*) with pinned connections (Figure 5.8, Detail 1).

Each C-shaped wall at the Fiber Model portion is modeled using stick-models, discretized in five vertical beam-elements (DBE) in each story (Figure 5.8, Elevation West, and South). The beam-elements have sections using multiple fibers. Corners and toes of the flanges are modeled using 10 by 10 and 8 by 8 concrete fibers in Story 4-5 and Story 6-14, respectively, and steel fibers in the actual location of longitudinal bars (Figure 5.8, Sec-1b', 2, 3).In Story 4-5, the field of webs and flanges are discretized using 10 by 108 and 10 by 37 fibers of concrete, respectively (Figure 5.8, Sec-1b'), whereas in Story 6-14, webs and flanges are discretized in 8 by 103 and 8 by 37 fibers of concrete, respectively (Figure 5.8, Sec-2, 3). The longitudinal reinforcement is modeled using multiple fibers equally spaced at the location of the actual reinforcement curtains. Rigid beam-elements (*elasticBeamColumn*) are used to connect the stick-models with the BTM of the coupling beams in each level (Figure 5.8, Elevation West, and South).

The connection between the EBTM and Fiber Model is shown in Sec-L1 (Figure 5.8). Slabs framing the C-shaped walls and coupling beams are modeled as explained in the previous section. Gravitational loads were applied as tributary nodal forces at every floor level. The solution strategy used *LoadControl* integrator. An in-house TCL script was

developed to automatically change the type of *algorithm* and *test*, and to adjust the *test* parameters: maximum number of iterations *iter*, and tolerance criteria *tol*, to attain convergence.

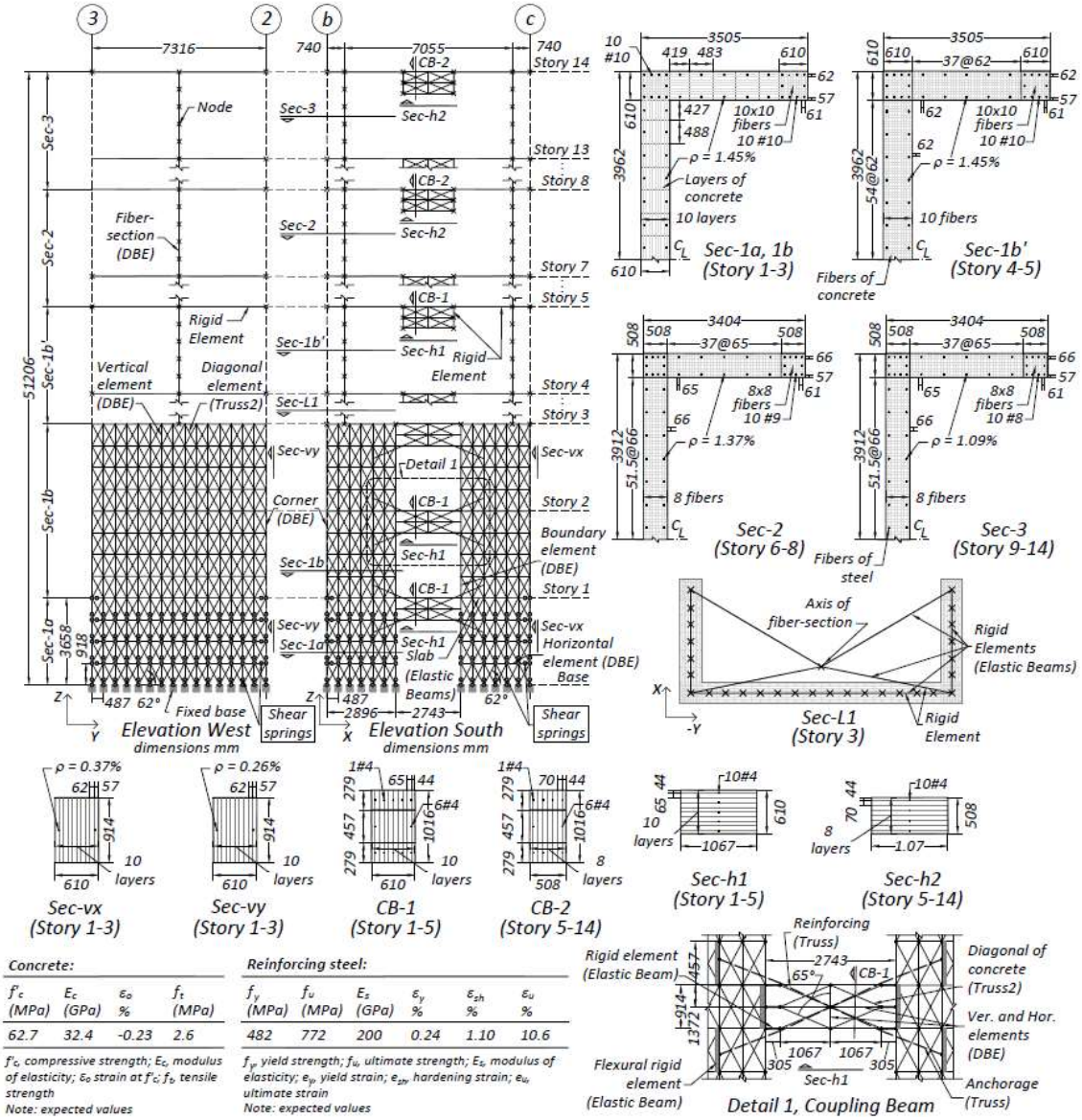

Figure 5.8. Core Wall case study building, Hybrid Fiber-Section – Enhanced Beam-Truss Model.

5.7 Nonlinear static analysis

5.7.1 Description of case studies

Three different types of models of the Core Wall case study building were created for nonlinear static analyses, i.e., Fiber Model, Hybrid Fiber-Section – Beam-Truss Model (HyBTM), and HyEBTM.

In the Fiber Model, the Core Wall was modeled all along with the height as described above for the Fiber Model portion of the HyEBTM, including the first three stories, whereas the HyBTM was equal to the HyEBTM, except that in the former, the out-of-plane nonlinear shear response was not included. The Fiber Model and the HyBTM were used as benchmarks to evaluate the HyEBTM. Two HyEBTM cases were run to study the influence of the out-of-plane shear strength on the lateral response. The first case, *HyBTM10*, assumed $f_{Vo} = 1$, $f_{Vc} = 1$ and $f_{Vs} = 0.75$, and the second, *HyBTM15*, assumed $f_{Vo} = 1.5$, $f_{Vc} = 1$ and $f_{Vs} = 1$.

Additional to gravity loading, the models were subjected to monotonic displacement-control lateral loading in X and Y-direction. Two load patterns were used, i.e., 1st mode shape and triangular with resultant at H/3, where H is the total height. The resultant set of case studies is listed in Table 5-3.

DisplacementControl integrator was used in the solution strategy with a TCL script that, like with *LoadControl* integrator, automatically adjusted *algorithm*, *test*, *iter*, *tol*, and additionally, the increment of displacement, *incr*. The solver used was *SparseSYM*, and the method to impose constraints was *Transformation*. Tributary lateral forces were applied at every floor level, and the displacements were controlled at the top of the model. The models were intended to run up to top drift ratio $\Theta = 4.9\%$ (2500 mm) for 1st mode shape load

pattern and up to Θ = 3.9% (2000 mm) for triangular load pattern. Some models stopped before the corresponding target when very steep degradation was captured.

Table 5-3. Nonlinear static analysis cases.

Case Name	Type of Model	Load Pattern	fV_o	fV_c	fV_s	Loading Direction
Fiber-Model-1st-X	Fiber Model	1st mode	-	-	-	X
Fiber-Model-1st-Y	Fiber Model	1st mode	-	-	-	Y
Fiber-Model-1/3-X	Fiber Model	Triangular	-	-	-	X
Fiber-Model-1/3-Y	Fiber Model	Triangular	-	-	-	Y
HyBTM-1st-X	HyBTM	1st mode	-	-	-	X
HyBTM -1st-Y	HyBTM	1st mode	-	-	-	Y
HyBTM -1/3-X	HyBTM	Triangular	-	-	-	X
HyBTM -1/3-Y	HyBTM	Triangular	-	-	-	Y
HyEBTM10-1st-X	HyEBTM	1st mode	1	1	0.75	X
HyEBTM10-1st-Y	HyEBTM	1st mode	1	1	0.75	Y
HyEBTM10 -1/3-X	HyEBTM	Triangular	1	1	0.75	X
HyEBTM10 -1/3-Y	HyEBTM	Triangular	1	1	0.75	Y
HyEBTM15-1st-X	HyEBTM	1st mode	1.5	1	1	X
HyEBTM15-1st-Y	HyEBTM	1st mode	1.5	1	1	Y
HyEBTM15 -1/3-X	HyEBTM	Triangular	1.5	1	1	X
HyEBTM15 -1/3-Y	HyEBTM	Triangular	1.5	1	1	Y

5.7.2 Results of Fiber-Model

Figure 5.9a shows a comparison of the base shear force – top displacement (F–D) for the different Fiber Models. The peak base shear V_{max} for *Fiber-Model-1/3-X* was $0.70A_{cv}\sqrt{f'_c}$ (MPa), which is 95% larger than the V_{max} for *Fiber-Model-1st-X*. For *Fiber-Model-1/3-Y*, V_{max} was $0.62A_{cv}\sqrt{f'_c}$ (MPa), 120% larger than the corresponding value for *Fiber-Model-1st-Y*. V_{max} for *Fiber-Model-1/3-X* and *Fiber-Model-1/3-Y* exceeded by 41% and 26%, respectively, the shear force limit of the ACI 318-19 (ACI 318-19, 2019), i.e., $V_{ave\text{-}ACI\text{-}limit} = \phi \cdot 0.66A_{cv}\sqrt{f'_c}$ (MPa), where ϕ is 0.75. All models maintained the capacity throughout the analysis, except for *Fiber-Model-1/3-Y*, which exhibited steep degradation at Θ = 3.6%, because of bar fracture.

Cases with lateral loading in X-direction exhibited the earliest yielding in tension at the base longitudinal reinforcement. In *Fiber-Model-1/3-X* first yielding occurred at Θ = 0.17%, whereas in *Fiber-Model-1st-X* this was at Θ = 0.3%. Yielding of longitudinal reinforcement at Story 6, where section and steel ratio are decreased, occurred only in *Fiber-Model-1st-X* and *Fiber-Model-1st-Y*, at Θ = 1.9% in both cases; however, plastic hinges were not developed at that story.

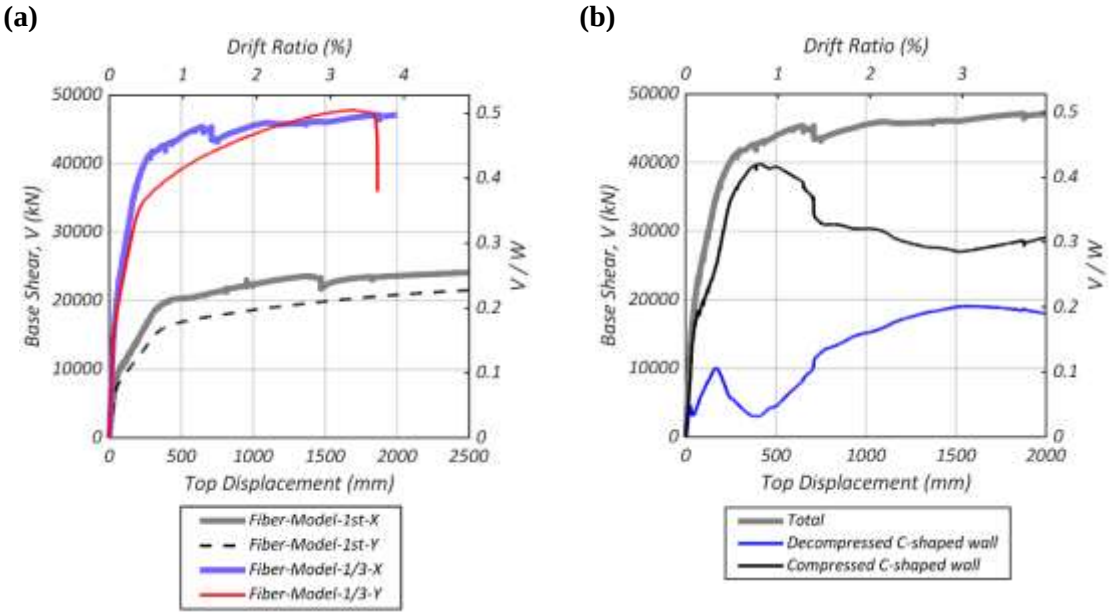

Figure 5.9. (a) Comparison of base shear force – top displacement for the Fiber Model. **(b)** Decomposition of base shear force for *Fiber-Model-1/3-X*.

The earliest onset of softening in the core concrete occurred in *Fiber-Model-1/3-X* and *Fiber-Model-1st-X*, at Θ = 0.76% and 1.6%, respectively, whereas corresponding concrete crushing occurred at Θ = 1.3% and 2.7%. First yielding in diagonal reinforcement of the coupling beams occurred at Θ = 0.33% at level 2, and Θ = 2.1% at level 6, in *Fiber-Model-1/3-X* and *Fiber-Model-1st-X*, respectively. In *Fiber-Model-1/3-X*, the yielding of

diagonal reinforcement spread at Stories 1-6, whereas in *Fiber-Model-1st-X*, this spread at Stories 1-9.

Figure 5.9b shows the decomposition of the base shear force for *Fiber-Model-1/3-X*. Most of the base shear was resisted by the compressed C-shaped wall, which resisted up to $1.2A_{cv}\sqrt{f'_c}$ (MPa), 92% of the base shear. This shear force exceeded by 93% the limit in the ACI 318-19 (2019), i.e., $V_{pier\text{-}ACI\text{-}limit} = \phi \cdot 0.83A_{cv}\sqrt{f'_c}$ (MPa), where ϕ is 0.75.

5.7.3 Results of Hybrid BTM

F–D responses of the HyBTM for 1st mode shape and triangular load patterns are shown in Figures 5.10 and 5.11, respectively (labeled "Total"). V_{max} for *HyBTM-1/3-X* was $0.6A_{cv}\sqrt{f'_c}$ (MPa) (Figure 5.11a), 68% larger than the corresponding value for *HyBTM-1st-X* (Figure 5.10a). The F–D response of *HyBTM-1/3-X* exhibited degradation; V_{max} occurred at Θ = 0.9%, whereas for *HyBTM-1st-X*, the base shear force increased throughout the analysis. A similar situation was observed for lateral loading in Y-direction. For *HyBTM-Model-1/3-Y*, the F–D response exhibited degradation after attained V_{max}, i.e., $0.46A_{cv}\sqrt{f'_c}$ (MPa), at Θ = 1.4% (Figure 5.11b), whereas for *HyBTM-Model-1st-Y*, V_{max} was considerable smaller, $0.25A_{cv}\sqrt{f'_c}$ (MPa), and the response did not exhibit degradation (Figure 5.10b). The code limit $V_{ave\text{-}ACI\text{-}limit}$ was only exceeded by *HyBTM-1/3-X*, where the V_{max} was 21% larger than the limit.

Figures 5.10 and 5.11 also show the decomposition of the base shear force. At V_{max}, most of the base shear force was resisted by the compressed flanges in *HyBTM-1st-X* and *HyBTM-1/3-X*, and by the webs in *HyBTM-1st-Y* and *HyBTM-1/3-Y*. The compressed flanges resisted 62% of the V_{max} in *HyBTM-1st-X*, and the rest of the shear force was resisted in similar portions by the decompressed flanges and the webs (Figure 5.10a). In

HyBTM-1st-Y, 72% of the V_{max} was resisted by the webs, whereas the compressed and the decompressed flanges resisted 15% and 13%, respectively.

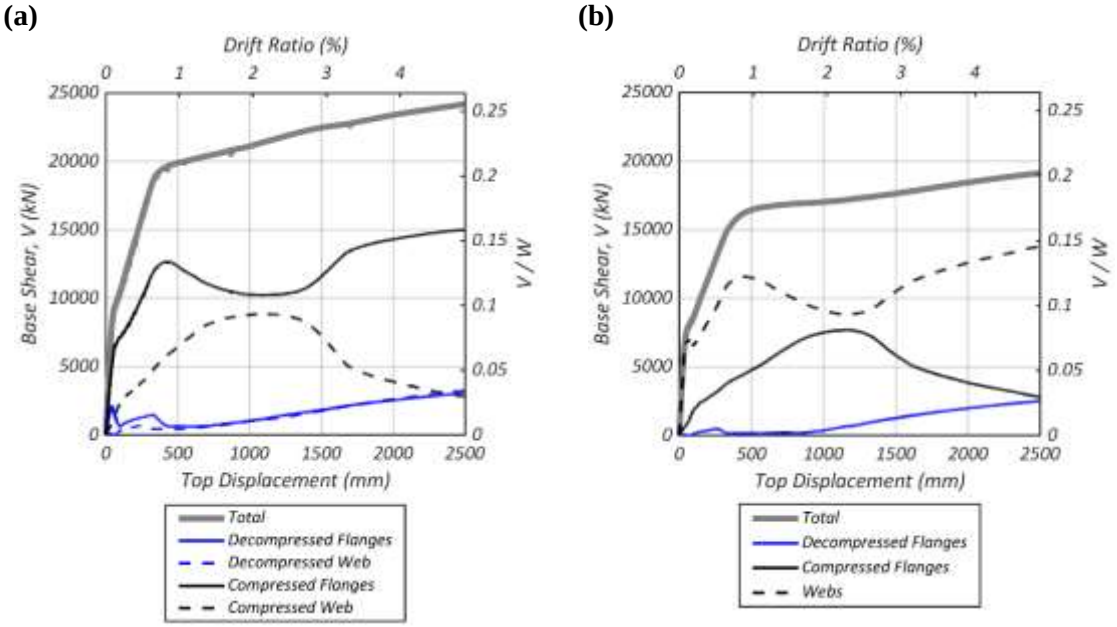

Figure 5.10. Decomposition of base shear force. **(a)** *HyBTM-1st-X*. **(b)** *HyBTM-1st-Y*.

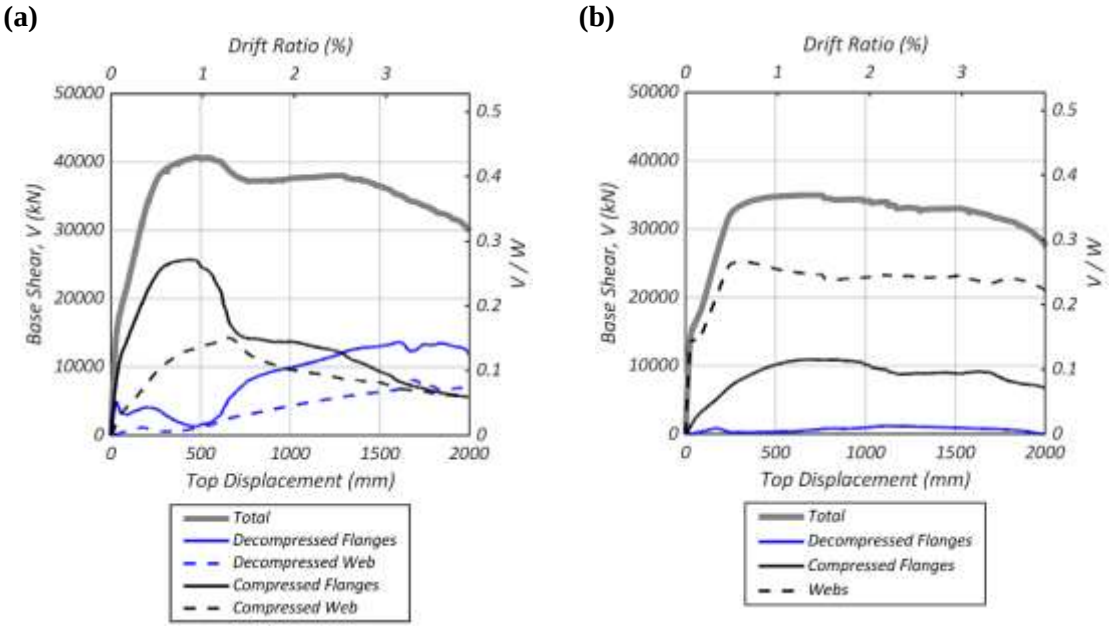

Figure 5.11. Decomposition of base shear force. **(a)** *HyBTM-1/3-X*. **(b)** *HyBTM-1/3-Y*.

For *HyBTM-1/3-X*, the maximum shear force in the compressed flanges occurred at the same time as V_{max}, at Θ = 0.9%, and it was $0.76A_{cv}\sqrt{f'_c}$ (MPa) (Figure 5.11a). The shear force resisted by the compressed flanges was 63% of the base shear force, which exceeded $V_{pier\text{-}ACI\text{-}limit}$ by 22%. At the same drift, the compressed web resisted 31% of the base shear force. As the compressed flanges exhibited a steep degradation, the shear resisted by the compressed web kept increasing, peaking at $0.5b_w d\sqrt{f'_c}$ (MPa), where b_w is the width of the member, and d is the effective depth. In *HyBTM-1/3-Y*, the maximum shear force resisted by the webs was $0.33A_{cv}\sqrt{f'_c}$ (MPa), at Θ = 0.6%, whereas the maximum shear force resisted by the compressed flanges was $0.44b_w d\sqrt{f'_c}$ (MPa), at V_{max}, Θ = 1.4% (Figure 5.11b). At this drift, the webs resisted 67% of the base shear force, and the compressed flanges 31%.

The onset of yielding in tension in longitudinal reinforcement at the base was computed first for *HyBTM-1/3-X* and *HyBTM-1st-X*. First yielding occurred for *HyBTM-1/3-X* in the toes of the compressed C-shaped wall (boundary elements), at Θ = 0.23%, and for *HyBTM-1st-X* in the decompressed corners, at Θ = 0.29%. Bar fracture was computed only for *HyBTM-1/3-X*, which occurred at Θ = 3.3%. Yielding of longitudinal reinforcement at Story 6 was computed for *HyBTM-1st-X*, at Θ = 2.7%. Throughout the analysis, the longitudinal strains were smaller than 0.0061, and plastic hinging did not occur at that story in any case.

First yielding of horizontal reinforcement occurred for *HyBTM-1/3-X*, *HyBTM-1/3-Y*, *HyBTM-1st-X*, and *HyBTM-1st-Y at* Θ = 0.68%, 0.45%, 2.6% and 1.3%, respectively. The largest values of horizontal strains were computed for *HyBTM-1/3-X*, *HyBTM-1/3-Y*. In *HyBTM-1/3-X*, peak horizontal strain, i.e., 0.078, was located in the compressed flanges

close to the corner base, and, in *HyBTM-1/3-Y*, corresponding strain, i.e., 0.10, was located in the compressed end of the webs, close to the base.

The earliest yielding of diagonal reinforcement occurred for *HyBTM-1/3-X* in the coupling beams of Story 4 at Θ = 0.41%. The yielding spread to coupling beams at Stories 1, 3-5. Except for the strains in the coupling beams at Story 1 in *HyBTM-1/3-X*, with peak strain equal to 0.023, the strains of diagonal reinforcement stayed in the yield plateau.

The earliest core concrete softening and crushing, in the vertical direction, occurred at the base of compressed corners in the models using triangular load patterns. First concrete softening for *HyBTM-1/3-X* was at Θ = 0.67%, whereas first crushing occurred at Θ = 1.1%; for *HyBTM-1/3-Y*, corresponding drift ratios were 0.9% and Θ = 1.5%. Concrete softening in the diagonal direction occurred for *HyBTM-1/3-X*, *HyBTM-1/3-Y*, *HyBTM-1st-X*, and *HyBTM-1st-Y at* Θ = 0.93%, 1.5%, 4.8% and 4.7%, respectively, whereas concrete crushing occurred for *HyBTM-1/3-X* and *HyBTM-1/3-Y* at Θ = 1.2% and 2%, respectively, no concrete crushing was computed for *HyBTM-1st-X* and *HyBTM-1st-Y*.

5.7.4 Results of Hybrid Enhanced BTM

HyEBTM10

F–D responses of *HyEBTM10-1st-X* and *HyEBTM10-1st-Y* (Figure 5.12) were very similar to the corresponding responses of *HyBTM-1st-X* and *HyBTM-1st-Y* (Figure 5.10). Since *HyEBTM10-1st-X* and *HyEBTM10-1st-Y* did not exhibit degradation, V_{max} in both cases was computed at the end of the analyses, i.e., Θ = 4.9%. For *HyEBTM10-1st-X* V_{max} was $0.35A_{cv}\sqrt{f'_c}$ (MPa), and for *HyEBTM10-1st-Y* it was $0.25A_{cv}\sqrt{f'_c}$ (MPa). *HyEBTM10-1/3-X* and *HyEBTM10-1/3-Y* computed peak base shear force at Θ = 0.9%. V_{max} for *HyEBTM10-1/3-X* was $0.58A_{cv}\sqrt{f'_c}$ (MPa) (Figure 5.13a), 17% larger than V_{ave}-

$_{ACI\text{-}limit}$, and V_{max} for *HyEBTM10-1/3-Y* was $0.45A_{cv}\sqrt{f'_c}$ (MPa) (Figure 5.13b). The F–D response of *HyEBTM10-1/3-X* exhibited steep degradation, and the analysis stopped at Θ = 1.4%. Softening in *HyEBTM10-1/3-Y* was initially gradual; however, at Θ = 2.7%, the response exhibited very steep degradation, and the analysis stopped at Θ = 2.8%.

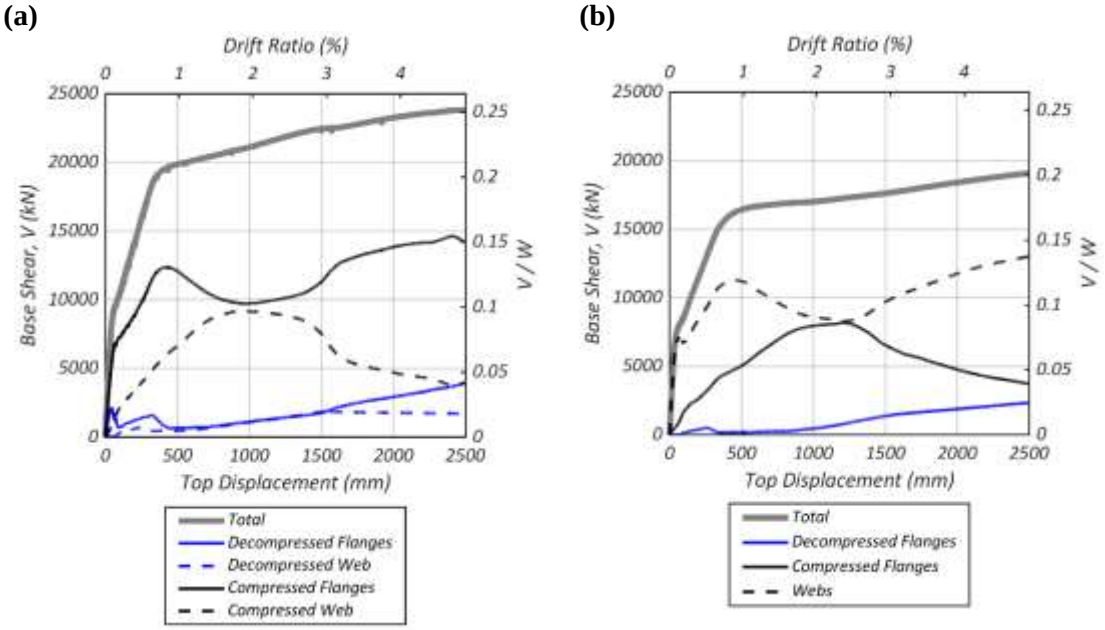

Figure 5.12. Decomposition of base shear force. **(a)** *HyEBTM10-1st-X*. **(b)** *HyEBTM10-1st-Y*.

The decompositions of base shear forces for *HyEBTM10-1st-X* and *HyEBTM10-1st-Y* (Figure 5.12) were very similar to corresponding results for *HyBTM-1st-X* and *HyBTM-1st-Y* (Figure 5.10). The most notorious difference occurred in the apportioning of base shear resisted by the decompressed webs in *HyEBTM10-1st-X* and *HyBTM-1st-X*. The shear force of the decompressed web steadily increased for *HyBTM-1st-X*, whereas the shear force resisted in *HyEBTM10-1st-X* peaked at Θ = 2.9%. For *HyEBTM10-1/3-X*, the maximum shear force in the compressed flanges, i.e., $0.73A_{cv}\sqrt{f'_c}$ (MPa), occurred at Θ = 0.6% (Figure 5.13a), which exceeded $V_{pier\text{-}ACI\text{-}limit}$ by 17%. Very steep response degradation

was exhibited by the compressed flanges, which ended up losing 78% of the strength. As the compressed flanges degraded, the shear force resisted by the compressed web peaked at $0.6b_w d\sqrt{f'_c}$ (MPa). At V_{max}, the shear force resisted by the compressed flanges was 57%, the compressed web resisted 32%, the decompressed flanges 8%, and the decompressed web 3%. By the end of the analysis, the shear force resisted by the decompressed flanges peaked, resisting 45% of the base shear force, then, their response suddenly dropped, while all other components exhibited softening and the analysis stopped. The maximum shear force resisted by the webs in *HyEBTM10-1/3-Y*, i.e., $0.33A_{cv}\sqrt{f'_c}$ (MPa), occurred at Θ = 0.6%, whereas the maximum shear force resisted by the compressed flanges was $0.51b_w d\sqrt{f'_c}$ (MPa), and it occurred at Θ = 1.6% (Figure 5.13b).

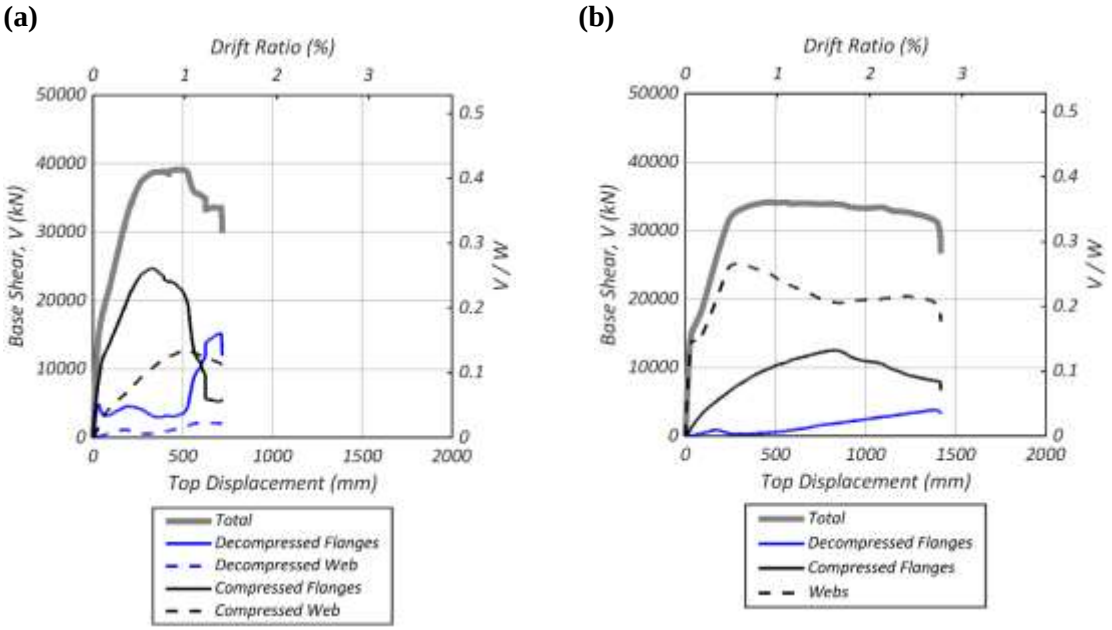

Figure 5.13. Decomposition of base shear force. **(a)** *HyEBTM10-1/3-X*. **(b)** *HyEBTM10-1/3-Y*.

At V_{max}, the shear force resisted for the webs was 57%, for the compressed flanges 29%, and for the decompressed flanges 14%.

The earliest yielding of longitudinal reinforcement at Story 1 occurred in *HyEBTM10-1/3-X* and *HyEBTM10-1/3-Y*. For *HyEBTM10-1/3-X*, first yielding in tension was at Θ = 0.2%, in the boundary elements of the compressed C-shaped wall, whereas the first yielding in compression was at Θ = 0.59%, in the compressed corners. In *HyEBTM10-1/3-Y*, the decompressed corners exhibited first yielding in tension at Θ = 0.28. Plastic hinging did not occur in upper stories, and bar fracture was not computed in any case.

First yielding of horizontal reinforcement in *HyEBTM10-1st-X* and *HyEBTM10-1st-Y* occurred at 0.83% and 1.08%, respectively, whereas in *HyEBTM10-1/3-X* and *HyEBTM10-1/3-Y* this was at Θ = 0.26% and 0.3%. The largest horizontal strains were computed for *HyEBTM10-1/3-X* and *HyEBTM10-1/3-Y*, i.e., 0.11. In *HyEBTM10-1st-X*, the peak strain was 0.018, and, in *HyEBTM10-1st-Y* corresponding strain was 0.011. Peak horizontal strains were located in the compressed flanges close to the corner base for *HyEBTM10-1st-X* and *HyEBTM10-1/3-X*, and, in the compressed end of the webs, for *HyEBTM10-1st-Y* and *HyEBTM10-1/3-Y*.

In *HyEBTM10-1/3-X*, yielding of diagonal reinforcement occurred only in the coupling beams of Story 4, at Θ = 0.41%. However, the diagonal reinforcement of coupling beams in other lower stories, i.e., 1-6, was close to yielding, the peak strains in these cases were at least 0.0018. For *HyEBTM10-1st-X*, the first yielding of diagonal reinforcement occurred in the coupling beams of Story 4, at Θ = 0.41%. The yielding spread to coupling beams at Stories 4-8; in all cases, the peak strains stayed in the yield plateau.

First softening of core concrete in the vertical direction, for *HyEBTM10-1st-X*, *HyEBTM10-1st-Y* and *HyEBTM10-1/3-Y*, occurred at Θ = 2.4%, 2.3% and 1.6%, respectively. Corresponding concrete crushing occurred at Θ = 3.2%, 3.1% and 1.9%. No

softening of core concrete was computed for *HyEBTM10-1/3-X*. For lateral loading in X-direction, peak vertical strain in compression, i.e., -0.027, was computed for *HyEBTM10-1st-X*. The smallest strains in these cases were located at the base of the compressed corners. In Y-direction, the smallest vertical strains were computed for *HyEBTM10-1/3-Y*, and these were located at the base of the boundary element. Peak strain in compression, in this case, was -0.032.

For *HyEBTM10-1/3-X*, *HyEBTM10-1/3-Y*, and *HyEBTM10-1st-X*, concrete softening in the diagonal direction occurred *at* Θ = 0.76%, 1.1% and 3.8%, respectively, whereas corresponding concrete crushing occurred for *HyEBTM10-1/3-X* and *HyEBTM10-1/3-Y* at Θ = 1.1% and 1.8%. No concrete softening was computed for *HyEBTM-1st-Y*, neither concrete crushing for *HyEBTM10-1st-X*. For lateral loading in the X-direction, the smallest diagonal strains were computed in *HyEBTM10-1st-X*, and these occurred in the compressed flanges at the base of the corners. Peak strain in compression, in this case, was -0.054. In Y-direction, peak diagonal strain in compression, i.e., -0.074, was computed for *HyEBTM10-1/3-Y*. The smallest strains were located in the compressed end of the webs at the base of the corners.

For lateral loading in the X-direction, the first softening of the shear response occurred at the corners' base of the compressed C-shaped wall, from there, softening gradually spread toward the center of the web. In *HyEBTM10-1/3-X*, the shear strength, V_o, was reached in the compressed corners at Θ = 0.1%, and corresponding residual strength V_{res} was reached at Θ = 1.2%, whereas in *HyEBTM10-1st-X*, V_o occurred at Θ = 0.27% and V_{res} was not reached.

The first softening of out-of-plane shear response in the compressed web occurred at $\Theta = 0.15\%$ and 0.54%, for *HyEBTM10-1/3-X* and *HyEBTM10-1st-X*, respectively. In the decompressed C-shaped wall, the softening of the shear response also spread from the corners' base to the center of the web. In *HyEBTM10-1st-X*, first V_o occurred at $\Theta = 0.29\%$, and, in *HyEBTM10-1st-X*, this occurred at $\Theta = 2\%$. The first softening of the shear response, for loading in Y-direction, occurred at the base of the compressed corners, and it spread to the center of the flanges. First V_o in *HyEBTM10-1/3-Y* was at $\Theta = 0.13\%$ and corresponding V_{res} at $\Theta = 1.6\%$. For *HyEBTM10-1st-Y*, first V_o occurred at $\Theta = 0.4\%$, and in this case, the response did not reach V_{res}.

In the compressed flanges, the first softening of out-of-plane shear response occurred at $\Theta = 0.20\%$ and 0.64%, for *HyEBTM10-1/3-Y* and *HyEBTM10-1st-Y*, respectively. In the decompressed side, the softening of the shear response also spread from the corners' base to the center of the flanges, V_o occurred at $\Theta = 2.5\%$ and 3.4% in *HyEBTM10-1st-Y* and *HyEBTM10-1st-Y*, respectively.

HyEBTM15

F–D responses of HyEBTM15 for 1st mode shape load patterns were almost identical to the corresponding responses of HyBTM (Figure 5.10) and HyEBTM10 (Figure 5.12). Moreover, the decompositions of base shear forces for *HyEBTM15-1st-X* and *HyEBTM15-1st* were very similar to computed responses for *HyBTM-1st-X* and *HyBTM-1st-Y*, respectively. Therefore, the following report mainly focuses on responses to the triangular load pattern (Figure 5.14).

For *HyEBTM15-1/3-X*, V_{max} was $0.60A_{cv}\sqrt{f'_c}$ (MPa) (Figure 5.14a), 21% larger than $V_{ave\text{-}ACI\text{-}limit}$. V_{max} for *HyEBTM15-1/3-Y* was $0.45A_{cv}\sqrt{f'_c}$ (MPa) (Figure 5.14b), which

resulted 10% smaller than the corresponding $V_{ave\text{-}ACI\text{-}limit}$ value. Peak base shear forces where computed at Θ = 1.1% and 1.2%, for *HyEBTM15-1/3-X* and *HyEBTM15-1/3-Y*, respectively. Initial degradation of *HyEBTM15-1/3-X* resulted in the loss of 11% of the strength at Θ = 1.6%. At Θ = 2.5%, the F–D response exhibited a second, very steep, event of degradation, which led to the loss of 80% of the strength at Θ = 3.6%, when the analysis stopped. Gradual softening after peaking was computed for *HyEBTM15-1/3-Y*; however, the F–D response exhibited very steep degradation at Θ = 3.1%, and the analysis stopped at Θ = 3.2%, with 20% loss of strength.

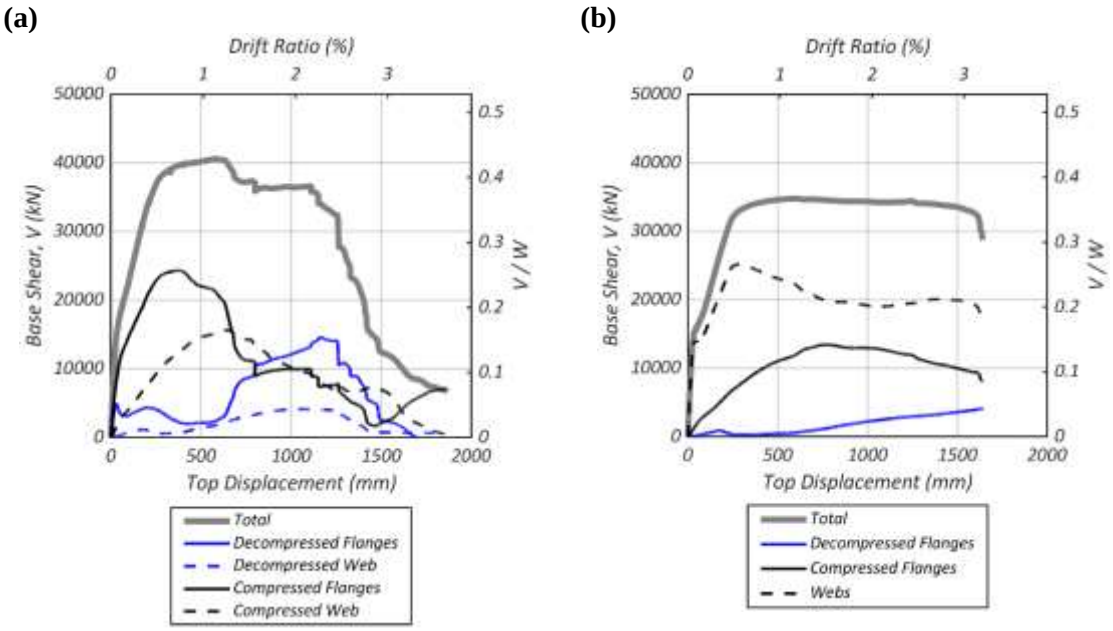

Figure 5.14. Decomposition of base shear force. **(a)** *HyEBTM15-1/3-X*. **(b)** *HyEBTM15-1/3-Y*.

For *HyEBTM15-1/3-X*, at V_{max}, the shear force resisted by the compressed flanges was 53%, the compressed web resisted 37%, the decompressed flanges 6% and the decompressed web 4%. The maximum shear force resisted by the compressed flanges was $0.72A_{cv}\sqrt{f'_c}$ (MPa), which exceeded $V_{pier\text{-}ACI\text{-}limit}$ by 16%. This peak occurred at Θ = 0.7%

(Figure 5.14a). The compressed flanges exhibited very steep degradation at Θ = 1.2%, and these lost up to 71% of the strength by the end of the analysis. The peak shear force resisted by the compressed web, i.e., $0.55 b_w d \sqrt{f'_c}$ (MPa) occurred at Θ = 1.3%, whereas the peak shear resisted by the decompressed flanges, i.e., $0.43 b_w d \sqrt{f'_c}$ (MPa), occurred at Θ = 2.3%. At this drift, the base shear force was $0.84 V_{max}$, and the largest portion was resisted by the decompressed flanges, i.e., 43%. Then, the shear response of the decompressed flanges suddenly dropped, while all other components exhibited softening, and the analysis stopped at 3.6%.

For in *HyEBTM15-1/3-Y*, at V_{max}, the shear force resisted by the webs was 64%, the compressed flanges resisted 34%, and the decompressed flanges 2%. The maximum shear force resisted by the webs and by the compressed flanges was $0.33 A_{cv} \sqrt{f'_c}$ (MPa) and $0.55 b_w d \sqrt{f'_c}$ (MPa), respectively (Figure 5.14b). Peak force for the webs occurred at Θ = 0.5%, and for the flanges at Θ = 1.5%.

In *HyEBTM15-1/3-X*, the first yielding in the longitudinal reinforcement in tension occurred in the boundary elements of the compressed C-shaped wall, at Θ = 0.21%, whereas the first yielding in compression occurred in the compressed corners, at 0.38%. For *HyEBTM15-1/3-Y*, first yielding in tension occurred in the decompressed corners, at Θ = 0.29%, and the first yielding in compression occurred in the compressed corners, at Θ = 0.44%. Bar fracture was not computed in any case, and plastic hinging did not occur in upper stories.

First yielding of horizontal reinforcement for *HyEBTM15-1/3-X* and *HyEBTM15-1/3-Y*, was at Θ = 0.38% and 0.42%, respectively. For *HyEBTM15-1/3-X*, peak horizontal strains were located in the compressed flanges close to the corners' base, and, for

HyEBTM15-1/3-Y theses occurred in the compressed end of the webs. *HyEBTM15-1/3-X* exhibited the largest horizontal strains.

In *HyEBTM15-1/3-X*, the diagonal reinforcement of the coupling beams in Stories 1, 3-5 exhibited yielding. First yielding occurred in the coupling beams of Story 4, at Θ = 0.41%. The peak strains of diagonal reinforcement were at least 0.0019 for the coupling beams in Stories 1-6.

First core concrete softening in vertical direction for *HyEBTM15-1/3-X* occurred at Θ = 1.3%, and for *HyEBTM15-1/3-Y* at Θ = 1.4%, whereas corresponding concrete crushing occurred at Θ = 1.4% and 1.9%. In both cases, the first softening was located in the compressed corners; however, for *HyEBTM15-1/3-X*, the first crushing was in the base of the compressed web, and, for *HyEBTM15-1/3-Y* it was in the base of the compressed flanges.

For *HyEBTM15-1/3-X* and *HyEBTM15-1/3-Y*, concrete softening in the diagonal direction occurred at Θ = 0.9% and 1.3%, respectively, whereas corresponding concrete crushing occurred at Θ = 1.3% and 2.2%. In *HyEBTM15-1/3-X*, the peak diagonal strains in compression, i.e., -0.11, were located in the compressed flanges at the corners' base, and, in *HyEBTM15-1/3-Y* the peak strains, i.e., -0.07, were located in the compressed end of the webs, at the corners' base.

The first softening of the shear response was computed for *HyEBTM15-1/3-X* in the base of the corners at the compressed C-shaped wall, from there, softening of the out-of-plane shear response progressed gradually to the center of the web. V_o was reached in the compressed corners at Θ = 0.19%, and V_{res} at Θ = 1.3%.

The first softening of the shear response in the compressed web occurred at $\Theta = 0.33\%$. The decompressed C-shaped wall also exhibited softening, the first softening was at $\Theta = 1\%$, in the web base next to the decompressed corners. For *HyEBTM15-1/3-Y*, the first softening of the shear response spread from the base of the compressed corners to the center of the flanges. First V_o in the corners was at $\Theta = 0.27\%$, and corresponding V_{res} at $\Theta = 2.1\%$, whereas first V_o in the compressed flanges was at $\Theta = 0.44\%$. In the decompressed C-shaped wall, the first softening of the out-of-plane shear response occurred in the base of the flanges, at $\Theta = 1.7\%$.

Base shear apportioning for the flanges and webs of *HyEBTM15-1/3-X* are shown in Figures 5.15a and 5.15b, respectively. Results for two drift ratios are plotted, i.e., Θ = 0.72%, which is the drift at peak shear force for the compressed flanges, and Θ = 1.3%, which is the drift at peak shear force for the compressed web.

At $\Theta = 0.72\%$, most of the base shear force in the compressed flanges was resisted by the compressed corners, i.e., 34%; the rest of the length of the flanges resisted 27% (Figure 5.15a). As degradation took place in the compressed flanges, at Θ = 1.3%, the distribution of the shear force became more uniform, the base shear force resisted in the corners reduced to 8%, and the rest of the length resisted 36%. Since both drift ratios corresponded to load steps well before to final degradation of the F–D response, the contribution of the decompressed flanges was close to zero, except for the region of the boundary element, where at least 4% of the base shear force was resisted (Figure 5.15a). Most of the base shear force resisted by the compressed web was resisted in the region adjacent to the corners ($2 \cdot 0.24 l_{web}$), i.e., 24% and 28%, at Θ = 0.72% and 1.3%, respectively; whereas the central region ($0.37 l_{web}$) resisted 7% at $\Theta = 0.72\%$ and 11% at Θ

= 1.3% (Figure 5.15b). The contribution of the decompressed web to the total strength was very limited, at Θ = 0.72% this was close to zero, and at Θ = 1.3%, the decompressed web resisted 4% of the base shear force in the regions adjacent to the corners and 1% in the central region (Figure 5.15b).

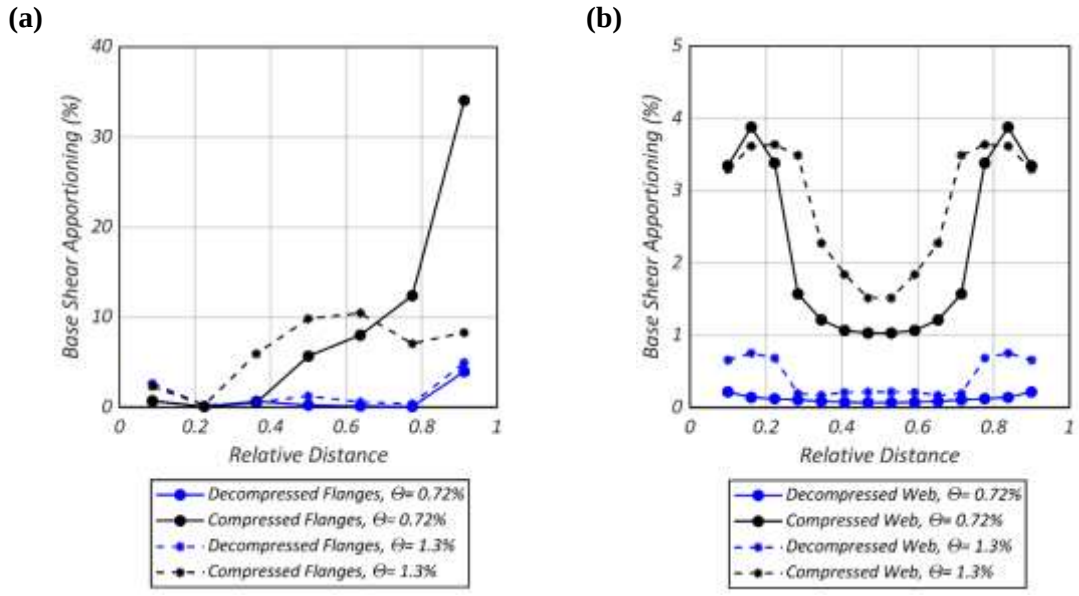

Figure 5.15. Base shear force apportioning for *HyEBTM15-1/3-X*. **(a)** Flanges. **(b)** Webs.

Figure 5.16a shows the base shear apportioning for the flanges of *HyEBTM15-1/3-Y*, and Figure 5.16b shows the corresponding information for the webs. Results were plotted for Θ = 0.53% and 1.5%, which are the drifts at peak shear force for webs, and compressed flanges, respectively. In the compressed flanges, most of the base shear force was resisted in the region adjacent to the corners ($2 \cdot 0.39 l_{flange}$), i.e., 16% and 25% at Θ = 0.53% and 1.5%, respectively, whereas the region adjacent to the boundary element, including it, ($2 \cdot 0.43 l_{flange}$), resisted 6% at Θ = 0.53% and 14% at Θ = 1.5%. The contribution of the decompressed flanges to the total strength was very limited (Figure 5.16a). At Θ = 0.53% and 1.5%, most of the shear force in the webs was resisted in the

region adjacent to the compressed corners, including it ($2 \cdot 0.32 l_{web}$), i.e., 70% and 51%, respectively. The rest of the webs' length ($2 \cdot 0.68 l_{web}$) resisted 7% of the base shear force at both drifts (Figure 5.16b).

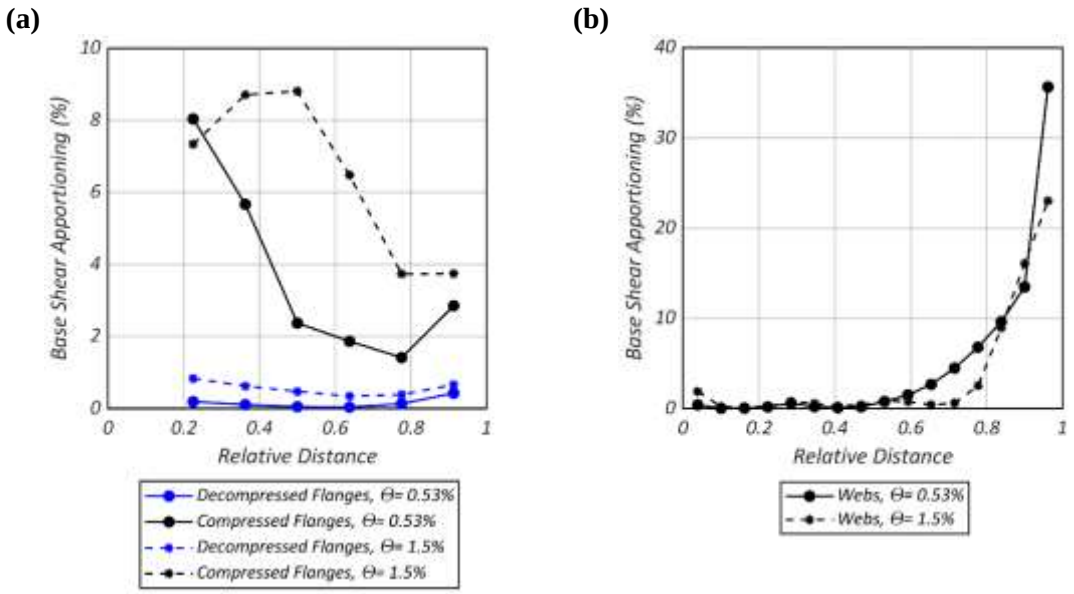

Figure 5.16. Base shear force apportioning for *HyEBTM15-1/3-Y*. **(a)** Flanges. **(b)** Webs.

Figure 5.17a shows the deformed shape of *HyEBTM15-1/3-X* at the end of the analysis, i.e., Θ = 3.6%. Out-of-plane nonlinear shear deformations in the compressed C-shape wall began at the corners' base region, and these spread toward the web, however most of the shear deformations localized in horizontal planes in the corners and vertical planes in the web adjacent to the corners. The compressed flanges exhibited in-plane shear failure, very large horizontal deformation, and diagonal crushing occurred (Figure 5.17b). The strength of the decompressed C-shaped wall played an important role after the failure of the compressed C-shaped wall (Figure 5.14a). In the decompressed C-shaped wall, the softening of the out-of-plane shear response began in the region of the corners' base, and it progressed toward the center of the web. By the end of the analysis, the shear

deformations localized at the second level of the grid, i.e., 914 mm from the base. The decompressed flanges exhibited in-plane shear failure, with very localized horizontal deformation adjacent to the boundary elements, in spite of the boundaries themselves, did not fail in shear.

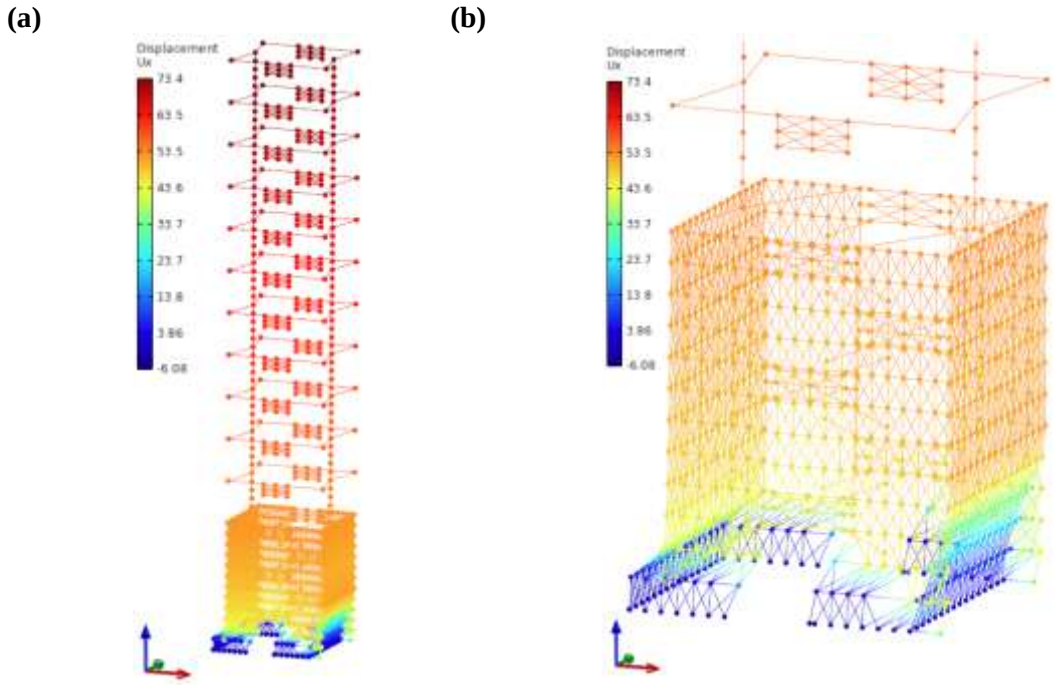

Figure 5.17. Deformed shape for *HyEBTM15-1/3-X* at Θ = 3.6% (1x, inches). **(a)** General View. **(b)** Close up.

5.7.5 Comparison and discussion of results

Fiber-Model-1st-X, HyBTM-1st-X, HyEBTM10-1st-X and *HyEBTM15-1st-X*

Figure 5.18a compares the F–D responses of models subjected to 1st mode shape load pattern in the X-direction. Initially, the responses were very similar, but from Θ = 0.7%, the shear forces began increasing more rapidly for *Fiber-Model-1st-X*, which was expected since Fiber Models did not account for shear deformations. Then, *Fiber-Model-1st-X* exhibited some limited softening at Θ = 3%, and by the end of the analyses, i.e., Θ =

4.9%, the four models attained very similar shear strengths, with V_{max}, ranging $0.35–0.36A_{cv}\sqrt{f'_c}$ (MPa). Limit of the ACI 318-19 (2019), i.e., $V_{ave\text{-}ACI\text{-}limit} = \phi \cdot 0.66A_{cv}\sqrt{f'_c}$ (MPa) ($\phi = 0.75$), was not exceeded. The responses of the Hybrid Models were almost identical throughout the analyses, which indicated that the out-of-plane shear response did not play a role in the F–D responses.

Most of the base shear force was resisted by the compressed C-shaped wall. Peak shear forces ranged $0.56–0.59A_{cv}\sqrt{f'_c}$ (MPa), where the minimum value was computed for *HyEBTM10-1st-X* and maximum for *Fiber-Model-1st-X*. In the compressed flanges, the peak shear forces ranged from $0.41–0.44A_{cv}\sqrt{f'_c}$ (MPa), the minimum and maximum values were computed for *HyEBTM15-1st-X* and *HyBTM-1st-X*, respectively. The corresponding limit, i.e., $V_{pier\text{-}ACI\text{-}limit} = \phi \cdot 0.83A_{cv}\sqrt{f'_c}$ (MPa), was not exceeded.

The largest strains in the longitudinal reinforcement at the base occurred for *Fiber-Model-1st-X*, which was expected since the lateral deformations in this model are related to the bending of the C-shaped walls. For the same reason, the largest strains in the diagonal reinforcement were also exhibited for *Fiber-Model-1st-X*. Yielding in *Fiber-Model-1st-X* occurred in coupling beams of Stories 1-9, whereas in Hybrid Models yielding occurred in Stories 4-8. First yielding in the horizontal reinforcement occurred for *HyEBTM10-1st-X*, at $\Theta = 0.83\%$, whereas *HyBTM-1st-X* and *HyEBTM15-1st-X* exhibited first yielding at $\Theta = 2.6\%$, which indicated that the out-of-plane shear deformations played a role in it. A similar situation occurred for diagonal concrete softening, first softening occurred for *HyEBTM10-1st-X*, at $\Theta = 3.8\%$, whereas *HyBTM-1st-X* and *HyEBTM15-1st-X* exhibited first softening at $\Theta = 4.8\%$. Since the diagonal concrete softening occurred late in the analyses, the F–D responses did not exhibit degradation in any case.

Figure 5.20a compares the inter-story drift ratios Θ_s computed for the different models at the top drift ratio Θ = 4.9%. For Stories 1-3, Θ_s ranged 3%–4.7%, where the minimum value was for *Fiber-Model-1st-X* and the maximum for *HyEBTM10-1st-X*. For Stories 4-14, the four models computed similar Θ_s, with values for *Fiber-Model-1st-X* slightly larger than the values for the Hybrid Models, the largest Θ_s was 5.3%. It is possible to observe that the inter-story drift ratios could be underestimated by the Fiber Model in the lower stories, where the shear deformations played a role, even in these cases, which did not exhibit shear failure.

Fiber-Model-1st-Y, HyBTM-1st-Y, HyEBTM10-1st-Y* and *HyEBTM15-1st-Y

The F–D responses of models subjected to the 1st mode shape load pattern in Y-direction were very similar up to Θ = 0.66%; from there, the shear forces for *Fiber-Model-1st-Y* were larger than corresponding forces for the other models (Figure 5.18b). No softening was exhibited in any case. Practically equal F–D responses were computed for the Hybrid Models throughout the analyses since no influence of the out-of-plane shear response was observed on the overall response.

By the end of the analysis, i.e., Θ = 4.9%, V_{max} for *Fiber-Model-1st-Y* was $0.28A_{cv}\sqrt{f'_c}$ (MPa), 12% larger than in the other three cases. The peak shear forces in the webs ranged $0.15–0.18A_{cv}\sqrt{f'_c}$ (MPa), the minimum value occurred for *HyEBTM10-1st-Y*, whereas the maximum for *HyBTM-1st-Y*. Limits $V_{ave\text{-}ACI\text{-}limit}$ and $V_{pier\text{-}ACI\text{-}limit}$ were not exceeded in any case.

At the base, the peak strains in tension in the longitudinal reinforcement ranged 0.048–0.055, where the minimum value was for *HyBTM-1st-Y*, and the maximum for *Fiber-Model-1st-Y*; as expected, pure bending lateral displacements generated largest

longitudinal strains for the Fiber Model. The maximum longitudinal strains in the hybrid models occurred for *HyEBTM10-1st-Y*, which indicated that the out-of-plane shear response also influenced the longitudinal strains.

Additionally, the out-of-plane shear deformations played a role in the strains of the horizontal reinforcement since the earliest yielding on it occurred for *HyEBTM10-1st-X* and *HyEBTM15-1st-X*, at Θ = 1.1%. The peak strains ranged 0.0084-0.011, where the minimum value was for *HyBTM-1st-Y*, and the maximum for *HyEBTM10-1st-X*. Moreover, the largest peak in compression for the diagonal strains in the concrete, i.e., -0.0048, also occurred for H*yEBTM10-1st-X*.

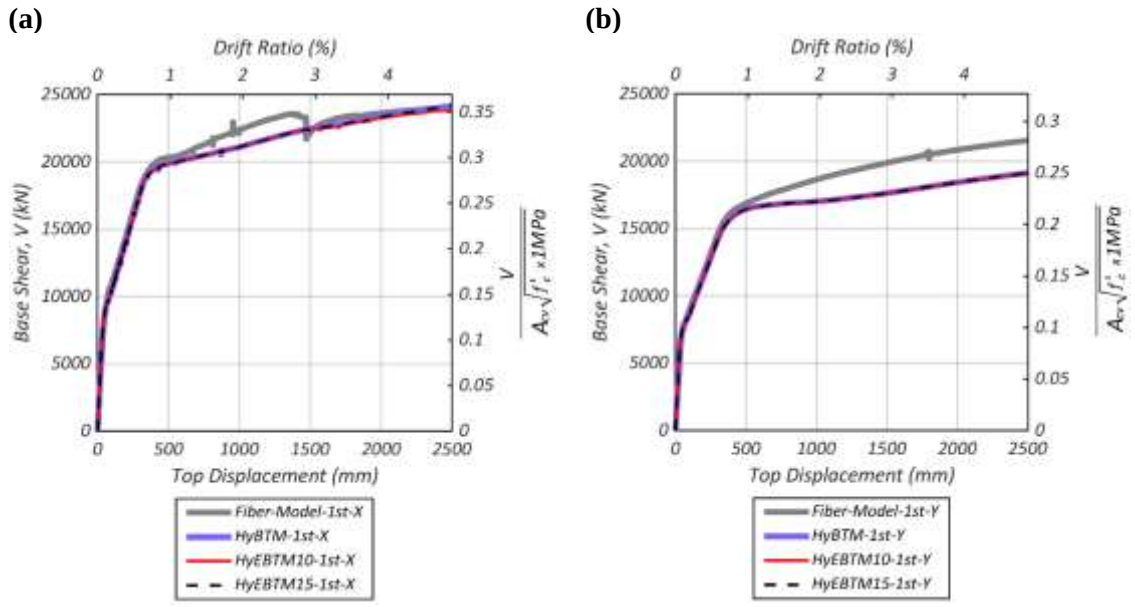

Figure 5.18. Comparison of base shear force – top displacement for Fiber Model, HyBTM and HyEBTM, 1st mode shape load pattern. **(a)** X-direction. **(b)** Y-direction.

Fiber-Model-1/3-X, HyBTM-1/3-X, HyEBTM10-1/3-X and *HyEBTM15-1/3-X*

F–D responses of models subjected to triangular load pattern in the X-direction are compared in Figure 5.19a. Similar responses were computed for the linear part of the pushover curves, i.e., up to Θ = 0.1%. From there, the shear forces in *Fiber-Model-1/3-X*

began increasing more rapidly than the forces in the Hybrid Models. The overall responses of the Hybrid Models were similar up to Θ = 0.64%. At that drift, the *HyEBTM10-1/3-X* response flattened, as the shear forces in *HyBTM-1/3-X* and *HyEBTM15-1/3-X* increased. The shear forces in *Fiber-Model-1/3-X* mostly kept increasing throughout the analysis, up to Θ = 3.9%, whereas the other models exhibited large degradation due to shear failure at different drifts.

V_{max} ranged $0.58–0.7A_{cv}\sqrt{f'_c}$ (MPa), as before, the largest peak shear force corresponded to the Fiber Model, i.e., *Fiber-Model-1/3-X*, the minimum value was computed for *HyEBTM10-1/3-X*. The peak shear force for *HyBTM-1/3-X* and *HyEBTM15-1/3-X* was $0.66A_{cv}\sqrt{f'_c}$ (MPa). The in-plane nonlinear shear response played an important role not only on V_{max}, but on the overall response since large degradation for *HyBTM-1/3-X* was computed, whereas for *Fiber-Model-1/3-X* it was not. Limited influence of the out-of-plane shear strength on V_{max} was observed, V_{max} computed for *HyEBTM10-1/3-X* was slightly smaller than the V_{max} for *HyEBTM15-1/3-X*. The peak shear forces exceeded more than 17% $V_{ave\text{-}ACI\text{-}limit}$. Peak shear forces resisted by the compressed C-shaped wall ranged $1–1.2A_{cv}\sqrt{f'_c}$ (MPa), where the minimum value was computed for *HyEBTM10-1/3-X* and maximum for *Fiber-Model-1/3-X*. In the compressed flanges, the peak shear forces ranged from $0.72–0.76A_{cv}\sqrt{f'_c}$ (MPa), the minimum and maximum values were computed for *HyEBTM15-1/3-X* and *HyBTM-1/3-X*, respectively. Corresponding limit $V_{pier\text{-}ACI\text{-}limit}$ was exceeded by more than 16%, which was consistent with the shear failures exhibited by the Hybrid Models.

After the peak shear force was attained by the Hybrid Models, the shear force decreased to $0.8V_{max}$ at Θ = 3.6%, 1.4%, and 2.4% for *HyBTM-1/3-X*, *HyEBTM10-1/3-X*,

and *HyEBTM15-1/3-X*, respectively. Large influence of the out-of-plane nonlinear shear response on the overall response was observed since the degradation in *HyEBTM10-1/3-X* and *HyEBTM15-1/3-X* occurred earlier than the degradation in *HyBTM-1/3-X*.

The out-of-plane shear deformations also played a role in the local response. First yielding in the horizontal reinforcement occurred for *HyEBTM10-1/3-X* and *HyEBTM15-1/3-X*, at Θ = 0.26% and 0.38%, respectively, whereas *HyBTM-1/3-X* exhibited first yielding at Θ = 0.68%. The model with the smallest out-of-plane shear strength, i.e., *HyEBTM10-1/3-X*, exhibited the earliest yielding. Additionally, earliest diagonal concrete softening and crushing also occurred for *HyEBTM10-1/3-X*, at Θ = 0.76% and 1.1%, respectively.

The earliest yielding in the longitudinal reinforcement at the base occurred for *Fiber-Model-1/3-X*, at Θ = 0.17%. Moreover, the largest longitudinal strain, i.e., 0.06, up to the ultimate drift of *HyEBTM10-1/3-X*, i.e., Θ = 1.4%, (Figure 5.19a), occurred for *Fiber-Model-1/3-X*. As expected, the Hybrid Models exhibited less mobilization of the longitudinal strains than the Fiber Model. The earliest yielding in the diagonal reinforcement was also computed for *Fiber-Model-1/3-X*, yielding occurred in coupling beams of Stories 1-7, whereas in *HyBTM-1/3-X* and *HyEBTM15-1/3-X* yielding occurred in Stories 1, 3-5. In *HyEBTM10-1/3-X*, the yielding was limited to Story 4, since in this case, the analysis stopped first than the other cases.

The inter-story drift ratios Θ_s computed for the different models at Θ = 1.4%, i.e., the ultimate top drift ratio of *HyEBTM10-1/3-X*, are compared in Figure 5.20b. Θ_s ranged 0.98%–4.2% for Stories 1-3, where the minimum Θ_s was computed for *Fiber-Model-1/3-X* and the maximum for *HyEBTM10-1/3-X*. For Stories 4-14, the Hybrid Models computed

similar Θ_s, with values for *HyEBTM10-1/3-X* slightly smaller; the minimum value was Θ_s = 1.1%. In these stories, *Fiber-Model-1/3-X* computed the largest Θ_s; the maximum value was Θ_s = 1.5%. The results showed that very large localization of lateral deformations occurred in Story 1 at Θ = 1.4%, especially for *HyEBTM10-1/3-X*, as expected, since it exhibited shear failure at this drift ratio. However, large localization was also observed in *HyBTM-1/3-X,* and *HyEBTM15-1/3-X*, in spite of these cases, did not exhibit ultimate degradation at Θ = 1.4%.

Fiber-Model-1/3-Y, HyBTM-1/3-Y, HyEBTM10-1/3-Y* and *HyEBTM15-1/3-Y

The F–D responses of models subjected to the triangular load pattern in Y-direction were similar up to Θ = 0.07% (Figure 5.19b). Then, the shear forces in *Fiber-Model-1/3-Y* increased more rapidly than the forces in the other models. The capacity of *Fiber-Model-1/3-Y* steadily increased up to Θ = 3.6%, where the response exhibited steep degradation. Base shear forces for the Hybrid Models peaked early, i.e., at Θ = 1.4%, 0.9% and 1.2%, for *HyBTM-1/3-Y*, *HyEBTM10-1/3-Y* and *HyEBTM15-1/3-Y*, respectively. For *HyBTM-1/3-Y*, softening was gradual throughout the analysis, i.e., up to Θ = 3.9%. However, F–D responses of *HyEBTM10-1/3-Y* and *HyEBTM15-1/3-Y*, which initially exhibited gradual softening, experienced very steep degradation at Θ = 2.7%, and 3.1%, respectively. In the Fiber Model, the longitudinal strains were mobilized to bar fracture, whereas in the Hybrid Models occurred shear failure.

It is clear that the in-plane shear response played a role in the overall responses. Moreover, the out-of-plane shear response influenced the F–D responses, especially the displacement capacity, since the earliest ultimate degradation occurred for the model with the smallest out-of-plane shear strength, i.e., *HyEBTM10-1/3-Y*.

The strains in the horizontal reinforcement and in the concrete in diagonal direction were also influenced by the out-of-plane shear deformations. The earliest yielding in the horizontal reinforcement, which occurred at Θ = 0.3%, was computed for *HyEBTM10-1/3-Y*. Furthermore, the earliest diagonal concrete softening and crushing occurred for *HyEBTM10-1/3-Y*, at Θ = 1.1% and 1.8%, respectively.

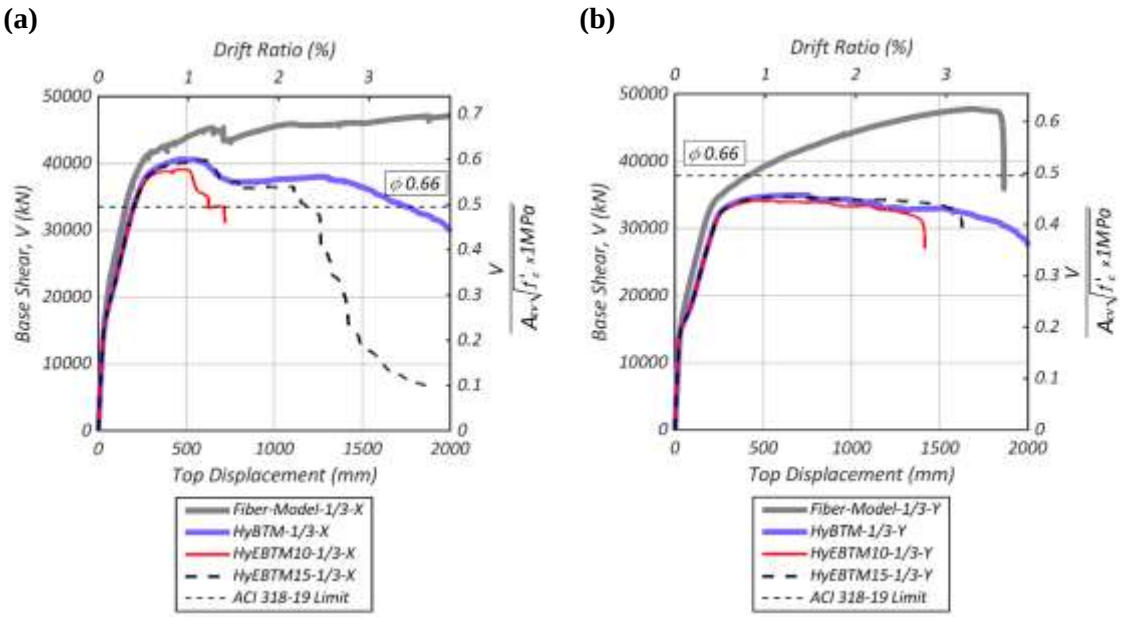

Figure 5.19. Comparison of base shear force – top displacement for Fiber Model, HyBTM and HyEBTM, triangular load pattern. **(a)** X-direction. **(b)** Y-direction.

The largest V_{max} was computed for *Fiber-Model-1/3-Y*, i.e., $0.62A_{cv}\sqrt{f'_c}$ (MPa), whereas the smallest for *HyEBTM10-1/3-Y* and *HyEBTM15-1/3-Y*, i.e., $0.45A_{cv}\sqrt{f'_c}$ (MPa).

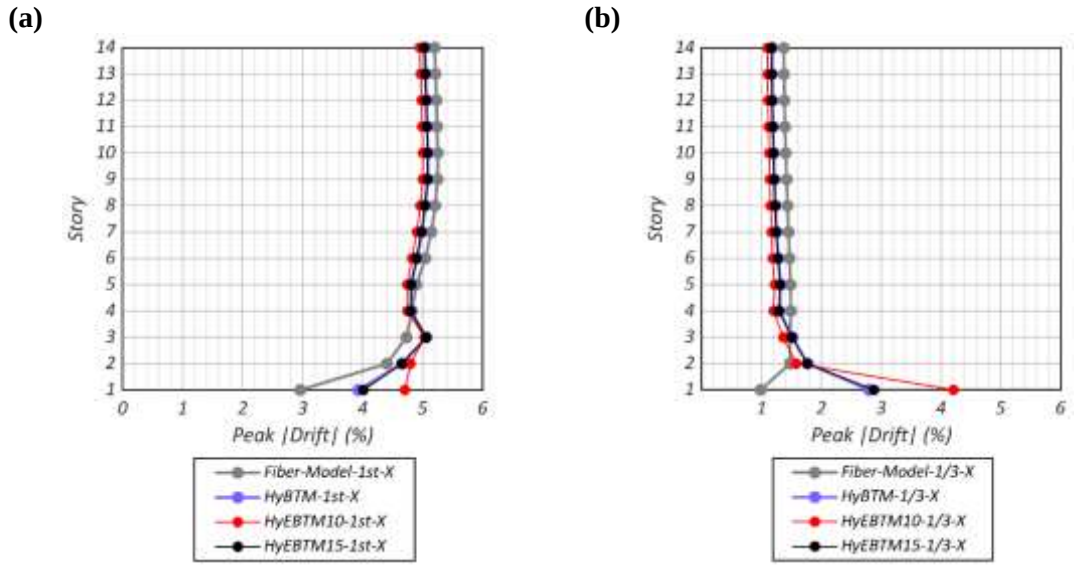

Figure 5.20. Comparison of inter-story drift ratios for Fiber Model, HyBTM and HyEBTM, X-direction. **(a)** 1st mode shape load patter, Θ = 4.9%. **(b)** Triangular load pattern, Θ = 1.4%.

Limited influence of out-of-plane shear response on V_{max} was observed, since V_{max} for *HyBTM-1/3-Y*, i.e., $0.46A_{cv}\sqrt{f'_c}$ (MPa), was very similar to the value computed for *HyEBTM10-1/3-Y* and *HyEBTM15-1/3-Y*. $V_{ave\text{-}ACI\text{-}limit}$ was exceeded only for *Fiber-Model-1/3-Y*, by 25%. The peak shear force in the webs was $0.33A_{cv}\sqrt{f'_c}$ (MPa), in the three Hybrid Models, which did not exceed $V_{pier\text{-}ACI\text{-}limit}$. The fact that the Enhanced Hybrid Models exhibited brittle shear failures, as peak shear force limits of the ACI 318-19 (2019) were not exceeded, seems inconsistent; however, it is necessary to notice that steep degradation took place at relatively large drift ratios.

As expected, the Fiber Model exhibited the largest mobilization of the longitudinal strains. The earliest yielding in the longitudinal reinforcement at the base was computed for *Fiber-Model-1/3-Y*, at Θ = 0.3%, moreover, the largest longitudinal strain, i.e., 0.059, computed at the ultimate drift of *HyEBTM10-1/3-Y*, i.e., Θ = 2.8%, (Figure 5.19b), also occurred for *Fiber-Model-1/3-Y*.

5.8 Conclusions

This paper enhanced the Beam-Truss Model (BTM) developed for nonlinear analysis of reinforced concrete structures, including in-plane nonlinear shear response and nonlinear flexural warping, to compute the out-of-plane nonlinear shear response, for the analysis of Core-Wall-Building systems. The enhanced Beam-Truss Model (EBTM) considered the out-of-plane shear deformations via nonlinear shear springs, which used the built in-house material *PinHardwP*, implemented in OpenSees, to compute shear response dependent on axial forces. Hysteretic rules and calibration equations were proposed.

The EBTM was combined in series with a Fiber-Section Model to improve the computational economy, resulting in the Hybrid Fiber-Section - Enhanced Beam-Truss Model (HyEBTM). In this novel model, the lower stories of the Core Wall were modeled using EBTM, whereas the upper stories adopted Fiber-Section Model. Displacement-based elements with PDelta geometric transformation and diagonal truss-elements with Corotational transformation were used.

The HyEBTM was applied to study the lateral response of a 14-story building with a central core formed by two C-shaped coupled walls. The structure building was assumed to be located in downtown Los Angeles. Monotonic nonlinear static analyses were carried out with 1st mode shape lateral pattern (up to drift ratio Θ = 4.9%) and triangular load pattern (up to Θ = 3.9%). The load patterns were considered independently in the direction of coupling (X-direction) and in the direction of the cantilever (Y-direction). The out-of-plane shear response was bounded running cases for two extreme levels of out-of-plane shear strength. Fiber-Section Models and Hybrid Fiber-Section – Beam-Truss Models

(hyBTM) were used as references. Overall and local responses were compared for the different case studies.

The following conclusions are drawn on the overall response:

- The height of the result of lateral forces influences the lateral strength and displacement capacity of the Core Wall. Base shear forces computed for the triangular load pattern were 1.7–2.2 times larger than base shear forces for 1st mode shape load pattern. HyBTM and HyEBTM subjected to 1st mode shape load pattern did not fail, but they failed for the triangular load pattern.
- The models that considered in-plane shear response computed smaller lateral strengths than the models that did not. HyBTM and HyEBTM computed up to 26% smaller lateral strengths than the corresponding Fiber-Section Models. The in-plane shear response had a large influence on the displacement capacity of the Core Wall in the X-direction for triangular load pattern. Since the Fiber Model did not exhibit failure, whereas the HyBTM did, at Θ = 2.5%.
- The out-of-plane shear response had a limited influence on the lateral strength of the Core Wall. Lateral strengths computed for HyEBTM were at most 3% larger than those for HyBTM. However, the out-of-plane shear response had a large influence on the displacement capacity of the models with the triangular load pattern. The drift ratios at the onset of ultimate degradation were 16%–52% smaller for HyEBTM than for HyBTM.
- The peak shear forces in the models exceeded the ACI 318-19 (2019) limit, i.e., $\phi \cdot 0.66 A_{cv} \sqrt{f'_c}$ (MPa), by 17%–41% for the triangular load pattern in the X-

direction, where the maximum value was for Fiber-Section Model. For Y-direction, the limit was exceeded only for the Fiber-Section Model, by 25%.

- For the load patterns in the X-direction, the compressed C-shaped wall resisted at least 86% of the base shear force in HyBTM and HyEBTM, and at least 93% in the Fiber-Section Models, at V_{max}.
- At V_{max}, the compressed flanges resisted 53%–63% of the base shear force, for the analyses in X-direction, whereas, the webs resisted 64%–72%, for the analyses in the Y-direction.
- The peak shear force in the compressed flange (analyses in X-direction) exceeded by 16%–22% the ACI 318-19 (2019) limit, i.e., $\phi \cdot 0.83 A_{cv} \sqrt{f'_c}$ (MPa). The peak shear force in the webs did not exceed this limit (analyses in the Y-direction).
- At V_{max}, the compressed web resisted 12%–37% of the base shear force for the analyses in the X-direction, whereas, the compressed flanges resisted 15%–34%, for the analyses in the Y-direction. The minimum values occurred for 1st shape mode load pattern and the maximum values for the triangular pattern.

The following conclusions are drawn on the local response:

- The in-plane shear deformations inhibited the spread of yielding in the diagonal reinforcement of the coupling beams. For the Fiber-Section Models, the coupling beams of up to 9 stories exhibited yielding, whereas, for HyBTM and HyEBTM, at most 5 stories did.
- The out-of-plane shear response influenced the deformations in the horizontal reinforcement of the Core Walls. HyEBTM exhibited yielding of horizontal

reinforcement at drift ratios 17%–68% smaller than corresponding drift ratios in HyBTM.

- The out-of-plane shear response influenced the diagonal concrete deformation mainly for the triangular load patter. In this case, HyEBTM exhibited diagonal concrete crushing at drift ratios 9%–27% smaller than corresponding drift ratios in HyBTM.

Base on the models developed and the conclusions drawn, possible future research could include:

- Carry out the experimental verification of the lateral response of Core-Wall Building systems, with a focus on the in-plane and out-of-plane apportioning of the base shear force.
- Include the buckling of longitudinal reinforcement in the analysis of the Core-Wall-Building systems.
- Include the interaction of in-plane shear response and out-of-plane shear response explicitly.
- Extend this study to the seismic response of Core-Wall-Building systems using Nonlinear Response History Analysis.

5.9 Acknowledgments

Chapter 5, in part, is currently being prepared for submission for publication of the material. Alvarez, Rodolfo; Restrepo, Jose I.; and Panagiotou, Marios. The dissertation author was the primary investigator and author of this paper.

The authors would like to thank the Mexican Government for providing financial support through the *Consejo Nacional de Ciencia y Tecnología* (CONACYT). This work was also supported by the *University of California Institute for Mexico and the United States* (UC MEXUS) and the program *Becas Fulbright - García Robles* (COMEXUS).

REFERENCES

ACI 318-14. (2014). *Building Code Requirements for Structural Concrete (ACI 318-14) and Commentary (ACI 318R-14)*. Farmington Hills, MI: American Concrete Institute.

ACI 318-19. (2019). *Building Code Requirements for Structural Concrete (ACI 318-19) and Commentary (ACI 318R-19)*. Farmington Hills, MI: American Concrete Institute.

Adebar, P., Ibrahim, A. M. M., & Bryson, M. (2008). Test of High-Rise Core Wall : Effective Stiffness for Seismic Analysis. *ACI Structural Journal*, *104*(5), 549–560.

Almeida, J., Prodan, O., Rosso, A., & Beyer, K. (2017). Tests on Thin Reinforced Concrete Walls Subjected to In-plane and Out-of-plane Cyclic Loading. *Earthquake Spectra*, *33*(1), 323–345. https://doi.org/10.1193/101915EQS154DP

Alvarez-Sanchez, R., & Restrepo, J. I. (2017). Framework for Simulation of Reinforced Concrete Walls Based on OpenSees-MATLAB Using Beam-Truss Model. *XXI National Congress of Earthquake Engineering*, (1). Mexican Society of Earthquake Engineering.

Alvarez, R., Restrepo, J. I., Panagiotou, M., & Santhakumar, A. R. (2019). Nonlinear Cyclic Truss Model for Analysis of Reinforced Concrete Coupled Structural Walls. *Bulletin of Earthquake Engineering, Special Issue: Nonlinear Modeling of Reinforced Concrete Structural Walls and Wall Systems*, (0123456789). https://doi.org/10.1007/s10518-019-00639-8

Arabzadeh, H., & Galal, K. (2018). Seismic-Response Analysis of RC C-Shaped Core Walls Subjected to Combined Flexure, Shear, and Torsion. *Journal of Structural Engineering (United States)*, *144*(10). https://doi.org/10.1061/(ASCE)ST.1943-541X.0002181

Arteta, C. A., Araújo, G. A., Torregroza, A. M., Martínez, A. F., & Lu, Y. (2019). Hybrid Approach for Simulating Shear – Flexure Interaction in RC Walls with Nonlinear Truss and Fiber Models. *Bulletin of Earthquake Engineering*, (0123456789). https://doi.org/10.1007/s10518-019-00681-6

Arteta, C. A., To, D., & Moehle, J. (2014). Experimental Response of Boundary Elements of Code-Compliant Reinforced Concrete Shear Walls. *10th U.S. National Conference on Earthquake Engineering*. https://doi.org/10.4231/D37H1DN29

ASCE 41-13. (2013). *Seismic Evaluation and Retrofit of Existing Buildings (41-13)*. Reston, VA: American Society of Civil Engineers.

ASCE 41-17. (2017). *Seismic Evaluation and Retrofit of Existing Buildings (41-17)*. Reston, VA: American Society of Civil Engineers.

ASCE 7-16. (2016). *Minimum Design Loads and Associated Criteria for Buildings and Other Structures*. Reston, VA: American Society of Civil Engineers.

Barbachyn, S. M., Kurama, Y. C., & Mcginnis, M. J. (2015). *Large-Scale Experimental Evaluation of Post-Tensioned Coupled Shear Wall Systems for Seismic Regions*. Retrieved from https://ptcoupledwalls.nd.edu/documents/Report-NDSE-2015-01.pdf

Barbosa, A. R. (2011). *Simplified Vector-Valued Probabilistic Seismic Hazard Analysis and Probabilistic Seismic Demand Analysis: Application to the 13-Story NEHRP Reinforced Concrete Frame-Wall Building Design Example*. University of California San Diego.

Beattie, G. J. (2004). *Design of Slender Precast Concrete Wall Panels – Experimental Testing.* Judgeford, New Zealand.

Binney, J. R. (1972). *Diagonally Reinforced Coupling Beams*. University of Caterbury.

Boivin, Y., & Paultre, P. (2010). Seismic Performance of a 12-Storey Ductile Concrete Shear Wall System Designed According to the 2005 National Building Code of Canada and the 2004 Canadian Standard Association Standard A23.3. *Canadian Journal of Civil Engineering*, *37*(1), 1–16. https://doi.org/10.1139/L09-115

Boroschek, R., Bonelli, P., Restrepo, J. I., Retamales, R., & Contreras, V. (2014). Lessons from the 2010 Chile Earthquake for Performance Based Design and Code Development. In *Performance-Based Seismic Engineering: Vision for an Earthquake Resilient Society* (Vol. 32, pp. 143–157). https://doi.org/10.1007/978-94-017-8875-5

Carreño, R. (2018). *Characterization of Large Diameter Reinforcing Bars Under Large Strain Cyclic Reversals*. University of California San Diego.

CCA. (2018). Demountable Mechanical Strain Gauge (DEMEC). Retrieved from British Cement and Concrete Association website: https://www.thenbs.com/PublicationIndex/documents?Pub=BCA

Chai, Y. H., & Elayer, D. T. (1999). Lateral Stability of Reinforced Concrete Columns under Axial Reversed Cyclic Tension and Compression. *ACI Structural Journal*, *96*(5), 780–789.

Chrysanidis, T. A., & Tegos, I. A. (2012). The Influence of Tension Strain of Wall Ends to Their Resistance Against Lateral Instability for Low-Reinforced Concrete Walls. *15th World Conference on Earthquake Engineering (15WCEE)*. Lisbon, Portugal.

Coleman, J., & Spacone, E. (2001). Localization Issues in Nonlinear Frame Elements. *Journal of Structural Engineering*, *127*(November), 1257–1265.

Collins, M. P., & Mitchell, D. (1997). *Prestressed Concrete Structures*. Toronto, Canada:

Response Publications.

Constantin, R., & Beyer, K. (2012). Modelling of Reinforced Concrete Core Walls Under Bi-Directional Loading. *Proceedings 15th World Conference on Earthquake Engineering*.

Constantin, R., & Beyer, K. (2016). Behaviour of U-Shaped RC Walls under Quasi-Static Cyclic Diagonal Loading. *Engineering Structures*, *106*, 36–52. https://doi.org/10.1016/j.engstruct.2015.10.018

CSI. (2018). *ETABS*. Retrieved from https://www.csiamerica.com/

Dashti, F. (2017). *Out-of-plane Instability of Rectangular Reinforced Concrete Walls under In-plane Loading* (University of Canterbury). https://doi.org/10.13140/RG.2.2.31057.58728

Dashti, F., Dhakal, R. P., & Pampanin, S. (2017a). Numerical Modeling of Rectangular Reinforced Concrete Structural Walls. *Journal of Structural Engineering*, *143*(6). https://doi.org/10.1061/(asce)st.1943-541x.0001729

Dashti, F., Dhakal, R. P., & Pampanin, S. (2017b). Tests on Slender Ductile Structural Walls Designed According to New Zealand Standard. *Bulletin of the New Zealand Society for Earthquake Engineering*, *50*(4), 504–516.

Dashti, F., Dhakal, R., & Pampanin, S. (2015). Development of Out-of-plane Instability in Rectangular RC Structural Walls. *2015 NZSEE Conference*. Christchurch, New Zealand: NZSEE.

Dhakal, R. P., & Maekawa, K. (2002). Modeling for Postyield Buckling of Reinforcement. *Journal of Structural Engineering*, *128*(9), 1139–1147. https://doi.org/10.1061/(ASCE)0733-9445(2002)128:8(995)

Dodd, L. L., & Restrepo-Posada, J. I. (1995). Model for Predicting Cyclic Behavior of Reinforcing Steel. *Journal of Structural Engineering*, *121*(3), 433–445.

Fischinger, M. A., Vidic, T. O., & Fajfar, P. (1992). Nonlinear Seismic Analysis of Structural Walls Using the Multiple-Vertical-Line-Element Model. In H. Krawinkler & P. Fajfar (Eds.), *Nonlinear Seismic Analysis of RC Buildings* (pp. 191–202). London and New York: Elsevier Science Publishers Ltd.

Fischinger, M., Rejec, K., & Isakovic, T. (2012). Modeling Inelastic Shear Response of RC Walls. *15th World Conf. on Earthquake Engineering*. Lisbon, Portugal.

Fleischman, R. B., Restrepo, J. I., Pampanin, S., Maffei, J. R., Seeber, K., & Zahn, F. A. (2014). Damage Evaluations of Precast Concrete Structures in the 2010-2011 Canterbury Earthquake Sequence. *Earthquake Spectra*, *30*(1), 277–306.

Fry, J. A., Hooper, J. D., & Klemencic, R. (2010). Core Wall Case Study Design for Pacific Earthquake Engineering Research/California Seismic Safety Commission. *Structural Design of Tall and Special Buildings*, *19*(1–2), 61–75. https://doi.org/10.1002/tal.544

Galano, L., & Vignoli, A. (2000). Seismic Behavior of Short Coupling Beams with Different Reinforcement Layouts. *ACI Structural Journal*, *97*(6).

Gomes, A., & Appleton, J. (1997). Nonlinear Cyclic Stress-Strain Relationship of Reinforcing Bars Including Buckling. *Engineering Structures*, *19*(10), 822–826. https://doi.org/10.1016/S0141-0296(97)00166-1

Goodsir, W. J. (1985). *The Design of Coupled Frame-Wall Structures for Seismic Actions*. University of Canterbury.

Gormak, P. J. (1974). *Non-Linear Finite Element Analysis of Shear Walls and Two Dimensional Reinforced Concrete Structures*. University of Canterbury.

Haro, A. G., Kowalsky, M., & Chai, Y. H. (2019). Out-of-plane Buckling Instability Limit State for Boundary Regions of Special RC Structural Walls. *Bulletin of Earthquake Engineering*, (0123456789). https://doi.org/10.1007/s10518-019-00667-4

Haro, A. G., Kowalsky, M., Chai, Y. H., & Lucier, G. W. (2018). Boundary Elements of Special Reinforced Concrete Walls Tested Under Different Loading Paths. *Earthquake Spectra*, *34*(3), 1267–1288. https://doi.org/10.1193/081617EQS160M

Hoult, R. D., Goldsworthy, H. M., & Lumantarna, E. (2018). Plastic Hinge Length for Lightly Reinforced C-Shaped Concrete Walls. *Journal of Earthquake Engineering*, *00*(00), 1–32. https://doi.org/10.1080/13632469.2018.1453419

Hsu, T. T. C., & Mo, Y. L. (2010). Unified Theory of Concrete Structures. In *Unified Theory of Concrete Structures*. https://doi.org/10.1002/9780470688892

Inada, K., Chosa, K., Sato, H., & Kono, S. (2008). Seismic Performance of RC L-Shaped Core Structural Walls. *The 14th World Conference on Earthquake Engineering*. Beijing, China.

Isakovic, T., & Fischinger, M. (2019). Assessment of a Force – Displacement Based Multiple - Vertical - Line Element to Simulate the Non - Linear Axial – Shear – Flexure Interaction Behaviour of Reinforced Concrete Walls. *Bulletin of Earthquake Engineering*, (0123456789). https://doi.org/10.1007/s10518-019-00680-7

Johnson, B. (2010). *Anchorage Detailing Effects on Lateral Deformation Components of RC Shear Walls*. University of Minnesota.

Kam, W. Y., Pampanin, S., & Elwood, K. (2011). Seismic Performance of Reinforced Concrete Buildings in the 22 February Christchurch (Lyttelton) Earthquake. *Bulletin*

of the New Zealand Society for Earthquake Engineering, *44*(4), 239–278. https://doi.org/10.5459/bnzsee.44.4.239-278

Kolozvari, K., Kalbasi, K., Orakcal, K., Massone, L. M., & Wallace, J. (2019). Shear-Flexure-Interaction Models for Planar and Flanged Reinforced Concrete Walls. *Bulletin of Earthquake Engineering*, *17*(12), 6391–6417. https://doi.org/10.1007/s10518-019-00658-5

Kolozvari, K., Orakcal, K., & Wallace, J. W. (2015). Modeling of Cyclic Shear-Flexure Interaction in Reinforced Concrete Structural Walls. I: Theory. *Journal of Structural Engineering (United States)*, *141*(5), 1–10. https://doi.org/10.1061/(ASCE)ST.1943-541X.0001059

Kolozvari, K., & Wallace, J. W. (2016). Practical Nonlinear Modeling of Reinforced Concrete Structural Walls. *Journal of Structural Engineering*, *142*(12), G4016001. https://doi.org/10.1061/(asce)st.1943-541x.0001492

Kono, S., Sakamoto, K., & Sakashita, M. (2011). Simulation of Seismic Load Resistance of Core-Walls for Tall Buildings. *Applied Mechanics and Materials*, *82*, 386–391. https://doi.org/10.4028/www.scientific.net/AMM.82.386

Koutromanos, I., & Bowers, J. (2016). Enhanced strain beam formulation resolving several issues of displacement-based elements for nonlinear analysis. *Journal of Engineering Mechanics*, *142*(9), 1–12. https://doi.org/10.1061/(ASCE)EM.1943-7889.0001111

Kwan, A. K. H. (1993). Improved Wide-Column-Frame Analogy for Shear/Core Wall Analysis. *J. Struct. Eng.*, *119*(2), 420–437.

LATBSDC-17. (2017). *An Alternative Procedure for Seismic Analysis and Design of Tall Buildings Located in the Los Angeles Region* (2017 Editi). Los Angeles Tall Buildings Structural Design Council.

LeBorgne, M. R. (2012). *Modeling the Post Shear Failure Behavior of Reinforced Concrete Columns*. University of Texas Austin.

Lehman, D. E., Turgeon, J. A., Birely, A. C., Hart, C. R., Marley, K. P., Kuchma, D. A., & Lowes, L. N. (2013). Seismic Behavior of a Modern Concrete Coupled Wall. *J. Struct. Eng.*, *139*(August), 1371–1381. https://doi.org/10.1061/(ASCE)ST.1943-541X.0000853

Leng, K., Chintanapakdee, C., & Hayashikawa, T. (2014). Seismic Shear Forces in Shear Walls of a Medium-Rise Building Designed by Response Spectrum Analysis. *Engineering Journal*, *18*(4), 73–95. https://doi.org/10.4186/ej.2014.18.4.73

Lequesne, R. D., Wight, J. K., & Parra-Montesinos, G. J. (2010). Seismic Detailing and Behavior of Coupled-Wall Systems with High-Performance Fiber-Reinforced

Concrete. In Canadian Association for Earthquake Engineering (Ed.), *9th U.S. National and 10th Canadian Conf. on Earthquake Engineering*. Ottawa, Canada.

Lu, Y. (2014). *Three-Dimensional Seismic Analysis of Reinforced Concrete Wall Buildings at Near-fault Sites*. University of California San Diego.

Lu, Y., & Panagiotou, M. (2013). Three-Dimensional Cyclic Beam-Truss Model for Nonplanar Reinforced Concrete Walls. *Journal of Structural Engineering*, *140*(3), 04013071. https://doi.org/10.1061/(asce)st.1943-541x.0000852

Lu, Y., & Panagiotou, M. (2015). Earthquake Damage-Resistant Tall Buildings at Near Fault Regions Using Base Isolation and Rocking Core Walls. In ASCE (Ed.), *Structures Congress 2015* (pp. 1266–1277).

Lu, Y., & Panagiotou, M. (2016). Three-Dimensional Beam-Truss Model for Reinforced Concrete Walls and Slabs - Part 2: Modeling Approach and Validation for Slabs and Coupled Walls. *Earthquake Engng Struct. Dyn.* https://doi.org/10.1002/eqe.2720

Lu, Y., Panagiotou, M., & Koutromanos, I. (2014). *Three-Dimensional Beam-Truss Model for Reinforced-Concrete Walls and Slabs Subjected to Cyclic Static or Dynamic Loading*.

Lu, Y., Panagiotou, M., & Koutromanos, I. (2016). Three-Dimensional Beam-Truss Model for Reinforced Concrete Walls and Slabs - Part 1: Modeling Approach, Validation, and Parametric Study for Individual Reinforced Concrete Walls. *Earthquake Engng Struct. Dyn.* https://doi.org/10.1002/eqe.2719

Mander, J. B., Priestley, J. N., & Park, R. (1988). Theoretical Stress-Strain Model for Confined Concrete. *Journal of Structural Engineering*, *114*(8), 1804–1826.

Massone, L., Polanco, P., & Herrera, P. (2014). Experimental and Analytical Response of RC Wall Boundary Elements. *10th U.S. National Conference on Earthquake Engineering: Frontiers of Earthquake Engineering*. Anchorage, Alaska: EERI.

MathWorks. (2018). *MATLAB*. Retrieved from http//cn.mathworks.com

McKenna, F. (2018). *OpenSees*. Retrieved from http://opensees.berkeley.edu/

McKenna, F. (2019). *OpenSees*. Retrieved from http://opensees.berkeley.edu/

Mehmood, T., Warnitchai, P., Ahmed, M., & Qureshi, M. I. (2017). Alternative Approach to Compute Shear Amplification in High-Rise Reinforced Concrete Core Wall Buildings Using Uncoupled Modal Response History Analysis Procedure. *Structural Design of Tall and Special Buildings*, *26*(4), 1–18. https://doi.org/10.1002/tal.1314

Menegon, S. J., Wilson, J. L., Lam, N. T. K., & Gad, E. F. (2017). Experimental Testing

of Reinforced Concrete Walls in Regions of Lower Seismicity. *Bulletin of the New Zealand Society for Earthquake Engineering*, *50*(4), 494–503. https://doi.org/10.5459/bnzsee.50.4.494-503

Mihaylov, B. I., & Franssen, R. (2017). Shear-Flexure Interaction in the Critical Sections of Short Coupling Beams. *Engineering Structures*, *152*, 370–380. https://doi.org/10.1016/j.engstruct.2017.09.024

Moehle, J. P., Acevedo, C., & Creagh, A. (2010). Exploratory Tests of Wall Boundary Elements Subjected to Alternating Tensile and Compressive Loadings. In PEER (Ed.), *2010 PEER Annual Meeting*.

Moharrami, M., Koutromanos, I., Panagiotou, M., & Girgin, S. C. (2015). Analysis of Shear-Dominated RC Columns Using the Nonlinear Truss Analogy. *Earthquake Engng Struct. Dyn.*, (44), 677–694. https://doi.org/10.1002/eqe.2480

Mohr, D., Lehman, D., & Lowes, L. (2007). Performance-Based Design and Nonlinear Modeling of Coupled Shear Walls and Coupling Beams. *2007 Structures Congress: New Horizons and Better Practices*, 1–8. https://doi.org/10.1061/40946(248)25

Munir, A., & Warnitchai, P. (2012). The Cause of Unproportionately Large Higher Mode Contributions in the Inelastic Seismic Responses of High-Rise Core-Wall Buildings. *Earthquake Engng Struct. Dyn.*, *41*(April), 2195–2214. https://doi.org/10.1002/eqe.2182

Naish, D., Fry, A., Klemencic, R., & Wallace, J. (2013a). Reinforced Concrete Coupling Beams — Part I : Testing. *ACI Structural Journal*, *110*(6), 1067–1075.

Naish, D., Fry, A., Klemencic, R., & Wallace, J. (2013b). Reinforced Concrete Coupling Beams — Part II : Modeling. *ACI Structural Journal*, *110*(6), 1067–1075.

Najam, F. A. (2018). A Modified Response Spectrum Analysis Procedure to Determine Nonlinear Seismic Demands of High - Rise Buildings with Shear Walls. *Struct Design Tall Spec Build*, (January), 1–19. https://doi.org/10.1002/tal.1409

Nakachi, T., Toda, T., & Tabata, K. (1996). Experimental Study on Deformation Capacity of RC Core Walls After Flexural Yielding. *11th World Conference on Earthquake Engineering*. Acapulco, Mexico.

NEHRP. (2014). *Recommendations for Seismic Design of Reinforced Concrete Wall Buildings Based on Studies of the 2010 Maule , Chile Earthquake*.

NSR-10. (2010). *Reglamento Colombiano de Construccion Sismo Resistente*. Bogota D.C. Colombia: Comision Asesora Permanente para Regimen de Construcciones Sismo Resistentes.

NZS 3101. (1982). *Code of Practice for Design of Concrete Structures*. Wellington, New Zealand: Standards Association of New Zealand.

NZS 3101. (2006). *Concrete Structures Standard Part 1 & 2*. Wellington, New Zealand: Standards New Zealand.

NZSS-1900. (1965). *New Zealand Standard Model Building By-Law, Basic Design Loads*. Wellington, New Zealand: New Zealand Standards Institute.

Oesterle, R. G., Fiorato, A. E., Johal, L. S., Carpenter, J. E., Russell, H. G., & Corley, W. G. (1976). *Earthquake Resistant Structural Walls: Test of Isolated Walls*.

Ozselcuk, A. R. (1989). *Experimental and Analytical Studies of Coupled Wall Structures.* University of California Berkeley.

Panagiotou, M. (2017). Seismic Response of Medium-Rise and Tall RC Core-Wall Buildings at Near-Fault Regions and Simplified Calculation of Design Demands. *2017 Conference of the Los Angeles Tall Buildings Structural Design Council*, (c), 1–19.

Panagiotou, M., & Restrepo, J. I. (2009). Dual-Plastic Hinge Design Concept for Reducing Higher-Mode Effects on High-Rise Cantilever Wall Buildings. *Earthquake Engng Struct. Dyn.*, *38*, 1359–1380. https://doi.org/10.1002/eqe.905

Panagiotou, M., & Restrepo, J. I. (2011). Displacement-Based Method of Analysis for Regular Reinforced-Concrete Wall Buildings: Application to a Full-Scale 7-Story Building Slice Tested at UC–San Diego. *Journal of Structural Engineering*, *137*(6), 677–690. https://doi.org/10.1061/(asce)st.1943-541x.0000333

Panagiotou, M., Restrepo, J. I., & Conte, J. P. (2011). Shake-Table Test of a Full-Scale 7-Story Building Slice. Phase I: Rectangular Wall. *Journal of Structural Engineering*, *137*(6), 691–704. https://doi.org/10.1061/(asce)st.1943-541x.0000332

Panagiotou, M., Restrepo, J. I., Schoettler, M., & Kim, G. (2012). Nonlinear Cyclic Truss Model for Reinforced Concrete Walls. *ACI Structural Journal*, *109*(2), 205–214.

Parra-Torres, P. F. (2015). *Stability of Reinforced Concrete Wall Boundaries*. University of California Berkeley.

Parra, P. F., Arteta, C. A., & Moehle, J. P. (2015). Stability of Reinforced Concrete Wall Boundaries. *Structural Engineering Frontier Conference*. Yokohama, Japan: Tokyo Institute of Technology.

Parra, P. F., & Moehle, J. P. (2017). Stability of Slender Wall Boundaries Subjected to Earthquake Loading. *ACI Structural Journal*, *114*(6), 1627–1636. https://doi.org/10.14359/516851700836

Paulay, T. (1969). *The Coupling of Shear Walls Vol 2*. University of Canterbury.

Paulay, T., & Goodsir, W. J. (1985). The Ductility of Structural Walls. *Bulletin of the New Zealand National Society for Earthquake Engineering*, *18*(3), 250–269.

Paulay, T., & Priestley, M. J. N. (1992). *Seismic Design of Reinforced Concrete and Masonry Buildings*. New York: John Wiley and Sons.

Paulay, T., & Priestley, M. J. N. (1993). Stability of Ductile Structural Walls. *ACI Structural Journal*, *90*(4), 385–392.

Paulay, T., & Santhakumar, A. R. (1976). Ductile Behavior of Coupled Shear Walls. *Journal of the Structural Division*, *102*(1), 93–108.

Petracca, M., Candeloro, F., & Camata, G. (2017a). STKO: A Revolutionary Visualization Toolkit for OpenSees. *OpenSees Days Europe, First European Conference on OpenSees*. Porto, Portugal.

Petracca, M., Candeloro, F., & Camata, G. (2017b). *STKO User Manual*. Pescara, Italy: ASDEA Software Technology.

Poudel, A., Lequesne, R. D., & Lepage, A. (2018). *Diagonally Reinforced Concrete Coupling Beams: Effects of Axial Restraint*. (September), 39.

Presland, R. (1999). *Seismic Performance of Retrofitted Reinforced Concrete Bridge Piers*. University of Canterbury.

Rajapakse, R. M. C. M., Wijesundara, K. K., Nascimbene, R., Bandara, C. S., & Dissanayake, R. (2019). Accounting Axial-Moment-Shear Interaction for Force-Based Fiber Modeling of RC Frames. *Engineering Structures*, *184*(May), 15–36. https://doi.org/10.1016/j.engstruct.2019.01.075

Rashid, J., Dowell, R., & Dameron, R. (2000). Recent Advances in Concrete Material Modeling and Application To the Seismic Evaluation and Retrofit of California Bridges. *Proc. 12th World Conference on Earthquake Engineering, Auckland, New Zealand, Paper No.*, 1–8.

Razvi1, S., & Saatcioglu, M. (1999). Confinement Model for High-Strength Concrete. *J. Struct. Eng.*, *125*(March), 281–289.

Restrepo-Posada, J. I. (1993). *Seismic Behaviour of Connections between Precast Concrete Elements*. University of Canterbury.

Restrepo, J. I., & Rahman, A. (2007). Seismic Performance of Self-Centering Structural Walls Incorporating Energy Dissipators. *Journal of Structural Engineering*, *133*(11), 1560–1570. https://doi.org/10.1061/(asce)0733-9445(2007)133:11(1560)

Rokugo, K., Iwasa, M., Susuki, T., & Koyanagi, W. (1989). Testing Method to Determine Tensile Softening Curve and Fracture Energy of Concrete. *Fracture Toughness and Fracture Energy*, 153–163.

Rosso, A., Almeida, J. P., & Beyer, K. (2016). Stability of Thin Reinforced Concrete Walls under Cyclic Loads: State-of-the-art and New Experimental Findings. *Bulletin of Earthquake Engineering*, *14*(2), 455–484. https://doi.org/10.1007/s10518-015-9827-x

Santhakumar, A. R. (1974). *The Ductility of Coupled Shear Walls*. University of Canterbury.

Shiu, K. N., Aristizabal-Ochoa, J. D., Barney, G. B., Fiorato, A. E., & Corley, W. G. (1981). *Earthquake Resistant Structural Walls: Coupled Wall Tests*. Stokie, IL.

Stevens, N., Uzumeri, S., Collins, M., & Will, T. (1991). Constitutive Model for Reinforced Concrete Finite Element Analysis. *ACI Structural Journal*, *88*(1), 49–59.

Taleb, R., Tani, M., & Kono, S. (2016). Performance of Confined Boundary Regions of RC Walls Under Cyclic Reversal Loadings. *Journal of Advanced Concrete Technology*, *14*(4), 108–124. https://doi.org/10.3151/jact.14.108

TBI 17. (2017). *Guidelines for Performance Based Seismic Design of Tall Buildings*. Berkeley, CA.

Thomsen, J. H., & Wallace, J. W. (1995). *Displacement Based Design of Reinforced Concrete Structural Walls: an Experimental Investigation of Walls with Rectangular and T-Shaped Cross-Sections*.

Thomsen, J. H., & Wallace, J. W. (2004). Displacement-Based Design of Slender Reinforced Concrete Structural Walls — Experimental Verification. *J. Struct. Eng.*, *130*(4), 618–630.

Toprak, A. E., Bal, I. E., & Gülay, F. G. (2015). Review on the Macro-Modeling Alternatives and a Proposal for Modeling Coupling Beams in Tall Buildings. *Bulletin of Earthquake Engineering*, *13*(8), 2309–2326. https://doi.org/10.1007/s10518-014-9720-z

Tran, T. A., Motter, C. J., Segura, C., & Wallace, J. W. (2017). Strength and Deformation Capacity of Shear Walls. *16th World Conference on Earthquake Engineering*, 1–10. Santiago, Chile.

Tuna, Z., Gavridou, S., Wallace, J. W., Nagae, T., & Matsumori, T. (2012). 2010 E-Defense Four-Story Reinforced Concrete and Post-Tensioned Buildings - Preliminary Comparative Study of Experimental and Analytical Results. *15th World Conference on Earthquake Engineering, Lisbon Portugal*. Lisbon, Portugal.

Ugalde, D., Parra, P. F., & Lopez, D. (2019). Assessment of the Seismic Capacity of Tall Wall Buildings Using Nonlinear Finite Element Modeling. *Bulletin of Earthquake Engineering*, (0123456789). https://doi.org/10.1007/s10518-019-00644-x

Vallenas, J. M., Bertero, V. V., & Popov, E. P. (1979). *Hysteretic Behavior of Reinforced Concrete Structural Walls*.

Vecchio, F. J., & Collins, M. P. (1986). The Modified Compression-Field Theory for Reinforced Concrete Elements Subjected to Shear. *ACI Journal*, *83–22*(2), 219–231. https://doi.org/10.14359/10416

Vulcano, A. (1992). Use of Wall Macroscopic Models in the Nonlinear Analysis of RC Frame-Wall Structures. *World Conference on Earthquake Engineering*. Rotterdam, Netherlands: Balkema.

Wallace, J. W. (2012). Behavior, Design, and Modeling of Structural Walls and Coupling Beams - Lessons from Recent Laboratory Tests and Earthquakes. *International Journal of Concrete Structures and Materials*, *6*(1), 3–18. https://doi.org/10.1007/s40069-012-0001-4

Wallace, J. W., Massone, L. M., Bonelli, P., Dragovich, J., Lagos, R., Lüders, C., & Moehle, J. (2012). Damage and Implications for Seismic Design of RC Structural Wall Buildings. *Earthquake Spectra*, *28*(SUPPL.1), 281–299. https://doi.org/10.1193/1.4000047

Wang, B., Jiang, H., & Lu, X. (2017). Experimental and Numerical Investigations on Seismic Behavior of Steel Truss Reinforced Concrete Core Walls. *Engineering Structures*, *140*, 164–176. https://doi.org/10.1016/j.engstruct.2017.02.055

Zekioglu, A., Willford, M., Jin, L., & Melek, M. (2007). Case Study Using the Los Angeles Tall Buildings Structural Design Council Guidelines: 40-Storey Concrete Core Wall Building. *Structural Design of Tall and Special Buildings*, *16*(5), 583–597. https://doi.org/10.1002/tal.434

Zhang, P., Restrepo, J. I., Conte, J. P., & Ou, J. (2017). Nonlinear Finite Element Modeling and Response Analysis of the Collapsed Alto Rio Building in the 2010 Chile Maule Earthquake. *Structural Design of Tall and Special Buildings*, *26*(16). https://doi.org/10.1002/tal.1364

Zhao, J., & Sritharan, S. (2007). Modeling of Strain Penetration Effects in Fiber-Based Analysis of Reinforced Concrete Structures. *ACI Structural Journal*, *104*(2), 133–141.

Zhao, Z. Z., Kwan, A. K. H., & He, X. G. (2004). Nonlinear Finite Element Analysis of Deep Reinforced Concrete Coupling Beams. *Engineering Structures*, *26*(1), 13–25. https://doi.org/10.1016/j.engstruct.2003.08.014